university of groningen

SURGICAL ROBOTICS LABORATORY

Control of tetherless magnetic helical devices using a synchronized rotating magnetic actuation system Zhengya Zhang

Control of Tetherless Magnetic Helical Devices Using A Synchronized Rotating Magnetic Actuation System

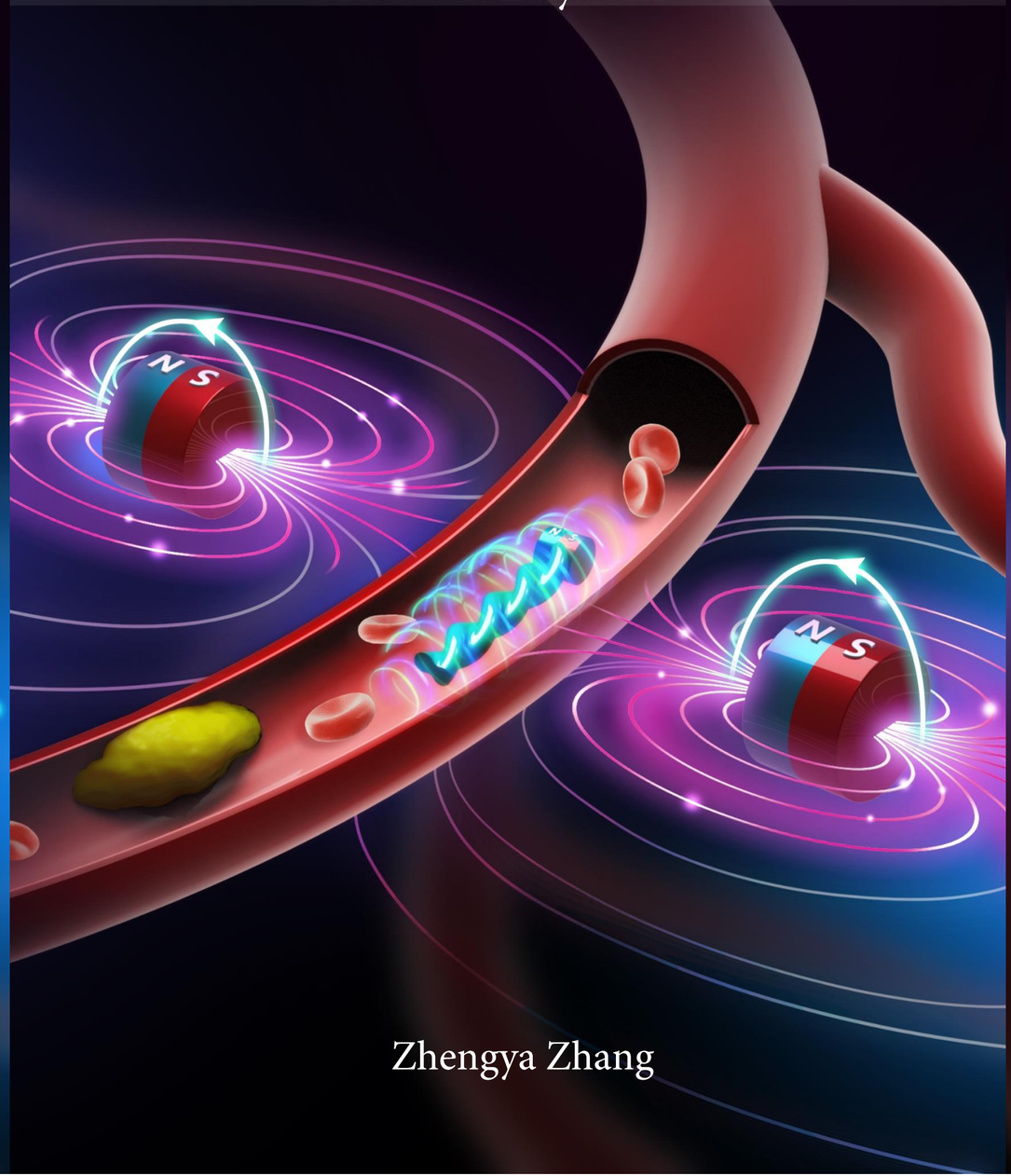

Zhengya Zhang

Invitation

You are cordially invited to attend the public defense of the PhD thesis entitled

Control of Tetherless Magnetic Helical Devices Using A Synchronized Rotating Magnetic Actuation System

By

Zhengya Zhang

Monday
9 September 2024
12:45 hrs

In the Aula of the Academy Building of the University of Groningen

Broerstraat 5,
Groningen

Paranymphs:

Zihan Wang
Zhuoyue Wang

CONTROL OF TETHERLESS MAGNETIC HELICAL DEVICES USING A SYNCHRONIZED ROTATING MAGNETIC ACTUATION SYSTEM

Zhengya Zhang

university of groningen

Control of Tetherless Magnetic Helical Devices Using A Synchronized Rotating Magnetic Actuation System

PhD thesis

to obtain the degree of PhD at the
University of Groningen
on the authority of the
Rector Magnificus Prof. J.M.A. Scherpen
and in accordance with
the decision by the College of Deans.

This thesis will be defended in public on

Monday 9 September 2024 at 12.45 hours

by

Zhengya Zhang

born on 16 November 1988
in Anhui, China

Supervisors

Prof. S. Misra

Dr. I.S.M. Khalil

Assessment Committee

Prof. W. Xue

Prof. M. Hong

Dr. P. K. Sharma

This work is part of the research project MAESTRO.

The reported research is supported by the European Research Council (ERC) under the European Union Horizon 2020 Research, Innovation programme under Grant 866494 project MAESTRO, and China Scholarship Council.

This dissertation has been approved by:

Prof. Dr. Sarthak Misra
Dr. Islam S. M. Khalil

Cover design: Zhengya Zhang
Lay-out: Sumit Mohanty
Printed by: Ipskamp

In memory of my grandma

Samenvatting

Tetherless magnetische helische apparaten (TMHDs), inclusief varianten in de vorm van een helix, schroef en twist, tonen aanzienlijk potentieel in biomedische toepassingen, met name vanwege hun vermogen om op afstand te worden aangestuurd om diep in weefsels binnen het menselijk lichaam te navigeren. Het primaire doel van dit proefschrift is om stabiele en effectieve navigatie van TMHDs te bereiken in fysiologische omgevingenen en daarmee het fundament te leggen voor hun integratie in biomedische toepassingen zoals gerichte geneesmiddelafgifte en materiaalverwijdering. **Hoofdstuk 1** biedt een uitgebreid overzicht van verschillende aspecten met betrekking tot TMHDs, waaronder hun diverse varianten, magnetische aandrijfsystemen, lokalisatiesensortechnologieën, en hun uitgebreide toepassingen in het biomedische veld. Dit overzicht dient als waardevolle referentie voor de ontwikkeling van op permanente magneten gebaseerde robotische systemen in **Hoofdstuk 2**, en het ontwerp en de controle van TMHDs in **Hoofdstukken 3 en 4**.

Het magnetische veld dat wordt geproduceerd door robotsystemen op basis van elektromagneten en permanente magneten is een haalbare optie als externe stimulus om de beweging van een TMHD in fysiologische omgevingen mogelijk te maken. **Hoofdstuk 2** presenteert een op permanente magneten gebaseerd robotisch systeem met een open configuratie, waarbij twee gesynchroniseerde roterende permanente magneten worden gebruikt om tijd-variërende roterende magnetische velden te genereren. Deze velden worden gebruikt om een koppel te genereren op een TMHD in stromingsomgevingen met een laag Reynolds-getal. De configuratie van het systeem is verticaal symmetrisch, waardoor permanente magneten een gradiëntvrije ruimte kunnen uitoefenen binnen het midden van de werkruimte. De kinematica van configuratie naar positie en de mapping van positie naar veld van het systeem zijn afgeleid. Een dergelijke afleiding vormt de basis voor het realiseren van de bewegingsbesturing van TMHDs in driedimensionale ruimte. Het kinematische systeem heeft één translatie-vrijheidsgraad en drie rotatie-vrijheidsgraden, waardoor het de houding van actuatormagneten met vier vrijheidsgraden kan regelen. Het niet-lineaire inverse kinematische probleem wordt opgelost met behulp van

een optimalisatie-algoritme. De experimentele resultaten van dit niveau van controle tonen aan dat de gemiddelde absolute fout en de maximale volgfout van driedimensionale bewegingsbesturing respectievelijk 1.18 mm en 2.64 mm zijn.

Om het gewenste zwemgedrag van TMHDs in fysiologische omgevingen te bereiken, is het van essentieel belang om de factoren te onderzoeken die hun zwemgedrag beïnvloeden onder die specifieke omstandigheden. **Hoofdstuk 3** presenteert een variant van TMHD, genaamd tetherless magnetische schroefvormige apparaten (TSMDs), die wordt gekenmerkt door het gesloten-lusgedrag van een agar gel weefselmodel met behulp van ons op permanente magneten gebaseerde robotische systeem. De voorgestelde gesloten-lus besturingsstrategie maakt gebruik van een analytische berekening van de zwemsnelheid van de TSMD in visco-elastische vloeistoffen en de magnetische punt-dipool benadering van magnetische velden. De analytische oplossing is gebaseerd op de Stokes/Oldroyd-B vergelijkingen, en de voorspellingen worden vergeleken met experimentele resultaten bij verschillende aandrijffrequenties van de TSMD. Onze metingen komen overeen met de theoretische voorspelling van het analytische model vóór de step-out frequentie van de schroef, vanwege de lineariteit van het analytische model. We demonstreren open-lus besturing in tweedimensionale ruimte, en punt-tot-punt gesloten-lus bewegingsbesturing van de TSMD (lengte en diameter van respectievelijk 6 mm en 2 mm) met een maximale positioneringsfout van 1,8 mm.

Hoofdstuk 4 presenteert een variant van TMHD, genaamd tetherless twist-vormige magnetische apparaten (TTMDs), die wordt onderzocht met een analyse van invloedrijke factoren zoals TTMD-geometrische parameters (aantal starts, straal, spoed en amplitude) en aandrijffrequentie op de TTMD-zwemsnelheid in visco-elastische vloeistoffen. Experimenten worden uitgevoerd in een agar gel fantoom onder de aandrijving van een gesynchroniseerd roterend magnetisch veld. De zwemsnelheid van elk type TTMD verkregen uit experimenten werd vergeleken met die voorspeld door een bestaand model voor zwemsnelheid onder een specifieke conditie. Door deze vergelijking ontdekten we het effectieve voorspellingsvermogen van het model voor de TTMD-zwemsnelheid bij lage aandrijffrequenties (onder de step-out frequentie), maar merkten we een afname in nauwkeurigheid op bij hoge aandrijffrequenties (in de buurt van of boven de uitstapfrequentie). Het zwemsnelheid voorspellingsmodel wordt vervolgens toegepast in de con-

text van TTMD-bewegingsbesturings-experimenten, waarbij de geschiktheid ervan voor TTMD-bewegingsbesturing wordt onthuld, met name bij het voorspellen van TTMD-zwemsnelheid in visco-elastische vloeistoffen bij lage aandrijffrequenties (onder de step-out frequentie). Deze mogelijkheid draagt bij aan tijdsbesparing bij het berekenen van TTMD positie informatie.

Hoofdstuk 5 schetst de belangrijkste bevindingen van dit proefschrift, samen met toekomstige richtingen. Het huidige werk legt het fundament voor de volgende stadia in de toepassing van TMHDs in de biomedische techniek.

Summary

Tetherless magnetic helical devices (TMHDs), including helix-, screw-, and twist- shaped variants, exhibit considerable potential in biomedical applications, particularly for their capacity to be remotely controlled to navigate deep tissues within the human body. The primary aim of the thesis is to achieve stable and effective navigation of TMHDs in physiological environments, thereby laying the groundwork for their integration into biomedical applications such as targeted drug delivery and material removal. **Chapter 1** provides a comprehensive overview of various aspects related to TMHDs, encompassing their diverse variants, magnetic actuation systems, localization sensing technologies, and their extensive applications in the biomedical field. This overview serves as a valuable reference for the development of permanent magnet-based robotic systems in **Chapter 2**, and the design and control of TMHDs in **Chapters 3 and 4**.

The magnetic field produced by electromagnet- and permanent magnet-based robotic systems is a viable option as an external stimulus to enable the motion of a TMHD in physiological environments. **Chapter 2** provides a permanent magnet-based robotic system with an open configuration using two synchronized rotating permanent magnets to generate time-varying rotating magnetic fields. These fields are used to apply torque on a TMHD in low-Reynolds-number flow regimes. The configuration of the system is vertically symmetric, allowing permanent magnets to exert gradient-free space within the center of the workspace. The configuration-to-pose kinematics and the pose-to-field mapping of the system are derived. Such derivation is the basis for realizing the motion control of TMHDs in three-dimensional space. The kinematic system holds one translational degree of freedom (DOF) and three rotational DOFs, allowing it to control the pose of actuator magnets with four DOFs. The nonlinear inverse kinematic problem is solved using an optimization algorithm. The experimental results of this level of control demonstrate that the mean absolute error and the maximum tracking error of three-dimensional motion control are 1.18 mm and 2.64 mm, respectively.

To attain the desired swimming behaviors of TMHDs in physiological environments, it is imperative to investigate the factors that impact

their swimming behaviors in those specific conditions. **Chapter 3** presents one variant of TMHD, called tetherless screw-shaped magnetic devices (TSMDs), which is characterized by the closed-loop behavior of an agar gel tissue phantom using our permanent magnet-based robotic system. The proposed closed-loop control strategy capitalizes on an analytical calculation of the swimming speed of the TSMD in viscoelastic fluids and the magnetic point-dipole approximation of magnetic fields. The analytical solution is based on the Stokes/Oldroyd-B equations, and its predictions are compared to experimental results at different actuation frequencies of the TSMD. Our measurements match the theoretical prediction of the analytical model before the step-out frequency of the screw, owing to the linearity of the analytical model. We demonstrate open-loop control in two-dimensional space and point-to-point closed-loop motion control of the TSMD (length and diameter of 6 mm and 2 mm, respectively) with a maximum positioning error of 1.8 mm.

Chapter 4 presents one variant of TMHD, called tetherless twist-shaped magnetic devices (TTMDs), which is examined with an analysis of influential factors such as TTMD geometry parameters (Number of Starts, Radius, Pitch, and Amplitude) and actuation frequency on TTMD swimming speed in viscoelastic fluids. Experiments are performed in an agar gel phantom under the actuation of a synchronized rotating magnetic field. The swimming speed of each type of TTMD obtained from experiments was compared with that predicted by an existing swimming speed prediction model under a specific condition. Through this comparison, we discover the model's effective prediction capability for TTMD swimming speed at low actuation frequencies (below the step-out frequency), yet note a decrease in accuracy at high actuation frequencies (near or above the step-out frequency). The swimming speed prediction model is then applied in the context of TTMD motion control experiments, revealing its suitability for TTMD motion control, particularly in predicting TTMD swimming speed in viscoelastic fluids at low actuation frequencies (below the step-out frequency). This capability contributes to time savings in computing TTMD position information.

Chapter 5 outlines the primary findings of this thesis, along with future directions. The present work establishes the groundwork for the subsequent stages in the application of TMHDs in biomedical engineering.

Contents

1

Introduction

Miniature devices, varying in size from micrometers to millimeters, with the ability to perform specific tasks, hold significant applications in the field of biomedicine [1]–[3], environmental protection [4]–[6], aerospace [7]–[9]. Based on the energy sources that actuate the miniature devices, they can be classified into acoustic devices [10]–[12], optical devices [13]–[15], magnetic devices [16]–[18]. Among these devices, magnetic devices attract the most attention because of their exceptional precision in control, versatility, and low power consumption. In particular, tetherless magnetic devices, as a subclass of magnetic device, are distinguished with their wireless actuation capabilities. Tetherless magnetic devices achieve wireless actuation through their responsiveness to the stimuli of the external magnetic field. Thereon, the motion control of tetherless magnetic devices becomes attainable by manipulating the characteristics of an external magnetic field, such as intensity, direction, and spatial distribution. Such wireless controllability opens up the possibility of remotely using miniature tetherless magnetic devices as tools in environments where larger instruments are impractical. As a result, it enables them a competitive advantage, notably in minimizing patient trauma during surgical interventions, exemplified in procedures like minimally invasive surgery [19]–[23].

Categorized by the flexibility of materials composing their structure, tetherless magnetic devices fall into two primary divisions: tetherless magnetic rigid devices and tetherless magnetic soft devices. Tetherless magnetic rigid devices are fashioned from rigid or hard materials, ensuring stable, robust frameworks ideal for precise control and stability-centric tasks.

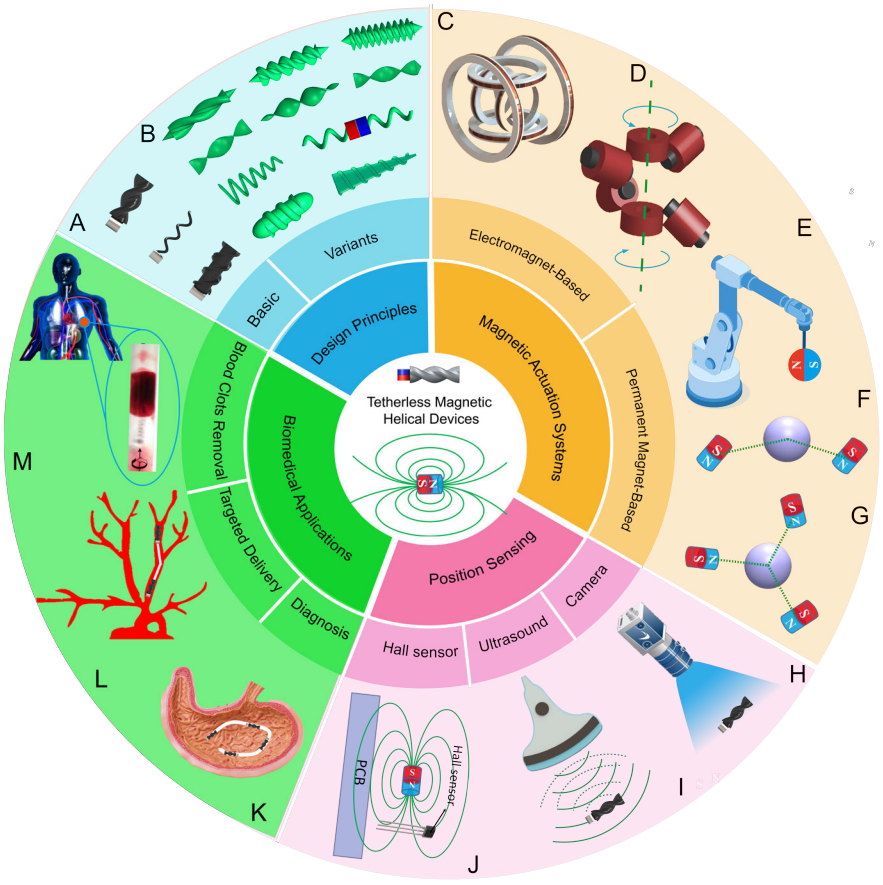

Figure 1.1: Design, actuation, localization, and application of tetherless magnetic helical devices (TMHDs): (A) The basic types of TMHDs, (B) The variants of TMHDs, (C) Stationary electromagnetic actuation system, (D) Mobile electromagnetic actuation system, (E) Single permanent magnet-based actuation system, (F) Dual permanent magnet-based actuation system, (G) Multiple permanent magnet-based actuation system, (H) Hall sensor-based position sensing, (I) Utrasound-based position sensing, (J) Camera-based position sensing, (K) Medical Diagnosis, (L) Targeted Delivery, (M) Blood clots removal.

Conversely, tetherless magnetic soft devices are fashioned using flexible or extensible materials, granting them flexibility and deformability [24]–[28], making them better suited for adaptive environments or applications necessitating suppleness. The body of tetherless magnetic rigid devices can

be designed into various shapes such as spherical shape [29], helical shape [30], or burr-like porous spherical structure [31], to enhance their maneuverability in complex environments. Tetherless magnetic rigid devices with a helical shape, called tetherless magnetic helical devices (TMHDs), undergo rotational motion when subjected to a rotating magnetic field. Such rotation creates a twisting motion in the surrounding fluid, generating a reactive force that propels the TMHDs forward.

To encapsulate the evolution of TMHDs, several pertinent examples will be presented, highlighting the design principles, actuation systems, position sensing, and applications within the biomedical sphere (Fig. 1.1). Section 1.1 delves into the design principles. TMHDs are divided into basic types (Fig. 1.1A) and variants derived from these basic types (Fig. 1.1B). Section 1.2 introduces magnetic actuation systems categorized into two groups: those utilizing electromagnetic coils and those relying on permanent magnets. Further subdivision reveals that electromagnetic coils-based actuation systems can be classified into stationary and mobile types (Figs. 1.1C and 1.1D), while permanent magnet-based actuation systems can be categorized as single permanent magnet-based type (Fig. 1.1E), dual permanent magnet-based type (Fig. 1.1F), and multiple permanent magnet-based type (Fig. 1.1G). Section 1.3 explores position sensing technology utilized by TMHDs, involving camera vision-based sensing (Fig. 1.1H), ultrasound-based sensing (Fig. 1.1I), and hall sensor-based sensing (Fig. 1J). Section 1.4 introduces the biomedical uses of TMHDs, encompassing three areas: medical diagnosis (Fig. 1.1K), targeted delivery (Fig. 1.1L), and blood clots removal (Fig. 1.1M). The final section offers our perspectives and highlights the challenges encountered within the domain of TMHDs.

1.1 Design principles of tetherless magnetic helical devices

TMHDs can navigate in a low-Reynolds-number environment due to their miniature dimensions. Under low-Reynolds-number environments, viscous forces are relatively pronounced, while inertial effects are comparatively weak. This results in fluid behavior being primarily governed by viscous effects. Researchers have created diverse shapes by modifying the elements that make up a TMHD, catering to task requirements in low-Reynolds-

number environments. The elements making up the structure of a TMHD include basic types, head tip types, and geometric parameters, as depicted in Fig. 1.2(a). The three fundamental types of TMHDs are those that are helix-shaped, screw-shaped, and twist-shaped. The ends of a TMHD can be designed as either flat or tapered, depending on the specific requirements for drilling. The geometrical parameters, such as the pitch, diameter, length, taper, frame thickness, and cross-section shape, can be fine-tuned to achieve optimal propulsion efficiency. Achieving such optimization demands a thorough understanding of the swimming characteristics of TMHDs. The optimal design of TMHDs is predominantly undertaken through theoretical studies, experimental methodologies, or simulation techniques facilitated by specialized software.

Tetherless helix-shaped magnetic devices (THMDs), as a subclass of TMHD, have been extensively studied to improve their swimming performance. In theoretical research, Purcell introduced a comprehensive propulsion model [44], [45], facilitating the computation of non-fluidic applied torque and force on a THMD using translational and angular speeds encapsulated in a propulsion matrix. Each element of this matrix is a function of THMD geometrical parameters and fluid viscosity, employing the resistive force theory [46]. This model provides a quantifiable means for exploring the impact of THMD geometry and fluid viscosity on swimming speed within a low-Reynolds-number environment. It establishes a foundation for optimizing THMD design to improve its fluidic performance. Building upon this model, Wang *et al.* investigated the influence of geometric parameters, such as pitch, radius, and frame thickness of a THMD (Fig. 1.2(b)-i), on its swimming performance [32]. This performance was characterized by parameters such as relative velocity, relative maximum velocity, relative step-out frequency, and the relative slope of v/ω (where v and ω represent the translational velocity and angular velocity of a THMD, respectively). These investigations were conducted theoretically to establish a foundation for the geometric design of THMDs. Xin *et al.* introduced a new type of conical hollow THMDs (Fig. 1.2(b)-ii), showcasing a 50% enhancement in forward swimming capability and a 70% reduction in lateral drift compared to straight THMDs through experimental approaches [33]. In addition, employing numerical simulation using the finite element method through commercial software presents a viable approach for optimizing THMD geometric features. Quispe *et al.* explored the optimization

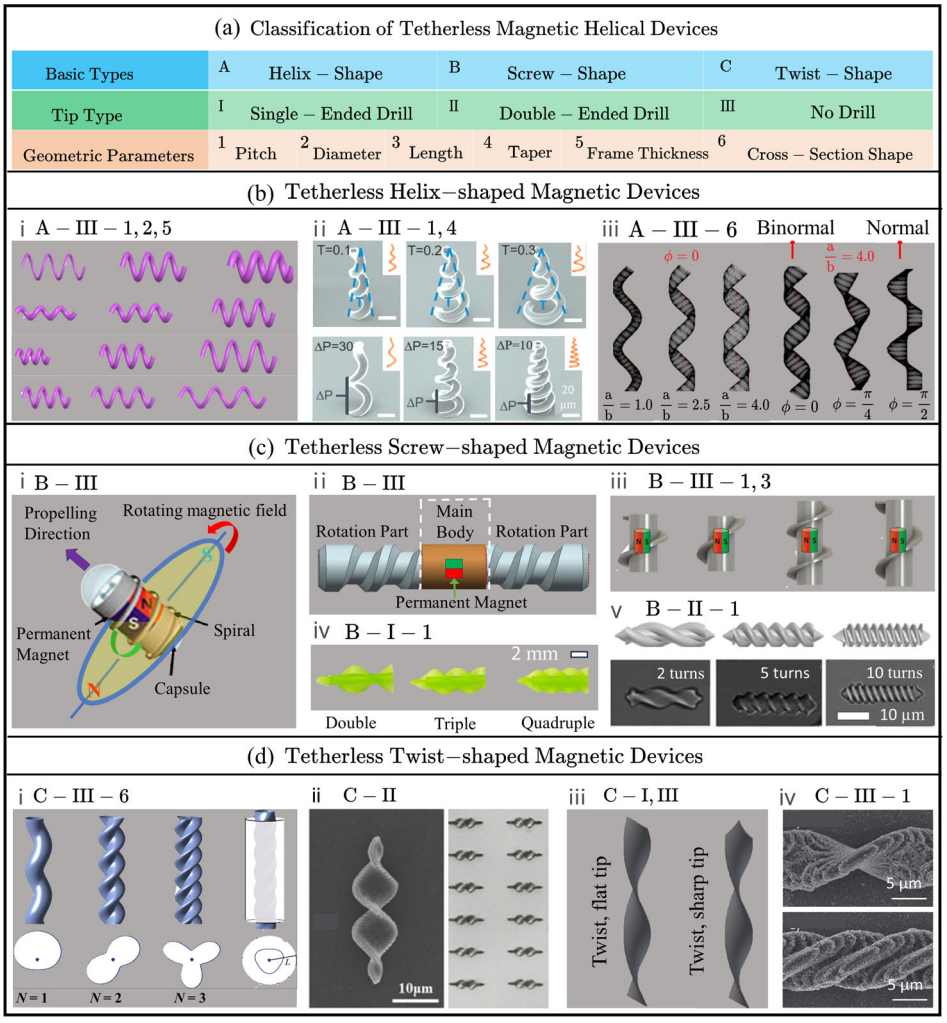

Figure 1.2: Optimal design of tetherless magnetic helical devices (TMHDs). (a) A table shows the elements that make up the structure of a TMHD: three basic types (helix- screw- and twist-type), three tip types (single-ended drill, single-ended drill, and no drill), and geometric parameters (such as pitch, diameter, length, taper, frame thickness, and cross-section shape). (b) Tetherless helix-shaped magnetic devices (THMDs). i, A-III-1,2,5 [32]. ii, A-III-1,4 [33]. iii, A-III-6 [34]. (c) Tetherless screw-shaped magnetic devices (TSMDs). i, B-III [35]. ii, B-III, [36]. iii, B-III-1,3 [37]. iv, B-I-1, [38]. v, B-II-1 [39]. (d) Tetherless twist-shape magnetic devices (TTMDs). i, C-III-6 [40]. ii, C-II [41]. iii, C-II [42]. iv, C-III-1 [43].

of two geometric characteristics linked to the helical shape and cross-section shape (Fig. 1.2(b)-iii) to attain optimal performance in both swimming and pumping [34]. In this context, fluid and structural dynamics are handled using the finite element method with the support of commercial software, COMSOL Multiphysics.

Tetherless screw-shaped magnetic devices (TSMDs), as a subclass of TMHD, have primarily been designed as magnetic capsules. Such designs require researchers to consider not only their swimming capability but also their proficiency to perform particular tasks in the optimal design of the devices' structure. Kusuda *et al.* reported a TSMD designed in the shape of a capsule with an integrated permanent magnet (Fig. 1.2(c)-i). In this instance, the capsule undergoes rotation propelled by a rotating magnetic field. This process generates thrust through the spiral structure on the outer surface of the capsule, allowing for either forward or reverse movement based on the direction of rotation. Guo *et al.* proposed a novel TSMD featuring a symmetrical structure (Fig. 1.2(c)-ii) and gravity compensation, showcasing optimal dynamic traits for forward-backward, upward-downward motion, and inclined plane motion [36]. Leclerc *et al.* devised TSMDs with different pitches and lengths (Fig. 1.2(c)-iii), determining the optimal design for swimming performance through assessment based on average vertical velocity and maximum recorded speed [37]. Lee *et al.* fabricated the TSMDs with varying pitches (Fig. 1.2(c)-iv) to analyze their impact on thrust force and ascertain the optimal pitch for improved propulsion and drilling performance within a three-dimensional (3-D) phantom vascular network [38]. Furthermore, the structure of TSMDs is demonstrated to be not only associated with their locomotion performance but also connected to the interactions between the TSMDs and immune cells. Yasa *et al.* found that macrophages and splenocytes from mice can differentiate and trigger diverse immune responses depending on the helical turn numbers of the TSMDs (Fig. 1.2(c)-v). This phenomenon occurs even when these TSMDs share identical sizes, bulk physical properties, and surface chemistries. Interestingly, the two-turn TSMDs, which demonstrated superior locomotion performance, also turned out to be the most immunogenic [39]. Therefore, optimizing the structure of TSMMs is a viable approach for achieving high locomotion performance and low immunogenicity simultaneously.

Tetherless twist-shaped magnetic devices (TTMDs), as a subclass of

TMHD, have predominantly been developed as magnetic drillers or drug-delivery carriers. Li *et al.* proposed a swimming speed prediction model for TTMDs (Fig. 1.2(d)-i) in viscoelastic fluids, providing guidance for the structural optimization of TTMDs [40]. Li *et al.* revealed that employing a distinctive twisted helical structure, in conjunction with a high aspect ratio in cross-section (Fig. 1.2(d)-ii), facilitates effective navigation of a TTMD with a diameter in the hundreds of micrometers within mouse liver tissue [41]. This provides a reference for the geometric design of TTMDs to move within dense biological tissue. Jia *et al.* reported a TTMD featuring a double-curved conical ribbon structure (Fig. 1.2(d)-iii), with the objective of attaining enhanced stability and eliminating swinging during low-frequency spiral propulsion [42]. In certain scenarios, such as drug delivery, besides pursuing the devices' swimming performance, there is also a need to pursue their load-carrying capacity. Peters *et al.* found that single twist-type TTMDs (Fig. 1.2(d)-iv) exhibit a surface area increase exceeding 150% compared to the THMD with similar feature size without sacrificing the forward speed of more than one body length per second [43]. This results in a micro-robotic platform for swimming with improved load capacity, making it suitable for potential biomedical applications in the future.

1.2 Magnetic actuation systems

Magnetic actuation systems can be categorized into electromagnetic coil-based actuation systems and permanent magnet-based actuation systems. Each system type comes with its own set of strengths and weaknesses. The selection of the most suitable actuation system depends on the particular application scenarios. For instance, in situations requiring a complete shutdown of the magnetic field, the preferred choice would be an electromagnetic coil-based actuation system. Conversely, in scenarios where avoiding the use of an external power source to generate a magnetic field is crucial, a permanent magnet-based actuation system might be the optimal selection.

1.2.1 Electromagnetic coil-based actuation systems

Electromagnet-based actuation systems can generate a relatively uniform magnetic field, which is crucial for specific experiments and tests, especially

when a stable and consistent magnetic field is necessary. Moreover, modulating the coil size and electrical current enables exact adjustment of the magnetic field's strength and orientation, ensuring heightened precision in experimental settings.

The electromagnet-based actuation system can be broadly classified into two main types: stationary, in which electromagnetic coils remain immobile; and mobile, in which either a portion or all of the electromagnetic coils are designed to be movable. One simple and reliable method for constructing a stationary electromagnetic actuation system is to involve the use of orthogonal pairs of coils [47]–[50]. Typically, an electromagnetic actuation system is structured with three sets of orthogonal Helmholtz coils, where each set comprises two identical coils strategically positioned at a specified separation distance (Fig. 1.3(a)). Such an electromagnetic actuation system allows for the accurate and uniform generation of a magnetic field within the central region under controlled conditions. Numerous applications have utilized it for the manipulation of magnetic devices [51]–[56]. To enhance flexibility and exert greater control over the resulting magnetic field, researchers have proposed electromagnetic actuation systems comprising an increased number of coils, exhibiting a more complex configuration. Khalil *et al.* employed an eight-coils-based actuation system (Fig. 1.3(b)). The eight coils are divided into two sets, namely the lower set and upper set, with each set consisting of four coils. The lower set includes four coils positioned at a 45-degree angle to the horizontal plane, and the upper set also contains four coils with a comparable orientation. These sets are mounted orthogonally to each other. This system can produce a maximum magnetic field of 85 mT, and field gradients of 1.62 T/m [57].

Unlike stationary systems that boost their flexibility by augmenting the number of coils, mobile electromagnetic actuation systems improve their flexibility and control capability by enabling controlled movement of the coils. Sikorski *et al.* introduced an electromagnetic actuation system named BigMag (Fig. 1.3(c)), comprising six coils positioned on two symmetrical mobile frames, with each frame accommodating three coils [58]. The system produces magnetic fields of at least 40 mT in all directions within its operational area and delivers gradients of up to 1 T/m. Utilizing the BigMag, Venkiteswaran *et al.* executed the manipulation of a magnetic soft robot employing torque-based actuation [59], or gradient-based actuation [62]. Oliveira *et al.* performed closed-loop motion control on an unteth-

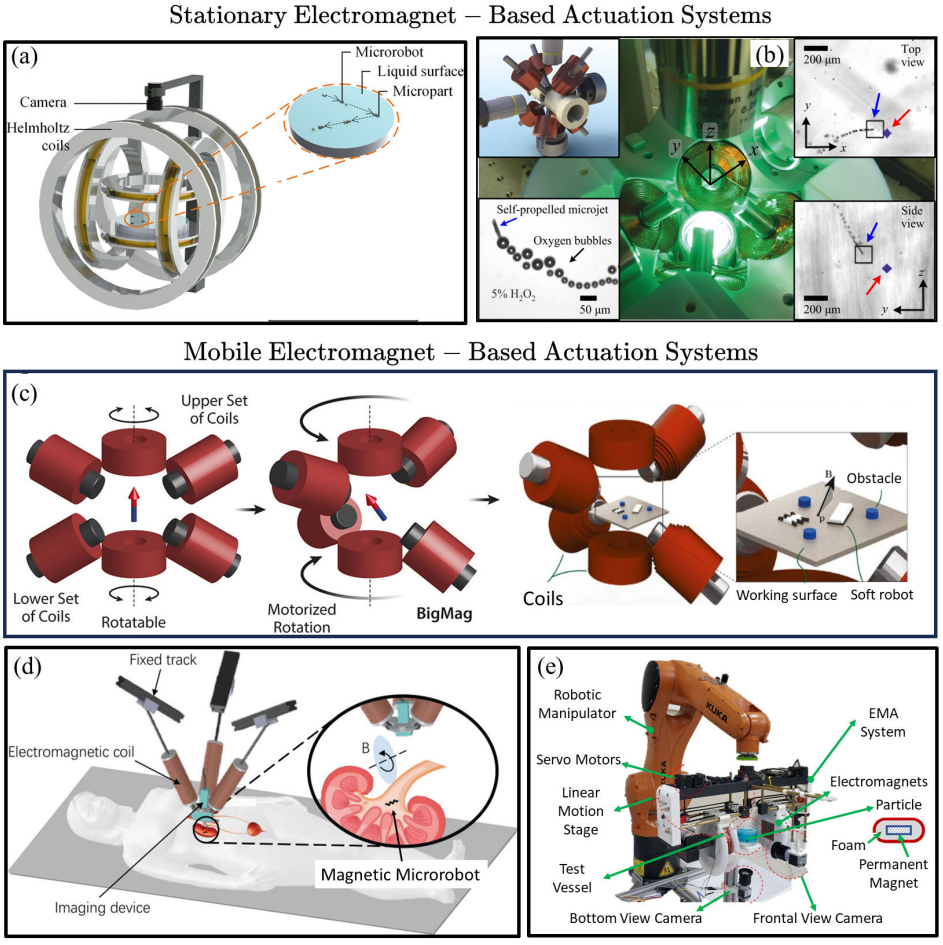

Figure 1.3: Electromagnet-based actuation systems. Stationary electromagnet based actuation systems: (a) Helmholtz coils-based actuation system [56]. (b) Eight electromagnetic coils-based actuation system [57]. Mobile electromagnet-based actuation systems: (c) Six electromagnetic coils-based actuation system (BigMag) [58] [59], (d) Three parallel mobile coils-based electromagnetic actuation system (DeltaMag) [60], (e) Industrial robot-assisted electromagnetic actuation system [61].

ered magnetically-actuated soft robot using ultrasound images for feedback [63]. Despite superior performance in steering magnetic devices, BigMag's workspace size is limited. To pursue extensive workspace, Yang *et al.* pre-

sented an electromagnetic actuation system named DeltaMag (Fig. 1.3(d)), employing parallel mobile coils [64]. The workspace diameter of DeltaMag is 70% of the overall prototype diameter. In a subsequent phase, the study delved into the optimal parameter design of a DeltaMag, which comprises three mobile coils [65]. Utilizing DeltaMag, Yang *et al.* conducted path-following experiments with a magnetic microrobot in a stomach-like model [60]. Additionally, they introduced a navigation framework, representing the initial stride towards achieving autonomous control of a magnetic microrobot in a large workspace [66]. To increase flexibility in the positioning of the coils in a DeltaMag, one improved approach is to replace all the linkages with robotic arms. This approach may address potential constraints within the workspace of the DeltaMag. Following this line of thought, Du *et al.* developed an electromagnetic actuation system named RoboMag, comprising three 4-axis robotic arms capable of independently adjusting the relative positions of three mobile coils [67]. The RoboMag prototype has the capability to program a magnetic field at a specified point within a hemispherical space with a diameter of 152 mm. Utilizing RoboMag, they navigated a magnetic device with the assistance of ultrasound imaging in phantoms mimicking tissue with branching and tortuous structures [68]. An alternative approach for coils with mobility is to mount the coils at the end effector of an industrial robotic manipulator. Alasli *et al.* showcased an electromagnetic actuation system integrating a 6-degree-of-freedom industrial robotic manipulator with electromagnets that can move coaxially (Fig. 1.3(e)) [61].

Nevertheless, electromagnet-based actuation systems require a substantial amount of electrical power to generate a magnetic field, leading to heightened energy consumption. Consequently, achieving a magnetic field of sufficient intensity or stability might not be feasible in certain situations. An alternative solution to tackle this issue could be a permanent magnet-based actuation system.

1.2.2 Permanent magnet-based actuation systems

Permanent magnet-based actuation systems can produce a continuous magnetic field without requiring external power supply maintenance. Typically, these actuation systems can be classified into single permanent magnet-based actuation systems, dual permanent magnet-based actuation systems,

and multi permanent magnet-based actuation systems.

Single permanent magnet-based actuation systems often require simplified system complexity because handling a single permanent magnet is generally less intricate than controlling multiple magnets. A popular method for constructing such a system involves utilizing an industrial robot to manipulate an actuator permanent magnet (Fig. 1.4(a)), thereby regulating the magnetic field and field gradient at the magnet's location on magnetic devices [69], [70]. Despite the rapid and convenient setup of the actuation system with this approach, singularities may still be present in the system [71]. To address this issue, Wright *et al.* reported an actuation system (Fig. 1.4(b)), incorporating three omniwheels to achieve holonomic control over the orientation of its magnet's dipole, enabling continuous rotation of its magnet around any axis [72].

In contrast to single permanent magnet-based actuation systems, dual permanent magnet-based actuation systems allow for better adjustment and manipulation of the magnetic gradient, providing increased versatility in magnetic field shaping. Valdastri *et al.* reported an actuation system (Fig. 1.4(c)) comprising two industrial robots with permanent magnets at the end-effectors [73]. This configuration provides heightened flexibility and adaptability for collaborative tasks, where the two industrial robots collaborate to efficiently execute complex operations. Consequently, the system becomes well-suited for a broader range of applications. However, the integration of two industrial robots can result in a more complex system, requiring sophisticated control algorithms and coordination mechanisms. Hosney *et al.* presented an actuation system consisting of two distinct modules, each integrated with a permanent magnet and attached to a robotic platform (Fig. 4(d)). The noteworthy feature of this system lies in the synchronized rotation of the two permanent magnets [74]. Systems of this nature possess the ability to diminish or weaken the magnetic gradient force acting on the magnetic devices, consequently stabilizing their motion.

Multi-permanent magnet-based actuation systems employ a set of permanent magnets to achieve comparable control precision for magnetic devices, offering the possibility of enhanced field and gradient strength with minimal heat generation. Son *et al.* proposed an actuation system utilizing an array of approximately 100 permanent magnets (Fig. 1.4(e)). This configuration establishes a robust magnetic force trap with magnetic gradients of around 7 T/m within soft tissue [75]. The magnetic robot exhibits

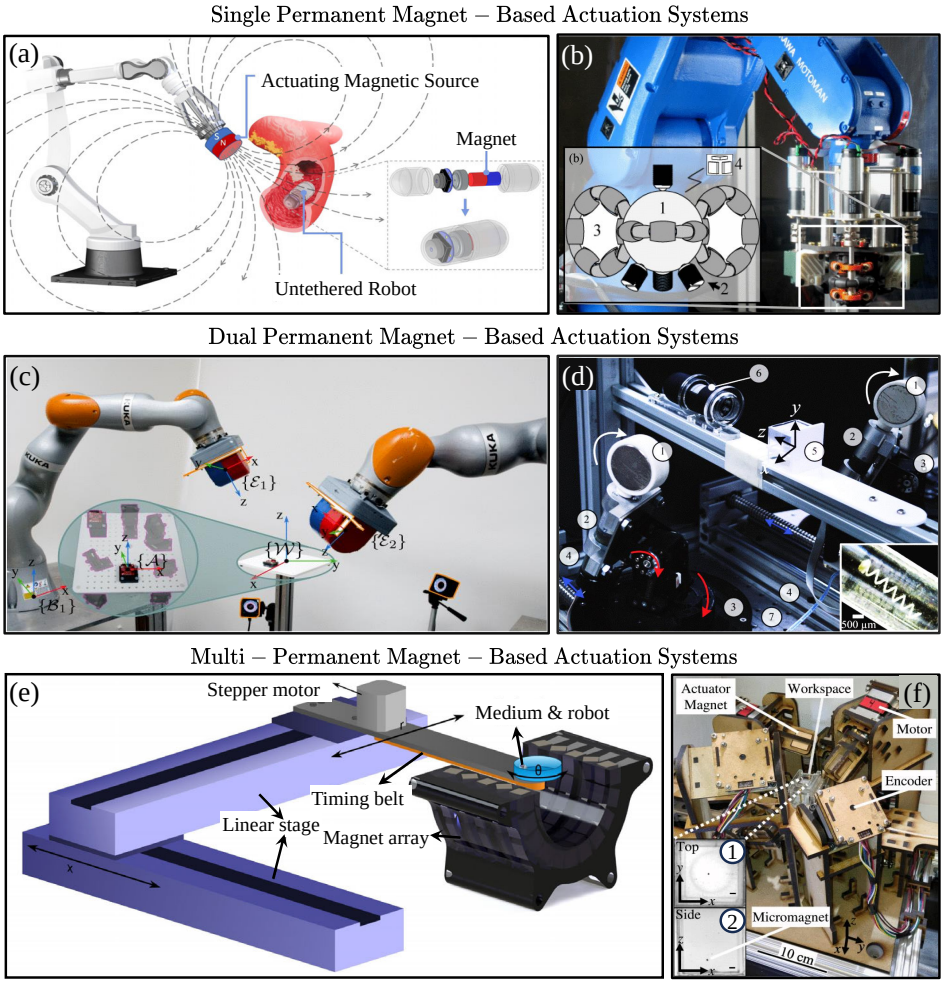

Figure 1.4: Permanent magnet-based actuation systems. Single permanent magnet-based actuation systems: (a) An industrial robot is attached with a cylindrical magnet [69], (b) An industrial robot is attached with a spherical magnet [72]. Dual permanent magnet-based actuation systems: (c) Two industrial robots are equipped with magnets at their end-effectors [73], (d) Two robotic platforms are equipped with magnets at their end-effectors. [74]. Multi-permanent magnet-based actuation systems: (e) An array of approximately 100 magnets is combined with linear and rotational motion stages to navigate magnetic devices [75], (f) Eight magnets are configured without any translational movement [76].

a natural tendency to move toward the center of the array, even without active control. Ryan *et al.* introduced an actuation system equipped with eight permanent magnets (Fig. 1.4(f)), eliminating the necessity for any potentially translational motion of the control magnets. This design results in a secure and cost-effective system [76]. The system showcases the capability to generate fields and field gradients in various directions with variable strengths ranging from zero to 30 mT and 0.83 T/m, respectively.

Moreover, the integration of electromagnetic coils and permanent magnets in an actuation system is also regarded as a feasible solution [77], [78]. The selection between electromagnetic coil-based, permanent magnet-based actuation systems, or integration systems involving both electromagnetic coils and permanent magnets relies on specific application needs while considering factors such as flexibility, adaptability, and system complexity.

1.3 Position sensing

Position sensing technology is essential for the precise navigation of magnetic devices, especially in intricate biological environments. Numerous position sensing technologies, including both image-based and magnetic sensor-based approaches, have been developed for localizing magnetic devices. Image-based approach captures visual information regarding the position of the magnetic robot and its surroundings, utilizing techniques such as camera vision imaging (Fig. 1.5(a)) [79], UltraSound (US) imaging (Fig. 1.5(b)) [80]–[83], Photoacoustic Imaging (PAI) [84]–[86], Magnetic Particle Imaging (MPI) [87]–[89], Magnetic Resonance Imaging (MRI) [90]–[92], X-ray imaging [93]–[95], and Optical Coherence Tomography (OCT) [96]. Such an approach can provide real-time images to guide and monitor the movement of magnetic devices.

The magnetic sensor-based approach determines the position of a magnetic device by measuring the strength and direction of the magnetic field using magnetic sensors such as Hall-effect sensors or magnetoresistive sensors. For example, Géron *et al.* investigated a 2D measurement system specifically designed for micro-robotic applications (Fig. 1.5(c)), employing a Hall-effect sensor array [97]. They also assessed how different physical parameters, such as sensor density and the number of measurements, influence localization errors. Son *et al.* devised a magnetic localization system comprising a 2-D array (8×8) of mono-axial Hall-effect sensors, measur-

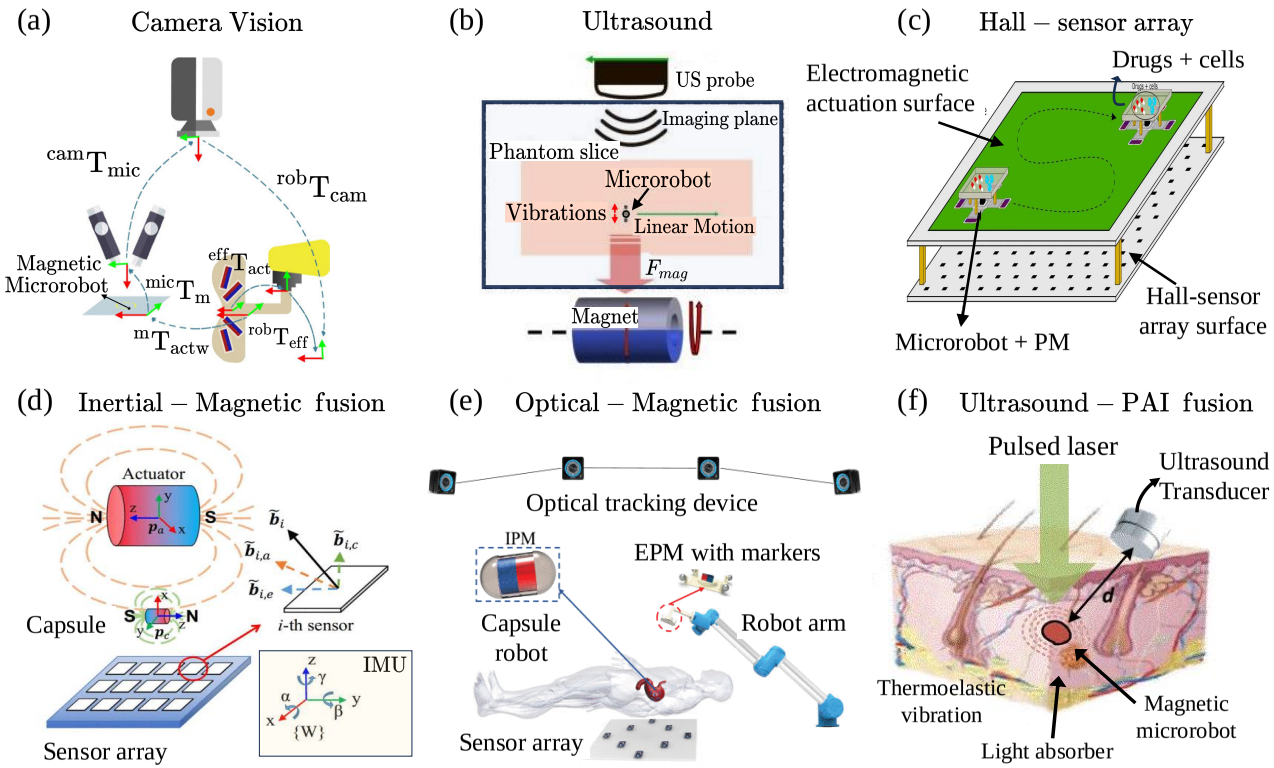

Figure 1.5: Position sensing technologies. (a) Vision-based position sensing [79], (b) Ultrasound-based position sensing [80], (c) Hall sensor-based position sensing [97], (d) Inertial-Magnetic fusion position sensing [98], (e) Optical-Magnetic fusion position sensing [99], (f) Ultrasound-PAI fusion position sensing [100].

ing perpendicular magnetic fields at their designated positions [101]. This system successfully achieved 5-D localization for an untethered mesoscale magnetic robot. Vergne *et al.* created a localization system comprising a 2-D array of 3-D magnetoresistive sensors, called a magnetic field camera, enabling the tracking of a millimeter-sized robot at a refresh frequency of 2 Hz [102]. In addition, researchers have developed sensor fusion technologies to enhance the localization accuracy of magnetic devices. Using Inertial-Magnetic fusion technology, Li *et al.* facilitated a comprehensive estimation of the 6-DOF pose for a magnetic capsule (Fig. 1.5(d)) [98]. Vedaei *et al.* devised a fusion algorithm that integrates all data to deduce the traveled path and visualize the trajectory of a magnetic capsule [103]. Using Optical-Magnetic fusion technology, Shi *et al.* presented an innovative framework for optical-magnetic fusion tracking (Fig. 1.5(e)), specifically designed for real-time monitoring of a magnetically actuated capsule robot [99]. Turan *et al.* utilized deep learning methodologies to tackle the issue of sensor fusion in managing asynchronous and asymmetric sensor data for endoscopic capsule robots, thereby obviating the need for sensor calibration [104]. Utilizing Ultrasound-PAI fusion technology, Gao *et al.* demonstrated a notable enhancement in image contrast on a vessel-mimicking phantom through the amalgamation of ultrasound reflection and optical absorption contrasts (Fig. 1.5(f)) [100]. This advancement could potentially be applied for non-invasive tracking of a magnetic device in non-transparent environments [105]. In addition to these, various other sensor fusion techniques exist, such as Optical-RF (Radio Frequency) fusion technology [106] and Optical-Ultrasound fusion technology [107]. Sensor fusion technology provides powerful tools and methods for positioning magnetic devices, enabling precise localization and navigation in complex and uncertain environments.

1.4 Biomedical applications

As advancements in the design, fabrication, actuation principles, and localization of TMHDs continue to evolve, numerous biomedical applications have emerged to serve their intended purposes. These include medical diagnosis, targeted drug delivery, and removal of blood clots in both *in vivo* and *ex vivo* environments. Consequently, researchers have been evaluating their effectiveness in various biomedical scenarios, offering valuable insights for potential clinical applications.

In the application of medical diagnostics, TMHDs can carry various sensors for detecting internal lesions within the human body. This capability aids physicians in precisely diagnosing diseases and formulating effective treatment strategies. For instance, Qin et al. developed a tumor detection system employing a TMHD composed of PVA/MA/Fe3O4, which incorporates the fluorescent probe SYBR Green. This innovative approach exhibits significant promise for targeted tumor DNA detection, thereby facilitating early detection of cancer [108]. In the application of targeted drug delivery, TMHDs not only reduce systemic side effects but also boost the therapeutic effectiveness of the administered drugs. For example, Lee *et al.* developed a biocompatible and hydrolyzable TMHD for drug delivery, equipped with the capability to separate and retrieve magnetic nanoparticles from the TMHD using a reducing agent (dithiothreitol) and an external stimulus (near-infrared) [109]. In the application of blood clot removal, TMHDs can precisely locate and remove blood clots, reducing damage to surrounding tissues and the occurrence of complications compared to traditional methods such as thrombolytic drugs and surgical thrombectomy. For example, Khalil *et al* reported the mechanical rubbing against blood clots by a TMHD under ultrasound guidance [110]–[112]. To enhance the efficiency of mechanical rubbing of blood clots, Yang *et al.* proposed a strategy to maximize the contribution of magnetic forces to the forward motion of a TMHD by optimizing the coil motion [113]. Aside from these, TMHDs hold considerable promise for a variety of other biomedical applications, such as targeted gene delivery [114] and targeted therapy [115].

In summary, TMHDs demonstrate extensive potential in the realm of biomedical engineering. As technology advances and evolves, an array of new application areas and opportunities will emerge.

1.5 Challenges and prospects

Potential challenges in the clinical utilization of TMHDs encompass: (1) Resistance to interference. In the complex environment within living organisms, TMHDs may encounter hindrances from diverse obstacles, potentially resulting in setbacks in biomedical applications, such as targeted transport. Successfully surmounting these obstacles and improving the adaptability and stability of TMHDs across different environments present challenging tasks. (2) Efficiency in Task Execution. For specific applications, such as

blood clot removal, achieving a higher clearance efficiency is crucial in this context. (3) Biocompatibility: The biocompatibility of TMHD materials is a critical issue. Ensuring the TMHDs pose no harm to biological tissues and does not induce immune reactions is a fundamental requirement for their clinical application in medical environments. (4) Validation of Therapeutic Effectiveness: In clinical scenarios, it becomes imperative to verify the therapeutic efficacy of TMHDs. This encompasses ensuring their capability to proficiently administer medications, conduct surgical procedures, or carry out various therapeutic tasks.

The future development prospects may include: (1) Enhancing Work Environment Adaptability: Elevate the adaptability of magnetic helical devices to diverse working conditions, encompassing their ability to adapt to the intricate environments within living organisms. (2) Advancing Multifunctionality: Develop TMHDs with extended capabilities, including diagnosis, targeted delivery, self-degradation, etc., to broaden their scope of applications in the medical field. (3) Improvement in Biocompatibility: Increase research endeavors to improve the biocompatibility of TMHDs within living organisms, enhancing their suitability for medical and biological applications. (4) Exploration of Collaborative Operations: Delve into the collaborative functionalities of multiple TMHDs for the performance of complex tasks. This could involve coordinated motion, information exchange, and collective behavior. In addition, exploring the nanoscale development of TMHDs holds significant promise for potential applications in both nanomedicine and nanomanufacturing. These prospects underscore the wide array of opportunities for propelling TMHDs forward and their potential influence across multiple domains, encompassing medicine, biotechnology, and beyond.

1.6 Research objective of the thesis

The objective of this thesis is to design and establish a permanent magnet-based robotic system for stable navigation of TMHDs in physiological environments (such as the vitreous humor of the human eye). Additionally, the thesis seeks to examine how the geometric parameters of TMHDs impact their swimming behaviors in fluidic environments. Thereon, the exploration of TMHD swimming behaviors is integrated into the implementation of TMHD motion control. Here, the **first research question (RQ.1)** is

encountered in this doctoral thesis–

RQ.1

How to build a permanent magnet-based robotic system with a large gradient-free workspace enabling tetherless magnetic helical devices to move controllably in physiological environments?

Chapter 2 presents a robotic system that incorporates two synchronized rotating permanent magnets, aiming to achieve 3-D motion control of a TMHD in physiological environments. Agar gel phantoms are selected to simulate physiological environments. In comparison to the actuation systems utilizing one single rotating permanent magnet, those utilizing two synchronized rotating permanent magnets can eliminate or weaken the lateral gradient force subjected to the TMHD. This results in the stabilization of TMHD motion [74]. A symmetrical configuration is employed to ensure the symmetric installation of the two permanent magnets through physical constraints, enabling the stable generation of a gradient-free space between the two permanent magnets. Such a feature allows us to focus on the directional control of a TMHD without needing to account for the magnetic gradient force acting on the TMHD within the gradient-free space, thereby optimizing and streamlining TMHD motion control. Furthermore, the essential tasks for establishing this system encompass the analysis of forward kinematics (mapping from joint space variables to the orientation of the field-rotation axis) and inverse kinematics (mapping from the desired orientation of the field-rotation axis to the desired joint space variables). To express the synthetic magnetic field at any point precisely, an exact magnetic field model is employed [116]. The effectiveness of the system is confirmed through the execution of 3-D closed-loop motion control experiments of a TMHD.

Chapter 3 focuses on the incorporation of a swimming speed prediction model in the motion control of TMHDs. This prediction model is derived based on the assumption that a TMHD undergoes force-free rotation. In **Chapter 2**, the existence of a gradient space between the two synchronized rotating permanent magnets has already been demonstrated, confirming that our permanent magnet-based robotic system can satisfy the conditions required for the utilization of the prediction model. This confirmation paves

the way for the potential application of the prediction model in guiding the motion control of TMHDs within our permanent magnet-based robotic system. Thus, the **second research question (RQ.2)** of this doctoral thesis examines –

RQ.2

How to incorporate a swimming speed prediction model into the motion control of tetherless magnetic helical devices in our permanent magnet-based robotic system?

A control strategy to implement TMHD motion control using the prediction model is proposed in **Chapter 3**. Nonetheless, there is room for further optimization of the control strategy. In **Chapter 4**, a novel control strategy is developed. First, a relationship model is aimed to be built between the synchronized rotation of two identical permanent magnets (characterized by the dipole-rotation axis) and the corresponding magnetic field (characterized by the field-rotation axis) based on the point-dipole model. Then, the correlation between the actuation frequency of synchronized rotating permanent magnets and the swimming speed of TMHDs in an agar gel phantom is explored. This exploration involves validating the swimming speed prediction model. Finally, the motion direction control for a TMHD can be translated into the orientation control for the field-rotation axis, while the motion speed control for a TMHD can be translated into the angular speed control for the dipole-rotation axis. Considering this, the (**third research question (RQ.3)**) of this doctoral thesis explores –

RQ.3

How does the field-rotation axis correlate with the dipole-rotation axis when the two permanent magnets are rotating synchronously?

In **Chapter 5**, the findings from the preceding sections are summarized, and future directions for these research studies are delineated. The present work establishes the foundation for the prospective application of TMHDs in the realm of biomedical engineering.

1.7 Scientific output

The research presented in this doctoral thesis has contributed to the following peer-reviewed articles:

1.7.1 Peer-reviewed international conference article

1. **Z. Zhang**, A. Klingner, S. Misra, and I. S.M.Khalil, *Control of magnetically driven screws in a viscoelastic medium*, in Proceedings of the IEEE/RSJ International Conference on Intelligent Robots and Systems (IROS), Las Vegas, NV, USA, 2020, pp. 25–29.

1.7.2 Peer-reviewed journal articles

1. **Z. Zhang**, A. Klingner, S. Misra, and I. S.M.Khalil, *Design and Control of a Permanent Magnet-Based Robotic System for Navigating Tetherless Magnetic Devices in Viscous Environments*, IEEE Transactions on Automation Science and Engineering, 2024. (Under review)

2. **Z. Zhang**, A. Klingner, S. Misra, and I. S.M.Khalil, *Hydrodynamic Behavior of Twist-Shaped Magnetic Microrobots in Viscoelastic Fluids Driven by a Synchronized Rotating Magnetic Actuation System*, IEEE Transactions on Medical Robotics and Bionics, 2024. (Under review)

3. M. Kaya, F. Stein, P. Padmanaban, **Z. Zhang**, J. Rouwkema, I. S.M.Khalil, and S. Misra, *Visualization of micro-agents and surroundings by real-time multicolor fluorescence microscopy*, Scientific reports, vol. 12, no. 1, p. 13375, 2022.

1.7.3 Abstracts

1. **Z. Zhang**, I. S.M.Khalil, and S. Misra, *3D Control of Magnetically Driven Microrobots in Viscoelastic Medium*, Proceedings of the W.J.Kolff Annual Research days, Groningen, Netherlands, 2021.

2. **Z. Zhang**, I. S.M.Khalil, and S. Misra, *A permanent magnet-based robotic system for the motion control of tetherless magnetic devices*, Proceedings of the W.J.Kolff Annual Research days, Groningen, Netherlands, 2022.

2

Design and Control of a Permanent Magnet-Based Robotic System for Navigating Tetherless Magnetic Devices in Viscous Environments

Note: *Following chapter is adapted from the article "Design and Control of a Permanent Magnet-Based Robotic System for Navigating Tetherless Magnetic Devices in Viscous Environments" by* ***Z. Zhang****, A. Klingner, S. Misra, and I. S.M.Khalil (2024) submitted to "IEEE Transactions on Automation Science and Engineering"*

Abstract

Small-scale tetherless magnetic devices (TMDs) that are driven using external stimuli have potential applications in minimally invasive surgery. The magnetic field produced by electromagnet- and permanent magnet-based robotic systems is a viable option as an external stimulus to enable the motion of a TMD in viscous and viscoelastic media. In order to realize the navigation of TMDs in fluidic environments, we design a permanent magnet-based robotic system with an open configuration using two synchronized rotating magnetic dipoles to generate time-varying magnetic fields. These fields are used to apply torque on a TMD in low-Reynolds-number flow regimes. The configuration of the system is vertically symmetric, allowing permanent magnets to exert homogeneous magnetic fields within

the center of the workspace. We derive the configuration-to-pose kinematics and the pose-to-field mapping of the system. Such derivation is the basis for realizing the motion control of TMDs in three-dimensional space. The kinematic system holds one translational degree of freedom (DOF) and three rotational DOFs, allowing it to control the pose of actuator magnets with four DOFs. The nonlinear inverse kinematic problem is solved using an optimization algorithm. The experimental results of this level of control demonstrate that the mean absolute error and the maximum tracking error of three-dimensional motion control are 1.18 mm and 2.64 mm, respectively.

2.1 Introduction

Small-scale tetherless magnetic devices (TMDs) have the potential to improve minimally invasive medicine by precision surgery due to their dexterity [117], allowing them to access regions inaccessible by tethered surgical devices. With these merits, small-scale TMDs have attracted significant attention for being utilized in biomedical applications such as targeted drug delivery [118], [119], nanotechnology [120], [121], microfluidic [122], [123] and biomedical [111], [124] applications. One of the challenges in these applications is the precise TMD motion control along a prescribed trajectory [125]–[127]. The vast majority of TMD motion control is achieved by using electromagnet-based robotic systems [128]–[131]. Despite the merit of high controllability of generated uniform magnetic field (including orientation and strength control) by changing the coil current and the ability to turn off the magnetic field completely, these systems have some shortcomings, such as the difficulty of scaling up to the size of *in vivo* application due to the restriction of the projection distance of the field gradient and heat emission problem due to the low efficiency of electric-to-magnetic conversion caused by the electromagnetic coils [132]. In contrast to electromagnet-based robotic systems, permanent magnet-based robotic systems can generate stronger magnetic fields [133] and have no heat emission problem. In particular, those with open configurations can be scaled up to the size of *in vivo* applications [134]. Consequently, permanent magnet-based robotic systems become increasingly popular.

Depending on how a TMD is propelled, permanent magnet-based robotic systems can be classified based on the applied driving mode: (1) Torque-driven mode, which serves the magnetic torque as the main form of actu-

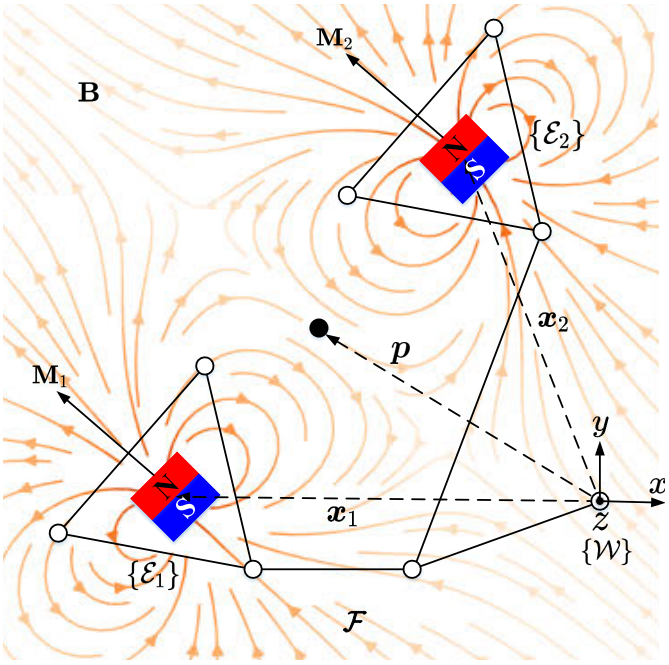

Figure 2.1: The magnetic field at a point ($\boldsymbol{p}$) is characterized by the configuration-to-pose kinematics ($\mathcal{F}$), and the pose-to-field mapping ($\mathbf{B}$) under the global frame of reference $\{\mathcal{W}\}$. Additionally, the ith magnetic source is arranged in a local frame of reference $\{\mathcal{E}_i\}$.

ation and propels a TMD (e.g., a helical microrobot) by rotating it. (2) Force-driven mode which serves magnetic force (i.e., the force due to magnetic gradient) as the main form of actuation and propels TMD by pulling it. (3) Torque-force-driven mode, which serves either one of them (magnetic torque and force) or both of them as effective forms of actuation and to propel a TMD by rotating it or pulling it or both. Furthermore, permanent magnet-based robotic systems in each mode can be generalized into three categories based on the number of actuator magnets: (1) Using one actuator magnet. (2) Using two actuator magnets. (3) Using an array of actuator magnets.

Permanent magnet-based robotic systems in torque-driven mode rotate actuator magnets to generate a rotating magnetic field, resulting in a

magnetic torque, which is the main source of actuation exerted on TMDs. With using one actuator magnet, Mahoney *et al.* have proposed a method to control the magnetic field at a point in space to be rotated about any desired axis with a constant frequency, thus the TMD motion is controlled by aligning the TMD's dipole moment with the applied magnetic field [135]. Nelson *et al.* have provided a solution to generate two independent rotating magnetic fields with any desired field-rotation axes at any two points, allowing it for the independent motion control of two TMDs [136]. Wright *et al.* have developed a robotic system by attaching a mechatronic device to the end of a robotic manipulator such that the mechatronic device houses a uniformly magnetized spherical magnet, enabling holonomic control of the heading of the spherical magnet and allowing the rotation axis of the spherical magnet to be set arbitrarily [72]. Despite the controllability of the field-rotation axis, such systems may produce unnecessary magnetic force, which creates a tendency for a TMD to move toward the actuator magnet. This unnecessary magnetic force can be reduced by increasing the distance between the TMD and the actuator magnet, yet the applied magnetic torque on the TMD is inevitably weakened. To overcome this undesired behavior, Mahoney *et al.* have presented a strategy to substantially reduce the magnetic force while maximizing the magnetic torque by limiting the absolute upper boundary on the magnitude of maximum magnetic force for any orientation of TMD dipole moment [137]. This strategy can diminish the magnetic force yet not eliminate it. With using two actuator magnets, Hosney *et al.* have designed a robotic system by rotating the two actuator magnets synchronously for the wireless motion control of a helical microrobot, which stabilizes the motion of the microrobot by eliminating the magnetic field gradient within the workspace of the microrobot and develops gravity compensation technology by manipulating the angular speed and motion direction of the microrobot [74]. Further, this system has been applied to the biomedical application of removing blood clots by controlling the motion of a TMD with the positioning feedback of an ultrasound system [110]. With using an array of actuator magnets, Zhang *et al.* have implemented a method of arranging the rotational actuator magnets circumferentially to generate a rotating magnetic field in the center area of the circle and obtain a synchronous reversing magnetic field with constant strength [138]. Qiu *et al.* have developed a robotic system incorporating four rotary actuator magnets, which can generate a rotating magnetic field

with the orientation of the field-rotation axis being arbitrary in a plane [139]. Although these systems using an array of actuator magnets can generate rotating magnetic fields without the translational movement of actuator magnets, the number of DOFs of these robotic systems to control the magnetic field is potentially restricted.

Permanent magnet-based robotic systems in force-driven mode generate a magnetic gradient field, resulting in a magnetic force exerted on TMDs as the main source of actuation. With using one actuator magnet, Khalil *et al.* have demonstrated a robotic system that attaches the actuator magnet to the end-effector of a robotic arm, achieving the kinematic control of paramagnetic microparticles in 3-D space with the manipulation of the exerted field gradient on the dipole of the microparticles [140]. Mahoney *et al.* have first demonstrated a 5-DOF manipulation of an untethered magnetic capsule by a 6-DOF robotic manipulator with the feedback of only 3-DOF capsule position [141]. Magnetic force and torque are utilized to control the total force (the sum of magnetic force, gravitational force, and buoyancy force) applied on the capsule and the capsule's orientation, respectively. With using two actuator magnets, Shapiro *et al.* have demonstrated the capability of a robotic system consisting of an arrangement of two permanent magnets to create magnetic force and eventually to push therapeutic nanoparticles [142]. Amokrane *et al.* have optimized a robotic system to produce a maximum push-pull force on magnetic microparticles by manipulating magnetic field gradient, enabling the navigation of microparticles in cortical microvasculature network [143]. With using an array of actuator magnets, Abbes *et al.* have reported a robotic system with a magnetic unit being attached to the end-effector of a robotic arm such that the magnetic unit consists of four actuator magnets, demonstrating the steerability to push and pull the magnetic microparticles in viscous fluids [144]. Son *et al.* have presented a robotic system that can create a strong magnetic force trap, enabling a cylindrical millirobot to penetrate continuously into soft tissue. The penetration motion is assisted by the induced magnetic torque, which directs the orientation of the millirobot to the center of the array of actuator magnets [75]. In comparison to the systems in torque-driven mode, those in force-driven mode at the same level require more energy consumption in the propulsion of TMDs in fluids, making the systems in force-driven mode more suitable in use for the scenarios of driving small-scale TMDs when requiring to limit the size of actuator magnets.

Permanent magnet-based robotic systems in torque-force-driven mode generate a rotating magnetic field and gradient field, resulting in a magnetic torque and force, as the main sources of actuation simultaneously, exerted on TMDs. These systems can be selectively switched to torque-driven mode or force-driven mode according to the specific application, giving them extraordinary versatility. With using one actuator magnet, Mahoney *et al.* have proposed a method to convert the magnetic force into a lateral force by manipulating the actuator magnet to be rotated with a specific trajectory. Such an operation can make a TMD be simultaneously pushed and rolled on a surface, inducing potentially enhanced rolling motion (higher rolling velocity), or it may be used for the scenarios of levitating device [145]. This method relies on the specific rotation control of the actuator magnet. By using two actuator magnets, Honey *et al.* have introduced a strategy of combining the propulsion force converted from the magnetic torque and the magnetic force, which is proven to decrease the drilling time of blood clots [146]. Pittiglio *et al.* have developed a robotic system using two independent serial manipulators, which can generate a magnetic field with a high degree of manipulability by controlling the pose of two actuator magnets collaboratively, enabling the system to work in torque-force-driven mode suitably [147]. Using an array of actuator magnets, Ryan *et al.* have built a robotic system to create fields and field gradients in any direction in three-dimensional (3-D) path-following tasks and shown that this system is able to implement 1-D and 2-D motion control via rolling as well as 3-D motion control via gradient pulling [76]. The disadvantage of this system is that the size of the workspace is severely restricted unless extremely large size actuator magnets are utilized [148].

In this chapter, we focus on permanent magnet-based robotic systems in torque-driven mode. Our system has an open configuration without using commercial robotic arms. The system holds one translational DOF and three rotational DOFs, enabling it to control the pose of two actuator magnets collaboratively with four DOFs. Further, the system is arranged with a vertically symmetric configuration to exert homogeneous magnetic fields within the center of the workspace. This symmetric configuration is physically constrained through a connecting plate, which simplifies the yawing motion control of the field-rotation axis within the center region of the workspace by only driving one robotic joint. As a result, this leads to an ease of yawing motion control of TMDs. Besides, the forward (from

joint space variables to the orientation of field-rotation axis) and inverse kinematics (from the desired orientation of field-rotation axis to desired joint space variables) of the system are analyzed, which serves as a basis for implementing TMD motion control. Our system is verified to have the ability to achieve TMD motion control in torque-driven mode. The remainder of the chapter is organized as follows: Section 2.2 provides the forward and inverse kinematic analysis of the magnet-based robotic system. Section 2.3 analyzes the possible unreachable zone of the field-rotation axis at the central point of the workspace. Section 2.4 investigates the magnetic field and field gradient within the workspace. Section 2.5 validates the ability of the system to control the motion of TMDs through closed-loop motion control experiments conducted in an agar gel phantom.

2.2 Magnetic-based robotic system

We consider a time-varying rotating magnetic field produced by the superposition of the contributions of multiple dipole sources. These dipole sources are fixed in three-dimensional space by a robotic configuration and exert a controlled magnetic torque on a TMD in low Reynolds (Re) numbers.

2.2.1 Magnetic actuation using multiple magnetic source

The magnetic field generated by multiple permanent magnets is characterized by the configuration-to-pose kinematics and the pose-to-field mapping. If a translation and rotation of multiple permanent magnets (with magnetic moment $\mathbf{M}_i$ for $i = 1, \ldots, k$) using a robotic configuration would result in a superimposed magnetic field ($\mathbf{B}(\boldsymbol{p})$), then the magnitude and direction of the magnetic field at position $\boldsymbol{p}$ are completely characterized by the joint space variables $\boldsymbol{q} \in \mathbb{R}^n$. The configuration-to-pose kinematics of such a robotic configuration is given by

$$\{\boldsymbol{R}_i, \boldsymbol{x}_i\} = \mathcal{F}(\boldsymbol{q}), \quad \text{for} \quad i = 1, \ldots, k, \tag{2.1}$$

where $\boldsymbol{R}_i$ and $\boldsymbol{x}_i$ characterize the rotation and translation of the ith magnetic source using the forward kinematic mapping $\mathcal{F} : \mathbb{R}^n \to \{\mathbb{R}^3, SO(3)\}$,

respectively. We can compute the magnetic field produced by each magnetic moment ($\mathbf{M}_i$) in the global frame of reference $\{\mathcal{W}\}$ as follows:

$$\mathbf{B}(\boldsymbol{p}) = \sum_{i=1}^{k} \left(\mathbf{B}(\boldsymbol{x}_i, \mathbf{M}_i) \mid_{\mathcal{W}}\right), \tag{2.2}$$

where $\mathbf{B}(\boldsymbol{x}_i, \mathbf{M}_i) \mid_{\mathcal{W}}$ is the magnetic field due to the ith magnetic source with respect to the global frame of reference. Further, the magnetic field vector of $\mathbf{B}(\boldsymbol{x}_i, \mathbf{M}_i) \mid_{\mathcal{W}}$ in Equation (3.2) can be calculated by

$$\begin{bmatrix} \mathbf{B}(\boldsymbol{x_i}, \mathbf{M}_i) \mid_{\mathcal{W}} \\ 0 \end{bmatrix} = {}^{\mathcal{W}}\mathbf{T}_{\mathcal{E}_i} \begin{bmatrix} \mathbf{B}(\boldsymbol{x_i}, \mathbf{M}_i) \mid_{\mathcal{E}_i} \\ 0 \end{bmatrix}, \tag{2.3}$$

where ${}^{\mathcal{W}}\mathbf{T}_{\mathcal{E}_i}$ is the homogeneous transformation between the global frame of reference and the ith frame of reference of the magnetic source $\{\mathcal{E}_i\}$, as shown in Fig 1. Further, $\mathbf{B}(\boldsymbol{x}_i, \mathbf{M}_i) \mid_{\mathcal{E}_i}$ is the magnetic field due to the ith magnetic source in the local frame $\{\mathcal{E}_i\}$. The properties of the magnetic field $\mathbf{B}(\boldsymbol{p})$ are completely characterized by the pose of each magnetic moment ($\mathbf{M}_i$) and can be manipulated using the joint space variables ($\boldsymbol{q}$).

Fig. 2.1 shows the magnetic field produced by two identical magnetic dipole sources. For $k = 1$ and away from the region between the magnetic dipole sources, the magnitude of the magnetic field decreases approximately as the inverse cube of the distance $|\boldsymbol{p} - \boldsymbol{x}_i|$. The magnitude of the field scales approximately as the sum of the inverse cube of $|\boldsymbol{p} - \boldsymbol{x}_i|$ when two dipole sources are incorporated. Therefore, it is desirable to consider the enclosed region between the two dipole sources in order to create larger field strength than any other locations away from this region. For a small enough workspace (around position $\boldsymbol{p}$), it is possible to create a relation between the magnitude of the field and the distance to the dipole sources by placing a position constraint on the dipole sources. In such a situation, the orientation of magnetic moment ($\mathbf{M}_i$) can be controlled using a robotic configuration to manipulate the magnetic field at the position $\boldsymbol{p}$. At this point, the relationship between the unit vector of field-rotation axis ($\hat{\boldsymbol{\omega}}$) and the unit vector of dipole-rotation axis ($\hat{\boldsymbol{\Omega}}$, refer to the rotation axis of the magnetic moment) can be characterized by the configuration of the permanent-magnet robotic system, as shown in Fig. 2.2.

2.2.2 Robotic configuration

Superimposing the magnetic field of multiple magnetic sources can generate a greater and more uniform field within the enclosed region between the permanent magnets. Translating and rotating these magnetic sources can be used for actuation. Therefore, we need to control the pose of the magnetic sources by robotically moving a robotic configuration in order to obtain the desired field-rotation axis for actuation at $\boldsymbol{p}$. Since we are considering a rotating magnetic field for actuation, the magnetic dipole of the ith source can be continuously rotated in synchrony with an angle θ_s ($\theta_s = \Omega t$ such that Ω is the angular velocity of each rotating dipole) about the ith dipole-rotation axis $\boldsymbol{\Omega}$. The orientation of these axes of rotation is completely characterized using the forward kinematics ($\mathcal{F}$).

To control the dipole-rotation axis $\boldsymbol{\Omega}$, a number of joints must be independently controlled. Here, we consider a translational base frame $\{\mathcal{A}\}$ supporting four actuated rotational joints. The pure translation of frame $\{\mathcal{A}\}$ with respect to the global frame of reference is characterized by the joint space variable q_1, which enables the superimposed field to be translated without affecting its spatial derivatives. The first and second rotational joints are orthogonally arranged to rotate frame $\{\mathcal{B}\}$ and $\{\mathcal{C}\}$ about the z_2- and x_3-axes, respectively, as shown in Fig 2.2(a). The rotation of frame $\{\mathcal{B}\}$ with respect to frame $\{\mathcal{A}\}$ and the rotation of frame $\{\mathcal{C}\}$ with respect to frame $\{\mathcal{B}\}$ are characterized by the joint space variable q_2 and q_3, which enables control of the yawing and pitching motion of the field-rotation axis at $\boldsymbol{p}$, respectively. Frame $\{\mathcal{C}\}$ supports two symmetrically placed actuated rotational joints aligned to rotate frame $\{\mathcal{D}_1\}$ and $\{\mathcal{D}_2\}$ about the z_4- and z_5-axes, respectively. The rotation of frame $\{\mathcal{D}_i\}$ with respect to frame $\{\mathcal{C}\}$ is characterized by the joint space variable q_4, which also enables the control of yawing motion of the field-rotation axis at $\boldsymbol{p}$. This allows us to have multiple control options (manipulating q_2 or q_4 or both of them) when planning a yawing motion of field-rotation axis at $\boldsymbol{p}$, and thus it improves the flexibility of our system. These joints are equally spaced with respect to the z-axis of the global frame of reference. Frame $\{\mathcal{T}_i\}$ is defined as the frame of reference of the ith permanent magnet, two magnetic sources rotate about the $\boldsymbol{o}^i$-axis of frame $\{\mathcal{T}_i\}$ such that their magnetic moment is orthogonal to these vectors. Further, frame $\{\mathcal{T}_i\}$ is only rigidly translational with respect to frame $\{\mathcal{D}_i\}$. In addition, the ro-

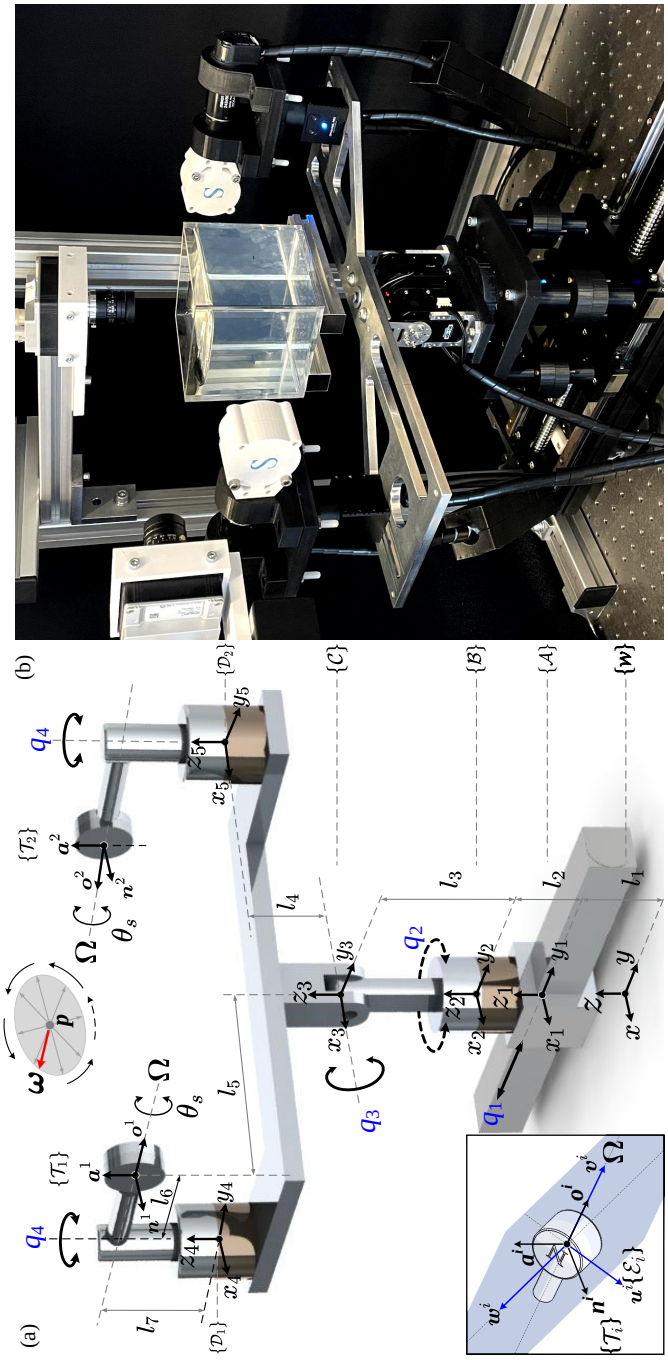

Figure 2.2: A permanent-magnet robotic system uses rotating dipole fields to produce a uniform magnetic field within a limited workspace. (a) Assignment of the frames to the setup, two cylindrical permanent magnets are attached to the end-effectors such that the magnetization vectors are perpendicular to the $\boldsymbol{o}^i$-axis. The two magnetic sources rotating synchronously around their self-rotation axis of $\boldsymbol{\Omega}$ are expected to generate a rotating magnetic field at $\boldsymbol{p}$ with the field-rotation axis of $\boldsymbol{\omega}$. (b) A container filled with an agar gel phantom providing the TMDs with a viscoelastic swimming environment is placed at the center of the workspace. The inset box indicates the frame $\{\mathcal{E}_i\}$ and $\{\mathcal{T}_i\}$ attached on ith magnetic dipole source.

tation of ith permanent magnet is characterized in frame $\{\mathcal{E}_i\}$ such that frame $\{\mathcal{E}_i\}$ is only rotational with respect to frame $\{\mathcal{T}_i\}$. The origin of $\{\mathcal{T}_i\}$ and that of frame $\{\mathcal{E}_i\}$ are overlapping and the $\boldsymbol{v}^i$-axis of frame $\{\mathcal{E}_i\}$ and the $\boldsymbol{o}^i$-axis of frame $\{\mathcal{T}_i\}$ are coincident.

The configuration of the permanent-magnet robotic system is shown in Fig. 2.2(a), which indicates the links and joints with the corresponding frames. The vector $\boldsymbol{q} \in \mathbb{R}^{4\times 1}$ is constructed with independent joint space variables such that $\boldsymbol{q} = [q_1, q_2, q_3, q_4]^{\mathrm{T}}$. Note that q_1 in $\boldsymbol{q}$ refers to a translational motion, and q_2, q_3 and q_4 in $\boldsymbol{q}$ refer to rotational motions. Besides the links and joints, Fig. 2.2(b) shows the permanent-magnet robotic system as well as the workspace. The configuration-to-pose kinematics of our robotic configuration characterizes the ith dipole-rotation axis in terms of the joint space variables such that

$$^{\mathcal{W}}\mathbf{T}_{\mathcal{D}_i} = {}^{\mathcal{W}}\mathbf{T}_{\mathcal{A}}\ {}^{\mathcal{A}}\mathbf{T}_{\mathcal{B}}\ {}^{\mathcal{B}}\mathbf{T}_{\mathcal{C}}\ {}^{\mathcal{C}}\mathbf{T}_{\mathcal{D}_i}, \tag{2.4}$$

where $^{\mathcal{W}}\mathbf{T}_{\mathcal{D}_i}$ is the homogeneous transformation matrix between the frame $\{\mathcal{D}_i\}$ and the global frame of reference. In Equation (2.4), $^{\mathcal{W}}\mathbf{T}_{\mathcal{A}}$ is the homogeneous transformation matrix between frame $\{\mathcal{A}\}$ and the global frame of reference, which is given by

$$^{\mathcal{W}}\mathbf{T}_{\mathcal{A}} = \begin{bmatrix} \mathbf{I} & \boldsymbol{x}_{\mathcal{A}}^{\mathcal{W}} \\ \mathbf{0}^{1\times 3} & 1 \end{bmatrix}. \tag{2.5}$$

where $\mathbf{I}$ is the unit matrix and $\boldsymbol{x}_{\mathcal{A}}^{\mathcal{W}}$ is the translation vector of the origin of frame $\{\mathcal{A}\}$ in the global frame of reference. Further, $\boldsymbol{x}_{\mathcal{A}}^{\mathcal{W}}$ is given by

$$\boldsymbol{x}_{\mathcal{A}}^{\mathcal{W}} = [0 \quad q_1 \quad 0]^{\mathrm{T}}. \tag{2.6}$$

The translation of the origin of frame $\{\mathcal{A}\}$ in the global frame of reference enables control of the translational motion of the superimposed field in the y-axis direction. Further, this translation partially determines the reachable zone of the field-rotation axis at $\boldsymbol{p}$. In Equation (2.4), $^{\mathcal{A}}\mathbf{T}_{\mathcal{B}}$ is the homogeneous transformation matrix between frame $\{\mathcal{B}\}$ and $\{\mathcal{A}\}$, which is given by

$$^{\mathcal{A}}\mathbf{T}_{\mathcal{B}} = \begin{bmatrix} {}^{\mathcal{A}}\mathbf{R}_{\mathcal{B}} & \boldsymbol{x}_{\mathcal{B}}^{\mathcal{A}} \\ \mathbf{0}^{1\times 3} & 1 \end{bmatrix}, \tag{2.7}$$

where $^{\mathcal{A}}\mathbf{R}_{\mathcal{B}}$ is the rotation matrix between frame $\{\mathcal{B}\}$ with respect to $\{\mathcal{A}\}$ and $\boldsymbol{x}_{\mathcal{B}}^{\mathcal{A}} = [0 \quad 0 \quad d_z^2]^{\mathrm{T}}$ is the translation vector of the origin of frame $\{\mathcal{B}\}$

in the frame $\{\mathcal{A}\}$. Further, d_z^2 is a constant determined by the mechanical dimensions of the system, and $d_z^2 = l_2$. In Equation (2.7), ${}^{\mathcal{A}}\mathbf{R}_{\mathcal{B}}$ is given by

$$ {}^{\mathcal{A}}\mathbf{R}_{\mathcal{B}} = \begin{bmatrix} \cos(q_2) & -\sin(q_2) & 0 \\ \sin(q_2) & \cos(q_2) & 0 \\ 0 & 0 & 1 \end{bmatrix}. \tag{2.8} $$

The rotation of frame $\{\mathcal{B}\}$ with respect to frame $\{\mathcal{A}\}$ enables control of the yawing motion of the field-rotation axis at $\boldsymbol{p}$. This yawing motion is important for the steering of TMDs. In Equation (2.4), ${}^{\mathcal{B}}\mathbf{T}_{\mathcal{C}}$ is the homogeneous transformation matrix between frame $\{\mathcal{C}\}$ and $\{\mathcal{B}\}$.

$$ {}^{\mathcal{B}}\mathbf{T}_{\mathcal{C}} = \begin{bmatrix} {}^{\mathcal{B}}\mathbf{R}_{\mathcal{C}} & \boldsymbol{x}_{\mathcal{C}}^{\mathcal{B}} \\ \mathbf{0}^{1\times 3} & 1 \end{bmatrix}, \tag{2.9} $$

where ${}^{\mathcal{B}}\mathbf{R}_{\mathcal{C}}$ is the rotation matrix of frame $\{\mathcal{C}\}$ with respect to frame $\{\mathcal{B}\}$ and $\boldsymbol{x}_{\mathcal{C}}^{\mathcal{B}} = [0 \quad 0 \quad d_z^3]^{\mathrm{T}}$ is the translation vector of the origin of frame $\{\mathcal{C}\}$ in the frame $\{\mathcal{B}\}$. Further, d_z^3 is a constant determined by the mechanical dimensions of the system, and $d_z^3 = l_3$. In Equation (2.9), ${}^{\mathcal{B}}\mathbf{R}_{\mathcal{C}}$ is given by

$$ {}^{\mathcal{B}}\mathbf{R}_{\mathcal{C}} = \begin{bmatrix} 1 & 0 & 0 \\ 0 & \cos(q_3) & -\sin(q_3) \\ 0 & \sin(q_3) & \cos(q_3) \end{bmatrix}. \tag{2.10} $$

The rotation of frame $\{\mathcal{C}\}$ with respect to frame $\{\mathcal{B}\}$ enables control of the pitching motion of the field-rotation axis at $\boldsymbol{p}$. This pitching motion is important for TMDs to swim upward or downward and follow a 3-D prescribed trajectory. In Equation (2.4), ${}^{\mathcal{C}}\mathbf{T}_{\mathcal{D}_i}$ is the homogeneous transformation matrix between frame $\{\mathcal{D}_i\}$ and $\{\mathcal{C}\}$, which is given by

$$ {}^{\mathcal{C}}\mathbf{T}_{\mathcal{D}_i} = \begin{bmatrix} {}^{\mathcal{C}}\mathbf{R}_{\mathcal{D}_i} & \boldsymbol{x}_{\mathcal{D}_i}^{\mathcal{C}} \\ \mathbf{0}^{1\times 3} & 1 \end{bmatrix}, \tag{2.11} $$

where ${}^{\mathcal{C}}\mathbf{R}_{\mathcal{D}_i}$ is the rotation matrix of frame $\{\mathcal{D}_i\}$ with respect to frame $\{\mathcal{C}\}$ and $\boldsymbol{x}_{\mathcal{D}_i}^{\mathcal{C}} = [d_x^4 \quad d_y^4 \quad d_z^4]^{\mathrm{T}}$ is the translation vector of the origin of frame $\{\mathcal{D}_i\}$ in the frame $\{\mathcal{C}\}$. Further, d_x^4, d_y^4 and d_z^4 are constants determined by mechanical dimensions of the system. For $i = 1$, $d_x^4 = l_5$, $d_y^4 = -l_6$ and $d_z^4 = l_4$. For $i = 2$, $d_x^4 = -l_5$, $d_y^4 = l_6$ and $d_z^4 = l_4$. In Equation (2.11), ${}^{\mathcal{C}}\mathbf{R}_{\mathcal{D}_i}$ is given by

$$ {}^{\mathcal{C}}\mathbf{R}_{\mathcal{D}_i} = \begin{bmatrix} \cos(q_4) & -\sin(q_4) & 0 \\ \sin(q_4) & \cos(q_4) & 0 \\ 0 & 0 & 1 \end{bmatrix}. \tag{2.12} $$

Like the function of rotation matrix ${}^{\mathcal{A}}\mathbf{R}_{\mathcal{B}}$, the rotation of frame $\{\mathcal{D}_i\}$ with respect to frame $\{\mathcal{C}\}$ also enables the control of yawing motion of the field-rotation axis at $\boldsymbol{p}$. However, this redundancy allows multiple options to control the yawing motion of the field-rotation axis at $\boldsymbol{p}$, and it expands the reachable zone of the field-rotation axis at $\boldsymbol{p}$. The configuration-to-pose kinematics of our robotic configuration characterizes the ith dipole-rotation axis in terms of the joint space variables such that

$$\begin{bmatrix}\hat{\boldsymbol{\Omega}}\\0\end{bmatrix} = {}^{\mathcal{W}}\mathbf{T}_{\mathcal{D}_i}\begin{bmatrix}\boldsymbol{o}^i_{\mathcal{D}_i}\\0\end{bmatrix} = {}^{\mathcal{W}}\mathbf{T}_{\mathcal{T}_i}\begin{bmatrix}\boldsymbol{o}^i\\0\end{bmatrix} = {}^{\mathcal{W}}\mathbf{T}_{\mathcal{E}_i}\begin{bmatrix}\boldsymbol{v}^i\\0\end{bmatrix}, \tag{2.13}$$

where $\boldsymbol{o}^i_{\mathcal{D}_i}$ characterizes the rotation axis of ith magnetic source in the frame $\{\mathcal{D}_i\}$. In configuration-to-pose kinematics, ${}^{\mathcal{W}}\mathbf{T}_{\mathcal{T}_i}$ is the homogeneous transformation matrix between the frame $\{\mathcal{T}_i\}$ and the global frame of reference, which is given by

$${}^{\mathcal{W}}\mathbf{T}_{\mathcal{T}_i} = {}^{\mathcal{W}}\mathbf{T}_{\mathcal{D}_i}\,{}^{\mathcal{D}_i}\mathbf{T}_{\mathcal{T}_i}. \tag{2.14}$$

Further, ${}^{\mathcal{D}_i}\mathbf{T}_{\mathcal{T}_i}$ is the homogeneous transformation matrix between the frame $\{\mathcal{T}_i\}$ and $\{\mathcal{D}_i\}$, which is given by

$${}^{\mathcal{D}_i}\mathbf{T}_{\mathcal{T}_i} = \begin{bmatrix}\mathbf{I} & \boldsymbol{x}^{\mathcal{D}_i}_{\mathcal{T}_i}\\ \mathbf{0}^{1\times 3} & 1\end{bmatrix}. \tag{2.15}$$

where $\boldsymbol{x}^{\mathcal{D}_i}_{\mathcal{T}_i} = [0 \quad d^5_y \quad d^5_z]^{\mathrm{T}}$ is the translation vector of the origin of frame $\{\mathcal{T}_i\}$ in frame $\{\mathcal{D}_i\}$. Further, d^5_y and d^5_z are constants determined by mechanical dimensions of the system. For $i = 1$, $d^5_y = l_6$ and $d^5_z = l_7$. For $i = 2$, $d^5_y = -l_6$ and $d^4_z = l_7$. Multiplying the solution for all transformation matrices results in the overall homogeneous transformation matrix ${}^{\mathcal{W}}\mathbf{T}_{\mathcal{T}_i}$ which governs the relation between the vector of joint space variables $\boldsymbol{q}$ and unit vector of dipole-rotation axis $\hat{\boldsymbol{\Omega}}$.

2.2.3 Mapping dipole-rotation axis to field-rotation axis

The unit vector of field-rotation axis $\hat{\boldsymbol{\omega}}$ at $\boldsymbol{p}$ is normal to the plane containing $\mathbf{B}(\boldsymbol{p})$, such that $\hat{\boldsymbol{\omega}}^{\mathrm{T}}\mathbf{B}(\boldsymbol{p}) = 0$ for all $\mathbf{M}_i$. Replacing $\mathbf{B}(\boldsymbol{p})$ with Equation (3.2) in this expression yields

$$\begin{bmatrix}\hat{\boldsymbol{\omega}}\\0\end{bmatrix}^{\mathrm{T}}\sum_{i=1}^{k}\left(\begin{bmatrix}\mathbf{B}(\boldsymbol{x_i},\mathbf{M}_i)\ |_{\mathcal{W}}\\0\end{bmatrix}\right) = 0, \tag{2.16}$$

Substituting Equation (3.3) into Equation (2.16) yields

$$\begin{bmatrix}\hat{\boldsymbol{\omega}}\\0\end{bmatrix}^{\mathrm{T}}\sum_{i=1}^{k}\left({}^{\mathcal{W}}\mathbf{T}_{\mathcal{E}_i}\begin{bmatrix}\mathbf{B}(\boldsymbol{x_i},\mathbf{M}_i)\mid_{\mathcal{E}_i}\\0\end{bmatrix}\right)=0, \tag{2.17}$$

such that,

$${}^{\mathcal{W}}\mathbf{T}_{\mathcal{E}_i}={}^{\mathcal{W}}\mathbf{T}_{\mathcal{T}_i}\,{}^{\mathcal{T}_i}\mathbf{T}_{\mathcal{E}_i}, \tag{2.18}$$

where ${}^{\mathcal{T}_i}\mathbf{T}_{\mathcal{E}_i}$ is the homogeneous transformation matrix between frame $\{\mathcal{E}_i\}$ and $\{\mathcal{T}_i\}$, which is given by

$${}^{\mathcal{T}_i}\mathbf{T}_{\mathcal{E}_i}=\begin{bmatrix}{}^{\mathcal{T}_i}\mathbf{R}_{\mathcal{E}_i} & \mathbf{0}^{3\times1}\\ \mathbf{0}^{1\times3} & 1\end{bmatrix}, \tag{2.19}$$

where ${}^{\mathcal{T}_i}\mathbf{R}_{\mathcal{E}_i}$ is the rotation matrix of frame $\{\mathcal{E}_i\}$ with respect to frame $\{\mathcal{T}_i\}$. Further, ${}^{\mathcal{T}_i}\mathbf{R}_{\mathcal{E}_i}$ is given by

$${}^{\mathcal{T}_i}\mathbf{R}_{\mathcal{E}_i}=\begin{bmatrix}\cos(\theta_s) & 0 & \sin(\theta_s)\\ 0 & 1 & 0\\ -\sin(\theta_s) & 0 & \cos(\theta_s)\end{bmatrix}. \tag{2.20}$$

Note that θ_s is a time-periodic angle, and its angular velocity controls the translational speed of a TMD. The generated magnetic field due to ith magnetic source in the frame $\{\mathcal{E}_i\}$ can be rewritten as

$$\mathbf{B}(\boldsymbol{x_i},\mathbf{M}_i)\mid_{\mathcal{E}_i}=(B_u^i\boldsymbol{u}^i+B_v^i\boldsymbol{v}^i+B_w^i\boldsymbol{w}^i),\quad\text{for}\quad i=1,2, \tag{2.21}$$

where $\boldsymbol{u}^i$, $\boldsymbol{v}^i$ and $\boldsymbol{w}^i$ are the unit axis vector of frame $\{\mathcal{E}_i\}$. Further, B_u, B_v and B_w are magnitudes of the magnetic field along the direction of $\boldsymbol{u}^i$-, $\boldsymbol{v}^i$- and $\boldsymbol{w}^i$-axis in frame $\{\mathcal{E}_i\}$, respectively. Substituting Equation (2.21) into Equation (2.17) yields

$$\begin{bmatrix}\hat{\boldsymbol{\omega}}\\0\end{bmatrix}^{\mathrm{T}}\sum_{i=1}^{k}{}^{\mathcal{W}}\mathbf{T}_{\mathcal{E}_i}\begin{bmatrix}B_u^i\boldsymbol{u}^i+B_w^i\boldsymbol{w}^i+B_v^i\boldsymbol{v}^i\\0\end{bmatrix}=0. \tag{2.22}$$

Substituting Equation (2.13) into expanded Equation (2.22) yields

$$\begin{bmatrix}\hat{\boldsymbol{\omega}}\\0\end{bmatrix}^{\mathrm{T}}\sum_{i=1}^{k}\left({}^{\mathcal{W}}\mathbf{T}_{\mathcal{E}_i}\begin{bmatrix}(B_u^i\boldsymbol{u}^i+B_w^i\boldsymbol{w}^i)\\0\end{bmatrix}+B_v^i\begin{bmatrix}\hat{\boldsymbol{\Omega}}\\0\end{bmatrix}\right)=0. \tag{2.23}$$

Hence the relationship between the unit vector of field-rotation axis $\hat{\boldsymbol{\omega}}$, the unit vector of dipole-rotation axis $\hat{\boldsymbol{\Omega}}$ and the vector of joint space variables $\boldsymbol{q}$ at position $\boldsymbol{p}$ is found.

2.2.4 Inverse kinematics

Given the desired unit vector of field-rotation axis $\hat{\boldsymbol{\omega}}^d$, then the problem of solving inverse kinematics is converted to that of solving Equation (2.23) with the orientation of the dipole moment of each magnetic source ($\mathbf{M}_i$) varying synchronously and periodically in time. The algorithm flow of solving inverse solutions based on the desired field-rotation axis is presented in Table 2.1. The frame parameters required for the algorithm are demonstrated in Table A.1 (*Please refer to* **Appendix A.2**) where the $l_1 = 0$ mm, $l_2 = 128$ mm, $l_3 = 60.6$ mm, $l_4 = 46$ mm, $l_5 = 175$ mm, $l_6 = 89$ mm, and $l_7 = 119$ mm.

Table 2.1: Pseudocode for Inverse Kinematics

Algorithm:	Solving inverse kinematics based on desired unit vector of field-rotation axis $\hat{\boldsymbol{\omega}}^d$ at a position $\boldsymbol{p}$
Input:	Position $\boldsymbol{p}$, unit axis vector $\hat{\boldsymbol{\omega}}^d$ and threshold δ_0
Output:	Desired vector of joint variables $\boldsymbol{q}^d$
01:	$q_1 \in$ [-150:150], $q_2 \in$ [-720°:720°], $q_3 \in$ [-90°:90°], $q_4 \in$ [-180°:180°],
02:	Initialize the vector of joint variables $\boldsymbol{q}$
03:	$\mathcal{H}_j(\boldsymbol{q}) \longleftarrow \boldsymbol{p}$ and $\hat{\boldsymbol{\omega}}^d$
04:	**for** $j = 1 : N$
05:	$\theta_s = (j/N) * 360°$
06:	$\mathcal{F}(\boldsymbol{q}) \longleftarrow \boldsymbol{q}$
07:	${}^{\mathcal{W}}\mathbf{T}_{\mathcal{D}_i} \longleftarrow \mathcal{F}(\boldsymbol{q})$
08:	${}^{\mathcal{W}}\mathbf{T}_{\mathcal{T}_i} \longleftarrow {}^{\mathcal{W}}\mathbf{T}_{\mathcal{D}_i}\,{}^{\mathcal{D}_i}\mathbf{T}_{\mathcal{T}_i}$
09:	${}^{\mathcal{W}}\mathbf{T}_{\mathcal{E}_i} \longleftarrow {}^{\mathcal{W}}\mathbf{T}_{\mathcal{T}_i}\,{}^{\mathcal{T}_i}\mathbf{T}_{\mathcal{E}_i}$
10:	${}^{\mathcal{W}}\mathbf{T}_{\mathcal{E}_i}^{-1} \longleftarrow {}^{\mathcal{W}}\mathbf{T}_{\mathcal{E}_i}$
11:	${}^{\mathcal{E}_i}\boldsymbol{p} \longleftarrow {}^{\mathcal{W}}\mathbf{T}_{\mathcal{E}_i}^{-1}\,\boldsymbol{p}$
12:	${}^{\mathcal{E}_i}\mathbf{B}(\boldsymbol{p}) \longleftarrow \mathbf{B}({}^{\mathcal{E}_i}\boldsymbol{p})$
13:	$[B_u^i \quad B_v^i \quad B_w^i] \longleftarrow {}^{\mathcal{E}_i}\mathbf{B}(\boldsymbol{p})$
14:	$\mathcal{H}_j(\boldsymbol{q}) \longleftarrow$ Equation (2.24)
15:	**if** $\mathcal{H}_j(\boldsymbol{q}) \leq \delta_0$
16:	$\boldsymbol{q}^d = \boldsymbol{q}$
17:	**break**;
18:	**end**
19:	**end**
20:	Return $\boldsymbol{q}^d$

In the algorithm, the increase and decrease of the value of joint space variable q_1 indicates the positive and negative linear motion of the translational joint, respectively. Similarly, the increase and decrease of the value of joint space variable q_2 (q_3 or q_4) indicates the counterclockwise and clockwise rotation of that revolute joint, respectively. In particular, our permanent-magnet robotic system allows two consecutive clockwise or counterclockwise rotations of frame $\{\mathcal{B}\}$ with respect to frame $\{\mathcal{A}\}$, which is characterized by joint space variable q_2 ($q_2 \in$ [-720°:720°]), enabling a TMD make two continuous clockwise or counterclockwise rotations. To maintain the synchronous rotation of a TMD with the rotating magnetic field, the magnetic torque must balance the drag torque on the TMD. We allow two rotating actuator permanent magnets to be close to each other to generate a greater magnetic torque than that with a single rotating actuator permanent magnet. To precisely model the magnetic field in the workspace between two actuator permanent magnets, we use an exact magnetic model (*Please refer to* **Appendix A.1**). With this model, the fitness function $\mathcal{H}_j(\boldsymbol{q})$ in Table 2.1 is designed as

$$\mathcal{H}_j(\boldsymbol{q}) = \frac{180}{\pi} \arccos \left[\frac{(\hat{\boldsymbol{\omega}}^d)^{\mathrm{T}} \sum_{i=1}^{k} \left(\mathbf{B}(\boldsymbol{x_i}, \mathbf{M}_i) \mid_{\mathcal{W}}\right)}{|\hat{\boldsymbol{\omega}}^d| \left| \sum_{i=1}^{k} \left(\mathbf{B}(\boldsymbol{x_i}, \mathbf{M}_i) \mid_{\mathcal{W}}\right) \right|} \right] - 90. \tag{2.24}$$

The fitness function is optimized to approach 0 using the Levenberg-Marquard (LM) algorithm. In Equation (2.24), $\sum_{i=1}^{k} \mathbf{B}(\boldsymbol{x_i}, \mathbf{M}_i) \mid_{\mathcal{W}}$ can be calculated through

$$\begin{bmatrix} \sum_{i=1}^{k} \mathbf{B}(\boldsymbol{x_i}, \mathbf{M}_i) \mid_{\mathcal{W}} \\ 0 \end{bmatrix} = \sum_{i=1}^{k} {}^{\mathcal{W}}\mathbf{T}_{\mathcal{E}_i} \begin{bmatrix} B_u^i & B_v^i & B_w^i & 0 \end{bmatrix}^{\mathrm{T}}. \tag{2.25}$$

Referring to Table 2.1, the desired vector of joint variables $\boldsymbol{q}^d$ and desired unit vector of dipole-rotation axis $\hat{\boldsymbol{\Omega}}^d$ can be calculated based on the desired unit vector of field-rotation axis $\hat{\boldsymbol{\omega}}^d$.

2.2.5 Control of a tetherless magnetic device

TMD motion control consists of two parts. One is TMD motion direction control, and the other is TMD motion speed control. The motion direction control of a TMD is implemented by manipulating the TMD rotation axis,

Table 2.2: Inverse Solutions at Separate Points from a Predefined 3-D Spiral Trajectory with Calculating the Desired Field-rotation Axis ($\hat{\boldsymbol{\omega}}^d$), Desired Dipole-rotation axis ($\hat{\boldsymbol{\Omega}}^d$) and Desired Vector of Joint Variables ($\boldsymbol{q}^d$) at 17 Representative Waypoints

Predefined 3-D trajectory	$\boldsymbol{p}$	P_1	P_2	P_3	P_4	P_5	P_6	P_7
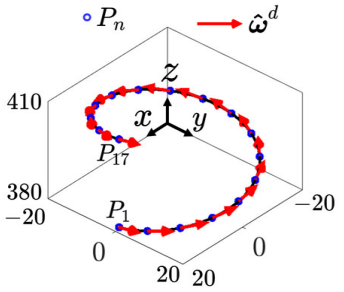	$\hat{\boldsymbol{\omega}}^d$	$\begin{bmatrix}0\\0.981\\0.194\end{bmatrix}$	$\begin{bmatrix}0.375\\0.906\\0.194\end{bmatrix}$	$\begin{bmatrix}0.694\\0.694\\0.194\end{bmatrix}$	$\begin{bmatrix}0.906\\0.375\\0.194\end{bmatrix}$	$\begin{bmatrix}0.981\\0\\0.194\end{bmatrix}$	$\begin{bmatrix}0.906\\-0.375\\0.194\end{bmatrix}$	$\begin{bmatrix}0.694\\-0.694\\0.194\end{bmatrix}$
	$\hat{\boldsymbol{\Omega}}^d$	$\begin{bmatrix}-0.023\\0.989\\0.147\end{bmatrix}$	$\begin{bmatrix}-0.393\\0.907\\0.149\end{bmatrix}$	$\begin{bmatrix}-0.706\\0.693\\0.148\end{bmatrix}$	$\begin{bmatrix}-0.916\\0.375\\0.143\end{bmatrix}$	$\begin{bmatrix}-0.991\\0.001\\0.134\end{bmatrix}$	$\begin{bmatrix}-0.916\\-0.381\\0.123\end{bmatrix}$	$\begin{bmatrix}-0.695\\-0.709\\0.117\end{bmatrix}$
	$\boldsymbol{q}^{\mathrm{d}}$	$\begin{bmatrix}-0.134\\3.729\\8.459\\-2.353\end{bmatrix}$	$\begin{bmatrix}5.493\\25.15\\8.573\\-1.728\end{bmatrix}$	$\begin{bmatrix}10.34\\46.48\\8.530\\-0.933\end{bmatrix}$	$\begin{bmatrix}13.86\\68.01\\8.225\\-0.283\end{bmatrix}$	$\begin{bmatrix}-15.30\\89.99\\7.679\\-0.026\end{bmatrix}$	$\begin{bmatrix}14.46\\113.0\\7.071\\-0.421\end{bmatrix}$	$\begin{bmatrix}11.47\\137.0\\6.704\\-1.405\end{bmatrix}$

P_8	P_9	P_{10}	P_{11}	P_{12}	P_{13}	P_{14}	P_{15}	P_{16}	P_{17}
$\begin{bmatrix}0.375\\-0.906\\0.194\end{bmatrix}$	$\begin{bmatrix}0\\-0.981\\0.194\end{bmatrix}$	$\begin{bmatrix}-0.375\\-0.906\\0.194\end{bmatrix}$	$\begin{bmatrix}-0.694\\-0.694\\0.194\end{bmatrix}$	$\begin{bmatrix}-0.906\\-0.375\\0.194\end{bmatrix}$	$\begin{bmatrix}-0.981\\0\\0.194\end{bmatrix}$	$\begin{bmatrix}-0.906\\0.375\\0.194\end{bmatrix}$	$\begin{bmatrix}-0.694\\0.694\\0.194\end{bmatrix}$	$\begin{bmatrix}-0.375\\0.906\\0.194\end{bmatrix}$	$\begin{bmatrix}0\\0.981\\0.194\end{bmatrix}$
$\begin{bmatrix}-0.362\\-0.925\\0.119\end{bmatrix}$	$\begin{bmatrix}0.0184\\-0.992\\0.126\end{bmatrix}$	$\begin{bmatrix}0.392\\-0.911\\0.131\end{bmatrix}$	$\begin{bmatrix}0.707\\-0.695\\0.132\end{bmatrix}$	$\begin{bmatrix}0.918\\-0.376\\0.126\end{bmatrix}$	$\begin{bmatrix}0.993\\0\\0.114\end{bmatrix}$	$\begin{bmatrix}0.920\\0.381\\0.0963\end{bmatrix}$	$\begin{bmatrix}0.698\\0.711\\0.0899\end{bmatrix}$	$\begin{bmatrix}0.367\\0.925\\0.094\end{bmatrix}$	$\begin{bmatrix}-0.0133\\0.994\\0.104\end{bmatrix}$
$\begin{bmatrix}6.355\\160.9\\6.838\\-2.265\end{bmatrix}$	$\begin{bmatrix}0.312\\183.4\\7.232\\-2.32\end{bmatrix}$	$\begin{bmatrix}-5.377\\205.0\\7.535\\-1.718\end{bmatrix}$	$\begin{bmatrix}-10.28\\226.4\\7.567\\-0.920\end{bmatrix}$	$\begin{bmatrix}-13.84\\248.0\\7.219\\-0.274\end{bmatrix}$	$\begin{bmatrix}-15.30\\270.0\\6.542\\-0.027\end{bmatrix}$	$\begin{bmatrix}-14.46\\292.9\\5.526\\-0.398\end{bmatrix}$	$\begin{bmatrix}-11.44\\316.8\\5.160\\-1.277\end{bmatrix}$	$\begin{bmatrix}-6.386\\340.4\\5.396\\-2.043\end{bmatrix}$	$\begin{bmatrix}-0.400\\362.9\\5.970\\-2.122\end{bmatrix}$

which is determined by the field-rotation axis at the TMD position. The motion speed control of a TMD is achieved by managing the actuation frequency of the applied rotating magnetic field. We assume a TMD is actuated by an external rotating magnetic field with a constant rotation frequency, thus the TMD motion speed is expected to be constant. Then, the motion control of the TMD is simplified to control the motion direction of the TMD. Given a predefined trajectory (*Please refer to* Table 2.2), which is expressed as the parametric equation $x = f(t), y = g(t), z = h(t)$, we break it down into 17 waypoints. Point P_n is the nth representative waypoint. The necessary TMD motion direction $\hat{\mathbf{U}}$ at each waypoint P_n is found as

$$\hat{\mathbf{U}}(P_n) = \frac{\begin{bmatrix} \frac{dx}{dt} & \frac{dy}{dt} & \frac{dz}{dt} \end{bmatrix}^{\mathrm{T}}}{\sqrt{(\frac{dx}{dt})^2 + (\frac{dy}{dt})^2 + (\frac{dz}{dt})^2}}. \tag{2.26}$$

Replacing the $\hat{\boldsymbol{\omega}}^d$ with $\hat{\mathbf{U}}(P_n)$ in Table 2.1, we can acquire the desired vector of joint variables ($\boldsymbol{q}^d$) at each waypoint, as shown in Table 2.2.

2.3 Orienting field-rotation axis

The challenge of aligning the field-rotation axis in a desired direction depends on factors such as the design of the robotic system and the constraints imposed by joint space variables. Since the orientation of the field-rotation axis, as denoted by the unit vector of the field-rotation axis, governs the motion direction of a TMD, it's imperative to analyze the difficulty level of orienting the field-rotation axis to the desired motion direction of the TMD. In this section, we'll presume the TMD is positioned at the central point of the workspace. The central point is defined as the middle point of the line segment between two actuator magnets' centroids when the system is at its initial state. The initial system state refers to $\boldsymbol{q} = \mathbf{0}^{4\times1}$. Subsequently, we'll evaluate the difficulty of aligning the field-rotation axis to a particular direction at this central point.

2.3.1 Yawing and pitching motion of field-rotation axis

The yawing and pitching motion of the field-rotation axis plays an important role in the motion direction control of a TMD.

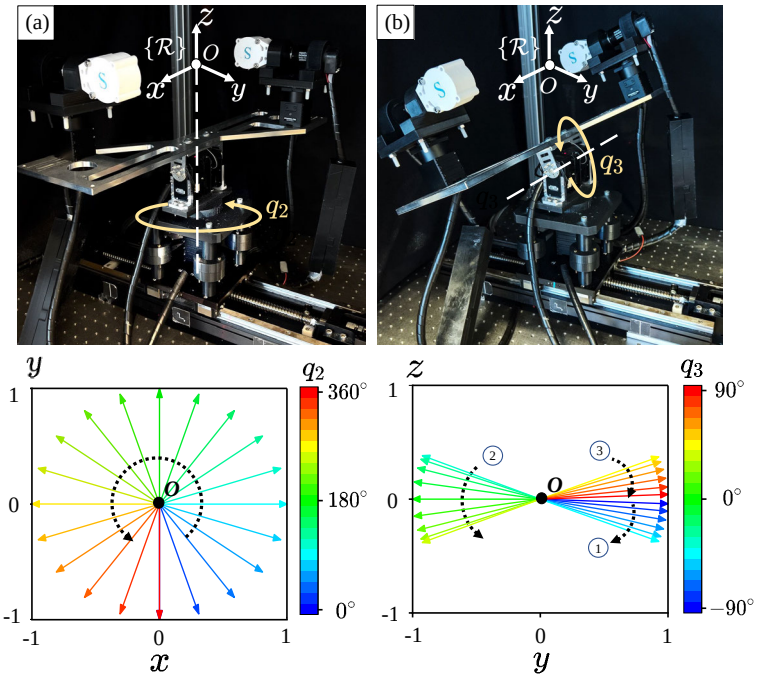

Figure 2.3: Characterization of the yawing motion and pitching motion of the unit vector of field-rotation axis with respect to joint space variables q_2 and q_3 at the central point of the workspace in the frame $\{\mathcal{R}\}$ $(Oxyz)$. The arrows indicate the unit vectors of the field-rotation axis. (a) The unit vector of the field-rotation axis rotates counterclockwise in the x-y plane as q_2 varies from 0° to 360°. (b) The vector of field-rotation axis first rotates clockwise as indicated by ①, then rotates counterclockwise as indicated by ②, and finally rotates clockwise back as indicated by ③ in y-z plane as q_3 varies from $-90°$ to 90°.

Specifically, at the central point, we associate the yawing motion of the field-rotation axis with joint space variable q_2, and the pitching motion with joint space variable q_3. Fig. 2.3 shows the orientation of field-rotation axis changes along with q_2 and q_3. The q_2 enables the yawing motion of the field-rotation axis at the central point, as shown in Fig. 2.3(a). The unit vector of the field-rotation axis rotates uniformly as q_2 varies at equal intervals over one revolution, which means the rotation of the field-rotation axis is synchronized with the rotation of q_2. Note that the unit vector of the

field-rotation axis at the case of $q_2 = 0°$ is overlapped by that at the case of $q_2 = 360°$. The q_3 enables the pitching motion of the field-rotation axis, as shown in Fig. 2.3(b). The unit vector of the field-rotation axis rotates non-uniformly as q_3 varies at equal intervals from $-90°$ to $90°$, which means the rotation of the field-rotation axis is not synchronized to the rotation of q_3. Meanwhile, the rotational direction of the unit vector of the field-rotation axis changes from clockwise ① to counterclockwise ②, and then back to clockwise ③.

2.3.2 Motion space of actuator magnets

The robotic joint space determines the motion space of actuator magnets, while the actuator magnets' motion space determines the field-rotation axis's reachable orientation zone at any point in the workspace. With revolute joints, the motion space of two actuator magnets is a hollow ellipsoid-like space and can be covered by an 800 mm × 800 mm × 500 mm cuboid, as shown in Fig. 2.4(a). With all joints (revolute plus translational joints), the motion space of two actuator magnets is a cylinder-like space and can be covered by an 800 mm × 1000 mm × 500 mm cuboid, as shown in Fig. 2.4(b).

2.3.3 Difficulty level of orienting the field-rotation axis

In this part, we will analyze the difficulty level of orienting the field-rotation axis towards different directions at the central point of the workspace. We assume that the position of the central point with respect to frame $\{\mathcal{A}\}$ (*Please refer to* Fig. 2.2) is unchanged. That is to say, the central point follows the translational motion of frame $\{\mathcal{A}\}$ along y-axis. Thus, the translational motion of the frame $\{\mathcal{A}\}$, which is characterized by the joint space variable q_1, does not affect the positions of actuator magnets ($\boldsymbol{x}_i$) and the orientation of the dipole-rotation axis ($\hat{\boldsymbol{\Omega}}$) in the frame $\{\mathcal{A}\}$. Therefore, the joint space variable q_1 does not influence the field-rotation axis at the central point since the field-rotation axis at any point in the workspace is purely a function of the actuator permanent magnets' positions ($\boldsymbol{x}_i$) and dipole-rotation axis' orientation ($\hat{\boldsymbol{\Omega}}$). Furthermore, to maximize the size of the workspace while maintaining a strong magnetic field strength, we set the joint space variable q_4 to 0. Thus, we design a new vector of joint space variables $\boldsymbol{q_n}$ that does not contain the joint space variables q_1 and q_4

such that $\boldsymbol{q_n} = [q_2\ q_3]^{\mathrm{T}}$. Then we investigate the unreachable zone of the field-rotation axis at the central point by only considering robotic revolute joints. The matrix $\mathbf{J}_{\mathcal{F}}(\boldsymbol{q_n}) \in \mathbb{R}^{3\times 2}$ is created to approximately map the small change ($\delta\boldsymbol{q_n}$) in the robotic joints to the small change ($\delta\hat{\boldsymbol{\omega}}$) in the orientation of field-rotation axis, which is expressed by

$$\delta\hat{\boldsymbol{\omega}} \approx \mathbf{J}_{\mathcal{F}}(\boldsymbol{q_n})\delta\boldsymbol{q_n}. \tag{2.27}$$

Equation (2.27) can be inverted to generate the inverse mapping of the desired change in the orientation of the field-rotation axis to a desired change in the robotic joints using Moore-Penrose pseudoinverse,

$$\delta\boldsymbol{q_n} \approx \mathbf{J}^{\dagger}_{\mathcal{F}}(\boldsymbol{q_n})\delta\hat{\boldsymbol{\omega}}. \tag{2.28}$$

where the Moore-Penrose pseudoinverse $\mathbf{J}^{\dagger}_{\mathcal{F}}(\boldsymbol{q_n})$ is the inverse mapping that minimizes $|\boldsymbol{q_n}|$ if the robotic system is over-actuated. The largest singular value of $\mathbf{J}^{\dagger}_{\mathcal{F}}(\boldsymbol{q_n})$ serves as a measure of the most extreme scenario where a change in the unit vector of the field-rotation axis is approximately mapped to a magnitude change in the robotic joints [71]. If the largest singular value approaches infinity, the robotic system is close to experiencing a kinematic singularity.

To assess the system's capability to make a TMD ascend or descend at the central point, we measure the difficulty of executing the system as the field-rotation axis approaches the vertical direction at the central point. The orientation of the field-rotation axis at the central point is characterized by angles θ and φ. Specifically, θ refers to the angle between the projection vector of the field-rotation axis and the positive x-axis, and the φ refers to the angle between the vector of the field-rotation axis and positive z-axis, as shown in Fig. 2.4(c). The ranges of angle θ and φ are set as [0° 360°] and [67.5° 112.5°], respectively. It shows the color map of the logarithmic largest singular value of $\mathbf{J}^{\dagger}_{\mathcal{F}}$ (the abbreviation of $\mathbf{J}^{\dagger}_{\mathcal{F}}(\boldsymbol{q_n})$) in the θ-φ plane at the central point. The color map reveals how hard it is for the field-rotation axis toward the orientation indicated by angle θ and ϕ. As φ decreases from 90° to 67.5° or increases from 90° to 112.5°, it gradually becomes harder. Therefore, it indicates that the more vertical the motion direction of a TMD, the more challenging it becomes for the system to implement. In our solution, we adopt a method of having the TMD ascend or descend in a spiral instead of vertically to achieve the TMD's arrival at the designated position.

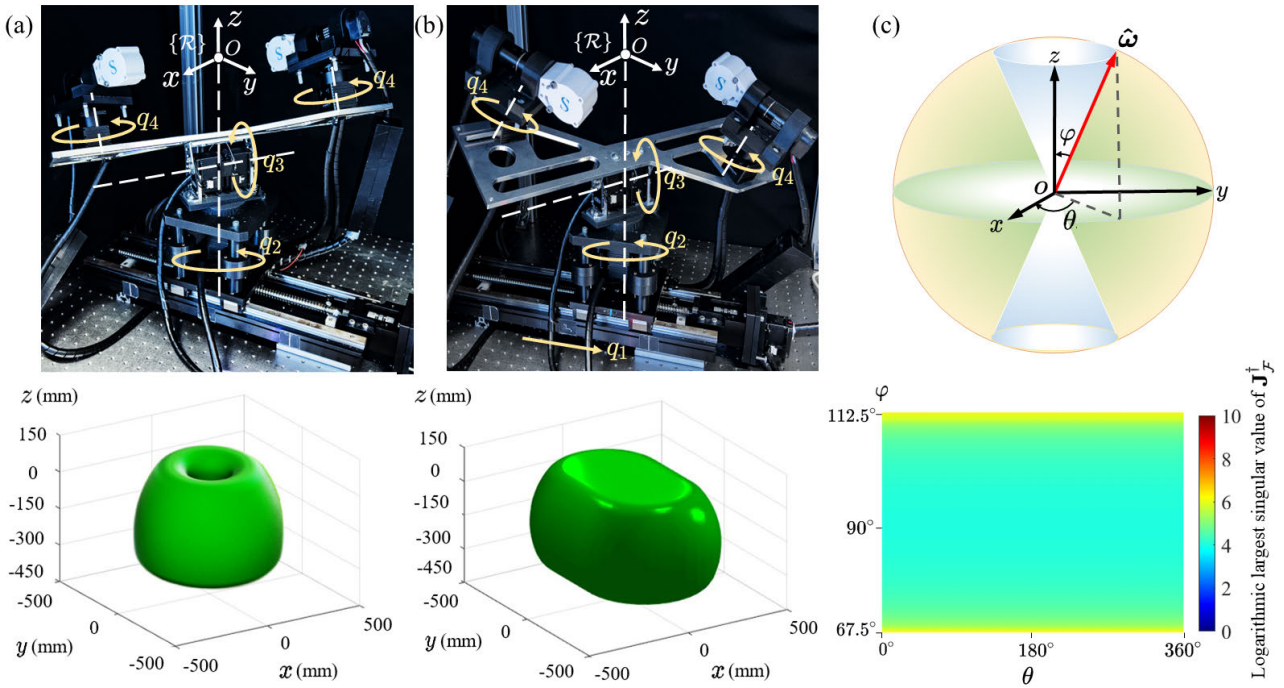

Figure 2.4: Mapping the robotic joint space to the orientation of the field-rotation axis at the central point (O) of the workspace. (a) The motion space of actuator magnets relative to robotic revolute joints. (b) The motion space of actuator magnets relative to robotic revolute and transnational joints. (c) The orientation of the field-rotation axis at the central point is characterized by the angle of θ and the angle of φ. The angle of θ is the one between the projection vector of the field-rotation axis and the positive x-axis, and the angle of φ is the one between the vector of the field-rotation axis and the positive z-axis. The range of θ is set as [0° 360°] while the range of φ is set as [0° 180°]. The largest singular value of Jacobin $\mathbf{J}_{\mathcal{F}}^{\dagger}$ in θ-φ plane, plotted in a logarithmic color scale.

2.4 Characterization of the magnetic field

Two identical permanent magnets, spaced apart by a distance of L_{mag}, are placed symmetrically on the x-axis relative to frame $\{\mathcal{R}\}$ with the unit vector of dipole-rotation axis ($\hat{\mathbf{\Omega}}$) paralleling to the y-axis, as shown in Fig. 2.5. The two identical permanent magnets are rotating in synchronization around the dipole-rotation axis ($\mathbf{\Omega}$) with a synchronous rotation angle of θ_s, resulting in a time-varying magnetic field $\mathbf{B}$ (magnetic flux density) and field gradient in the workspace of our permanent magnet-based robotic system. We study the variations in magnetic field strength and gradient ($|\mathbf{B}|$ and $|\nabla\mathbf{B}|$) within the spherical space centered at the origin and with a radius of r.

2.4.1 Magnetic field strength

For a fixed θ_s and a fixed L_{mag}, both maximum and minimum magnetic field strengths ($|\mathbf{B}|_{max}$ and $|\mathbf{B}|_{min}$) are present within a specific space. Similarly, for any θ_s and a fixed L_{mag}, both highest and lowest magnetic field strengths ($|\mathbf{B}|_{hig}$ and $|\mathbf{B}|_{low}$) are present within the same space.

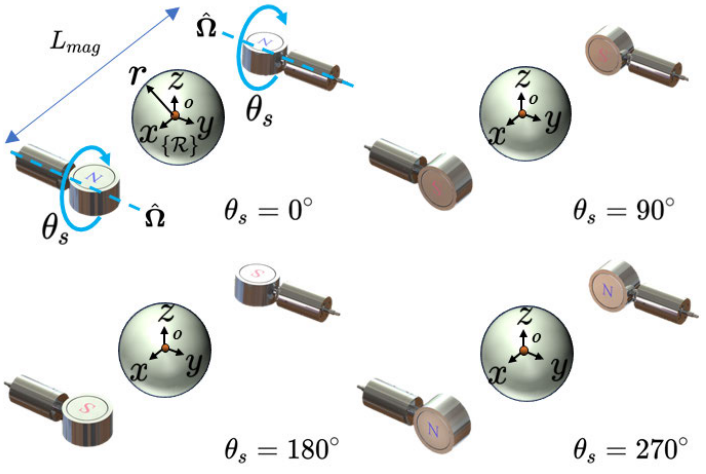

Figure 2.5: Two identical permanent magnets are rotated synchronously around the unit vector of dipole-rotation axis $\hat{\mathbf{\Omega}}$, resulting in a time-varying magnetic field within the center spherical space between the two magnets.

Variables such as θ_s, r, L_{mag}, and joint space variables (q_1, q_2, q_3 and q_4) contribute to a time-varying magnetic field within the workspace of our permanent magnet-based robotic system. In this section, we delve into the analysis of the evolving magnetic field and its gradient in the center spherical space resulting from these variables.

2.4.1.1 Synchronous rotation angle

To examine alterations in both magnetic field strength and gradient with variations in the synchronous rotation angle, we keep the radius of the central spherical space at several constant values (20, 30, 40, and 50 mm) and the distance between two actuator magnets constant such that $L_{mag} =$ 350 mm. As θ_s changes, both $|\mathbf{B}|_{max}$ and $|\mathbf{B}|_{min}$ will vary. This results in curves showing the changes of $|\mathbf{B}|_{max}$ and $|\mathbf{B}|_{min}$, as shown in Fig. 2.6(a, b, c, d). The red curve ($|\mathbf{B}|_{max}$), green curve ($|\mathbf{B}|_{min}$), and the region between them form a variation band. The variation band becomes wider at a larger center spherical space. The changes in $|\mathbf{B}|_{max}$ and $|\mathbf{B}|_{min}$ with respect to θ_s exhibit periodic behavior, with both of them sharing a period of 180°. Furthermore, we visualize the distribution of magnetic field strength over the surface of the central spherical spaces, while maintaining θ_s at specific fixed angles (0°, 30°, 60°, 90°, 120°, 150°, and 180°). Obviously, we observe that the magnetic field strength near the two actuator magnets is greater than in the central region of the sphere.

2.4.1.2 Radius of the center spherical space

The changes in $|\mathbf{B}|_{hig}$ and $|\mathbf{B}|_{low}$ with variations in r, while L_{mag} is fixed at 350 mm and θ_s varies from 0° to 360°, are illustrated in Fig. 2.6(e). The magnitudes of $|\mathbf{B}|_{hig}$ and $|\mathbf{B}|_{low}$ at different r are demonstrated in Table A.2 (*Please refer to* **Appendix A.3**). As r increases from 0 to 50 mm, the $|\mathbf{B}|_{hig}$ increases from 3.348 to 5.337 mT, whereas the $|\mathbf{B}|_{low}$ decreases from 1.704 to 1.167 mT, indicating that the rate at which the $|\mathbf{B}|_{hig}$ increases is faster than the rate at which the $|\mathbf{B}|_{low}$ decreases.

2.4.1.3 Distance between two actuator magnets

The changes in $|\mathbf{B}|_{hig}$ and $|\mathbf{B}|_{low}$ variations in the L_{mag}, while r is fixed at several constant values (20, 30, 40, 50 mm) and θ_s varies from 0° to 360°,

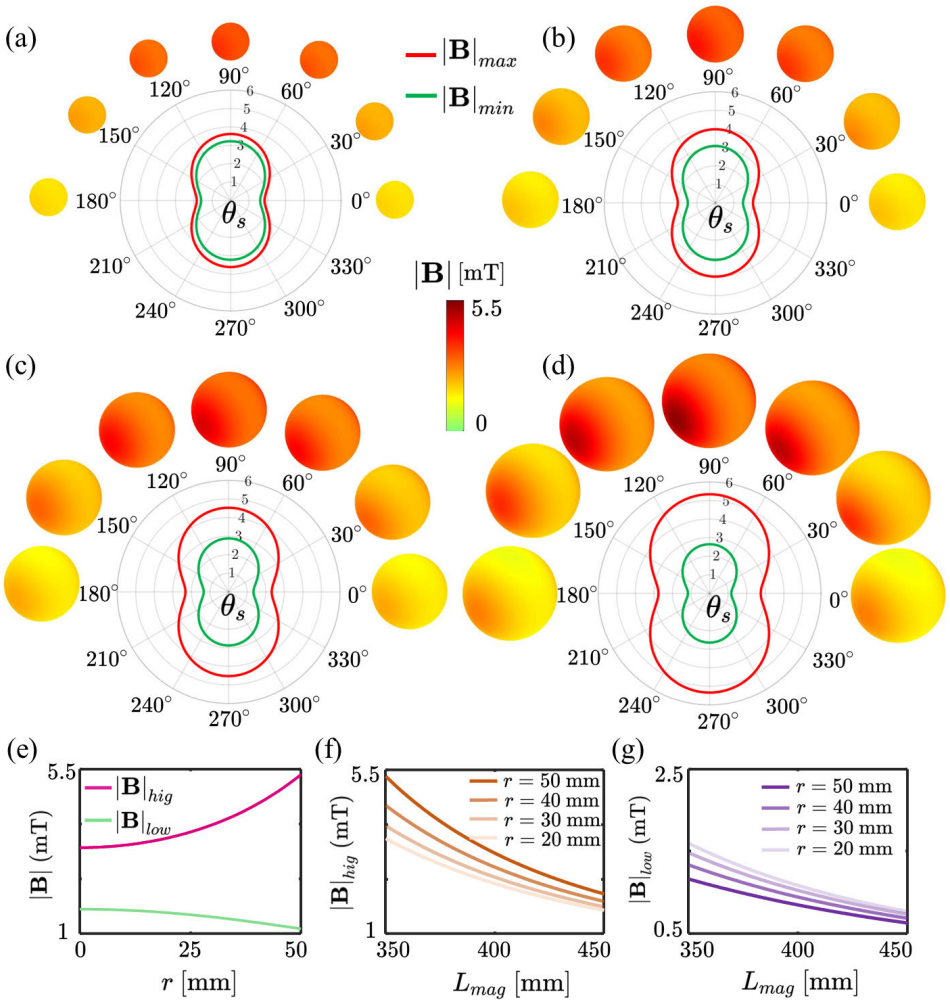

Figure 2.6: Time-varying magnetic field strength within the center spherical space. (a, b, c, d) The maximum and minimum magnetic field strengths ($|\mathbf{B}|_{max}$ and $|\mathbf{B}|_{min}$) vary within the central spherical space at several fixed radii ($r = 20, 30, 40, 50$ mm), while maintaining a fixed distance ($L_{mag} = 350$ mm) between two actuator magnets, throughout a single rotation period of the actuator magnets. The magnetic field strength distribution over the surface of the spherical space varies as synchronous rotation angle θ_s is fixed at several constant degrees (0°, 30°, 60°, 90°, 120°, 150° and 180°). (e) The changes of $|\mathbf{B}|_{hig}$ and $|\mathbf{B}|_{low}$ in relation to r when $L_{mag} = 350$ mm. (f and g) The changes of $|\mathbf{B}|_{hig}$ and $|\mathbf{B}|_{low}$ across various r in correlation with L_{mag}.

are shown in Fig. 2.6(f) and 2.6(g), respectively. As L_{mag} increases, $|\mathbf{B}|_{hig}$ decreases at a faster rate compared to $|\mathbf{B}|_{low}$. Further, the $|\mathbf{B}|_{hig}$ at a larger r decreases faster while $|\mathbf{B}|_{low}$ at a smaller r decreases faster. Specifically, as L_{mag} increases from 350 to 450 mm, the $|\mathbf{B}|_{hig}$ at $r = 20$, 30, 40 and 50 mm decreases from 3.615 to 1.658 mT, 3.973 to 1.757 mT, 4.526 to 1.904 mT and 5.337 to 2.108 mT, respectively. The $|\mathbf{B}|_{low}$ at $r = 20$, 30, 40 and 50 mm decreases from 1.605 to 0.771 mT, 1.489 to 0.737 mT, 1.340 to 0.692 mT and 1.167 to 0.638 mT, respectively.

2.4.2 Magnetic field gradient

Similar to the definition in magnetic field strength, for a fixed θ_s and a fixed L_{mag}, both the maximum and minimum magnetic field gradients ($|\nabla\mathbf{B}|_{max}$ and $|\nabla\mathbf{B}|_{min}$) are present within a specific space. Comparatively, for any θ_s with a fixed L_{mag}, both the highest and lowest magnetic field gradients ($|\nabla\mathbf{B}|_{hig}$ and $|\nabla\mathbf{B}|_{low}$) are also present within the same space.

2.4.2.1 Synchronous rotation angle

The change of maximum field gradient $|\nabla\mathbf{B}|_{max}$ along with θ_s, while r is fixed at several constant values (20, 30, 40, and 50 mm) and L_{mag} is fixed at 350 mm, is periodic with a period of 180°, as shown in Fig. 2.7(a, b, c, and d). In addition, the magnetic field gradient distribution on the surface of the center spherical space with the radius of 20, 30, 40, and 50 mm while keeping θ_s at a set of constant degrees (0°, 30°, 60°, 90°, 120°, 150°, and 180°) is visualized. It is evident that the magnetic field gradient is noticeably higher in the vicinity of the actuator magnets within the spherical space compared to the central portion of the sphere.

2.4.2.2 Radius of the center spherical space

The change in $|\nabla\mathbf{B}|_{hig}$ with variations in r, while L_{mag} is set at 350 mm, is shown in Fig. 2.7(e). The magnitudes of $|\nabla\mathbf{B}|_{hig}$ and $|\nabla\mathbf{B}|_{low}$ at different r are demonstrated in Table A.2 (*Please refer to* **Appendix A.3**). Note that $|\nabla\mathbf{B}|_{low}$ remains to be 0. With an increasing r, $|\nabla\mathbf{B}|_{hig}$ also exhibits a corresponding increase. As r increases from 0 to 50 mm, $|\nabla\mathbf{B}|_{hig}$ increases from 0 to 0.097 T/m.

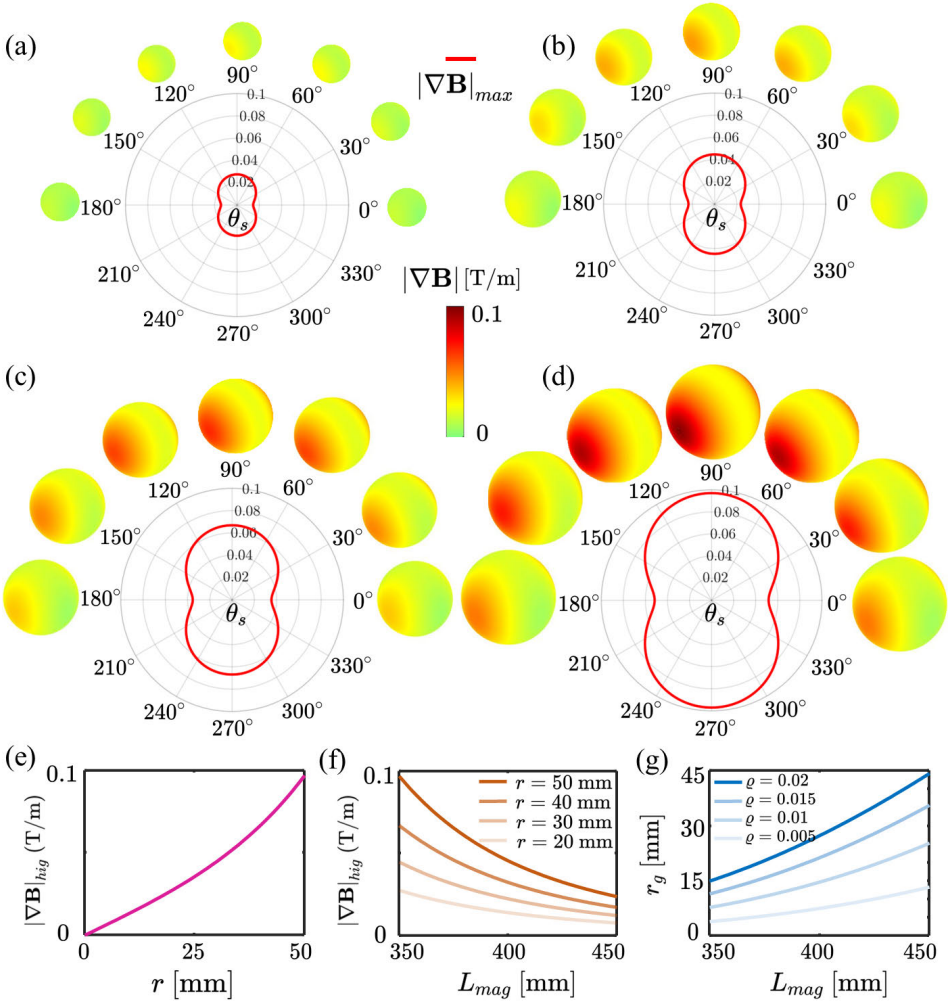

Figure 2.7: Time-varying magnetic gradient within the center spherical space. (a, b, c, and d) The maximum magnetic field gradient ($|\nabla \mathbf{B}|_{max}$) varies within the central spherical at several fixed radii ($r = 20, 30, 40, 50$ mm), while maintaining a fixed distance between two actuator magnets ($L_{mag} = 350$ mm), throughout a single rotation period of the actuator magnets. The magnetic field gradient distribution over the surface of the spherical space varies as synchronous rotation angle θ_s is at different degrees (0°, 30°, 60°, 90°, 120°, 150° and 180°). (e) The change of the $|\nabla \mathbf{B}|_{hig}$ in relation to r when $L_{mag} = 350$ mm. (f) The change of $|\nabla \mathbf{B}|_{hig}$ across various r in correlation with L_{mag}. (g) The change of the radius (r_g) of gradient-free space in relation to L_{mag} for a set of given thresholds (ϱ).

2.4.2.3 Distance between two actuator magnets

The change in $|\nabla \mathbf{B}|_{hig}$ with variations in L_{mag}, while r is fixed at several constant values (20, 30, 40, and 50 mm), is shown in Fig. 2.7(f). As L_{mag} increases, $|\nabla \mathbf{B}|_{hig}$ at a larger r decreases faster. Specifically, as L_{mag} increases from 350 mm to 450 mm, $|\nabla \mathbf{B}|_{hig}$ at r = 20, 30, 40 and 50 mm decreases from 0.028 to 0.008 T/m, 0.045 to 0.012 T/m, 0.067 to 0.017 T/m and 0.097 to 0.024 T/m, respectively.

2.4.2.4 Gradient-free space

A space is assumed to be gradient-free if the magnitude of magnetic field gradient within the space below a threshold (ϱ) such that $|\nabla \mathbf{B}|_{hig} \leq \varrho$. The threshold determines the degree of gradient-free space. A smaller threshold corresponds to a higher degree of gradient-free space. As L_{mag} increases, the radius (r_g) of the gradient-free space expands for a set of given thresholds, as shown in Fig. 2.7(g). Specifically, as L_{mag} increases from 350 to 450 mm, the r_g at ϱ = 0.005, 0.01, 0.015 and 0.02 increases from 3.86 to 13.23 mm, 7.67 to 25.29 mm, 11.38 to 35.65 mm, and 14.95 to 44.36 mm, respectively. In contrast, the desired distance (L^d_{mag}) between two actuator magnets can be calculated for the gradient-free space with a required size at a specified threshold. An algorithm for obtaining L^d_{mag} is given in **Appendix A.4**. The size of the gradient-free space can be enlarged by increasing the distance between the two actuator magnets. However, this comes at the expense of the average magnetic field strength in the gradient-free space. Hence, there is an optimal distance between the two synchronized rotating permanent magnets that ensures effective propulsion of the TMD while maximizing the available gradient-free space for its motion.

2.4.3 Joint space variables

We examine the influence of each joint space variable on $|\mathbf{B}|_{max}$, $|\mathbf{B}|_{min}$, and $|\nabla \mathbf{B}|_{max}$ under two different scenarios. The first scenario involves a fixed r and several fixed θ_s (Fig. 2.8). The second scenario features a fixed θ_s and several fixed r (Fig. 2.9).

In the first scenario, r is set to 50 mm, and θ_s is set at several fixed degrees (0°, 30°, 60°, and 90°). In Fig. 2.8(a), it indicates that the $|\mathbf{B}|_{max}$

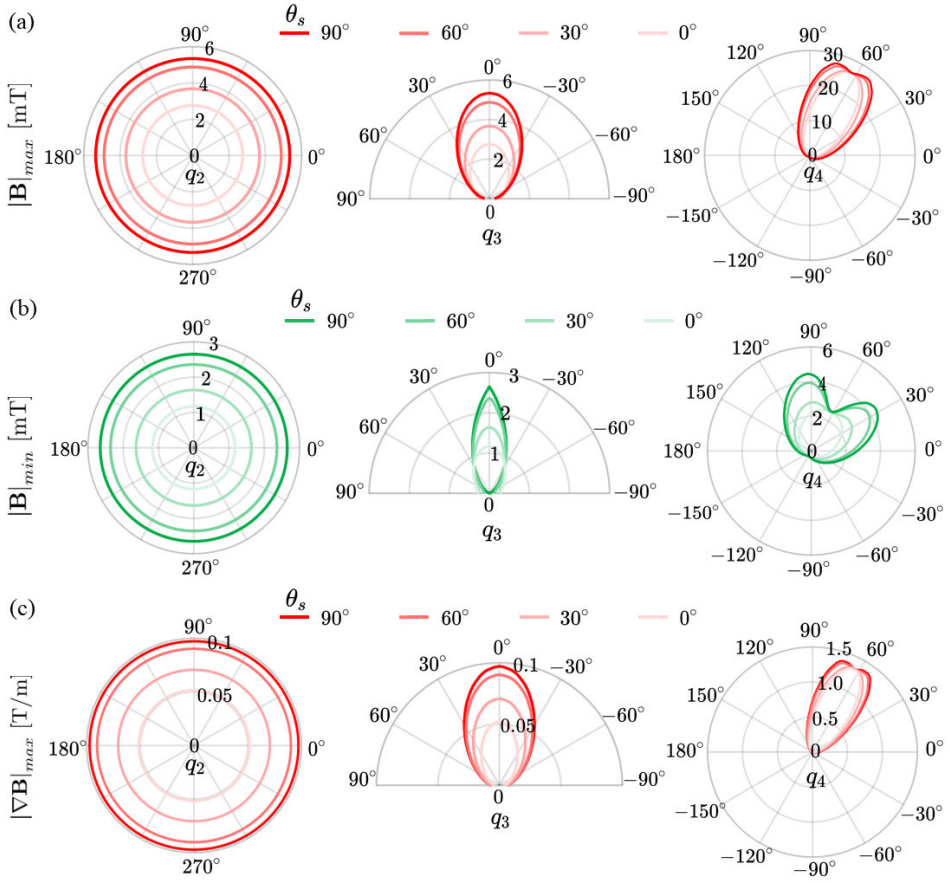

Figure 2.8: The influence of each joint space variable on the magnetic field strength and gradient within a center 50 mm-radius spherical space, as the synchronous rotation angle is set at several fixed degrees (0°, 30°, 60°, and 90°). (a and b) The changes of maximum and minimum magnetic field strengths. (c) The changes of maximum magnetic field gradient.

remains constant with variations in q_2. A rise is found as q_3 transitions from $-90°$ to 0°, and then a decline as q_3 changes from 0° to 90°. Further, the $|\mathbf{B}|_{max}$ is observed initially increase rapidly with the increase in q_4, then experience a slight decrease as q_4 continues to increase, followed by a minor rise, and finally undergoes a rapid decrease as q_4 further increases. By observing Fig. 2.8(a) and 2.8(b), we notice a similar trend in the influence

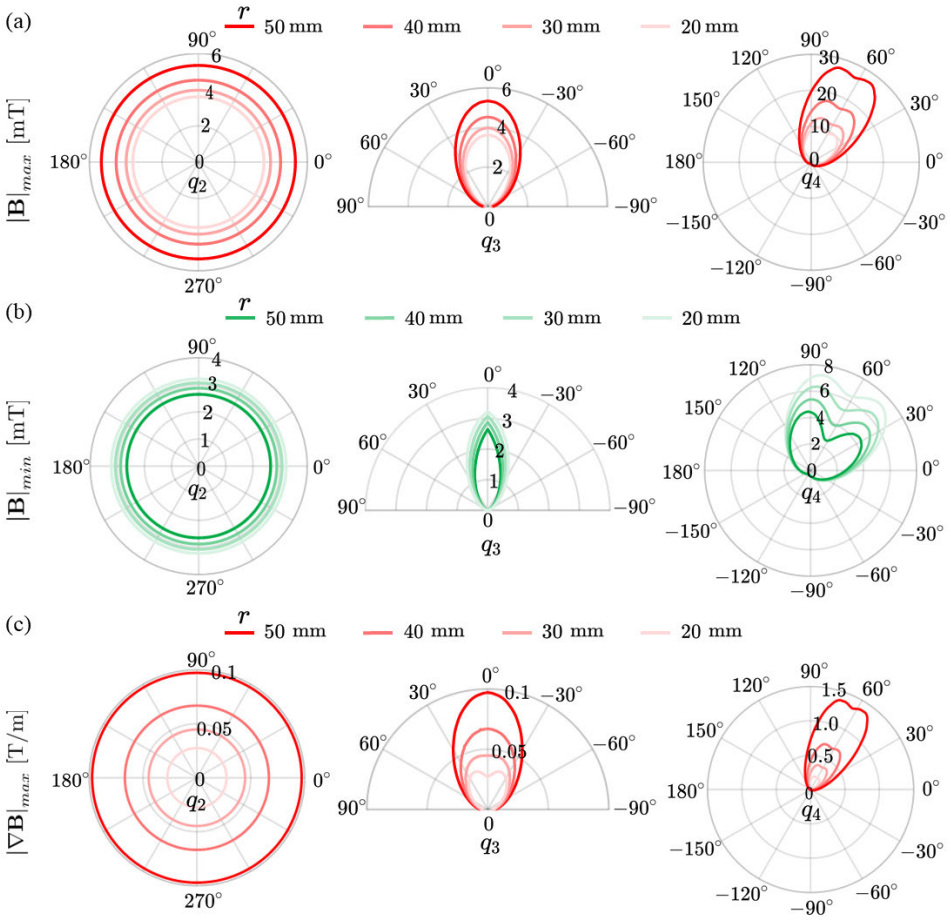

Figure 2.9: The influence of each joint space variable on the magnetic field strength and gradient within the center spherical space at a synchronous rotation angle of 90°, as the radius of the center spherical space is set at several fixed values (20 mm, 30 mm, 40 mm, 50 mm). (a and b) The changes of maximum and minimum magnetic field strengths. (c) The change of maximum magnetic field gradient

of q_2 as well as q_4 on $|\mathbf{B}|_{max}$ and $|\mathbf{B}|_{min}$ at a given θ_s. The influence of q_3 on $|\mathbf{B}|_{min}$ causes a notable shift when the θ_s is approximately 90°. By observing Fig. 2.8(a) and 2.8(c), a similar pattern emerges regarding the impact of each single joint variable on $|\mathbf{B}|_{max}$ and $|\nabla\mathbf{B}|_{max}$ at a given θ_s.

In the second scenario, θ_s is set to 90°, and r is set at several fixed

values (20, 30, 40, and 50 mm). In Fig. 2.9(a), the impact of each single joint variable on $|\mathbf{B}|_{max}$ at a specific r exhibits a pattern similar to that in Fig. 2.8(a). By observing Fig. 2.9(a) and 2.9(b), it is evident that $|\mathbf{B}|_{max}$ gradually increases, while $|\mathbf{B}|_{min}$ steadily decreases, as r increments from 20 to 50 mm at intervals of 10 mm. By observing Fig. 2.9(a) and 2.9(c), a consistent pattern is evident concerning the influence of each single joint variable on $|\mathbf{B}|_{max}$ and $|\nabla\mathbf{B}|_{max}$ when r is equal to 30, 40, or 50 mm. In Fig. 2.9(c), it reveals that when r is set to 20 mm, an oscillatory pattern is observed in $|\nabla\mathbf{B}|_{max}$ as q_3 changes from $-90°$ to $90°$. This oscillatory behavior is characterized by an initial increase, followed by a slight decrease, then another slight increase, and finally, a continuous decrease.

In both scenarios, the range of variation for $|\mathbf{B}|_{max}$ and $|\nabla\mathbf{B}|_{max}$, influenced by q_2 or q_3, falls within [0 5.5] mT and [0 0.1] T/m, respectively. Conversely, the range of variation for $|\mathbf{B}|_{max}$ and $|\nabla\mathbf{B}|_{max}$, influenced by q_4, spans [0 28] mT and [0 1.5] T/m, respectively. Furthermore, under both the first and second scenarios, the range of variation for $|\mathbf{B}|_{min}$, influenced by q_1, q_2, or q_3, extends to [0 2.7] mT and [0 3.3] mT, respectively. Conversely, the range of variation for $|\mathbf{B}|_{min}$, influenced by q_4, extends to [0 4.5] mT and [0 7.3] mT, respectively.

2.5 Closed-loop motion control

A TMD is controlled to follow three predefined 2-D trajectories and a 3-D spiral circular trajectory in an agar gel phantom to verify the capability of our permanent magnet-robotic system in TMD motion control. The TMD consists of a twisted body and a cylindrical magnet. The body of the TMD has a length of 4 mm and a diameter of 1.5 mm, and a weight of 0.0049 grams. The magnet of the TMD is made of Grade-N45 NdFeB and axially magnetized with the diameter of 1 mm and the height of 1 mm, and it has a weight of 0.0064 grams. The magnet is positioned at the tail, with its dipole moment being perpendicular to the helix axis of the TMD. The two identical actuator magnets are fabricated with cylindrical Grade-N45 NdFeB and axially magnetized. Each of them has a diameter of 45 mm and a height of 30 mm. Further, the actuator magnets are controlled to rotate synchronously. Each of them is driven by a Maxon motor (Planetary Gearhead GP 32 C D32 mm, 1.0-6.0 Nm, Ceramic Version) with a Maxon controller (EPOS2 50/5, Digital positioning controller, 5 A, 11-50 VDC).

The field-rotation axis's translational motion, characterized by joint space variable q_1, is implemented by a linear motion stage (KUA1505-520-150-A1-N3, X-Axis unit, Japan). Further, the motion stage is driven by an A1 actuator (MX-106R, Dynamixel Actuator). The yawing motion of the field-rotation axis, which is characterized by joint space variable q_2, is accomplished by an A2 actuator (H42P-020-S300-R, Servomoteur Dynamixel PRO PLUS). The pitching motion of the field-rotation axis, which is characterized by joint space variable q_3, is realized by two A1 actuators that are in synchronous control mode. Another yawing motion of the field-rotation axis, characterized by joint space variable q_4, is fulfilled by two A3 actuators (M42P-010-S260-R, Servomoteur Dynamixel PRO PLUS). To measure the real-time position and the moving direction of the TMD, two cameras (Aviator GIGE, avA1000-100gm, Basler AG, Ahrensburg, Germany) are mounted on orthogonal sides of the container. Besides, the TMD is immersed in an agar gel phantom, which is made of gelatine powder (Ec Nr: 232-554-6, Boom BV, Rabroekenweg, The Netherlands) and demineralized water with a mass ratio of 0.63 wt.%. To create the agar gel phantom, we pour the aqueous gelatin solution into a transparent cubic container with a length of 100 mm. Subsequently, the container is placed in a refrigerator at 3 degrees Celsius for 12 hours before the experiment.

2.5.1 Two-dimensional motion control

We implement 2-D closed-loop motion control experiments with two prescribed trajectories. To begin with, the prescribed "Triangle" and "Square" trajectories are broken into 32 and 18 representative waypoints, respectively. Then, the desired inverse solution at each representative point of prescribed trajectories is solved based on the algorithm presented in Table 2.1. Next, these inverse solutions provide the real-time reference positions for joint space variables during the implementations of TMD closed-loop motion control.

The prescribed (red) and actual (blue) trajectories with their tracking errors are indicated in each case, as shown in Fig. 2.10. It indicates that the maximum position tracking errors of the "Triangle" and "Square" trajectories are 1.94 mm and 1.20 mm, respectively. The TMD achieves an average motion speed of 0.27 mm/s during the closed-loop motion control. The increase in the motion speed of the TMD can be achieved by increas-

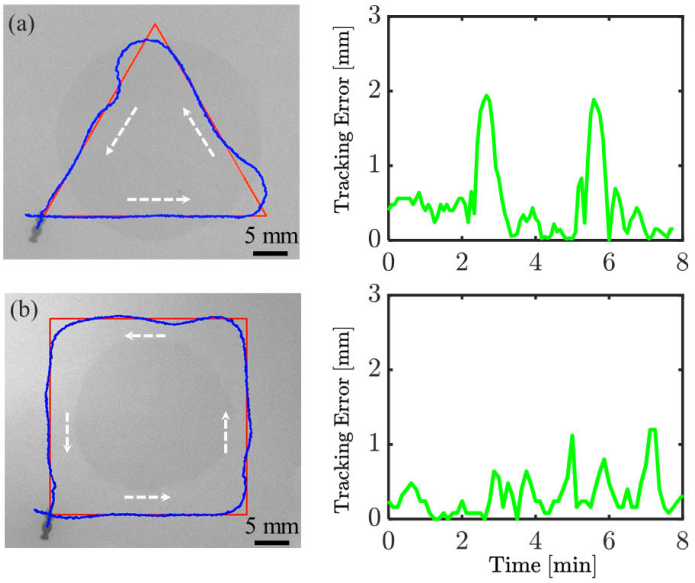

Figure 2.10: 2-D closed-loop motion control of a TMD to move along prescribed 2-D trajectories. (a) "Triangle" trajectory with its tracking error. (b) "Square" trajectory with its tracking error. The prescribed trajectories (red) and the actual trajectories (blue) are indicated. The TMD swims at an average motion speed of 0.27 mm/s, and a maximum tracking error of 1.94 mm during the 2-D closed-loop motion control. *Please refer to the accompanying video.*

ing the actuation frequency. However, increasing the TMD's motion speed requires the system to have the capability to respond quickly. Otherwise, it may lead to an increase in position tracking error *Please refer to the accompanying video.*

2.5.2 Three-dimensional motion control

We implement 3-D closed-loop motion control experiments with one prescribed trajectory. To begin with, the prescribed 3-D spiral trajectory is broken into 17 representative waypoints (*Please refer to* Table 2.2). These waypoints are evenly distributed on the predefined trajectory. The desired field-rotation axis at each representative waypoint is indicated by the red arrow. Given the representative waypoint P_n and the desired field-rotation axis $\hat{\boldsymbol{\omega}}^d$, the desired dipole-rotation axis $\hat{\boldsymbol{\Omega}}^d$, and the desired vector of joint

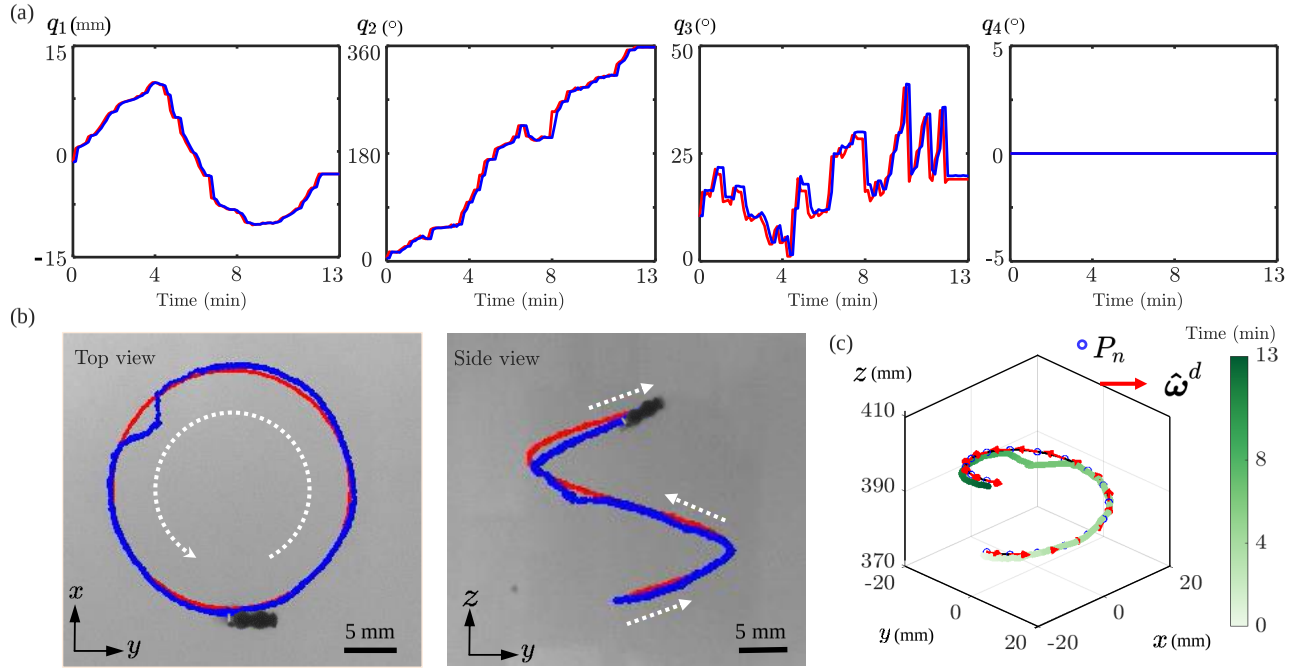

Figure 2.11: 3-D closed-loop motion control of a TMD is implemented using our permanent magnet-based robotic system. The TMD is controlled to follow a predefined 3-D spiral trajectory inside a square container (with a side length of 100 mm) filled with agar gel phantom. (a) The reference position (red) and actual position (blue) of each joint variable indicate the control input and output of each joint variable. (b) The actual track points from the top view form a circle with a diameter of 30.6 mm, and those in the side view from the rising spirals with a pitch of 19.0 mm. (c) The synthetic 3-D trajectory (green) indicates the mean absolute error compared to the predefined one (black) is 1.18 mm, and the maximum tracking error is 2.64 mm. The desired field-rotation axis at each representative point is indicated by a red arrow. *Please refer to the accompanying video.*

space variables $\boldsymbol{q}^d$ at each waypoint is calculated in Table 2.2 by using the algorithm presented in Table 2.1.

The time-dependent changes of reference (red) and actual (blue) positions in joint space variables are shown in Fig. 2.11(a). The time-dependent change of q_1 shows a tendency for the linear motion stage to move forth and back to follow the TMD motion in the y-axis direction. The time-dependent change of q_2 indicates that the bottom yawing motor approximately rotates 22° at two adjacent representative waypoints. The time-dependent change of q_3 indicates that the pitching motor decreases its pitching angle as the TMD moves upward. The time-dependent change of q_4 indicates that the two top yawing motors make a small rotation. As we look at the time-dependent changing trend of each joint space variable, the control system tends to keep the TMD at the center of the workspace throughout the process of controlling the TMD to move along the predefined trajectories.

Fig. 2.11(b) indicates the real-time position of the TMD at the top and side views. From the top view, the TMD trajectory forms a circle with a diameter of 30.6 mm. From the side view, the trajectory forms a spiral with a pitch of 19.0 mm. Further, Fig. 2.11(c) demonstrates that the mean absolute error of 3-D motion control, by calculating the average positioning error between the synthetic and predefined 3-D trajectory (green and black), is 1.18 mm, and the maximum tracking error is 2.64 mm. The experimental results reveal that the TMD can move controllably. *Please refer to the accompanying video.*

2.6 Conclusion

We develop a permanent magnet-based robotic system that enables motion control of TMDs. First, we derive a kinematic model that relates the field-rotation axis, the dipole-rotation axis, and the joint space variables. Then, we characterize the yawing and pitching motion of the field-rotation axis at the central point of the workspace. Next, we analyze the difficulty level of orienting the field-rotation axis at the central point of the workspace and observe that the system exhibits a greater degree of singularity as the field-rotation axis becomes more vertical. Then, we characterize the magnetic field and field gradient in the workspace and observe that the center region of the workspace is almost a gradient-free region. Finally, we demonstrate the capability of our robotic system to control a TMD moving

along prescribed trajectories in 2-D and 3-D space experimentally.

In addition, the inclusion of extra DOFs will allow our system to control the TMD motion with various strategies. Our system is not only capable of driving highly magnetized devices, like those containing NdFeB magnets for magnetization, but also caters to weakly magnetized devices, such as soft sperm robots that utilize injected magnetic particles for magnetization [149].

Chapter Overview

Actuation systems that utilize two synchronized rotating permanent magnets provide a notable advantage compared to those using only a single rotating permanent magnet. The use of two synchronized rotating magnets allows for the reduction or elimination of the lateral gradient force acting on a TMHD, resulting in more stable motion of the TMHD.

In **Chapter 2**, we introduce a permanent magnet-based robotic system that employs two synchronized rotating permanent magnets to achieve 3-D motion control of a TMHD in physiological environments. We verify the existence of a gradient-free space between the two synchronized rotating permanent magnets, confirming that our robotic system meets the necessary conditions for applying a swimming speed prediction model that assumes force-free rotation of the TMHD. This validation paves the way for utilizing the prediction model to guide TMHD motion control within our robotic system.

Consequently, in **Chapter 3**, we focus on integrating this prediction model into TMHD motion control. To achieve this, we characterize the TMHD swimming speed in relation to the actuation frequency of the rotating field. This characterization provides the foundation for designing the closed-loop control scheme for the TMHD based on the prediction model.

3

Closed-Loop Control of Magnetically-Driven Screws in a Viscoelastic Medium

Note: *Following chapter is adapted from the article "Closed-Loop Control of Magnetically-Driven Screws in a Viscoelastic Medium" by* ***Z. Zhang****, A. Klingner, S. Misra, and I. S. Khalil published in Proceedings of the IEEE/RSJ International Conference on Intelligent Robots and Systems (IROS), Las Vegas, NV, USA, 2020, pp. 25–29.*

Abstract

Magnetically-driven screws operating in soft tissue environments could be used to deploy localized therapy or achieve minimally invasive interventions. In this work, we characterize the closed-loop behavior of magnetic screws in an agar gel tissue phantom using a permanent magnet-based robotic system with an open configuration. Our closed-loop control strategy capitalizes on an analytical calculation of the swimming speed of the screw in viscoelastic fluids and the magnetic point-dipole approximation of magnetic fields. The analytical solution is based on the Stokes/Oldroyd-B equations, and its predictions are compared to experimental results at different actuation frequencies of the screw. Our measurements match the theoretical prediction of the analytical model before the step-out frequency of the screw, owing to the linearity of the analytical model. We demonstrate open-loop control in two-dimensional space, and point-to-point closed-loop motion control of the screw (length and diameter of 6 mm and 2 mm, respectively) with a maximum positioning error of 1.8 mm.

3.1 Introduction

There have been many successful biologically-inspired approaches to provide locomotion at low Reynolds number (Re) regime. Swimming using helical propulsion based on the *Escherichia coli* bacteria has been achieved by Bell *et al.* and Ghosh *et al.* using homogenous magnetic fields [150], [151]. These magnetic fields exert magnetic torque on the dipole of the helical microrobots, and hence allow them to rotate and move through screw-based motion in fluids and tissue [152]. The wireless control in fluidic environments, micrometer-level precision, and the small size of these microrobots make them viable for diverse clinical applications [153]-[154]. With helical propulsion, even so, more than with other actuation techniques, the microrobot has the ability to swim under a wide range of Re in the range of 0.01 to 1000. In addition, helical propulsion enables microrobots to swim in viscous fluids and drill through complex viscoelastic media. Therefore, they could potentially perform tasks in biological fluids and tissue.

Nelson *et al.* have developed an empirical model of magnetically-driven screws to predict the role of magnetic, rheological, and actuation parameters on the turning radius of the screw [155]. Schamel *et al.* have demonstrated that nanoscrews move controllably through high viscosity solutions [156]. They have also observed propulsion enhancement that exceeds the highest measured speeds in Newtonian fluids for heterogenous gel-like media with a mesh size larger than the swimmer size. Walker *et al.* have developed magnetic micropropellers that mimic bacteria in swimming through mucus by producing the enzyme urease to raise the pH locally and dissolve the mucus [157]. Wu *et al.* have also developed intravitreal delivery micropropellers that can be actively propelled through the vitreous humor to reach the retina [158]. Recently, Xu *et al.* have also demonstrated image-based visual servoing of helical microswimmers and arbitrary path following in two dimensions [159], [160]. These microrobots are typically actuated using uniform magnetic fields produced by orthogonal arrangements of electromagnetic coils with a relatively limited projection distance.

In contrast to actuation with an orthogonal arrangement of coils, Fountain *et al.* [161] and Mahoney *et al.* [162], [163] have demonstrated helical propulsion using non-uniform magnetic fields produced by a single rotating permanent magnet. The rotating permanent magnet is positioned

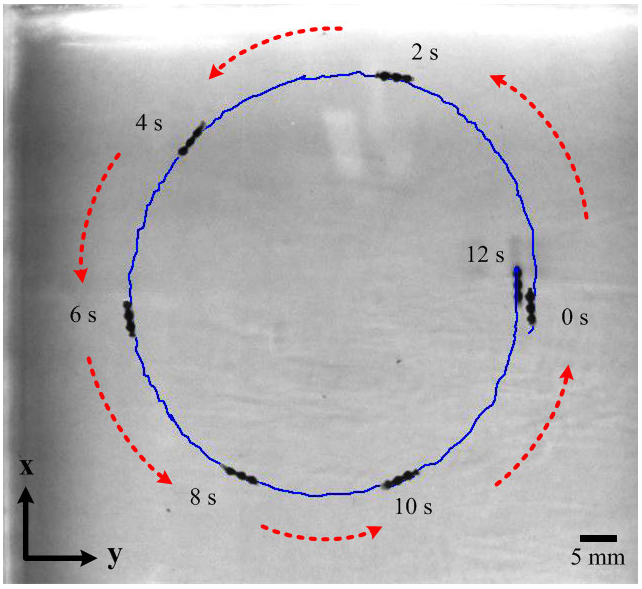

Figure 3.1: A magnetically-driven screw is moved controllably in soft tissue phantom (0.8 wt.% agar gel) at room temperature along a circular trajectory. The screw is actuated by two rotating dipole fields. The blue trajectory and the curved red arrows indicate the path and direction of the screw, respectively.

with a 6-DOF robotic manipulator to enable actuation over relatively large workspace compared to orthogonal arrangements of electromagnetic coils. Ryan and Diller have also presented a permanent magnet-based actuation system consisting of eight permanent magnets [164]. The eight permanent magnets can create fields and field gradients in any direction with variable magnitudes to achieve feedback control of microagents. It has also been demonstrated that the attractive forces acting on the microrobot can be converted into a lateral force using an open-loop trajectory by Mahoney *et al.* [165]. Alshafeei *et al.* [166] and Hosney *et al.* [74], [146] have also shown that the attractive forces along the lateral direction of the microrobot can be eliminated by using two synchronized rotating dipole fields, and open-loop control has been demonstrated inside a viscous medium to clear clogged vessels.

In this chapter, we study the closed-loop behavior of magnetically-driven screws in a viscoelastic medium (agar gel) under the influence of non-uniform rotating dipole fields (Fig. 3.1). A closed-loop control system is developed based on an analytical solution of the swimming speed of the screw and the magnetic point-dipole approximation of the magnetic fields, and we achieve the following:

1. Implement an analytical solution based on the Stokes/Oldroyd-B equations to predict the swimming speed of the screw [40], [167];
2. Characterization of the frequency response of magnetically-driven screws and comparison between measurements and analytical results;
3. Open-loop and point-to-point closed-loop control in agar gel.

The remainder of this paper is organized as follows: In Section 3.2, an analytical solution of the swimming speed of the magnetically-driven screw in viscoelastic fluids is used in the development of a closed-loop control system. Section 3.3 provides descriptions of our permanent magnet-based robotic system, characterization of the frequency response of the screw, and comparison with the theoretical predictions of the Stokes/Oldroyd-B equations, and open- and closed-loop control results. Finally, Section 3.4 concludes and provides directions for our future work.

3.2 Modeling and control of magnetically-driven screws

Magnetically-driven screws are immersed in low-Re medium and actuated using a non-uniform magnetic field.

3.2.1 Magnetically-driven screws

We consider a screw with magnetic dipole moment $\mathbf{m}$ perpendicular to its helix axis, consisting of a helical wave superimposed onto a cylinder of radius A. Its surface is described by [40], [167]

$$\mathbf{x}(\theta,\zeta) = A\rho(\theta)[\cos(v^*\zeta+\theta)\hat{\mathbf{x}} + \sin(v^*\zeta+\theta)\hat{\mathbf{y}}] + \zeta\hat{\mathbf{z}}, \tag{3.1}$$

where θ and ζ are helical coordinates such that $\theta \in [0, 2\pi)$ and $\zeta \in (-\infty, \infty)$. Further, the helical pitch is $2\pi/v^*$ and the pitch angle is given by

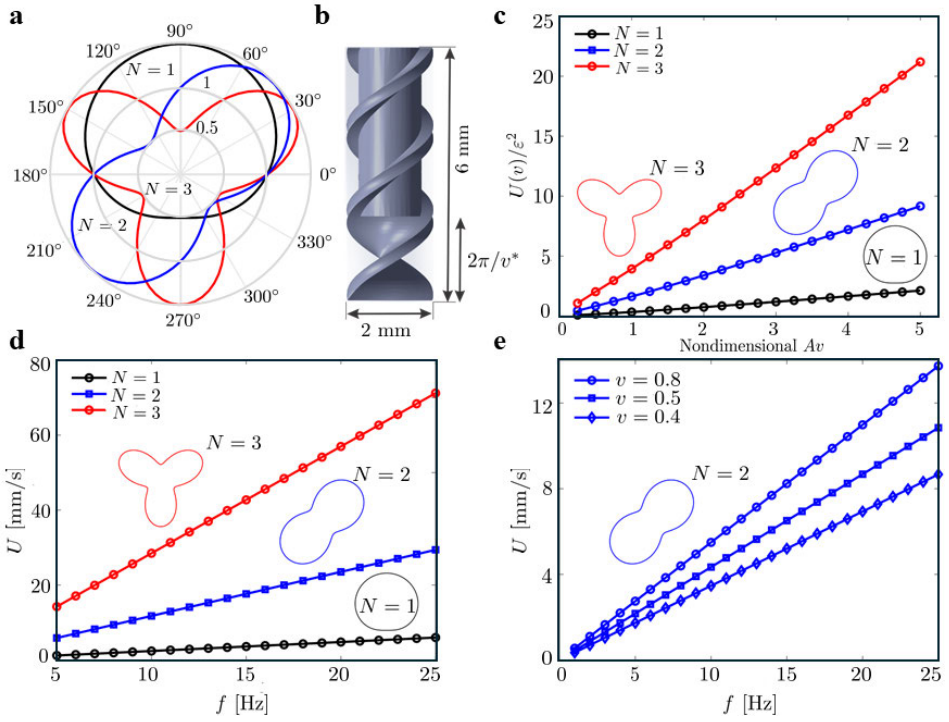

Figure 3.2: The profile of the screw influences its swimming speed in a viscoelastic medium. (a) Three representative screw profiles (ρ) are calculated using $\rho(\theta) = 1 + \epsilon \sin(N\theta)$, for $\epsilon = 0.5$, $N = 1:3$, and $\theta \in [0, 2\pi)$. N is the number of starts of the screw. (b) The permanent magnet with magnetization direction orthogonal to the long axis of the screw is fixed inside the cylinder (with radius A). (c) Swimming speed of the screw is calculated as function of v for $N = 1, 2, 3$. (d) The swimming speed (U) of the screw increases with the number of starts and the actuation frequency (f). (e) U increases with f and v for $N = 2$, and $\epsilon = 0.33$. The swimming velocity is calculated using equation (3.4).

$\gamma = \tan^{-1}(v^* A)$. The function $\rho(\theta) = A[1 + \varepsilon f(N\theta)]$ indicates the profile of the cross-section of the screw, where $f(N\theta)$ is a periodic function and N is the number of starts of the screw. Fig. 3.2(a) shows different profiles for the screw. The screw (Fig. 3.2(b)) is subject to a magnetic torque $\tau = \mathbf{m} \times (\mathbf{B}_1 + \mathbf{B}_2)$ exerted by two rotating dipole fields $\mathbf{B}_1$ and $\mathbf{B}_2$. These fields are generated by two rotating permanent magnets and modeled with the following point-dipole approximation [161]-[163]:

$$\mathbf{B}_i(\mathbf{p}) = \frac{\mu_0}{4\pi \mid \mathbf{p} \mid^3} \left(\frac{3(\mathbf{M}_i \cdot \mathbf{p})\mathbf{p}}{\mathbf{p}} - \mathbf{M}_i \right) \text{ for } i = 1, 2, \tag{3.2}$$

where μ_0 is the permeability of free space and $\mathbf{p}$ is the position vector of the screw with respect to the rotating permanent magnet. Further, $\mathbf{M}_i$ is the magnetic dipole moment of the ith permanent magnet. Because $\mathbf{M}$ rotates at a controlled constant angular velocity (results in translating speed as shown in Fig. 3.3(a)), $\mathbf{M}$ is constructed using $\mathbf{q}$ as

$${}^0\mathbf{T}_i^3(\mathbf{q}) = \begin{pmatrix} {}^0\mathbf{R}_i^3 & {}^0\mathbf{p}_i^3 \\ \mathbf{0}_{1\times 3} & 1 \end{pmatrix} \quad \text{for} \quad i = 1, 2, \tag{3.3}$$

where ${}^0\mathbf{T}_i^3(\mathbf{q})$ is the ith homogenous transformation matrix from the frame of reference of the ith permanent magnet to a reference frame and $\mathbf{q} = (\phi, \alpha, \beta)^T$ is a vector of the joint space coordinates. Further, ${}^0\mathbf{R}_i^3$ and ${}^0\mathbf{p}_i^3$ are the rotation matrix and position vector of the ith permanent magnet with respect to a frame of reference (Fig. 3.3(b)), respectively. The orientation of the actuating magnets is described using (3.3) and $\mathbf{M}$ is constructed using $\mathbf{q}$.

3.2.2 Swimming speed in viscoelastic fluid

The magnetic torque rotates the screw at angular speed ω and the following translating speed U [40], [167]:

$$U = 2A\omega\varepsilon^2 \sum_{q\geq 1} \frac{(1 + \beta q^2 De^2) \mid \hat{f}_q \mid^2}{1 + q^2 De^2} J_q, \tag{3.4}$$

where De is the Deborah number and given by

$$De = \lambda\omega, \tag{3.5}$$

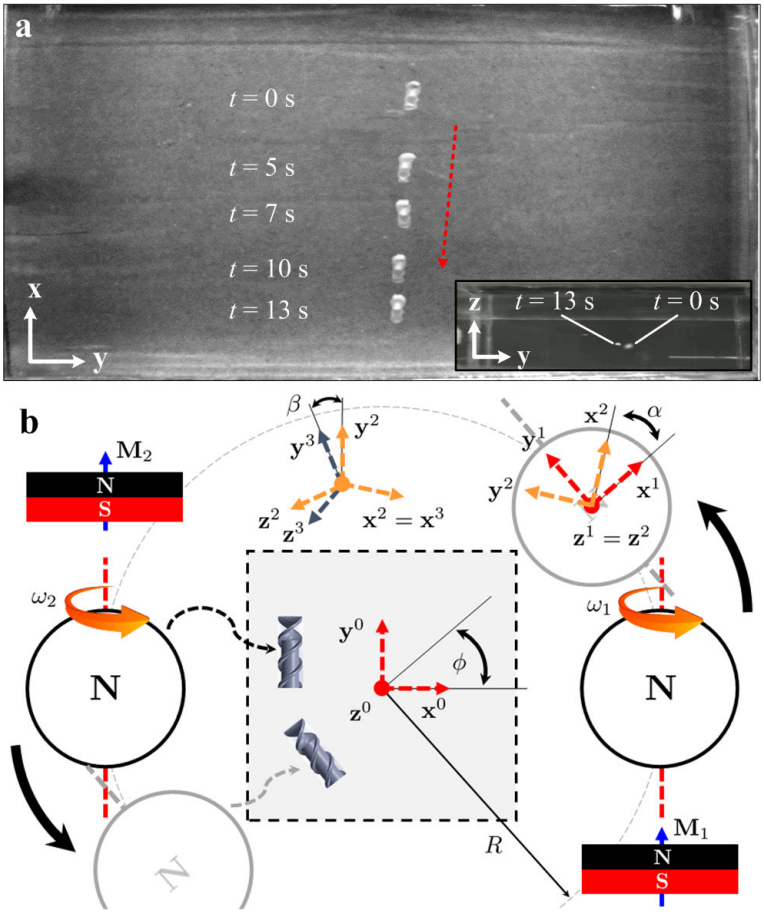

Figure 3.3: A magnetically-driven screw is moved controllably in soft tissue phantom. (a) The screw is actuated by two rotating permanent magnets with magnetic moment ($\mathbf{M}$) at angular speed ($\omega_1 = \omega_2$). (b) The pitch (β) and steering (α) angles of the permanent magnets enable the screw to rotate and achieve out-of-plane swim. The two permanent magnets are also rotated with respect to a reference frame of reference with angle ϕ. $\mathbf{M}_1$ and $\mathbf{M}_2$ are the magnetization vectors of the permanent magnets and reside along their long axes. The dashed square indicates the workspace (105 mm×105 mm×40 mm) of the system.

where λ is the fluid relaxation timescale. Further, β is the ratio of the solvent viscosity to the total viscosity of the solvent and polymer ($\beta = \eta_s/\eta$). In (3.4), $\hat{f}_q$ is Fourier analysis of the periodic function $f(N\theta)$ and the function J_q is calculated based on Bessel function K_x at $x = qv$, where v is the normalized pitch $v = v^* A$

$$J_q = \frac{q^2 A_q}{2}\left(2K_{q-1} - vK_q + \frac{vK_{q-1}^2}{K_q}\right), \tag{3.6}$$

where the constants A_q are calculated using

$$A_q = \frac{2\left(q + \frac{qvK_{q-1}}{K_q}\right)}{qK_q + qvK_{q-1} - \frac{2(q-2)}{v}K_{q-1} - \frac{(3q-2)K_{qi1}^2}{K_q} - \frac{qvK_{q-1}^3}{K_q^2}}. \tag{3.7}$$

Equation (3.4) predicts the swimming speed of the helix based on the characteristics of the viscoelastic medium, the parameters of the screw, and the angular speed of the screw. Fig. 3.2(c) shows the calculated swimming speed of the screw as a function of the helical pitch ($2\pi/v$) for three representative values of number of starts (N). The swimming speed increases with v and N, at an actuation frequency of 5 Hz. The swimming speed of the screw also depends on the actuation frequency. Figs. 3.2(d) and 3.2(e) show the calculated swimming speed of the screw at actuation frequency of $f \in [5, 25]$ Hz, and for three representative screw profiles, $f(\theta) = 1 + 0.5\sin(N\theta)$ for $N = 1:3$ and $\theta \in [0, 2\pi)$ and three representative helical pitches. The calculated speed of the screw increases with the actuation frequency and the number of starts of the screw profile.

3.2.3 Control system design

We assume that the external magnetic field and the magnetic dipole provide enough torque, and that the helix axis of the screw ultimately aligns with the magnetic field lines. Therefore, the direction of the screw is calculated based on the direction of the magnetic field at the position of the screw, and this assumption yields

$$\angle\mathbf{m} = \angle\mathbf{B}(\mathbf{p}) \quad \Rightarrow \quad \angle\mathbf{U} = \angle\mathbf{m} + \frac{\pi}{2}. \tag{3.8}$$

We also assume that the dipole fields are rotating below a step-out frequency (ω_{so}) of the screw. This step-out frequency limits the frequency response as the screw does not remain synchronized with the external magnetic fields. Therefore, the angular velocity of the rotating dipole fields is calculated using

$$\omega = \begin{cases} k_1 \mid \mathbf{p}_{\text{ref}} - \mathbf{p} \mid, & \omega < \omega_{\text{so}} \\ \kappa\omega_{\text{so}}, & \omega \geq \omega_{\text{so}} \end{cases} \tag{3.9}$$

where k_1 is a positive gain and $0 < \kappa < 1$. The control input (3.9) provides zero output for zero position tracking error $\mid \mathbf{p}_{\text{ref}} - \mathbf{p} \mid$, thereby decreasing the linear speed of the screw as it approaches the reference position. The second control input is the direction of the magnetic fields. This direction is controlled by the magnetization vectors of the rotating permanent magnets $\mathbf{M}_i$. The point-dipole model (3.2) is provided with the desired magnetic fields based on the orientation error of the screw. Therefore, the desired orientation of the magnetic field is calculated using

$$\angle\mathbf{B}(\mathbf{p}) = \tan^{-1}\left(\frac{\mid \mathbf{p}_{\text{ref}} - \mathbf{p} \mid_y}{\mid \mathbf{p}_{\text{ref}} - \mathbf{p} \mid_x}\right), \tag{3.10}$$

where $\mid \mathbf{p}_{\text{ref}} - \mathbf{p} \mid_{x,y}$ is the position error along x- and y-axis, respectively. The angle of the desired magnetic field $\angle\mathbf{B}(\mathbf{p})$ and its unit vector $\widehat{\mathbf{B}}(\mathbf{p})$ are used to construct $\mathbf{B}(\mathbf{p})$ and calculate $\mathbf{M}_i$ using (3.2). This calculation is done by setting $\mathbf{m} \times \mathbf{B}^{\text{d}} \Rightarrow \mathbf{k}_2(\dot{\mathbf{p}}_{\text{ref}} - \dot{\mathbf{p}})$ to calculate the desired magnetic field $\mathbf{B}^{\text{d}}$, where $\mathbf{k}_2$ is a positive-definite matrix. Fig. 3.4 shows the implementation of the control system.

3.3 Closed-loop motion control

Control of the screw is achieved using a permanent magnet-based robotic system inside agar gel tissue phantom.

3.3.1 System description

The magnetic control of the screw is done using two synchronized rotating dipole fields. Two permanent magnets (NdFeB) with axial magnetization are fixed to DC motors to generate rotating magnetic fields. The permanent

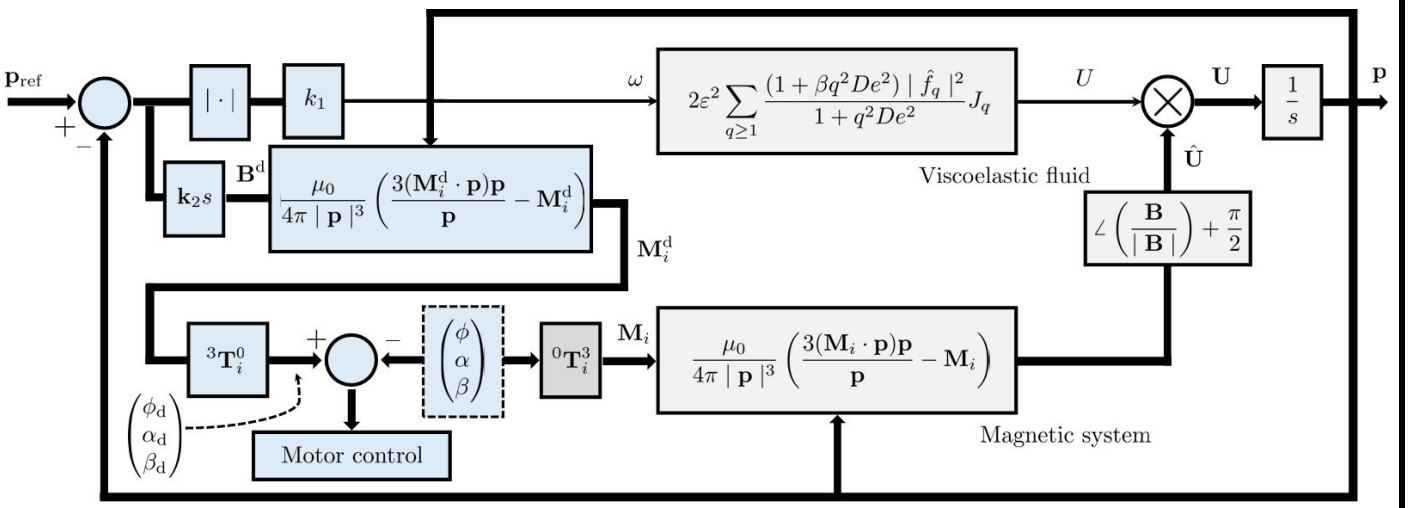

Figure 3.4: Closed-loop control of magnetically-driven screws is achieved based on an analytical solution of the swimming speed and the point-dipole model of the magnetic fields. The control inputs are the angular speed (ω) and orientation of the orientation of the magnetization vector ($\mathbf{M}$). The nominal parameters of the screw and viscoelastic fluid are used to calculate the variable (ε), viscosity ratio (β), Drborah number (De), and the function J_q.

magnets (R750F, Amazing Magnets LLC, California, U.S.A) with diameter and height of 40 mm and 20 mm have a magnetization of 1.72×10^{-4} A.m^2. The orientation of the DC motors are controlled independently to change the pitch and steering angles of the screws, as shown in Fig. 3.3. The pitch (β_i) and yaw (α_i) angles of each motor are controlled independently to control the pitch and steering angles of the screw, respectively. Each of these configurations is fixed to a rotational motion stage with radius R (rotates with angle ϕ), and the screw is allowed to swim between the rotating dipole fields. The screw is contained inside a reservoir (105 mm$\times$105 mm$\times$ 40 mm) made of acrylic and is allowed to swim within the center of the two rotating dipole fields. Its position and orientation are measured by two cameras (Aviator GIGE, avA1000-100gm, Basler AG, Ahrensburg, Germany) mounted above and in front of the reservoir. The length and diameter of the screw are 6 mm and 2 mm, respectively. The helix angle and the pitch are 45° and 2 mm, respectively. A cylindrical permanent magnet with a diameter of 1 mm and a length of 1 mm is fixed to the screw to provide a magnetic dipole moment along its radial direction. The configuration of the permanent magnets yields the following homogenous transformation:

$$ {}^{0}\mathbf{T}_{i}^{3}(\mathbf{q}) = \begin{pmatrix} c\phi c\alpha_i - s\phi s\alpha_i & a_i c\beta_i & -b_i s\beta_i & Rc\phi \\ s\phi c\alpha_i + c\phi s\alpha_i & c_i c\beta_i & d_i s\beta_i & Rs\phi \\ 0 & s\beta_i & c\beta_i & 0 \\ 0 & 0 & 0 & 1 \end{pmatrix} \tag{3.11} $$

where $a_i = -c\phi s\alpha_i - s\phi c\alpha_i$, $b_i = -c\phi s\alpha_i - s\phi c\alpha_i$, $c_i = -s\phi s\alpha_i + c\phi c\alpha_i$, and $d_i = s\phi s\alpha_i + c\phi c\alpha_i$. This homogenous transformation is used to determine the desired angles of the the actuating magnets based on the desired magnetization $\mathbf{M}^{\mathrm{d}}$.

Frequency response and motion control experiments are done inside agar gel at room temperature. Demineralized water and gelatine powder (Ec Nnr: 232-554-6, Boom BV, Rabroekenweg, The Netherlands) with a density of 0.68 g/ml are used to prepare the agar gel in three steps. The first step is heating until the gelatine powder dissolves at 70°. The second step is dilution to a concentration of 0.8 wt.% agar gel. Finally, the mixture is cooled for 12 hours in the reservoir.

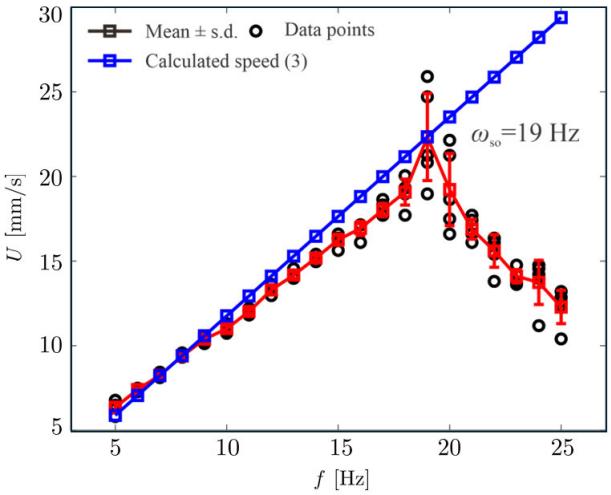

Figure 3.5: Frequency response of a 6-mm-long screw is characterized in 0.8 wt.% agar gel at room temperature. The screw is allowed to swim within the center of two rotating dipole fields inside a gelatin reservoir. The distance between the two rotating dipole fields is 21 cm, and the magnitude of the magnetic field at the position of the screw is 47 mT. The step-out (ω_{so}) of the screw is 19 Hz. Each data point represents the average swimming speed U of five trials at each actuation frequency f.

3.3.2 Frequency response characterization

The screw swimming speed is measured against the actuation frequency of the rotating dipole fields. The minimum and maximum magnitudes of the magnetic field at the position of the screw are 47 mT and 80 mT, respectively. The frequency response of the screw is shown in Fig. 3.5. Each data point represents the average swimming speed of five trials at each actuation frequency. The frequency response indicates that the screw does not follow the magnetic field lines above the actuation frequency of 19 Hz. Therefore, the step-out frequency of the screw is 19 Hz. At this frequency, the swimming speed is measured as 22.3 ± 2 mm/s. The frequency response of the screw indicates that the analytical solution of the Stokes/Oldroyd-B equations is in agreement with the measurements below the step-out frequency. Therefore, equation (3.4) is incorporated into the closed-loop control system and the actuation frequency is limited below 19 Hz.

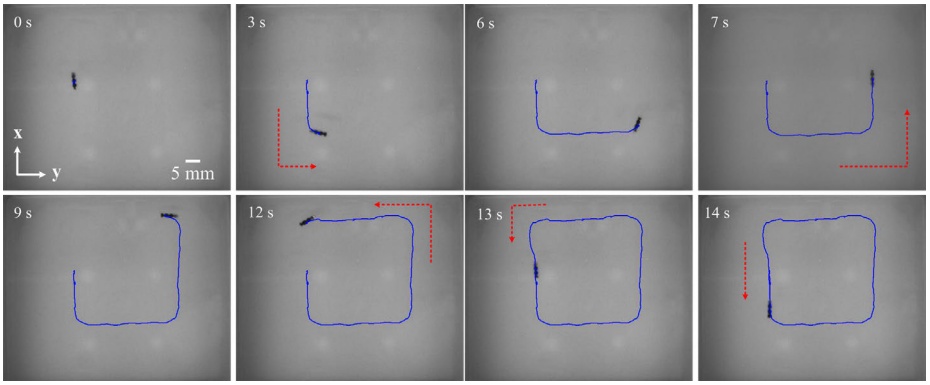

Figure 3.6: Open-loop control of a magnetically-guided screw is achieved along a square trajectory with an edge length of 36 mm in 0.8 wt.% agar gel at room temperature. *Please refer to the accompanying video.*

3.3.3 Open-loop control results

Fig. 3.1 shows superimposed still images demonstrating open-loop control of the screw. In this experiment, the steering angle and pitch angle of the permanent magnets are fixed and only the angular velocity of the rotating motion stage is set to a constant speed. This control enables the screw to swim along a circular trajectory. This result indicates that the screw can swim controllably using a single degree of freedom (ϕ) of the permanent magnet-based robotic system. Another representative open-loop trial is shown in Fig. 3.6. In this case, the screw is controlled to swim along a square trajectory with an edge length of 36 mm. Similarly to the circular trajectory, the angle ϕ is used to control the screw. In both examples, the magnets are synchronized, and the motion of the rotational stage is controlled based on the desired trajectory. In practice, the pitch and steering angles of the screw have to be controlled toward the reference position. *Please refer to the accompanying video.*

3.3.4 Point-to-point control results

Fig. 3.7(a) shows a representative closed-loop control trial of the screw toward three target positions. Small particles (red arrows) are added into the agar gel and used as targets for the screw. The targets are positioned at

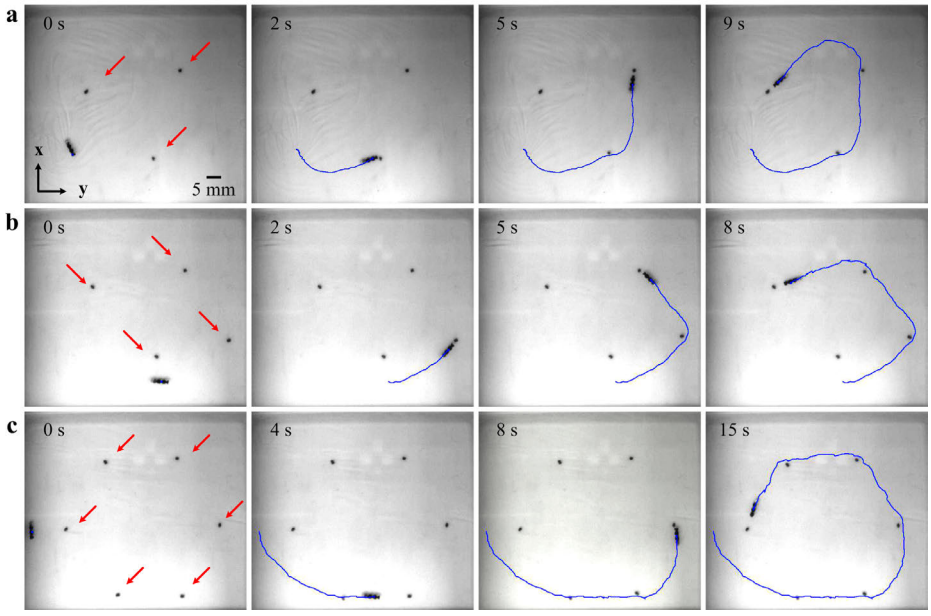

Figure 3.7: A magnetically-driven screw swims controllably toward reference positions (indicated by the red arrows) under the influence of controlled magnetic fields in 0.8 wt.% agar gel at room temperature. (a) The screw swims toward three reference positions with a maximum position error of 1.25 mm. (b) The screw swims toward four reference positions with a maximum position error of 1.82 mm. (c) The screw swims toward six target positions in a hexagon configuration with maximum position error of 1.69 mm. *Please refer to the accompanying video.*

random locations and separated with approximately 5-6 body length. In contrast to the previous open-loop control experiments, the position and orientation of the screw and the position of the targets are used in (3.9) and (3.10) to calculate the control inputs ω and $\angle\mathbf{B}(\mathbf{p})$. This angle is used to construct the desired direction of the magnetization vector of the actuating magnet using the point-dipole approximation of the field (3.2). Finally, the desired angles of the permanent magnet-based robotic system are calculated based on the homogenous transformation (3.11) and the desired magnetization vector $\mathbf{M}^{\mathrm{d}}$. The desired angles (ϕ, α, and β) are controlled and updated based on the reference position. In the case of Fig. 3.7(a), the

screw swims controllably toward three targets with a maximum position error of 1.25 mm. Similarly to Fig. 3.7(a), four markers (targets) are randomly inserted inside the agar gel, and the screw achieves point-to-point control with a maximum position error of 1.82 mm, as shown in Fig. 3.7(b). In Fig. 3.7(c), six particles are inserted in a hexagon configuration, and the screw achieves closed-loop control with a maximum position error of 1.69 mm. *Please refer to the accompanying video.*

The positioning error of the closed-loop control trials depends on the prescribed locations of the targets. Relatively small positioning error is observed when the targets are located in the swimming direction of the screw. The turning curvature of the screw depends on its swimming velocity, magnetic moment and magnetic field, geometry, and properties of the agar gel [155]. Therefore, it is possible to enhance the performance of the closed-loop control system by decreasing the turning curvature of the screw using the swimming speed during experimental runs. It is also possible to exert greater magnetic torque and decrease the turning radius by incorporating permanent magnets with relatively large magnetic moment during fabrication.

3.4 Conclusions and future work

Open- and closed-loop motion control of magnetically-driven screws are achieved using a permanent magnet-based robotic system in agar gel tissue phantom. The frequency response of the screw is characterized, and a good match is observed between measurements and calculated speeds based on an analytical solution of the Stokes/Oldroyd-B equations. The analytical solution and measurements are in agreement below the step-out frequency of the screw. In the case of open-loop control, we demonstrate the ability to swim along simple trajectories using single degree of freedom of the system. In the case of closed-loop control, the screw is controlled toward arbitrary targets with maximum position error of 1.82 mm.

As part of future studies, the magnetically-driven screw will be tested in real tissue and bodily fluids. This *ex vivo* study is essential to test the capability of our permanent magnet-based robotic system to actuate the screw in conditions encountered *in vivo* such as the time-varying flow rates, heterogenous and fibrous environments. The screw will also be fabricated using biodegradable polymer and drug will be incorporated into

its polymer matrix to deploy localized therapy in soft-tissue environment. In addition, the Stokes/Oldroyd-B equations will be compared to screws with different geometries (diameter, length, helical pitch, rim depth), different magnetic properties (magnetic moment and magnetic field), inside fluids with different rheological properties (viscosities), and near to a solid boundary. This comparison is essential to predict the speed of a wide range of magnetically-driven screws in different conditions.

Chapter Overview

In **Chapter 3**, we propose a control strategy that incorporates a swimming speed prediction model for TMHD motion control. However, there is room for further optimization of this control strategy.

Chapter 4 introduces an approach to reduce computational burden, thereby enhancing the control strategy. First, we establish a relationship model between the synchronized rotation of two identical permanent magnets (characterized by the dipole-rotation axis) and the corresponding magnetic field (characterized by the field-rotation axis) using the point-dipole model. Next, we explore the correlation between the actuation frequency of the synchronized rotating permanent magnets and the TMHD swimming speed in viscoelastic fluids, which includes validating the swimming speed prediction model. Finally, we translate TMHD motion direction control into orientation control of the field-rotation axis and TMHD motion speed control into angular speed control of the dipole-rotation axis. Additionally, we characterize the effect of TMHD geometric parameters on its swimming speed, providing a reference for selecting the optimal TMHD to achieve the fastest swimming performance.

4

Hydrodynamic Behavior of Tetherless Twist-Shaped Magnetic Devices in Viscoelastic Fluids Driven by a Synchronized Rotating Magnetic Actuation System

Note: *Following chapter is adapted from the article "Hydrodynamic Behavior of Tetherless Twist-Shaped Magnetic Devices in Viscoelastic Fluids Driven by a Synchronized Rotating Magnetic Actuation System" by* ***Z. Zhang****, A. Klingner, S. Misra, and I. S.M.Khalil (2024) under review in "IEEE Transactions on Medical Robotics and Bionics"*

Abstract

Tetherless magnetic helical devices, including helix-, screw-, and twist-shaped variants, hold significant potential for biomedical applications such as targeted drug delivery, cell transportation, and blood clot removal. This paper focuses explicitly on tetherless twist-shaped magnetic devices (TTMDs). Investigating the factors that influence the hydrodynamic performance of TTMDs in bodily fluids, such as the vitreous humor of the human eye, is essential for achieving the desired outcomes. We examine key parameters of TTMD geometry, including the number of starts, radius, pitch, and amplitude, along with actuation frequency, to understand their effects on TTMD swimming speed. Experiments are performed in

a viscoelastic (Oldroyd-B) fluid environment (agar gel phantom) using a synchronized rotating magnetic actuation system. The swimming speed of each type of TTMD obtained from experiments was compared with that predicted by an existing swimming speed prediction model under a specific condition. Through this comparison, we discover the model's effective prediction capability for TTMD swimming speed at low actuation frequencies (below the step-out frequency) yet note a decrease in accuracy at high actuation frequencies (near or above the step-out frequency). The swimming speed prediction model is then applied in the context of TTMD motion control experiments, revealing its suitability for TTMD motion control, particularly in predicting TTMD swimming speed in viscoelastic fluids at low actuation frequencies (below the step-out frequency). This capability contributes to time savings when computing TTMD position information.

4.1 Introduction

Owing to the small size to access hard-to-reach regions of the biological body and the safety of the applied actuation source (magnetic field) to biological tissue, tetherless magnetic helical devices have found a progressively comprehensive utilization in biomedical applications such as targeted drug delivery [109], [168], targeted gene transportation [114], [169], and blood clots cleaning [111], [112]. In order to enable the magnetic helical devices to move through the bodily fluids with high swimming performance, it is necessary to investigate their swimming characteristics in that fluidic environment.

In general, tetherless magnetic helical devices (TMHDs) can be categorized into three subclasses according to their fundamental shapes: tetherless helix-shaped magnetic devices (THMDs), tetherless screw-shaped magnetic devices (TSMDs), and tetherless twist-shaped magnetic devices (TTMDs) [170]. A THMD is distinguished by a slim filament enveloping an empty core. A TSMD consists of a helical filament wrapped around a solid center. A TTMD can be described as a ribbon undergoing torsion around its longitudinal axis. Due to the typical 'helical' structure, the three subtypes of TMHDs share the same movement mechanism. That is, the translational motion is converted by the rotation around their body axes. In addition to the fundamental shapes of the TMHDs, researchers have found that numerous factors can influence the swimming characteristics of the TMHDs

in fluids, such as TMHD geometrical parameters, the viscosity of the fluids, the strength of the applied magnetic field, and the surface hydrophobicity of the TMHDs.

The swimming characteristics of THMDs have undergone extensive examination through theoretical and experimental approaches. In theoretical studies, Purcell proposed a generalized propulsion model [44], [45], enabling the calculation of non-fluidic applied torque and force on a THMD using translational and angular speeds, represented by a propulsion matrix. Each matrix element is a function of THMD geometrical parameters and fluid viscosity based on the resistive force theory [46]. This model enables researchers to systematically investigate how the geometry of THMDs and fluid viscosity affect their swimming speed in a low-Reynolds-number environment. Such exploration lays the groundwork for optimizing THMD design to improve their swimming performance. With this model, Wang *et al.* optimized THMD design for maximum swimming speed by analyzing the impact of geometrical parameters, such as wire radius, helix pitch, and helix length, on swimming speed and propulsion efficiency [171]. Further, Ullrich *et al.* observed enhanced propulsion of a THMD in the presence of collagen fibers at a gelatin concentration of 1578 μg/mL by studying the effect of collagen concentration on THMD swimming speed [172], aligning with the experimental findings of Berg and Turner berg [173] and Magariyama's theory [174]. In addition, Ye *et al.* proposed a strategy to enhance THMD swimming performance by increasing surface material hydrophobicity [175].

The swimming characteristics of TSMDs have predominantly been explored through a combination of experimental and simulation methods. Cai *et al.* utilized a TSMD as a magnetic capsule, demonstrating its ability to execute drug delivery tasks by simulating its motion characteristics throughout the entire drug delivery process using Computational Fluid Dynamics (CFD) [119]. Seeking optimal design, Zhou *et al.* investigated a capsule-like TSMD geometrical parameters such as lead, number of spirals, spiral height, and cross-section in fluidic and tubular environments to quantify their impact on propulsion efficiency [176]. In another application, Leclerc *et al.* employed a TSMD as a magnetic driller, determining the most efficient design for removing human blood clots in vitro [177]. Additionally, Nelson *et al.* explored the influence of driller-like TSMD geometry and fluid viscosity on the turning radius within an agar gel phantom, developing an

empirical model [178].

The swimming characteristics of TTMDs have been studied in-depth through theoretical methods. Li *et al.* have proposed a swimming speed prediction model that can predict the swimming speed of a TTMD in viscoelastic fluids [40], [167]. The derivation of such a model occurs within the framework of force-free swimming of a TTMD in viscoelastic fluids, implying that the translational motion of the TTMD solely arises from its self-rotation. The electromagnetic actuation systems (such as those based on Helmholtz coils), which are capable of generating a rotating magnetic field with zero gradient, can fulfill the requirement for actuating the TTMD within that framework. Thus, this model can be employed to predict TTMD swimming speed in viscoelastic fluids when the TTMD is actuated by these electromagnetic actuation systems. In contrast, most permanent magnet-based actuation systems are limited in providing such actuation for the TTMDs within that framework due to the generation of gradient fields. However, a permanent magnet-based actuation system using two synchronized rotating permanent magnets can approximately generate a rotating magnetic field with zero gradient within a limited region between the two permanent magnets. Consequently, the applicability of this model may be extended to cases where the TTMDs are actuated by permanent magnet-based actuation systems.

In this paper, we investigate the TTMD swimming characteristics under an actuation system utilizing two synchronized rotating permanent magnets, and subsequently apply that to the TTMD motion control. The process of a twist-shape magnetic microrobot from design, fabrication, propulsion to motion control is shown in Fig. 4.1. We conduct experiments to quantify the swimming speed of TTMDs, each characterized by distinctive geometrical features, including variations in length, number of starts, pitch, diameter, and amplitude. These experiments are conducted over a range of actuation frequencies within an agar gel phantom. Concurrently, the step-out frequency of each type of TTMD is acquired. Moreover, we analyze the swimming speed of TTMDs across different actuation frequencies, comparing experimental observations with predictions from the swimming speed prediction model. Our results reveal that the model accurately predicts TTMD swimming speed at low actuation frequencies (below the step-out frequency). However, its accuracy diminishes when applied to higher actuation frequencies (close to or above the step-out frequency). The structure

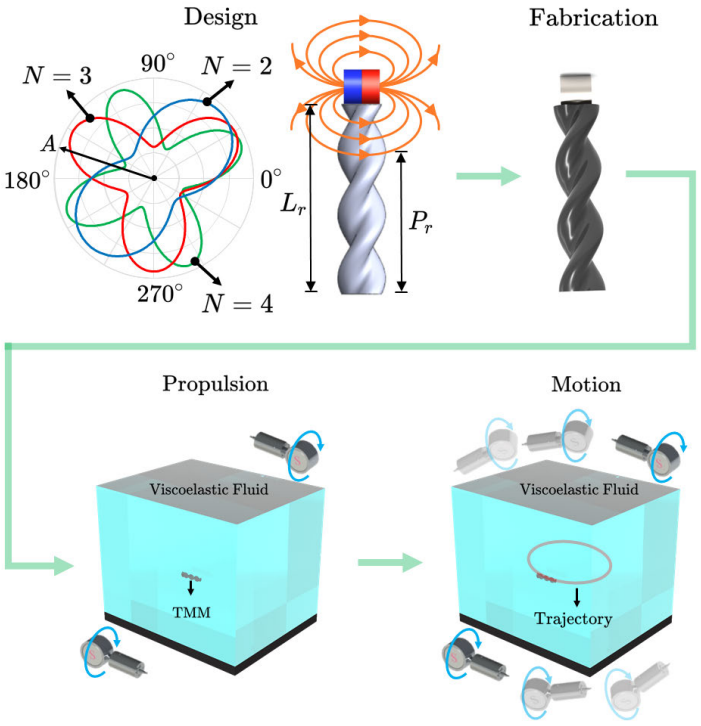

Figure 4.1: Process of a tetherless twist-shape magnetic device (TTMD) from design, fabrication, propulsion to motion control. The TTMD is conceptualized with the radius of A, the length of L_r, the pitch of P_r, the number of starts N, the amplitude ε, and the sectional profile of $\rho = A * (1 + \varepsilon f(N\theta))$, then fabricated by a 3D printer, next propelled by a rotating magnetic field generated by two synchronized rotating permanent magnets, and finally controlled to move along predefined trajectories under an actuation system comprising two synchronized rotating permanent magnets.

of the remainder of this paper is as follows: Section 4.2 presents the design and fabrication of TTMDs. Section 4.3 comprehensively characterizes the magnetic field at any position, generated by two synchronized rotating permanent magnets. Section 4.4 introduces the existing swimming speed prediction model and TTMD frequency response experiment. Section 4.5 demonstrates the practical implementation of the swimming speed predic-

tion model within the context of TTMD motion control. Finally, Section 4.6 offers conclusions regarding the swimming characteristics of TTMDs.

4.2 Design of tetherless twist-shaped magnetic devices

As depicted in Fig 4.1, a TTMD consists of a rigid body and a cylindrical magnet, with the dipole moment of the cylindrical magnet being perpendicular to the body axis of the TTMD. The sectional profile of a TTMD body is given by $\rho = A * (1 + \varepsilon f(N\theta))$ where $f(N\theta)$ is a periodic function and N is the number of starts of the twist. Therefore, the geometry of the twisted body is determined by several parameters, namely the number of starts N, the radius A, the length L_r, the pitch P_r and the amplitude ε.

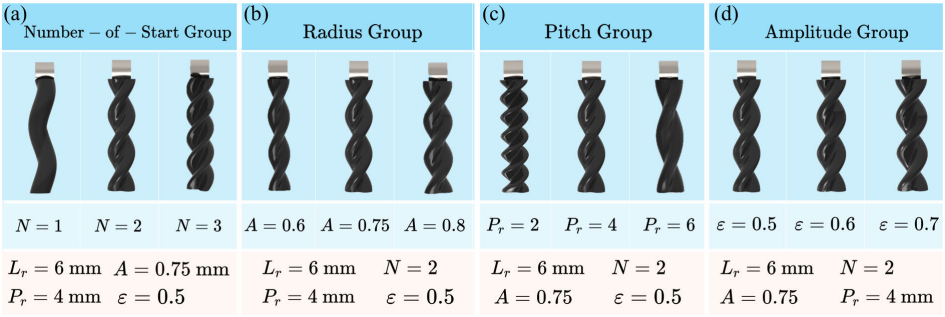

Figure 4.2: Group of tetherless twist-shaped magnetic devices. (a) Number-of-Start group ($1 \leq N \leq 3$), $P_r = 4$ mm, $L_r = 6$ mm, $A = 0.75$ mm and $\varepsilon = 0.5$; (b) Radius group (0.6 mm$\leq A \leq$ 0.8 mm), $N = 2$, $P_r = 4$ mm, $L_r = 6$ mm and $\varepsilon = 0.5$; (c) Pitch group (2 mm$\leq P_r \leq$6 mm), $N = 2$, $L_r = 6$ mm, $A = 0.75$ mm and $\varepsilon = 0.5$; (d) Amplitude group ($0.5 \leq \varepsilon \leq$0.7), $N = 2$, $P_r = 4$ mm and $L_r = 6$ mm and $A = 0.75$ mm.

The TTMD bodies are designed with four groups named Number-of-Start group, Radius group, Pitch group, and Amplitude group, as shown in Fig. 4.2. Each group has three types of TTMD. In the Number-of-Start group, the TTMDs are designed with a different number of starts ($1 \leq N \leq 3$), and the additional geometrical parameters of the TTMDs are given as $L_r = 6$ mm, $P_r = 4$ mm, $A = 0.75$ mm and $\varepsilon = 0.5$. In the Radius

group, the TTMDs are designed with different radii (0.6 mm$\leq A \leq$0.8 mm), and the additional geometrical parameters are given as, $L_r = 6$ mm, $N = 2$, $P_r = 4$ mm and $\varepsilon = 0.5$. In the Pitch group, the TTMDs are designed with different pitches (2 mm$\leq P_r \leq$6 mm), and the additional geometrical parameters of the TTMDs are given as $L_r = 6$ mm, $N = 2$, $A = 0.75$ mm and $\varepsilon = 0.5$. Lastly, in the Amplitude group, the TTMDs are designed with different amplitudes ($0.5 \leq \varepsilon \leq 0.7$), and the additional geometrical parameters are given as, $L_r = 6$ mm, $N = 2$, $P_r = 4$ mm, and $A = 0.75$. The TTMD bodies are fabricated by a 3D printer (FormlabsForm2), and the printing material is Formlabs photopolymer resin (BLACK FLGPBK04).

4.3 Characterization of magnetic field

The orientation of the field-rotation axis and the angular velocity of the magnetic field are crucial in the control of TTMD motion direction and speed, respectively. Here, we characterize the magnetic field generated by two synchronized rotating permanent magnets, as shown in Fig 4.3(a).

4.3.1 Rotation axis of magnetic field

The rotation axis of the magnetic field can be described by the unit vector of the field-rotation axis. Assume two identical permanent magnets are controlled to rotate in synchronization using a control system. Then the superimposed magnetic field $\mathbf{B}$ at $\boldsymbol{p}$ can be expressed using the point-dipole model, which is given by

$$\mathbf{B} = \sum_{i=1}^{k} \frac{\mu_0}{4\pi \left|\boldsymbol{p}_i\right|^3} (3\hat{\boldsymbol{p}}_i \hat{\boldsymbol{p}}_i^T - \mathbf{I})\mathbf{M} = \sum_{i=1}^{k} \frac{\mu_0}{4\pi \left|\boldsymbol{p}_i\right|^3} \mathbb{H}_i \mathbf{M}, \tag{4.1}$$

where μ_0 is the permeability of free space, $\mathbf{I}$ is the third-order identity matrix, $\boldsymbol{p}_i$ is a position vector which relates the position of ith actuator magnet and position $\boldsymbol{p}$ such that $\boldsymbol{p}_i = \boldsymbol{p} - \boldsymbol{x}_i$, and $\mathbb{H}_i = 3\hat{\boldsymbol{p}}_i \hat{\boldsymbol{p}}_i^{\mathrm{T}} - \mathbf{I}$. The desired unit vector of field-rotation axis $\hat{\boldsymbol{\omega}}^d$ is perpendicular to the plane in which $\mathbf{B}$ lies such that $\mathbf{B}^{\mathrm{T}} \hat{\boldsymbol{\omega}}^d = 0$ for all $\mathbf{M}$. Recognizing the matrix $\mathbb{H}_i$ is symmetric and replacing $\mathbf{B}$ with (4.1) in $\mathbf{B}^{\mathrm{T}} \hat{\boldsymbol{\omega}}^d = 0$ yields

$$\mathbf{B}^{\mathrm{T}} \hat{\boldsymbol{\omega}}^d = \frac{\mu_0}{4\pi} \mathbf{M}^{\mathrm{T}} \left(\sum_{i=1}^{k} \frac{\mathbb{H}_i}{\left|\boldsymbol{p}_i\right|^3} \right) \hat{\boldsymbol{\omega}}^d = 0. \tag{4.2}$$

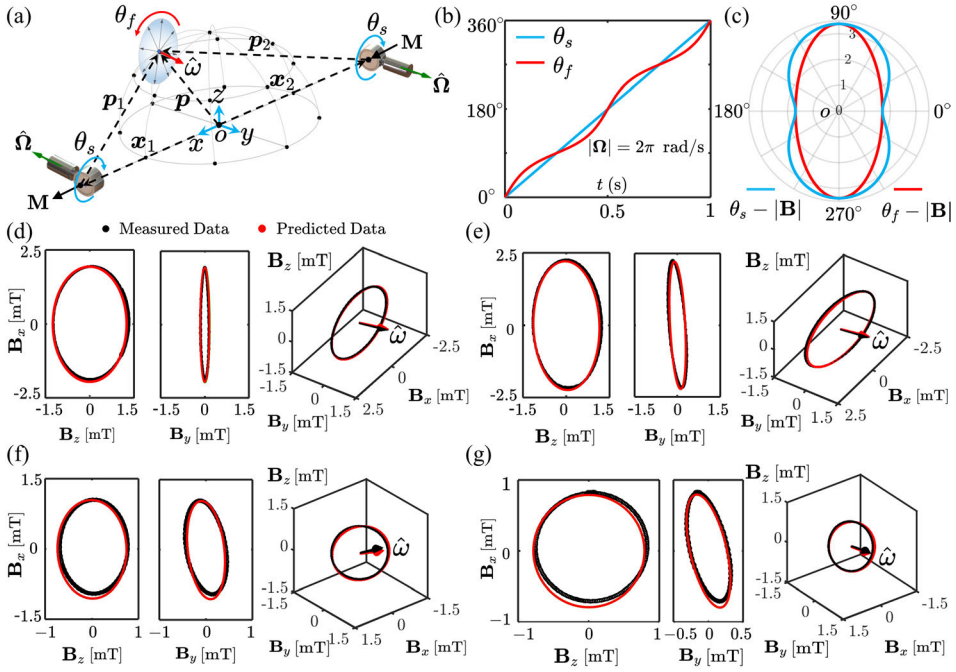

Figure 4.3: Two identical permanent magnets are synchronously rotating around the dipole-rotation axis $\mathbf{\Omega}$ with $\mathbf{M}$ perpendicular to $\hat{\mathbf{\Omega}}$, resulting in the generation of rotating magnetic field with a field-rotation axis of $\boldsymbol{\omega}$ at position $\boldsymbol{p}$. (a) Two permanent magnets are symmetrically positioned about the frame's origin along the x-axis. The unit vector of field-rotation axis $\hat{\boldsymbol{\omega}}$ and unit vector of dipole-rotation axis $\hat{\mathbf{\Omega}}$ are indicated by red and green arrows, respectively. (b) The synchronous rotation angle θ_s of permanent magnets and the field-rotation angle θ_f at the coordinate origin (O) vary in time while the angular velocity of dipole-rotation axis is set to be constant ($|\mathbf{\Omega}| = 2\pi$ rad/s). (c) Variations in magnetic field strength ($|\mathbf{B}|$) in relation to θ_s and θ_f. (d, e, f and g) The components of the magnetic field $\mathbf{B}$ are measured and predicted (black and red points) at arbitrary positions $\boldsymbol{p} = [0\ 75\ 20]^{\mathrm{T}}$, $\boldsymbol{p} = [5\ 50\ 45]^{\mathrm{T}}$, $\boldsymbol{p} = [5\ 100\ 60]^{\mathrm{T}}$ and $\boldsymbol{p} = [10\ 125\ 40]^{\mathrm{T}}$. The measured $\hat{\boldsymbol{\omega}}$ (black arrow) at positions $\boldsymbol{p} = [0\ 75\ 20]^{\mathrm{T}}$, $\boldsymbol{p} = [5\ 50\ 45]^{\mathrm{T}}$, $\boldsymbol{p} = [5\ 100\ 60]^{\mathrm{T}}$ and $\boldsymbol{p} = [10\ 125\ 40]^{\mathrm{T}}$ differed from the predicted $\hat{\boldsymbol{\omega}}$ (red arrow) by 1.43°, 1.73°, 2.44° and 2.65°, respectively. *Please refer to the accompanying video.*

Because $\sum_{i=1}^{k}(\mathbb{H}_i/|\boldsymbol{p}_i|^3)\hat{\boldsymbol{\omega}}^d$ is constant and $\mathbf{M}^{\mathrm{T}}\hat{\boldsymbol{\Omega}} = 0$, the solution for the desired dipole-rotation axis $\hat{\boldsymbol{\Omega}}^d$ where $\hat{\boldsymbol{\Omega}}^d$ is parallel to $\sum_{i=1}^{k}(\mathbb{H}_i/|\boldsymbol{p}_i|^3)\hat{\boldsymbol{\omega}}^d$ is the only solution that satisfies (4.2) and is invariant to the rotation of $\mathbf{M}$. Therefore, the inverse problem of obtaining the desired dipole-rotation axis $\hat{\boldsymbol{\Omega}}^d$ based on given $\hat{\boldsymbol{\omega}}^d$ and $\boldsymbol{p}_i$ is solved, and $\hat{\boldsymbol{\Omega}}^d$ can be found with

$$\hat{\boldsymbol{\Omega}}^d = \frac{(\sum_{i=1}^{k}\mathbb{H}_i/|\boldsymbol{p}_i|^3)\hat{\boldsymbol{\omega}}^d}{\left|(\sum_{i=1}^{k}\mathbb{H}_i/|\boldsymbol{p}_i|^3)\hat{\boldsymbol{\omega}}^d\right|}. \tag{4.3}$$

Equation (4.3) implies that the desired dipole-rotation axis varies in accordance with $\boldsymbol{p}_i$. Assuming the matrix $\sum_{i=1}^{k}\mathbb{H}_i/|\boldsymbol{p}_i|^3$ is inverse, there exists one dipole-rotation axis $\hat{\boldsymbol{\Omega}}$ to generate a unit vector of field-rotation axis $\hat{\boldsymbol{\omega}}$ for any $\boldsymbol{p}_i$. The forward problem of acquiring the unit vector of field-rotation axis $\hat{\boldsymbol{\omega}}$ at position $\boldsymbol{p}$ based on the given unit vector of dipole-rotation axis $\hat{\boldsymbol{\Omega}}$ is tackled, and the unit vector of field-rotation axis $\hat{\boldsymbol{\omega}}$ is found with

$$\hat{\boldsymbol{\omega}} = \frac{(\sum_{i=1}^{k}\mathbb{H}_i/|\boldsymbol{p}_i|^3)^{-1}\hat{\boldsymbol{\Omega}}}{\left|(\sum_{i=1}^{k}\mathbb{H}_i/|\boldsymbol{p}_i|^3)^{-1}\hat{\boldsymbol{\Omega}}\right|}. \tag{4.4}$$

Therefore, the inverse and forward relationship models are established between the unit vector of the dipole-rotation axis and the unit vector of the field-rotation axis, as presented in (4.3) and (4.4). It demonstrates that these models are associated with $\boldsymbol{p}_i$ $(i = 1, 2)$, indicating their correlation with the distance and direction of position $\boldsymbol{p}$ relative to the two permanent magnets in the actuation system employing two synchronized rotating permanent magnets. However, in the actuation system utilizing a single rotating permanent magnet, as presented in [179], the inverse and forward relationship models are exclusively associated with the direction of position $\boldsymbol{p}$ relative to the permanent magnet.

4.3.2 Rotation velocity of magnetic field

A relationship model has been established between the instantaneous angular velocity of the magnetic field ($|\boldsymbol{\omega}|$) and the instantaneous angular velocity of the permanent magnet ($|\boldsymbol{\Omega}|$) in the context of a rotating single permanent magnet, as detailed in [179]. However, a comparable model for the situation involving two synchronous rotating permanent magnets has

yet to be developed. Based on (4.1), the magnetic field strength at position $\boldsymbol{p}$ is purely a function of relative position $\boldsymbol{p}_i$ and $\mathbf{M}$. Further, we define $\mathbf{L} = \sum_{i=1}^{k}(\mathbb{H}_i/|\boldsymbol{p}_i|^3)$. Substituting $\mathbf{L}$ into (4.1) yields

$$\mathbf{B} = \frac{\mu_0 |\mathbf{M}|}{4\pi}\mathbf{L}\hat{\mathbf{M}} \tag{4.5}$$

Further, the magnetic field strength can be calculated as

$$|\mathbf{B}| = \frac{\mu_0 |\mathbf{M}|}{4\pi}\sqrt{\left|\mathbf{L}\hat{\mathbf{M}}\right|^2} = \frac{\mu_0 |\mathbf{M}|}{4\pi}\sqrt{\left|\hat{\mathbf{M}}^{\mathrm{T}}\mathbf{L}^2\hat{\mathbf{M}}\right|} \tag{4.6}$$

where $\hat{\mathbf{M}}$ is the unit dipole moment $\mathbf{M}$, which changes along with the synchronous rotation angle θ_s. In the plane containing all $\mathbf{M}$, we define an unit orthogonal basis for expressing $\mathbf{M}$, which are $\hat{\mathbf{M}}_0$ and $\hat{\mathbf{M}}_1$. Further $\hat{\mathbf{M}}_1 = \hat{\mathbf{M}}_0 \times \hat{\boldsymbol{\Omega}}$. We set θ_s as the angle between $\hat{\mathbf{M}}$ and $\hat{\mathbf{M}}_0$ and $\boldsymbol{\Theta} = [\cos\theta_s \;\; \sin\theta_s]^{\mathrm{T}}$, then $\hat{\mathbf{M}}$ can be expressed as

$$\hat{\mathbf{M}} = [\hat{\mathbf{M}}_0 \;\; \hat{\mathbf{M}}_1]\boldsymbol{\Theta} \tag{4.7}$$

Replacing $\hat{\mathbf{M}}$ with this in $\hat{\mathbf{M}}^{\mathrm{T}}\mathbf{L}^2\hat{\mathbf{M}}$ yields

$$\begin{aligned}\hat{\mathbf{M}}^{\mathrm{T}}\mathbf{L}^2\hat{\mathbf{M}} &= \boldsymbol{\Theta}^{\mathrm{T}}\begin{bmatrix}\hat{\mathbf{M}}_0^{\mathrm{T}}\\ \hat{\mathbf{M}}_1^{\mathrm{T}}\end{bmatrix}\mathbf{L}^2[\hat{\mathbf{M}}_0 \;\; \hat{\mathbf{M}}_1]\boldsymbol{\Theta}\\ &= \boldsymbol{\Theta}^{\mathrm{T}}\mathbf{A}\boldsymbol{\Theta}\end{aligned} \tag{4.8}$$

where $\mathbf{A}$ is a two-by-two positive definite matrix and is given by

$$\mathbf{A} = \begin{bmatrix}\hat{\mathbf{M}}_0^{\mathrm{T}}\mathbf{L}^2\hat{\mathbf{M}}_0 & \hat{\mathbf{M}}_0^{\mathrm{T}}\mathbf{L}^2\hat{\mathbf{M}}_1\\ \hat{\mathbf{M}}_1^{\mathrm{T}}\mathbf{L}^2\hat{\mathbf{M}}_0 & \hat{\mathbf{M}}_1^{\mathrm{T}}\mathbf{L}^2\hat{\mathbf{M}}_1\end{bmatrix} \tag{4.9}$$

we define λ_1 and λ_2 as the eigenvalue of matrix $\mathbf{A}$, and $\mathbf{v}_1$ and $\mathbf{v}_2$ as the unit eigenvectors of matrix $\mathbf{A}$ in regard to λ_1 and λ_2 respectively. Further, $\lambda_1 \geq \lambda_2$. The magnetic field strength $|\mathbf{B}|$ varies in an elliptical pattern and is given by

$$|\mathbf{B}| = \frac{\mu_0 |\mathbf{M}|}{4\pi}\sqrt{|\boldsymbol{\Theta}^{\mathrm{T}}\mathbf{A}\boldsymbol{\Theta}|} \tag{4.10}$$

and the maximum and minimum magnetic field strengths are

$$|\mathbf{B}|_{max} = \frac{\mu_0 |\mathbf{M}|}{4\pi}\sqrt{\lambda_1} \tag{4.11}$$

$$|\mathbf{B}|_{min} = \frac{\mu_0 |\mathbf{M}|}{4\pi}\sqrt{\lambda_2} \tag{4.12}$$

Note that the maximum and minimum magnetic field strength is achieved when $\mathbf{\Theta} = \mathbf{v}_1$ and $\mathbf{\Theta} = \mathbf{v}_2$ respectively. Thus, the synchronous angle θ_s can be solved under the two situations. Because of $\dot{\hat{\mathbf{M}}} = \mathbf{\Omega} \times \hat{\mathbf{M}}$, on basis of (4.5), it yields

$$\dot{\mathbf{B}} = \frac{\mu_0 |\mathbf{M}|}{4\pi}\mathbf{L}\dot{\hat{\mathbf{M}}} = \frac{\mu_0 |\mathbf{M}|}{4\pi}\mathbf{L}(\mathbf{\Omega} \times \hat{\mathbf{M}}) \tag{4.13}$$

Further, the vector of field-rotation axis $\boldsymbol{\omega}$ can be represented as

$$\boldsymbol{\omega} = \frac{1}{|\mathbf{B}|^2}\mathbf{B} \times \dot{\mathbf{B}} = \frac{1}{|\mathbf{B}|^2}\left(\frac{\mu_0 |\mathbf{M}|}{4\pi}\right)^2 \mathbf{L}\hat{\mathbf{M}} \times \mathbf{L}(\mathbf{\Omega} \times \hat{\mathbf{M}}) \tag{4.14}$$

Let's square both sides of this formula and replace $\mathbf{\Omega}$ with $|\mathbf{\Omega}|\,\hat{\mathbf{\Omega}}$ yields

$$\frac{|\boldsymbol{\omega}|^2}{|\mathbf{\Omega}|^2} = \left(\frac{\mu_0 |\mathbf{M}|}{4\pi |\mathbf{B}|}\right)^4 (\mathbf{L}\hat{\mathbf{M}} \times \mathbf{L}(\hat{\mathbf{\Omega}} \times \hat{\mathbf{M}}))^2 \tag{4.15}$$

Note that $\hat{\mathbf{M}}$ and $\hat{\mathbf{\Omega}} \times \hat{\mathbf{M}}$ constitute a set of orthogonal basis. For simplicity, let's use $\mathbf{a}$ and $\mathbf{b}$ to represent $\hat{\mathbf{M}}$ and $\hat{\mathbf{\Omega}} \times \hat{\mathbf{M}}$, respectively. Rewriting (4.15) yields

$$\begin{aligned}
\frac{|\boldsymbol{\omega}|^2}{|\mathbf{\Omega}|^2} &= \left(\frac{\mu_0 |\mathbf{M}|}{4\pi |\mathbf{B}|}\right)^4 (|\mathbf{La}|^2 |\mathbf{Lb}|^2 - |\mathbf{La} \cdot \mathbf{Lb}|^2) \\
&= \left(\frac{\mu_0 |\mathbf{M}|}{4\pi |\mathbf{B}|}\right)^4 (\mathbf{a}^{\mathrm{T}}\mathbf{L}^2\mathbf{a} \cdot \mathbf{b}^{\mathrm{T}}\mathbf{L}^2\mathbf{b} - \mathbf{a}^{\mathrm{T}}\mathbf{L}^2\mathbf{b} \cdot \mathbf{b}^{\mathrm{T}}\mathbf{L}^2\mathbf{a}) \\
&= \left(\frac{\mu_0 |\mathbf{M}|}{4\pi |\mathbf{B}|}\right)^4 \det \begin{bmatrix} \mathbf{a}^{\mathrm{T}}\mathbf{L}^2\mathbf{a} & \mathbf{a}^{\mathrm{T}}\mathbf{L}^2\mathbf{b} \\ \mathbf{b}^{\mathrm{T}}\mathbf{L}^2\mathbf{a} & \mathbf{b}^{\mathrm{T}}\mathbf{L}^2\mathbf{b} \end{bmatrix}
\end{aligned} \tag{4.16}$$

Because of $\det\mathbf{A} = \lambda_1\lambda_2$ according to (4.9), we found

$$\frac{|\boldsymbol{\omega}|^2}{|\mathbf{\Omega}|^2} = \left(\frac{\mu_0 |\mathbf{M}|}{4\pi |\mathbf{B}|}\right)^4 \lambda_1\lambda_2 = \left(\frac{|\mathbf{B}|_{max} |\mathbf{B}|_{min}}{|\mathbf{B}|^2}\right)^2 \tag{4.17}$$

Hence, the expression for the instantaneous angular velocity of the magnetic field ($|\boldsymbol{\omega}|$), with the magnetic field rotating around $\hat{\boldsymbol{\omega}}$ at a position

in the workspace, in relation to the instantaneous angular velocity of the permanent magnets ($|\boldsymbol{\Omega}|$), with the permanent magnets rotating around $\hat{\boldsymbol{\Omega}}$, can be found as

$$|\boldsymbol{\omega}| = \left(\frac{|\mathbf{B}|_{max} \, |\mathbf{B}|_{min}}{|\mathbf{B}|^2} \right) |\boldsymbol{\Omega}| \tag{4.18}$$

where the $|\boldsymbol{\omega}|$ achieves maximum and minimum when the instant magnetic field strength $|\mathbf{B}|$ reaches its minimum and maximum values, respectively. Furthermore, the average angular velocity of the magnetic field ($|\bar{\boldsymbol{\omega}}|$) at a position in the workspace within a single rotation period (T) of permanent magnets is given by

$$\begin{aligned} |\bar{\boldsymbol{\omega}}| &= \frac{1}{\mathrm{T}} \int_0^{\mathrm{T}} |\boldsymbol{\omega}| \, dt = \frac{1}{\mathrm{T}} \int_0^{\mathrm{T}} \left(\frac{|\mathbf{B}|_{max} \, |\mathbf{B}|_{min}}{|\mathbf{B}|^2} \right) |\boldsymbol{\Omega}| \, dt \\ &= \frac{1}{\mathrm{T}} \int_0^{2\pi} \left(\frac{|\mathbf{B}|_{max} \, |\mathbf{B}|_{min}}{|\mathbf{B}|^2} \right) d\theta_s \end{aligned} . \tag{4.19}$$

where $\mathrm{T} = 2\pi/|\bar{\boldsymbol{\Omega}}|$ such that $|\bar{\boldsymbol{\Omega}}|$ is the average angular velocity of permanent magnets. By squaring both sides of (4.6), we obtain

$$\begin{aligned} |\mathbf{B}|^2 &= \left(\frac{\mu_0 \, |\mathbf{M}|}{4\pi} \right)^2 \left| \hat{\mathbf{M}}^{\mathrm{T}} \mathbf{L}^2 \hat{\mathbf{M}} \right| \\ &= \left(\frac{\mu_0 \, |\mathbf{M}|}{4\pi} \right)^2 \boldsymbol{\Theta}^{\mathrm{T}} \mathbf{A} \boldsymbol{\Theta} \\ &= \left(\frac{\mu_0 \, |\mathbf{M}|}{4\pi} \right)^2 [\cos\theta_s \;\; \sin\theta_s] \begin{bmatrix} \lambda_1 & \\ & \lambda_2 \end{bmatrix} \begin{bmatrix} \cos\theta_s \\ \sin\theta_s \end{bmatrix} \\ &= [\cos\theta_s \;\; \sin\theta_s] \begin{bmatrix} |\mathbf{B}|_{max}^2 & \\ & |\mathbf{B}|_{min}^2 \end{bmatrix} \begin{bmatrix} \cos\theta_s \\ \sin\theta_s \end{bmatrix} \end{aligned} \tag{4.20}$$

which yields

$$|\mathbf{B}|^2 = |\mathbf{B}|_{max}^2 \cos^2(\theta_s) + |\mathbf{B}|_{min}^2 \sin^2(\theta_s). \tag{4.21}$$

Substituting (4.21) into (4.19), and we solve the integral in (4.19), which yields

$$|\bar{\boldsymbol{\omega}}| = |\bar{\boldsymbol{\Omega}}|. \tag{4.22}$$

Therefore, within a single rotation period of the synchronized rotating permanent magnets, the average angular velocity of the magnetic field at any position is equal to that of permanent magnets.

In Fig. 4.3(b), we illustrate the changes over time in both the field-rotation angle θ_f and the synchronous rotation angle θ_s at the coordinate origin (O). These variations occur under the influence of a constant angular velocity ($|\boldsymbol{\Omega}| = 2\pi$ rad/s) of the synchronized rotating permanent magnets. Once the permanent magnets commence synchronous rotation, the θ_f and θ_s alternate in surpassing each other at each quarter-cycle moment, ultimately completing one full rotation simultaneously. In Fig. 4.3(c), it indicates that the magnetic field strength $|\mathbf{B}|$ follows an elliptical pattern with respect to θ_f. Due to the asynchrony between θ_f and θ_s, the variation in $|\mathbf{B}|$ with respect to θ_f differs from that with respect to θ_s. Figs. 4.3(d), 4.3(e), 4.3(f) and 4.3(g) display the components of the measured (depicted in black) and predicted (illustrated in red) magnetic field at arbitrary positions $\boldsymbol{p} = [0\ 75\ 20]^{\mathrm{T}}$, $\boldsymbol{p} = [5\ 50\ 45]^{\mathrm{T}}$, $\boldsymbol{p} = [5\ 100\ 60]^{\mathrm{T}}$ and $\boldsymbol{p} = [10\ 125\ 40]^{\mathrm{T}}$. At the respective positions, the observed direction $\hat{\boldsymbol{\omega}}$ (indicated by black arrows) exhibited variations of 1.43°, 1.73°, 2.44° and 2.65° in comparison to the predicted direction $\hat{\boldsymbol{\omega}}$ (shown by red arrows). These findings demonstrate the accuracy of the presented theory in predicting the magnetic field and the unit vector of the field-rotation axis.

4.3.3 Field-rotation axis along y-axis

Fig. 4.4(a) depicts the variation in the ratio of the angular velocity of magnetic field, $|\boldsymbol{\omega}|$, to the angular velocity of the two synchronized rotating permanent magnets, $|\boldsymbol{\Omega}|$, at positions along the y-axis from $\mathcal{P}_1$ to $\mathcal{P}_8$. We observe that the ratio reaches its maximum magnitude at positions from $\mathcal{P}_1$ to $\mathcal{P}_4$, while it reaches its minimum magnitude at positions from $\mathcal{P}_6$ to $\mathcal{P}_8$ when $\theta_s = 180°$. This observation highlights that when $\theta_s = 180°$, the magnetic field ($|\mathbf{B}|$) rotates most rapidly at positions from $\mathcal{P}_1$ to $\mathcal{P}_4$, whereas the magnetic field rotates most slowly at positions from $\mathcal{P}_6$ to $\mathcal{P}_8$. Further, Fig. 4.4(b) illustrates the variation of $|\mathbf{B}|$ with respect to the θ_f and θ_s at these positions. From $\mathcal{P}_1$ to $\mathcal{P}_8$, it shows a gradual decrease in both the maximum and minimum magnetic field strength ($|\mathbf{B}|_{max}$ and $|\mathbf{B}|_{min}$). From $\mathcal{P}_1$ to $\mathcal{P}_5$, the $|\mathbf{B}|_{max}$ and $|\mathbf{B}|_{min}$ gradually become equal, while the trend reverses from $\mathcal{P}_5$ to $\mathcal{P}_8$.

Fig. 4.4(c) depicts the measured and predicted magnetic field as well as the field-rotation axes, projected onto the x-z and x-y planes, at positions from $\mathcal{P}_1$ to $\mathcal{P}_8$. The permanent magnets are synchronously rotated at a

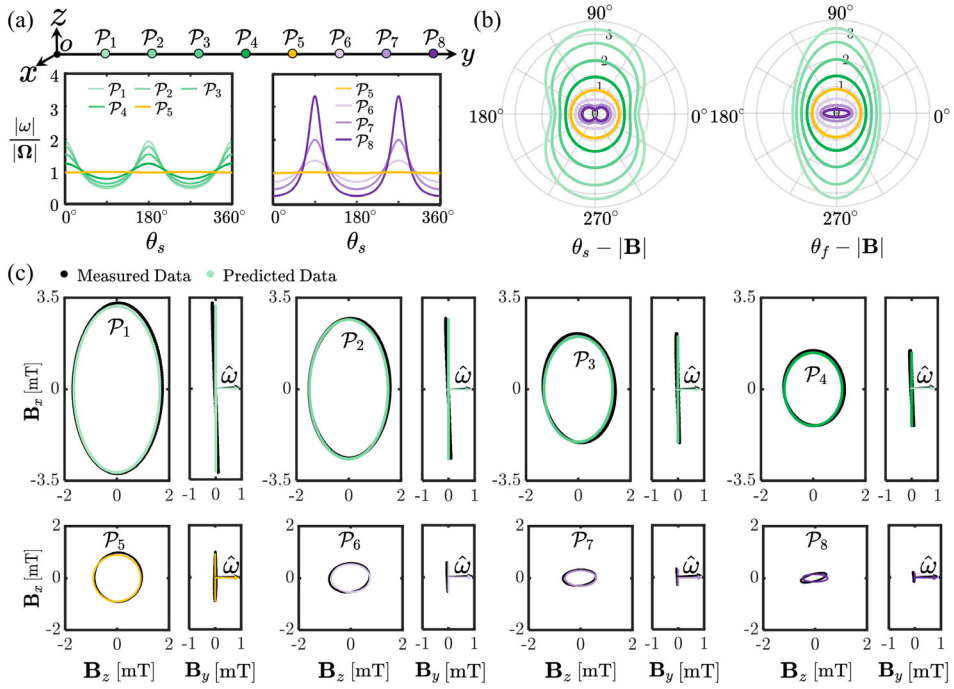

Figure 4.4: Characterization of the magnetic field at positions along the middle line between two synchronized rotating permanent magnets. (a) The simulation gives the change in the ratio of the angular velocity $|\boldsymbol{\omega}|$ of the magnetic field to the angular velocity $|\boldsymbol{\Omega}|$ of the synchronized rotating permanent magnets, at several positions on the middle line (which coincides with the y-axis) from position $\mathcal{P}_1$ to $\mathcal{P}_8$, within a rotation period of permanent magnets. The distance between any adjacent pair of positions is 25 mm. (b) The changes in magnetic field strength with respect to θ_s and θ_f at these positions. Position $\mathcal{P}_5$ is a neutral position where the magnetic field strength shows nearly circular variation with respect to both θ_s and θ_f. (c) The varying magnetic field measured (black points) and predicted (green, yellow, or purple points) at positions from $\mathcal{P}_1$ to $\mathcal{P}_8$ are indicated. The measured $\hat{\boldsymbol{\omega}}$ (black arrow) at positions from $\mathcal{P}_1$ to $\mathcal{P}_8$ differed from the predicted $\hat{\boldsymbol{\omega}}$ (green, yellow or purple arrow) by 2.02°, 1.99°, 1.83°, 2.91°, 3.00°, 1.51°, 3.81° and 2.74°, respectively. *Please refer to the accompanying video.*

constant angular velocity of 0.628 rad/s. The magnetic field components are measured using a magnetic sensor (Go Direct 3-Axis Magnetic Field Sensor) and predicted using (4.1). The measured $\hat{\boldsymbol{\omega}}$ is derived from the measured magnetic field using the least squares method, and the predicted $\hat{\boldsymbol{\omega}}$ is obtained using (4.4). The measured $\hat{\boldsymbol{\omega}}$ at positions from $\mathcal{P}_1$ to $\mathcal{P}_8$ differed from the predicted $\hat{\boldsymbol{\omega}}$ by 2.02°, 1.99°, 1.83°, 2.91°, 3.00°, 1.51°, 3.81° and 2.74° respectively. This finding illustrates that $\mathbf{B}$ and $\hat{\boldsymbol{\omega}}$ are closely predicted by the theory presented.

4.3.4 Neutral position

A neutral position is defined as a point where the magnetic field exhibits a circular variation pattern. In simpler terms, at the neutral position, the maximum and minimum magnetic field strengths are equal within a single rotation period of the permanent magnets. Position $\mathcal{P}_5$ acts as a neutral position where the magnetic field strength undergoes an almost circular variation with respect to both θ_s and θ_f. Remarkably, this neutral position remains unchanged regardless of the dipole moment's magnitude.

4.3.5 Magnetic field strength and gradient along y-axis

The magnetic field strength and gradient play pivotal roles in determining the magnetic torque and force exerted on a TTMD, consequently impacting its swimming speed in fluids. Consider a scenario where a TTMD moves along the y-axis under an actuation system of two synchronized rotating permanent magnets, as depicted in Fig. 4.5. We aim to characterize the magnetic field's strength and gradient along this axis.

As shown in Fig. 4.6(a), the component of the magnetic field, $\mathbf{B}_y$, remains constant at zero. In contrast, the components $\mathbf{B}_x$ and $\mathbf{B}_z$ undergo dynamic changes during a single rotation period of the permanent magnets. This observation suggests that the magnetic field, $\mathbf{B}$, rotates around the y-axis, with the unit vector of the field-rotation axis ($\hat{\boldsymbol{\omega}}$) aligned parallel to the y-axis, as illustrated in Fig. 4.6(b). As a result, a TTMD on the y-axis can move exclusively along the y-axis. As illustrated in Fig. 4.6(c), the components of the magnetic gradient, $\partial\mathbf{B}/\partial x$ and $\partial\mathbf{B}/\partial z$, remain consistently at zero. Conversely, the component of the magnetic field gradient, $\partial\mathbf{B}/\partial y$, undergoes dynamic changes during the rotation period of the permanent

magnets. The component $\partial \mathbf{B}/\partial y$ exhibits a positive magnitude at positions on the negative y-axis and a negative magnitude at positions on the positive y-axis. This observation indicates that the magnetic field gradient at positions on the y-axis is oriented parallel to the y-axis and consistently points towards the coordinate origin (O), as depicted in Fig. 4.6(d). If we place a TTMD along the negative y-axis and propel it towards a target location on the positive y-axis, its motion would be enhanced as it moves from its initial position to the origin, but dampened as it advances from the origin to the desired position on the positive y-axis.

However, we observe a region characterized by y and θ_s (outlined by the dashed box shown in Fig. 4.6(c)), where the magnetic field gradient approaches zero. This observation suggests the presence of a gradient-free line segment on the y-axis. Consequently, as a TTMD travels along this line segment, the gradient force it encounters can be approximated as zero. Therefore, when the TTMD moves along this line segment, it can be approximated as force-free motion. Further, we conduct experiments to verify the transnational motion of the TTMD under the actuation of two synchronized rotating permanent magnets. For comparison, we also study the curve motion of the TTMD under the actuation of a single rotating

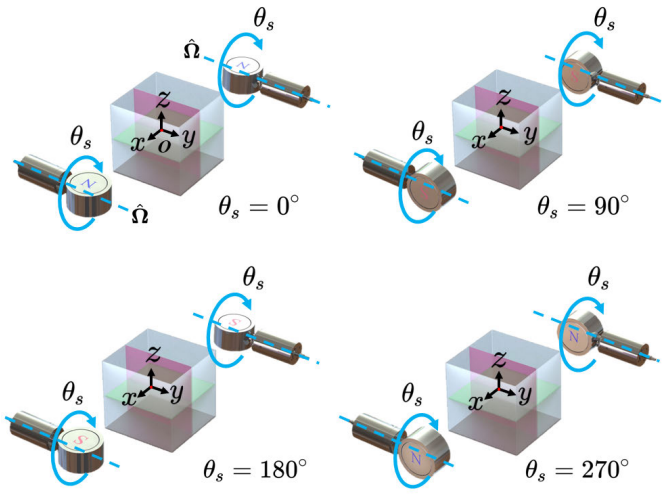

Figure 4.5: The poses of permanent magnets with respect to the synchronous rotation angle θ_s.

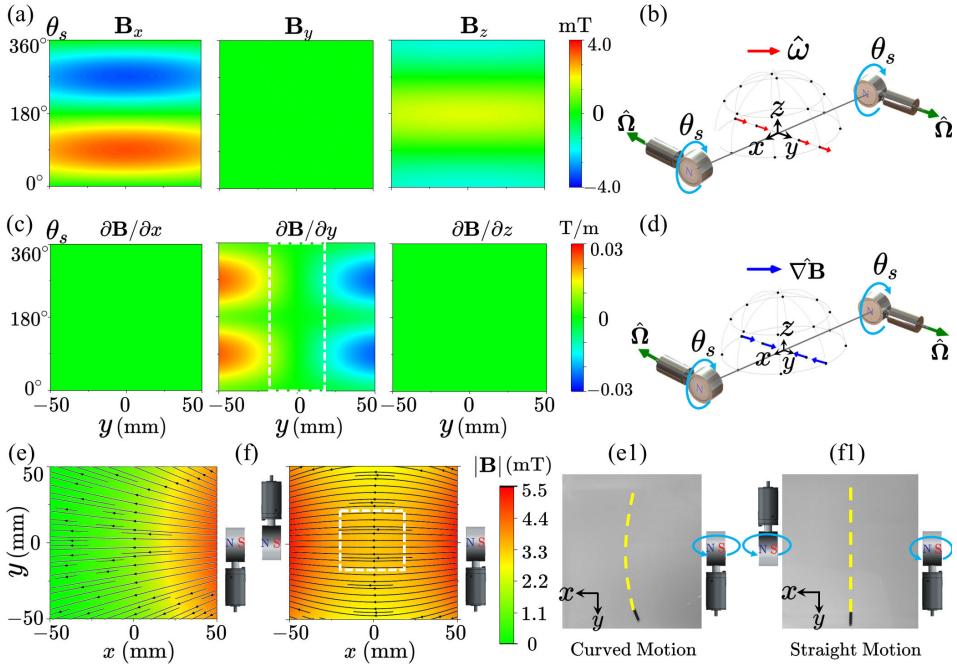

Figure 4.6: Characterization of time-varying magnetic field strength and gradient along y-axis under the actuation of two synchronized rotating permanent magnets. (a) The changes in the components of magnetic field ($\mathbf{B}_x$, $\mathbf{B}_y$ and $\mathbf{B}_z$) at positions on the y-axis are indicated within a rotation period of permanent magnets. (b) The unit vector of field-rotation axis $\hat{\boldsymbol{\omega}}$ at positions on y-axis is parallel to y-axis from the analysis of (a). (c) The changes in the components of magnetic field gradient ($\partial\mathbf{B}/\partial x$, $\partial\mathbf{B}/\partial y$ and $\partial\mathbf{B}/\partial z$) at positions on the y-axis are indicated within a rotation period of permanent magnets. The magnetic field gradient within the area outlined by the dashed box (characterized by y and θ_s) is close to zero, suggesting the existence of a line segment on the y-axis where the magnetic field gradient is nearly zero. (d) The unit vector of the magnetic field gradient ($\nabla\hat{\mathbf{B}}$) is parallel to the y-axis, and its orientation consistently directs towards the coordinate origin (O) at positions on the y-axis, resulting from the analysis of (c). (e and f) The magnetic field lines and strength within the central square region (100 mm × 100 mm) on the xOy plane are examined under two situations: employing a single permanent magnet-driven system (e) and a dual permanent magnet-driven system (f). The examination is conducted when the rotation angle of each permanent magnet is set to 90°. The square region (50 mm × 50 mm) indicated by the white dashed box in (f) approximately exhibits zero gradient. (e1 and f1) A TTMD undergoes actuation in both scenarios, resulting in curved motion (e1) and straight motion (f1) of the TTMD, respectively. *Please refer to the accompanying video.*

permanent magnet. In Fig. 4.6(e) and 4.6(f), both the magnetic field lines and the strength within the central square area (100 mm × 100 mm) on the xOy plane are displayed for the single-permanent magnet arrangement and the dual-permanent magnet arrangement, respectively. This display is provided with each permanent magnet rotated at 90°. In the dual-permanent magnet arrangement, a 50 mm × 50 mm square area is identified where the magnetic field lines are uniformly distributed. Additionally, there is minimal color variation in this square area, indicating insignificant changes in magnetic field strength. We refer to this area as the "gradient-free" region, outlined by the dashed box in Fig 4.6(f). However, this region is absent in the single-permanent magnet arrangement. Consequently, the TTMD exhibits curved and straight motion under the actuation of a single rotating permanent magnet and dual synchronized rotating permanent magnets, as depicted in Figs. 4.6(e1) and 4.6(f1)).

4.4 Characterization of swimming

To achieve the intended swimming behaviors of TTMDs within bodily fluids such as the vitreous humor of the human eye, it is crucial to examine factors such as fluid rheological parameters, TTMD geometrical parameters, and actuation frequency that may influence the TTMD swimming behaviors in this particular environment.

4.4.1 Swimming speed prediction model

The translating speed U of the TTMD at angular speed ω in viscoelastic fluids is modeled using [40], [167],

$$U = 2A\omega\varepsilon^2 \sum_{q\geq 1} \frac{(1+\beta q^2 De^2)\left|\hat{f}q\right|^2}{1+q^2De^2} J_q \tag{4.23}$$

where β is the ratio of solvent viscosity to the total viscosity, De is the Deborah number and is expressed as $De = \lambda\omega$ such that λ is the ratio of the fluid relaxation timescale and ω is the angular velocity of the TTMD.

$$J_q = \frac{q^2 A_q}{2}(2K_{q-1} - vK_q + \frac{vK_{q-1}^2}{K_q}) \tag{4.24}$$

where the symbol A_q is given by,

$$A_q = \frac{2(q + \frac{qvK_{q-1}}{K_q})}{qK_q + qvK_{q-1} - \frac{2(q-2)}{v}K_{q-1} - \frac{(3q-2)K_{q-1}^2)}{K_q} - \frac{qvK_{q-1}^3}{K_q^2}} \tag{4.25}$$

Note that this model is employed when the TTMD rotates without being attracted by external forces. According to the analysis in Section 4.3.5, This model is applicable for predicting the swimming speed of a TTMD when it moves within a gradient-free region, actuated by two synchronized rotating permanent magnets.

4.4.2 Rheological properties of agar gel phantom

The agar gel phantom, functioning as a viscoelastic fluid, is used to mimic the human bodily fluid environment. Consequently, the swimming characteristics of the TTMD within it are investigated. The agar gel phantom is prepared using gelatin powder (BOOM, EC 232-554-6, CAS/PREP 9000-70-8) as the solute and demineralized water as the solvent, with a concentration of 0.56 w.t.%. To evaluate its fluidic properties, we measure the rheological parameters of the agar gel phantom using a rheometer (MCR 92, SN83786884). As depicted in Fig. 4.7(a) and 4.7(b), the viscosity of the agar gel phantom decreases while the shear stress increases, along with the rise in shear rate. As depicted in Fig. 4.7(c) and 4.7(d), the decrease in storage modulus (G') while the increase in loss modulus (G''), and the increase in loss factor $\tan(\delta)$ are observed at a shear strain ranging from 1% to 1000%. The substantial increase in G'' can be correlated with the deterioration of the material structure in the agar gel phantom.

Note that the rheological property of the agar gel phantom with a low concentration (e.g., 0.56 w.t.%) is easily changed if it is left at room temperature. To prevent the agar gel phantom from changing its properties, keeping the experimental temperature close to that at which it was formed is significant. Besides, the rheological properties of the agar gel phantom are changed by the movement of a TTMD within it. This is due to the fact that the molecules of the agar gel phantom form a network with physical bonds that are susceptible to disruption by the movement of the TTMD. Thus, to ensure the accuracy of measuring the speed of a TTMD in an agar gel phantom, it is necessary to take measures to prevent the reuse of channels that the TTMD has already traversed.

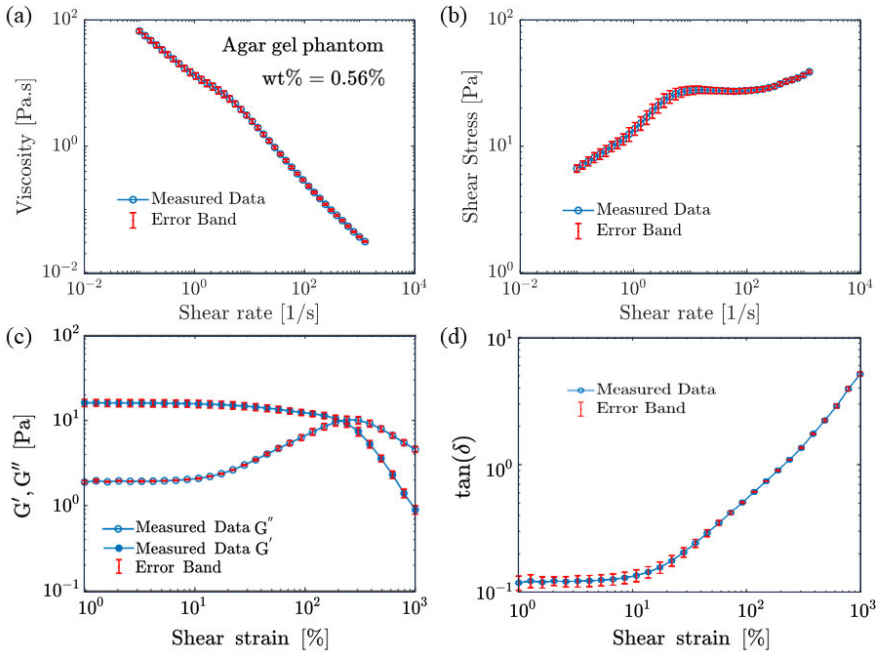

Figure 4.7: Rheological properties of agar gel phantom with a concentration of 0.56% at a temperature of 3 °C. (a) Changes in viscosity of the agar gel phantom in relation to its shear rate. (b) Changes in shear stress of the agar gel phantom in relation to its shear rate. (c) Amplitude sweep profile. Dependence of storage modulus (G') and loss modulus (G'') on strain at the angular frequency of 1 Hz. (d) Loss factor $\tan(\delta)$ of the agar gel phantom as a function of its shear strain.

4.4.3 Frequency response characterization

To better understand the impact of TTMD geometry and actuation frequency on the swimming performance of the device in viscoelastic fluids, we conducted a series of experiments. In these experiments, we systematically varied the geometric designs of the TTMD and tested its performance across different actuation frequencies within an agar gel phantom with a concentration of 0.56 wt.%. By analyzing the results, we may identify the optimal TTMD design and actuation parameters that maximize swimming efficiency in viscoelastic fluids.

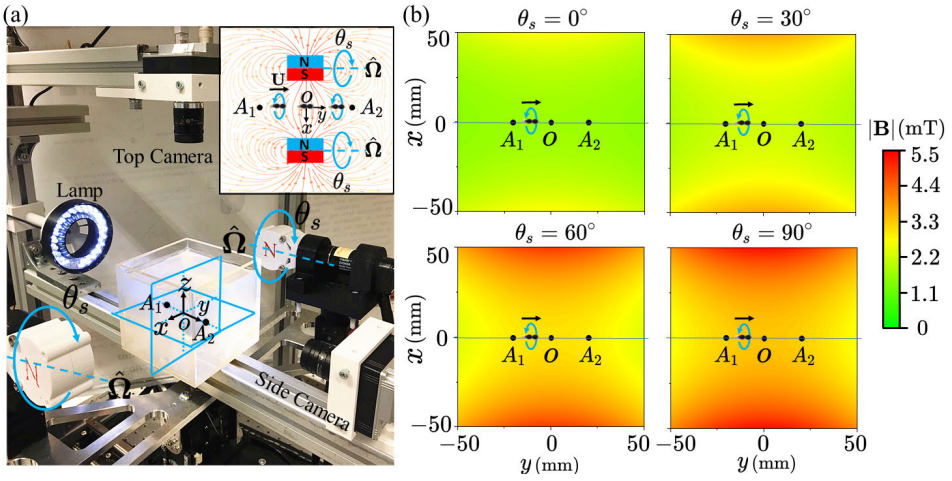

Figure 4.8: Experimental actuation system. The system incorporates two synchronized rotating permanent magnets, resulting in a rotating magnetic field to actuate TTMDs. The motion of the TTMDs is captured by cameras. (a) The TTMDs are arranged to move in an agar gel phantoms-filled cubical container with a side length of 100 mm. The container is placed in the central space between the two synchronized rotating permanent magnets. (b) The simulation provides the variations in the distribution of magnetic field strength across a 100 mm × 100 mm square area within the xOy plane, at several fixed synchronous rotation angles (0°, 30°, 60° and 90°).

4.4.3.1 Experimental method

The TTMDs are driven by a rotating magnetic field generated by an actuation system utilizing two identical permanent magnets, as shown in Fig. 4.8(a). Each permanent magnet (S-45-30-N, NdFeB, N45, Nickel-plated, Supermagnete) is actuated by a servo motor (Planetary Gearhead GP 32 C ϕ32 mm, 1.0 - 6.0 Nm, Ceramic Version, Maxon). Utilizing a positioning controller (EPOS2 50/5, Digital positioning controller, 5 A, 11 - 50 VDC, Maxon), the two identical permanent magnets are synchronized to rotate around the dipole-rotation axis of $\mathbf{\Omega}$. Concurrently, the real-time position of a TTMD is tracked by two cameras (Aviator GIGE, avA1000-100gm, Basler AG, Ahrensburg, Germany). TTMDs are arranged to move within a cubic container with side lengths of 100 mm, centrally located

within the workspace of the actuation system. Throughout the experiment, the container is submerged in a cold water reservoir and ice cubes are added to maintain the experimental temperature at or around 3 °C, ensuring stability of the properties of the phantom of agar gel.

TTMDs are anticipated to travel from positions A_1 to A_2, as illustrated in Fig. 4.8(b). Positions A_1 and A_2 are situated on the y-axis and exhibit symmetry about the coordinate origin O. The distance between positions A_1 and A_2 is 40 mm. The maximum magnetic field strengths at positions A_1, O, and A_2 are 3.61 mT, 3.35 mT, and 3.61 mT, respectively. The minimum magnetic field strengths at these positions are 1.84 mT, 1.70 mT, and 1.84 mT, respectively. Based on the analysis in Fig. 4.6 in Section (4.3.5), the TTMDs can move straight from position A_1 to A_2.

4.4.3.2 Experimental results

The TTMDs are categorized into four groups: Number-of-start group, Diameter group, Pitch group, and Amplitude group. Fig. 4.9 illustrates the results of frequency response experiments conducted on the TTMDs within each group. In each subgraph, the lines represent a linear increase in the TTMD swimming speed with the actuation frequency predicted by the model. The data aligns closely with the model predictions at low actuation frequencies. Furthermore, we experimentally determine the step-out frequency for each TTMD, which serves as a reference for setting the actuation frequency in TTMD motion control experiments. In the Number-of-start group, the step-out frequencies for TTMDs with $N = 2$ and $N = 3$ are 27 Hz and 26 Hz, respectively. It is important to note that no significant movement of the TTMD with $N = 1$ was observed when applying a rotating magnetic field frequency ranging from 1 to 30 Hz. In the Radius group, the step-out frequencies for TTMDs with $A = 0.75$ mm, and $A = 0.8$ mm are 27 Hz and 17 Hz, respectively. Note that the step-out frequency for TTMD with $A = 0.6$ mm is over 30 Hz. In the Pitch group, the step-out frequencies for TTMDs with $P_r = 2$ mm, $P_r = 4$ mm, and $P_r = 6$ mm are 17 Hz, 27 Hz, and 24 Hz, respectively. In the Amplitude group, the step-out frequencies for TTMDs with $\varepsilon = 0.5$, $\varepsilon = 0.6$, and $\varepsilon = 0.7$ are 27 Hz, 20 Hz, and 17 Hz, respectively.

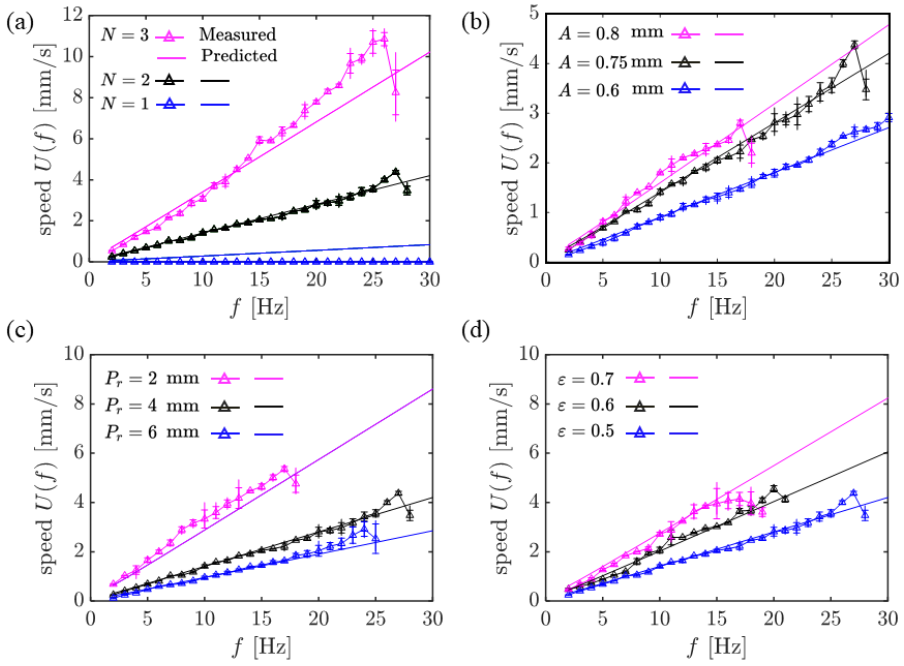

Figure 4.9: Frequency response results of TTMDs at each group in the agar gel phantom with a concentration of 0.56% at a temperature of 3 degrees Celsius. (a) Number-of-start group. (b) Radius group. (c) Pitch group. (d) Amplitude group. Lines in each subgraph represent the predicted values from the swimming speed prediction model.

4.5 Motion control

TTMD motion control includes motion speed control and motion direction control. The motion control scheme of a TTMD is shown in Fig 4.10. To achieve the desired swimming behavior in viscoelastic fluids, we can change the TTMD motion speed by adjusting the parameters presented in the swimming speed prediction model and manipulate the TTMD motion direction by managing the field-rotation axis at predefined positions with a permanent magnet-based robotic system. The robotic system has four DOFs, and the desired vector of joint space variables is indicated as $\boldsymbol{q}^d = [q_1\ q_2\ q_3\ q_4]^{\mathrm{T}}$. Initially, the TTMD is located at position $\boldsymbol{p}_0$. Based on the predefined position $\boldsymbol{p}_{\mathrm{ref}}$ and estimated current position $\boldsymbol{p}$ of the TTMD,

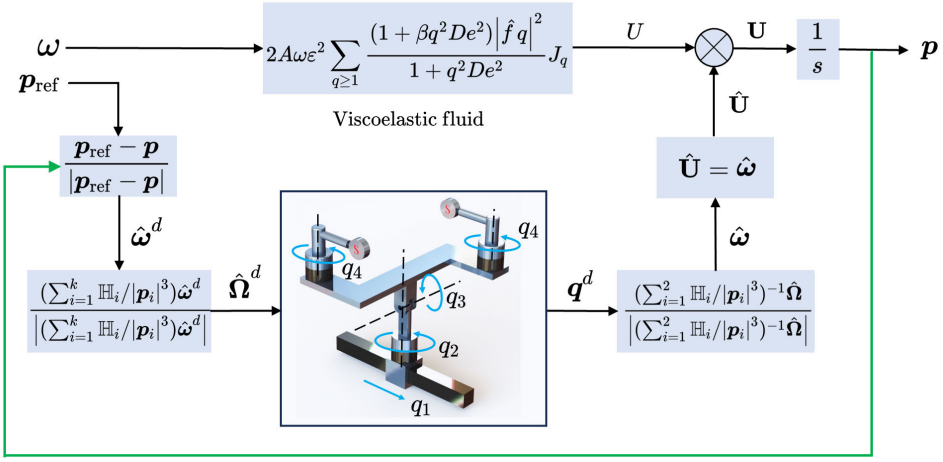

Figure 4.10: Motion control of TTMDs is accomplished through an analytical solution of the TTMD swimming speed and the theory presented in Section 4.3.

the desired field-rotation axis at position $\boldsymbol{p}$ is updated by

$$\hat{\boldsymbol{\omega}}^d = \frac{\boldsymbol{p}_{\text{ref}} - \boldsymbol{p}}{|\boldsymbol{p}_{\text{ref}} - \boldsymbol{p}|} \tag{4.26}$$

Following (4.3), the desired dipole-rotation axis $\hat{\boldsymbol{\Omega}}^d$ is derived from the desired field-rotation axis $\hat{\boldsymbol{\omega}}^d$. Subsequently, the desired vector of joint space variables $\boldsymbol{q}^d$ is obtained by solving the inverse kinematics of the permanent magnet-based robotic system. Then, the robotic system is executed with the input $\boldsymbol{q}^d$, and the TTMD motion direction characterized by $\hat{\mathbf{U}}$ is updated with the estimated current position $\boldsymbol{p}$. Finally, the TTMD motion control is achieved with the updated velocity vector $\mathbf{U}$, which is constructed by the motion direction $\hat{\mathbf{U}}$ and the predicted swimming speed U. We incorporate the swimming speed prediction model into the TTMD motion control experiments. Specifically, a TTMD with parameters $P_r = 4$ mm, $N = 2$, $L_r = 6$ mm, $A = 0.75$ mm, and $\varepsilon = 0.5$ is selected to execute predefined circular trajectories at different actuation frequencies within an agar gel phantom with a concentration of 0.56 w.t.%. The TTMD is directed to follow 'U', 'M', 'C', 'G', 'O', and 'S' trajectories at an actuation

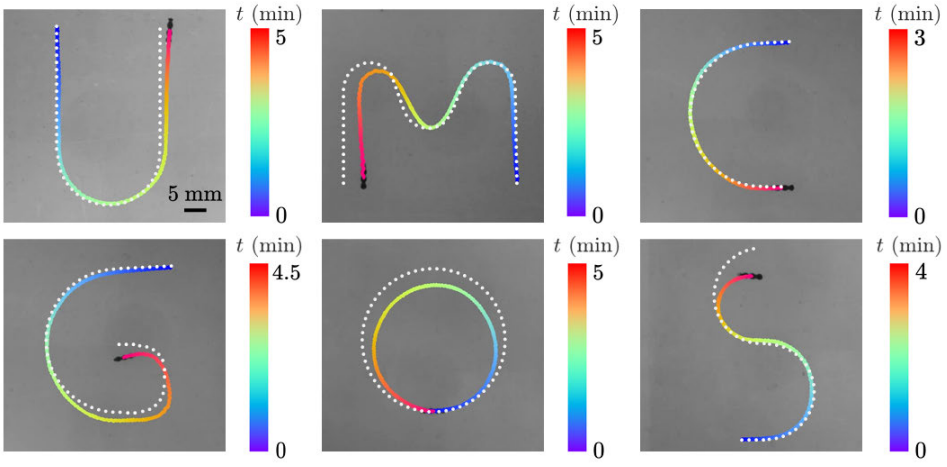

Figure 4.11: Motion control of a TTMD is achieved through utilization of a swimming speed prediction model, enabling the execution of trajectories labeled as 'U', 'M', 'C', 'G', 'O', and 'S'. These trajectories are conducted in 0.56 wt.% agar gel, maintained at a temperature of 3 degrees Celsius, and driven by an actuation frequency of 2 Hz. The representative points of predefined trajectories are indicated by white points, while the practical trajectories are indicated by solid lines, respectively. *Please refer to the accompanying video.*

frequency of 2 Hz. The experimental results of the TTMD motion control are depicted in Fig. 4.11.

The prediction model assumes a constant swimming speed for a TTMD at each point along the path in motion control experiments. However, in practical experiments, the swimming speed of a TTMD is not constant. Notably, during the execution of the 'S' trajectory by the TTMD, we observe that the time taken for the lower half-circle matches that of the upper half-circle, despite the lower half-circle having a larger radius. This suggests a higher average swimming speed during counterclockwise circular motion, leading to deviations from the predefined trajectory in the upper half-circle. Consequently, a significant positioning error, with a maximum of 4.50 mm, occurs in the later segment of trajectory 'M'. However, in trajectories without clockwise turns, such as 'U', 'C', 'G', and 'O', the maximum positioning error remains below 3.50 mm, indicating the controllability of the TTMD

under our control scheme. The average swimming speeds of the TTMD for 'U', 'M', 'C', 'G', 'O', and 'S' trajectories are 0.388 mm/s, 0.398 mm/s, 0.429 mm/s, 0.439 mm/s, 0.375 mm/s, and 0.350 mm/s, respectively. To mitigate positioning errors, one feasible approach is to allocate additional time when the TTMD rotates clockwise.

4.6 Conclusion

The effectiveness and limitations of a swimming speed prediction model are validated for predicting TTMD swimming speed in an agar gel phantom under the influence of two synchronized rotating permanent magnets. The practicality of the prediction model is confirmed in the context of TTMD motion control utilizing a permanent magnet-based robotic system. We discover an approximate gradient-free region between two synchronized rotating permanent magnets. This discovery proves that the TTMD propulsion within the gradient-free region satisfies the condition of utilizing the swimming speed prediction model. In addition, we observe that the swimming prediction model accurately predicts TTMD swimming speed at low actuation frequencies (below the step-out frequency). However, its accuracy diminishes at higher actuation frequencies (around or above the step-out frequency). Therefore, the prediction model is suitable for predicting the TTMD position information under low actuation frequencies (below the step-out frequency) in the TTMD motion control experiments. The implementation of the swimming speed prediction eliminates the need for additional imaging equipment to locate the TTMD, leading to simplified control strategies.

5

Conclusion

TMHDs hold significant promise in the field of biomedical applications, specifically in their ability to be remotely manipulated to navigate deep tissues within the human body, a task that proves difficult with conventional surgical instruments. Our ultimate goal is to utilize TMHDs for biomedical purposes such as targeted drug delivery and material removal. The current work serves as the foundation for achieving this ultimate goal. The goal of this thesis is stated as achieving stable and efficient navigation of TMHDs in physiological environments. To accomplish such a goal, the thesis explores the design, actuation, swimming behaviors, and motion control of TMHDs within physiological settings.

5.1 Discussions

5.1.1 Development of a permanent magnet-based robotic system

The permanent magnet-based robotic system is developed to navigate the TMHDs in physiological environments, as described in **Chapter 2**. In the system design, the configuration-to-pose kinematics and the pose-to-field mapping of the system are derived, which serves as the foundation for implementing motion control of TMHDs in three-dimensional space. Furthermore, a significant innovation involves the implementation of a symmetric configuration to physically constrain the positions of two permanent magnets symmetrically, enabling the stable generation of a gradient-free space

between two synchronized rotating permanent magnets. In this gradient-free space, the influence of magnetic field gradients on the motion control of the TMHDs can be disregarded. Instead, the focus is solely on the effect of the field-rotation axis on the direction of TMHD motion. This characteristic simplifies the motion control of a TMHD. Utilizing this setup, 3-D closed-loop motion control for a TMHD has been successfully implemented. The existence of this gradient-free space provides possibilities for applying a swimming speed prediction model in the TMHD motion control in **Chapters 3 and 4**. Therefore, the question (**RQ. 1**) involves how to build a permanent magnet-based robotic system with a large gradient-free workspace enabling TMHDs to move controllably in physiological environments has been addressed.

5.1.2 Utilization of a swimming speed prediction model

The motion control of TMHDs involves both direction control and speed control. The directional control of TMHDs can be achieved by manipulating the orientation of the magnetic field with our permanent magnet-based robotic system, as proposed in **Chapter 2**. To achieve speed control of TSMDs (a subclass of TMHD), the correlation between actuation frequency and swimming speed in agar gel phantom under the actuation of two synchronized rotating permanent magnets is investigated. Such correlation can be predicted using a swimming speed prediction model [40], [167], at a low actuation frequency (below the step-out frequency). Then the control of motion speed for a TSMD can be translated into the control of actuation frequency for the synchronized rotating permanent magnets.

The establishment condition of the swimming speed prediction model is that the translational motion of a TSMD is primarily attributed to its rotation rather than being influenced by external forces. **Chapter 2** demonstrates that two synchronized rotating magnets can create an approximate gradient-free space between them. This demonstration reveals that the TSMD experiences almost zero gradient force, indicating the potential to utilize this prediction model for motion control of the TSMD within our permanent magnet-based robotic system. Finally, a control scheme for integrating the prediction model into the TSMD motion control is proposed in **Chapter 3**. The application of this prediction model can reduce dependence on image sensing devices. Here the question (**RQ. 2**) involves how

to incorporate a swimming speed prediction model into the motion control of TMHDs in our permanent magnet-based robotic system has been addressed.

5.1.3 Hydrodynamic behavior of tetherless twist-shaped magnetic devices in viscoelastic fluids

To attain the intended swimming performance of TMHDs in physiological settings like the vitreous humor of the human eye (known as a viscoelastic fluid), it is imperative to explore variables such as TMHD geometric parameters and actuation frequency, which impact their swimming speed within such conditions. Li *et al.* introduced a prediction model incorporating the geometric parameters of TTMDs (a subclass of TMHD) and actuation frequency that can be utilized to predict the swimming speed of TTMDs in viscoelastic fluids [40], [167]. In **Chapter 4**, experiments are conducted to measure the TTMD swimming speed in an agar gel phantom (which serves as a viscoelastic environment) under the actuation of two synchronized rotating permanent magnets, aiming to validate the effectiveness of the prediction model. The prediction model's accuracy is confirmed at low actuation frequencies (below the step-out frequency), although its accuracy diminishes at high actuation frequencies (near or above the step-out frequency).

5.1.4 Correlation between the field-rotation axis and the dipole-rotation axis

The correlation between the field-rotation axis and the dipole-rotation axis is investigated under the influence of two synchronized rotating permanent magnets. As presented in Table 5.1, a comparison of this correlation between the actuation system utilizing a single rotating permanent magnet, as discussed in reference [179], and that employing two synchronized rotating permanent magnets, as detailed in **Chapter 4**, is provided. Thus, the question (**RQ. 3**) involves how to correlate the field-rotation axis with the dipole-rotation axis under the actuation of two synchronized rotating permanent magnets has been addressed.

In the actuation systems utilizing a single rotating permanent magnet, it is observed that the forward model (from the unit vector of the dipole-rotation axis to the unit vector of the field-rotation axis) and the inverse

Table 5.1: Comparative analysis of magnetic fields generated by a single rotating magnet and dual synchronized rotating magnets

Type	Single Rotating Permanent Magnet	Dual Synchronized Rotating Permanent Magnets
$\hat{\boldsymbol{\Omega}}^d$	$\hat{\boldsymbol{\Omega}}^d = \widehat{\mathbb{H}\hat{\omega}}$ where $\mathbb{H} = 3\hat{\boldsymbol{p}}\hat{\boldsymbol{p}}^{\mathrm{T}} - \mathbf{I}$	Equation (4.3)
$\hat{\boldsymbol{\omega}}$	$\hat{\boldsymbol{\omega}} = \widehat{\mathbb{H}^{-1}\hat{\boldsymbol{\Omega}}}$	Equation (4.4)
$\lvert\mathbf{B}\rvert$	$\lvert\mathbf{B}\rvert = \frac{\lvert\mathbf{M}\rvert}{4\pi\lvert\boldsymbol{p}\rvert^3}\sqrt{1+3(\hat{\mathbf{M}}^{\mathrm{T}}\hat{\boldsymbol{p}})^2}$	Equation (4.10)
$\lvert\mathbf{B}\rvert_{max}$	$\lvert\mathbf{B}\rvert_{\max} = \frac{\lvert\mathbf{M}\rvert}{4\pi\lvert\boldsymbol{p}\rvert^3}\sqrt{1+3\lvert\tilde{\boldsymbol{p}}\rvert^2}$ where $\tilde{\boldsymbol{p}} = (\mathbf{I} - \hat{\boldsymbol{\Omega}}\hat{\boldsymbol{\Omega}}^{\mathrm{T}})\hat{\boldsymbol{p}}$	Equation (4.11)
$\lvert\mathbf{B}\rvert_{min}$	$\lvert\mathbf{B}\rvert_{min} = \frac{\lvert\mathbf{M}\rvert}{4\pi\lvert\boldsymbol{p}\rvert^3}$	Equation (4.12)
$\lvert\omega\rvert$, $\lvert\boldsymbol{\Omega}\rvert$	$\lvert\boldsymbol{\omega}\rvert = \left(\frac{\lvert\mathbf{B}\rvert_{max}\lvert\mathbf{B}\rvert_{min}}{\lvert\mathbf{B}\rvert^2}\right)\lvert\boldsymbol{\Omega}\rvert$	Equation (4.18)

model (from the desired unit vector of the field-rotation axis to the desired unit vector of the dipole-rotation axis) at a position $\boldsymbol{p}$ are primarily associated with the direction of the position $\boldsymbol{p}$ relative to the permanent magnet. However, in the case of the actuation systems employing two synchronized rotating permanent magnets, it is indicated that these models are influenced by both the distance and direction of the position $\boldsymbol{p}$ relative to the two permanent magnets. Further, in the context of these two actuation systems, it's observed that the magnetic field strength, denoted as $|\mathbf{B}|$, exhibits similar behavior in both systems. More precisely, it fluctuates following an elliptical pattern. Additionally, the relationship between the instantaneous angular velocity of permanent magnets, $|\boldsymbol{\Omega}|$, and that of the generated magnetic field, $|\boldsymbol{\omega}|$, remains consistent, as presented in Equation (4.18).

5.1.5 Development of control strategy

In **Chapter 2**, an exact magnetic model is employed (*Please refer to* **Appendix A.1**), capable of accurately expressing the superimposed magnetic field at any position. This model is particularly useful to express the magnetic field at the position of a TMHD when it is in close proximity to the actuator magnets aiming for higher magnetic field strength to propel it effectively. However, due to the nonlinearity of this model, solving the inverse problem from the desired field-rotation axis to the desired dipole-rotation

axis is usually achieved using iterative algorithms, demanding substantial computational power when applied to TMHD motion control. To address this challenge, a control scheme based on the point-dipole model is developed in **Chapter 4**, which can directly solve the inverse problem with a mathematical equation (*Please refer to* Equation (4.3)). Thereby, it simplifies the real-time motion control of TMHDs.

5.2 Future directions

Future research endeavors may concentrate on enhancing the system's capability to effectively navigate TMHDs within physiological environments, such as biological fluids or tissues, and further exploring the application of TMHDs in biomedical contexts. These efforts could involve improving the permanent magnet-based robotic system, enhancing its precision and adaptability for navigating TMHDs in complex biological environments. Additionally, investigating the TMHD control strategy with consideration of position and pose uncertainty under the influence of two synchronized rotating permanent magnets could be a focus area. Exploring magnetic localization techniques for TMHDs under the actuation of two synchronized rotating permanent magnets may also be pursued to improve navigation accuracy. Furthermore, miniaturizing TMHDs to expand their utility within confined biological environments is another potential avenue for future research.

5.2.1 Improvement of the robotic system

The permanent magnet-based robotic system has been developed for stably navigating TMHDs in physiological environments. There's still room for improvement in this system. The system possesses four DOFs, allowing for directional manipulation of a TMHD in 3-D space. However, this number of DOFs is insufficient to meet the requirements for both directional control and gradient force control simultaneously, especially when a TMHD is controlled beyond gradient-free spaces.

Maintaining a symmetric configuration is crucial for reliably establishing gradient-free spaces. Combining a symmetric configuration with adequate DOFs would greatly enhance the system's ability to manipulate TMHDs. One practical approach is to integrate two additional linear mo-

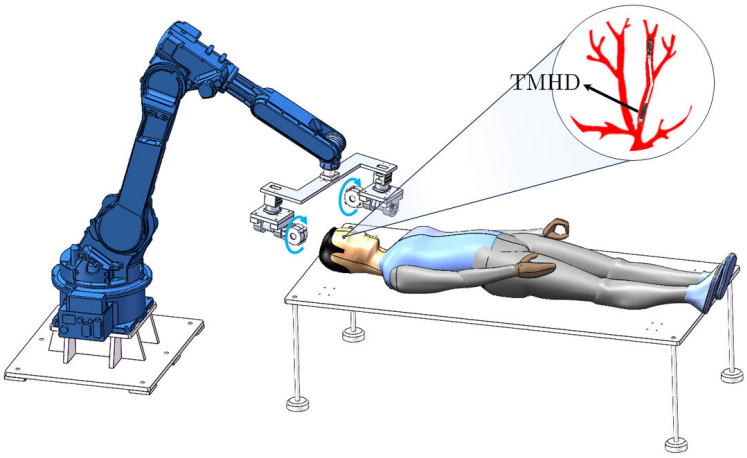

Figure 5.1: An approach to improve the current permanent magnet-based robotic system for minimally invasive surgery. The symmetric configuration to exert gradient-free space between two permanent magnets is attached to the end-effector of an industrial robot.

tion stages, allowing for the symmetric configuration to move linearly in the x-, y-, and z-directions in 3-D space. Another strategy could involve incorporating this symmetric configuration into the end-effector of an industrial robot, as illustrated in Fig. 5.1.

5.2.2 Optimal design of symmetric configuration

Our system utilizes a symmetric configuration with the objective of establishing a gradient-free space between the two synchronized rotating permanent magnets to streamline the motion control of TMHDs. Furthermore, efforts are made to achieve a robust magnetic field strength to provide sufficient propulsion for the TMHDs to overcome potential resistance while navigating complex environments. In Fig. 5.2(a), the poses of the two synchronized rotating permanent magnets relative to the synchronous rotation angle (θ_s) are illustrated. According to Figs. 2.6 and 2.7 in **Chapter 2**, both the magnetic field gradient and strength reach their highest magnitudes when θ_s is at 90° or 270° during one rotation period of the permanent magnets within a spherical space. The highest magnetic gradient and strength are denoted as $|\nabla \mathbf{B}|_{hig}$ and $|\mathbf{B}|_{hig}$, respectively.

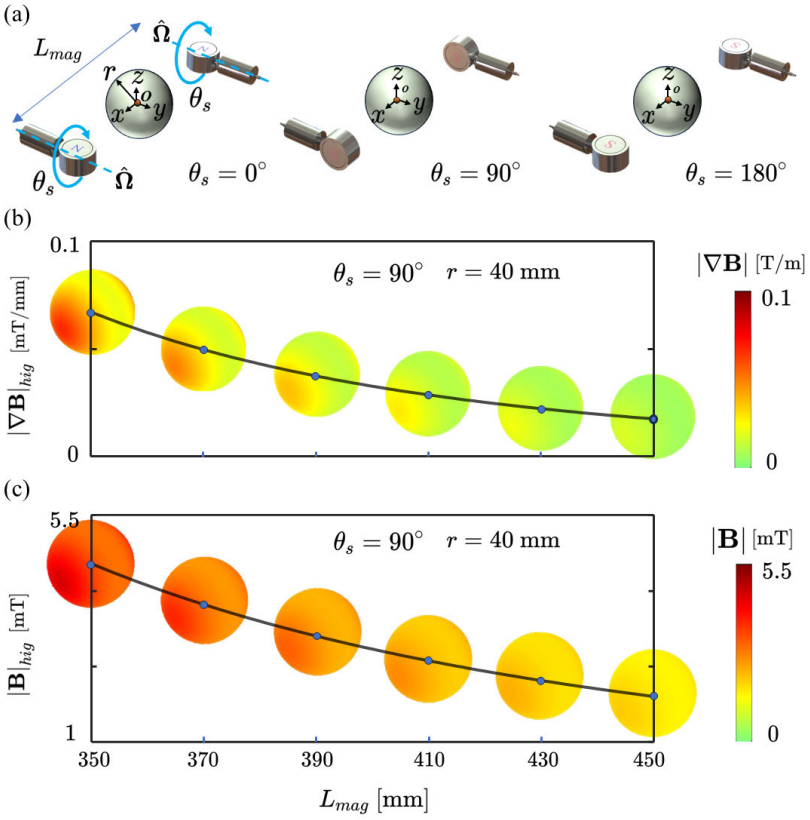

Figure 5.2: The changes in the highest magnitudes of the field strength and gradient within a spherical space between two synchronized rotating permanent magnets. (a) Poses of two synchronized rotating permanent magnets with a synchronous rotation angle of θ_s. (b and c) The highest magnetic field gradient and strength ($|\nabla \mathbf{B}|_{hig}$ and $|\mathbf{B}|_{hig}$) vary with changes in the distance (L_{mag}) between two permanent magnets. The distributions of magnetic field strength and gradient across the surface of the spherical space are depicted when θ_s and L_{mag} are set to 90° and 40 mm, respectively.

Assume a spherical space with the radius (r) of 40 mm, and setting θ_s to 90°. In Fig. 5.2(b), it's demonstrated that the highest magnitude of the magnetic field gradient ($|\nabla \mathbf{B}|_{hig}$) decreases as the distance between two

permanent magnets (L_{mag}) increases from 350 mm to 450 mm. This decrease is indicated by a gradual color change on the surface of the spherical space from red and yellow to green. These findings suggest that increasing the distance between the two permanent magnets can expand the gradient-free space. Similarly, Fig. 5.2(c) illustrates that the highest magnitude of the magnetic field ($|\mathbf{B}|_{hig}$) decreases as L_{mag} increases from 350 mm to 450 mm. This decrease is reflected in the color change from red to yellow on the surface of the spherical space. These results imply that increasing the distance between the two permanent magnets leads to a decrease in the average magnetic field strength within the spherical space. Therefore, increasing the distance between the two magnets enlarges the gradient-free space but decreases the magnetic field strength within it. Consequently, the optimal design of the symmetric configuration, which determines the optimal distance between the two permanent magnets, is crucial for minimizing the gradient force acting on a TMHD while maximizing the torque applied to it.

5.2.3 Control strategy with position and pose uncertainty of two synchronized rotating permanent magnets

In our assumptions, there is no deviation in the position and pose of the two synchronized rotating permanent magnets. However, real-world factors like vibrations can disrupt these ideal conditions. The positional inaccuracies of the permanent magnets and angular deviations of their magnetic moments relative to their rotation axis can result in deviations of the field-rotation axis at the position of a TMHD. As the field-rotation axis governs the motion direction of the TMHD, any angular deviation from the expected field-rotation axis can significantly affect the TMHD motion control. Therefore, enhancing the system's capability to control a TMHD in the presence of position and pose uncertainty of the two synchronized rotating permanent magnets is of utmost importance.

5.2.4 Magnetic localization of magnetic helical devices

Localizing TMHDs is crucial for their applications in biomedical fields such as targeted drug delivery. The model for the localization of TMHDs under the actuation of a single rotating permanent magnet has been well studied. However, such a model under the actuation of two synchronized rotating

permanent magnets has not received extensive study. In **Appendix B**, A magnetic device consisting of a magnet and a body is assumed, with a magnetic sensor embedded in the body. The magnetic field detected by the magnetic sensor is solely attributable to the influence of the two synchronized rotating permanent magnets. Based on these assumptions, a non-iterative approach for localizing a magnetic device under the actuation of two synchronized rotating permanent magnets is proposed. This model's functionality is not contingent upon the exact correlation between the instantaneous poses of synchronized rotating permanent magnets, characterized by their instantaneous dipole moments, and the generated magnetic field at the location of the magnetic device. This feature ensures that the accuracy of localization remains undisturbed even during the rapid rotation of synchronized rotating permanent magnets. Such a model can be utilized to localize a TMHD in future research.

5.2.5 Miniaturization and integration

Continued endeavors aimed at miniaturizing and integrating components can result in the creation of smaller, more compact TMHDs. This advancement would enable smoother integration into minimally invasive procedures and expand their utility within the body's confined spaces.

Bibliography

[1] J. Li, B. Esteban-Fernández de Ávila, W. Gao, L. Zhang, and J. Wang, "Micro/nanorobots for biomedicine: Delivery, surgery, sensing, and detoxification," *Science robotics*, vol. 2, no. 4, p. eaam6431, 2017.

[2] C. Xin, D. Jin, Y. Hu, L. Yang, R. Li, L. Wang, Z. Ren, D. Wang, S. Ji, K. Hu *et al.*, "Environmentally adaptive shape-morphing microrobots for localized cancer cell treatment," *ACS nano*, vol. 15, no. 11, pp. 18 048–18 059, 2021.

[3] J. G. Lee, R. R. Raj, N. B. Day, and C. W. Shields IV, "Microrobots for biomedicine: unsolved challenges and opportunities for translation," *ACS nano*, vol. 17, no. 15, pp. 14 196–14 204, 2023.

[4] L. Dekanovsky, B. Khezri, Z. Rottnerova, F. Novotny, J. Plutnar, and M. Pumera, "Chemically programmable microrobots weaving a web from hormones," *Nature Machine Intelligence*, vol. 2, no. 11, pp. 711–718, 2020.

[5] P. Mayorga-Burrezo, C. C. Mayorga-Martinez, and M. Pumera, "Photocatalysis dramatically influences motion of magnetic microrobots: Application to removal of microplastics and dyes," *Journal of Colloid and Interface Science*, vol. 643, pp. 447–454, 2023.

[6] H. Wang, Y. Jing, J. Yu, B. Ma, M. Sui, Y. Zhu, L. Dai, S. Yu, M. Li, and L. Wang, "Micro/nanorobots for remediation of water resources and aquatic life," *Frontiers in Bioengineering and Biotechnology*, vol. 11, p. 1312074, 2023.

[7] S. A. Hussain, S. Ward, O. Mahdavipour, R. Majumdar, and I. Paprotny, "Untethered microscale flight: Mechanisms and platforms for future aerial mems microrobots," in *Next-Generation Robotics II; and Machine Intelligence and Bio-inspired Computation: Theory and Applications IX*, vol. 9494. SPIE, 2015, pp. 108–119.

[8] N. Bolotnik, V. Chashchukhin, V. G. Gradetsky, D. Kozlov, I. Smirnov, A. Sukhanov, and A. Zhukov, "Design of mobile microrobots with thermomechanical actuators," in *2015 12th International Conference on Informatics in Control, Automation and Robotics (ICINCO)*, vol. 2. IEEE, 2015, pp. 252–258.

[9] D. S. Drew, N. O. Lambert, C. B. Schindler, and K. S. Pister, "Toward controlled flight of the ionocraft: a flying microrobot using electrohydrodynamic thrust with onboard sensing and no moving parts," *IEEE Robotics and Automation Letters*, vol. 3, no. 4, pp. 2807–2813, 2018.

[10] Y. Xiao, J. Zhang, B. Fang, X. Zhao, and N. Hao, "Acoustics-actuated microrobots," *Micromachines*, vol. 13, no. 3, p. 481, 2022.

[11] A. Aghakhani, A. Pena-Francesch, U. Bozuyuk, H. Cetin, P. Wrede, and M. Sitti, "High shear rate propulsion of acoustic microrobots in complex biological fluids," *Science Advances*, vol. 8, no. 10, p. eabm5126, 2022.

[12] Y. Deng, A. Paskert, Z. Zhang, R. Wittkowski, and D. Ahmed, "An acoustically controlled helical microrobot," *Science Advances*, vol. 9, no. 38, p. eadh5260, 2023.

[13] S. Nocentini, C. Parmeggiani, D. Martella, and D. S. Wiersma, "Optically driven soft micro robotics," *Advanced Optical Materials*, vol. 6, no. 14, p. 1800207, 2018.

[14] D. Zhang, F. P.-W. Lo, J.-Q. Zheng, W. Bai, G.-Z. Yang, and B. Lo, "Data-driven microscopic pose and depth estimation for optical microrobot manipulation," *Acs Photonics*, vol. 7, no. 11, pp. 3003–3014, 2020.

[15] A.-I. Bunea, D. Martella, S. Nocentini, C. Parmeggiani, R. Taboryski, and D. S. Wiersma, "Light-powered microrobots: challenges and opportunities for hard and soft responsive microswimmers," *Advanced Intelligent Systems*, vol. 3, no. 4, p. 2000256, 2021.

[16] H. Zhou, C. C. Mayorga-Martinez, S. Pané, L. Zhang, and M. Pumera, "Magnetically driven micro and nanorobots," *Chemical Reviews*, vol. 121, no. 8, pp. 4999–5041, 2021.

[17] H. Shen, S. Cai, Z. Wang, Z. Ge, and W. Yang, "Magnetically driven microrobots: Recent progress and future development," *Materials & Design*, p. 111735, 2023.

[18] C. Allard, "Adaptable navigation of magnetic microrobots," *Nature Reviews Materials*, pp. 1–1, 2024.

[19] F. Ullrich, C. Bergeles, J. Pokki, O. Ergeneman, S. Erni, G. Chatzipirpiridis, S. Pané, C. Framme, and B. J. Nelson, "Mobility experiments with microrobots for minimally invasive intraocular surgery," *Investigative ophthalmology & visual science*, vol. 54, no. 4, pp. 2853–2863, 2013.

[20] H. Banerjee, S. Shen, and H. Ren, "Magnetically actuated minimally invasive microbots for biomedical applications," *Electromagnetic Actuation and Sensing in Medical Robotics*, pp. 11–41, 2018.

[21] R. Chen, D. Folio, and A. Ferreira, "Study of robotized electromagnetic actuation system for magnetic microrobots devoted to minimally invasive ophthalmic surgery," in *2019 International Symposium on Medical Robotics (ISMR)*. IEEE, 2019, pp. 1–7.

[22] S. Jeon, S. H. Park, E. Kim, J.-y. Kim, S. W. Kim, and H. Choi, "A magnetically powered stem cell-based microrobot for minimally invasive stem cell delivery via the intranasal pathway in a mouse brain," *Advanced Healthcare Materials*, vol. 10, no. 19, p. 2100801, 2021.

[23] O. Koochakianfard, M. Sadedel, and M. Alizadeh, "Behavior-based navigation of in vivo magnetic micro robots in minimally invasive surgeries," in *2023 11th RSI International Conference on Robotics and Mechatronics (ICRoM)*. IEEE, 2023, pp. 451–456.

[24] V. Magdanz, I. S. Khalil, J. Simmchen, G. P. Furtado, S. Mohanty, J. Gebauer, H. Xu, A. Klingner, A. Aziz, M. Medina-Sánchez *et al.*, "Ironsperm: Sperm-templated soft magnetic microrobots," *Science advances*, vol. 6, no. 28, p. eaba5855, 2020.

[25] I. S. Khalil, A. Klingner, Y. Hamed, Y. S. Hassan, and S. Misra, "Controlled noncontact manipulation of nonmagnetic untethered mi-

crobeads orbiting two-tailed soft microrobot," *IEEE transactions on robotics*, vol. 36, no. 4, pp. 1320–1332, 2020.

[26] J. Liu, S. Yu, B. Xu, Z. Tian, H. Zhang, K. Liu, X. Shi, Z. Zhao, C. Liu, X. Lin *et al.*, "Magnetically propelled soft microrobot navigating through constricted microchannels," *Applied Materials Today*, vol. 25, p. 101237, 2021.

[27] M. Eshaghi, M. Ghasemi, and K. Khorshidi, "Design, manufacturing and applications of small-scale magnetic soft robots," *Extreme Mechanics Letters*, vol. 44, p. 101268, 2021.

[28] Y. Kim and X. Zhao, "Magnetic soft materials and robots," *Chemical reviews*, vol. 122, no. 5, pp. 5317–5364, 2022.

[29] G.-L. Jiang, Y.-H. Guu, C.-N. Lu, P.-K. Li, H.-M. Shen, L.-S. Lee, J. A. Yeh, and M. T.-K. Hou, "Development of rolling magnetic microrobots," *Journal of Micromechanics and Microengineering*, vol. 20, no. 8, p. 085042, 2010.

[30] C. Chautems, B. Zeydan, S. Charreyron, G. Chatzipirpiridis, S. Pané, and B. J. Nelson, "Magnetically powered microrobots: a medical revolution underway?" *European Journal of Cardio-Thoracic Surgery*, vol. 51, no. 3, pp. 405–407, 2017.

[31] J. Li, X. Li, T. Luo, R. Wang, C. Liu, S. Chen, D. Li, J. Yue, S.-h. Cheng, and D. Sun, "Development of a magnetic microrobot for carrying and delivering targeted cells," *Science Robotics*, vol. 3, no. 19, 2018.

[32] X. Wang, C. Hu, S. Pane, and B. J. Nelson, "Dynamic modeling of magnetic helical microrobots," *IEEE Robotics and Automation Letters*, 2021.

[33] C. Xin, L. Yang, J. Li, Y. Hu, D. Qian, S. Fan, K. Hu, Z. Cai, H. Wu, D. Wang *et al.*, "Conical hollow microhelices with superior swimming capabilities for targeted cargo delivery," *Advanced Materials*, vol. 31, no. 25, p. 1808226, 2019.

[34] J. E. Quispe, A. Bolopion, P. Renaud, and S. Régnier, "Enhancing swimming and pumping performance of helical swimmers at low

reynolds numbers," *IEEE Robotics and Automation Letters*, vol. 6, no. 4, pp. 6860–6867, 2021.

[35] Y. Kusuda, "A further step beyond wireless capsule endoscopy," *Sensor Review*, vol. 25, no. 4, pp. 259–260, 2005.

[36] J. Guo, S. Guo, X. Wei, and Y. Wang, "Development of wireless endoscope with symmetrical motion characteristics," *International journal of advanced robotic systems*, vol. 11, no. 9, p. 148, 2014.

[37] J. Leclerc, H. Zhao, and A. T. Becker, "3d control of rotating millimeter-scale swimmers through obstacles," in *2019 International Conference on Robotics and Automation (ICRA)*. IEEE, 2019, pp. 8890–8896.

[38] S. Lee, S. Lee, S. Kim, C.-H. Yoon, H.-J. Park, J.-y. Kim, and H. Choi, "Fabrication and characterization of a magnetic drilling actuator for navigation in a three-dimensional phantom vascular network," *Scientific reports*, vol. 8, no. 1, pp. 1–9, 2018.

[39] I. C. Yasa, H. Ceylan, U. Bozuyuk, A.-M. Wild, and M. Sitti, "Elucidating the interaction dynamics between microswimmer body and immune system for medical microrobots," *Science Robotics*, vol. 5, no. 43, p. eaaz3867, 2020.

[40] L. Li and S. E. Spagnolie, "Swimming and pumping by helical waves in viscous and viscoelastic fluids," *Physics of Fluids*, vol. 27, pp. 021 902–1–021 902–23, February 2015.

[41] D. Li, M. Jeong, E. Oren, T. Yu, and T. Qiu, "A helical microrobot with an optimized propeller-shape for propulsion in viscoelastic biological media," *Robotics*, vol. 8, no. 4, p. 87, 2019.

[42] Y. Jia, Z. Zhu, X. Jing, J. Lin, and M. Lu, "Fabrication and performance evaluation of magnetically driven double curved conical ribbon micro-helical robot," *Materials & Design*, vol. 226, p. 111651, 2023.

[43] C. Peters, O. Ergeneman, P. D. W. García, M. Müller, S. Pané, B. J. Nelson, and C. Hierold, "Superparamagnetic twist-type actuators

with shape-independent magnetic properties and surface functionalization for advanced biomedical applications," *Advanced Functional Materials*, vol. 24, no. 33, pp. 5269–5276, 2014.

[44] E. M. Purcell, "Life at low reynolds number," *American journal of physics*, vol. 45, no. 1, pp. 3–11, 1977.

[45] ——, "The efficiency of propulsion by a rotating flagellum," *Proceedings of the National Academy of Sciences*, vol. 94, no. 21, pp. 11 307–11 311, 1997.

[46] J. J. Abbott, K. E. Peyer, M. C. Lagomarsino, L. Zhang, L. Dong, I. K. Kaliakatsos, and B. J. Nelson, "How should microrobots swim?" *The international journal of Robotics Research*, vol. 28, no. 11-12, pp. 1434–1447, 2009.

[47] J. Choi, H. Choi, K. Cha, J.-o. Park, and S. Park, "Two-dimensional locomotive permanent magnet using electromagnetic actuation system with two pairs stationary coils," in *2009 IEEE International Conference on Robotics and Biomimetics (ROBIO)*. IEEE, 2009, pp. 1166–1171.

[48] A. Ramos-Sebastian, J. S. Lee, and S. H. Kim, "Multimodal locomotion of magnetic droplet robots using orthogonal pairs of coils," *Advanced Intelligent Systems*, vol. 5, no. 9, p. 2300133, 2023.

[49] X. Tang, Y. Li, X. Liu, D. Liu, Z. Chen, and T. Arai, "Vision-based automated control of magnetic microrobots," *Micromachines*, vol. 13, no. 2, p. 337, 2022.

[50] M. Sokolich, D. Rivas, Y. Yang, M. Duey, and S. Das, "Modmag: A modular magnetic micro-robotic manipulation device," *MethodsX*, vol. 10, p. 102171, 2023.

[51] A. W. Mahoney, N. D. Nelson, E. M. Parsons, and J. J. Abbott, "Non-ideal behaviors of magnetically driven screws in soft tissue," in *2012 IEEE/RSJ International Conference on Intelligent Robots and Systems*. IEEE, 2012, pp. 3559–3564.

[52] L. Yang, Q. Wang, C.-I. Vong, and L. Zhang, "A miniature flexible-link magnetic swimming robot with two vibration modes: design,

modeling and characterization," *IEEE Robotics and Automation Letters*, vol. 2, no. 4, pp. 2024–2031, 2017.

[53] J. Jiang, L. Yang, and L. Zhang, "Closed-loop control of a helmholtz coil system for accurate actuation of magnetic microrobot swarms," *IEEE Robotics and Automation Letters*, vol. 6, no. 2, pp. 827–834, 2021.

[54] A. Ramos-Sebastian and S. H. Kim, "Magnetic force-propelled 3d locomotion control for magnetic microrobots via simple modified three-axis helmholtz coil system," *Ieee Access*, vol. 9, pp. 128 755–128 764, 2021.

[55] H. Shen, S. Cai, Z. Wang, Z. Yuan, H. Yu, and W. Yang, "A programmable inchworm-inspired soft robot powered by a rotating magnetic field," *Journal of Bionic Engineering*, vol. 20, no. 2, pp. 506–514, 2023.

[56] L. Wang, M. Zhao, Y. He, S. Ding, and L. Sun, "Fish-like magnetic microrobots for microparts transporting at liquid surfaces," *Soft Matter*, vol. 19, no. 16, pp. 2883–2890, 2023.

[57] I. S. Khalil, V. Magdanz, S. Sanchez, O. G. Schmidt, L. Abelmann, and S. Misra, "Magnetic control of potential microrobotic drug delivery systems: nanoparticles, magnetotactic bacteria and self-propelled microjets," in *2013 35th Annual International Conference of the IEEE Engineering in Medicine and Biology Society (EMBC)*. IEEE, 2013, pp. 5299–5302.

[58] J. Sikorski, I. Dawson, A. Denasi, E. E. Hekman, and S. Misra, "Introducing bigmag—a novel system for 3d magnetic actuation of flexible surgical manipulators," in *2017 IEEE International Conference on Robotics and Automation (ICRA)*. IEEE, 2017, pp. 3594–3599.

[59] V. K. Venkiteswaran, D. K. Tan, and S. Misra, "Tandem actuation of legged locomotion and grasping manipulation in soft robots using magnetic fields," *Extreme Mechanics Letters*, vol. 41, p. 101023, 2020.

[60] Z. Yang, L. Yang, and L. Zhang, "3-d visual servoing of magnetic miniature swimmers using parallel mobile coils," *IEEE Transactions on Medical Robotics and Bionics*, vol. 2, no. 4, pp. 608–618, 2020.

[61] A. Alasli, L. Çetin, N. Akçura, A. Kahveci, F. C. Can, and Ö. Tamer, "Electromagnet design for untethered actuation system mounted on robotic manipulator," *Sensors and Actuators A: Physical*, vol. 285, pp. 550–565, 2019.

[62] V. K. Venkiteswaran and S. Misra, "Towards gradient-based actuation of magnetic soft robots using a six-coil electromagnetic system," in *2020 IEEE/RSJ International Conference on Intelligent Robots and Systems (IROS)*. IEEE, 2020, pp. 8633–8639.

[63] A. J. A. de Oliveira, J. Batista, S. Misra, and V. K. Venkiteswaran, "Ultrasound tracking and closed-loop control of a magnetically-actuated biomimetic soft robot," in *2022 IEEE/RSJ International Conference on Intelligent Robots and Systems (IROS)*. IEEE, 2022, pp. 3422–3428.

[64] L. Yang, X. Du, E. Yu, D. Jin, and L. Zhang, "Deltamag: An electromagnetic manipulation system with parallel mobile coils," in *2019 International Conference on Robotics and Automation (ICRA)*. IEEE, 2019, pp. 9814–9820.

[65] L. Yang, Z. Yang, M. Zhang, J. Jiang, H. Yang, and L. Zhang, "Optimal parameter design and microrobotic navigation control of parallel-mobile-coil systems," *IEEE Transactions on Automation Science and Engineering*, 2022.

[66] Z. Yang, L. Yang, and L. Zhang, "Autonomous navigation of magnetic microrobots in a large workspace using mobile-coil system," *IEEE/ASME Transactions on Mechatronics*, vol. 26, no. 6, pp. 3163–3174, 2021.

[67] X. Du, L. Yang, J. Yu, K. F. Chan, P. W. Y. Chiu, and L. Zhang, "Robomag: A magnetic actuation system based on mobile electromagnetic coils with tunable working space," in *2020 5th International Conference on Advanced Robotics and Mechatronics (ICARM)*. IEEE, 2020, pp. 125–131.

[68] X. Du, Q. Wang, D. Jin, P. W. Y. Chiu, C. P. Pang, K. K. L. Chong, and L. Zhang, "Real-time navigation of an untethered miniature robot using mobile ultrasound imaging and magnetic actuation

systems," *IEEE Robotics and Automation Letters*, vol. 7, no. 3, pp. 7668–7675, 2022.

[69] H. Wang, J. Cui, K. Tian, and Y. Han, "Three-degrees-of-freedom orientation manipulation of small untethered robots with a single anisotropic soft magnet," *Nature Communications*, vol. 14, no. 1, p. 7491, 2023.

[70] B. Ye, Y. Fu, S. Zhang, H. Wang, G. Fang, W. Zha, and A. K. Dwivedi, "Closed-loop active control of the magnetic capsule endoscope with a robotic arm based on image navigation," *Journal of Magnetism and Magnetic Materials*, vol. 565, p. 170268, 2023.

[71] A. W. Mahoney and J. J. Abbott, "5-dof manipulation of an untethered magnetic device in fluid using a single permanent magnet." in *Robotics: Science and Systems*. Citeseer, 2014.

[72] S. E. Wright, A. W. Mahoney, K. M. Popek, and J. J. Abbott, "The spherical-actuator-magnet manipulator: A permanent-magnet robotic end-effector," *IEEE Transactions on Robotics*, vol. 33, no. 5, pp. 1013–1024, 2017.

[73] T. da Veiga, G. Pittiglio, M. Brockdorff, J. H. Chandler, and P. Valdastri, "Six-degree-of-freedom localization under multiple permanent magnets actuation," *IEEE Robotics and Automation Letters*, 2023.

[74] A. Hosney, A. Klingner, S. Misra, and I. S. Khalil, "Propulsion and steering of helical magnetic microrobots using two synchronized rotating dipole fields in three-dimensional space," in *2015 IEEE/RSJ International Conference on Intelligent Robots and Systems (IROS)*. IEEE, 2015, pp. 1988–1993.

[75] D. Son, M. C. Ugurlu, and M. Sitti, "Permanent magnet array–driven navigation of wireless millirobots inside soft tissues," *Science Advances*, vol. 7, no. 43, p. eabi8932, 2021.

[76] P. Ryan and E. Diller, "Magnetic actuation for full dexterity microrobotic control using rotating permanent magnets," *IEEE Transactions on Robotics*, vol. 33, no. 6, pp. 1398–1409, 2017.

[77] M. Yousefi and H. Nejat Pishkenari, "Independent position control of two identical magnetic microrobots in a plane using rotating permanent magnets," *Journal of Micro-Bio Robotics*, vol. 17, no. 1, pp. 59–67, 2021.

[78] R. Khalesi, M. Yousefi, H. N. Pishkenari, and G. Vossoughi, "Robust independent and simultaneous position control of multiple magnetic microrobots by sliding mode controller," *Mechatronics*, vol. 84, p. 102776, 2022.

[79] A. Zarrouk, K. Belharet, and O. Tahri, "Vision-based magnetic actuator positioning for wireless control of microrobots," *Robotics and Autonomous Systems*, vol. 124, p. 103366, 2020.

[80] S. Pane, V. Iacovacci, E. Sinibaldi, and A. Menciassi, "Real-time imaging and tracking of microrobots in tissues using ultrasound phase analysis," *Applied Physics Letters*, vol. 118, no. 1, 2021.

[81] Q. Wang, Y. Tian, X. Du, H. Ko, B. Y. M. Ip, T. W. H. Leung, S. C. H. Yu, and L. Zhang, "Magnetic navigation of collective cell microrobots in blood under ultrasound doppler imaging," *IEEE/ASME Transactions on Mechatronics*, vol. 27, no. 5, pp. 3174–3185, 2021.

[82] Z. Yang, L. Yang, M. Zhang, N. Xia, and L. Zhang, "Ultrasound-guided wired magnetic microrobot with active steering and ejectable tip," *IEEE Transactions on Industrial Electronics*, vol. 70, no. 1, pp. 614–623, 2022.

[83] C. Li, S. Misra, and I. S. Khalil, "Navigation of untethered small-scale helical devices using magnetic system under ultrasound guidance," *IEEE Transactions on Medical Robotics and Bionics*, 2023.

[84] Y. Yan, W. Jing, and M. Mehrmohammadi, "Photoacoustic imaging to track magnetic-manipulated micro-robots in deep tissue," *Sensors*, vol. 20, no. 10, p. 2816, 2020.

[85] L. Xie, X. Pang, X. Yan, Q. Dai, H. Lin, J. Ye, Y. Cheng, Q. Zhao, X. Ma, X. Zhang *et al.*, "Photoacoustic imaging-trackable magnetic microswimmers for pathogenic bacterial infection treatment," *ACS nano*, vol. 14, no. 3, pp. 2880–2893, 2020.

[86] D. Li, Y. Zhang, C. Liu, J. Chen, D. Sun, and L. Wang, "Review of photoacoustic imaging for microrobots tracking in vivo," *Chinese Optics Letters*, vol. 19, no. 11, p. 111701, 2021.

[87] N. Talebloo, M. Gudi, N. Robertson, and P. Wang, "Magnetic particle imaging: current applications in biomedical research," *Journal of Magnetic Resonance Imaging*, vol. 51, no. 6, pp. 1659–1668, 2020.

[88] A. C. Bakenecker, A. von Gladiss, H. Schwenke, A. Behrends, T. Friedrich, K. Lüdtke-Buzug, A. Neumann, J. Barkhausen, F. Wegner, and T. M. Buzug, "Navigation of a magnetic micro-robot through a cerebral aneurysm phantom with magnetic particle imaging," *Scientific reports*, vol. 11, no. 1, p. 14082, 2021.

[89] M. Irfan and N. Dogan, "Comprehensive evaluation of magnetic particle imaging (mpi) scanners for biomedical applications," *IEEE Access*, vol. 10, pp. 86 718–86 732, 2022.

[90] D. Folio and A. Ferreira, "Two-dimensional robust magnetic resonance navigation of a ferromagnetic microrobot using pareto optimality," *IEEE Transactions on Robotics*, vol. 33, no. 3, pp. 583–593, 2017.

[91] S. Martel, "Combining pulsed and dc gradients in a clinical mri-based microrobotic platform to guide therapeutic magnetic agents in the vascular network," *International Journal of Advanced Robotic Systems*, vol. 10, no. 1, p. 30, 2013.

[92] M. E. Tiryaki, S. O. Demir, and M. Sitti, "Deep learning-based 3d magnetic microrobot tracking using 2d mr images," *IEEE Robotics and Automation Letters*, vol. 7, no. 3, pp. 6982–6989, 2022.

[93] H. Choi, G. Go, C. Lee, S. Y. Ko, S. Jeong, K. Kwon, J.-O. Park, and S. Park, "Electromagnetic actuation system for locomotive intravascular therapeutic microrobot," in *5th IEEE RAS/EMBS International Conference on Biomedical Robotics and Biomechatronics*. IEEE, 2014, pp. 831–834.

[94] K. T. Nguyen, G. Go, Z. Jin, B. A. Darmawan, A. Yoo, S. Kim, M. Nan, S. B. Lee, B. Kang, C.-S. Kim *et al.*, "A magnetically

guided self-rolled microrobot for targeted drug delivery, real-time x-ray imaging, and microrobot retrieval," *Advanced Healthcare Materials*, vol. 10, no. 6, p. 2001681, 2021.

[95] B. A. Darmawan, D. Gong, H. Park, S. Jeong, G. Go, S. Kim, K. T. Nguyen, S. Zheng, M. Nan, D. Bang *et al.*, "Magnetically controlled reversible shape-morphing microrobots with real-time x-ray imaging for stomach cancer applications," *Journal of Materials Chemistry B*, vol. 10, no. 23, pp. 4509–4518, 2022.

[96] D. Li, D. Dong, W. Lam, L. Xing, T. Wei, and D. Sun, "Automated in vivo navigation of magnetic-driven microrobots using oct imaging feedback," *IEEE Transactions on Biomedical Engineering*, vol. 67, no. 8, pp. 2349–2358, 2019.

[97] G. Géron, C. Prelle, H. Al Hajjar, J. Terrien, and M. U. Khan, "Characterization of a magnetic localization method based on hall effect sensor array for microrobot position tracking," *Journal of Micro and Bio Robotics*, vol. 18, no. 1, pp. 1–13, 2022.

[98] K. Li, Y. Xu, Z. Zhao, and M. Q.-H. Meng, "External and internal sensor fusion based localization strategy for 6-dof pose estimation of a magnetic capsule robot," *IEEE Robotics and Automation Letters*, vol. 7, no. 3, pp. 6878–6885, 2022.

[99] Q. Shi, T. Liu, S. Song, J. Wang, and M. Q.-H. Meng, "An optically aided magnetic tracking approach for magnetically actuated capsule robot," *IEEE Transactions on Instrumentation and Measurement*, vol. 70, pp. 1–9, 2021.

[100] F. Gao, X. Feng, and Y. Zheng, "Coherent photoacoustic-ultrasound correlation and imaging," *IEEE Transactions on Biomedical Engineering*, vol. 61, no. 9, pp. 2507–2512, 2014.

[101] D. Son, S. Yim, and M. Sitti, "A 5-d localization method for a magnetically manipulated untethered robot using a 2-d array of hall-effect sensors," *IEEE/ASME transactions on mechatronics*, vol. 21, no. 2, pp. 708–716, 2015.

[102] C. Vergne, J. Inácio, T. Quirin, D. Sargent, M. Madec, and J. Pascal, "Tracking of a magnetically navigated millirobot with a magnetic field camera," *IEEE Sensors Journal*, 2023.

[103] S. S. Vedaei and K. A. Wahid, "A localization method for wireless capsule endoscopy using side wall cameras and imu sensor," *Scientific reports*, vol. 11, no. 1, p. 11204, 2021.

[104] M. Turan, Y. Almalioglu, H. B. Gilbert, A. E. Sari, U. Soylu, and M. Sitti, "Endo-vmfusenet: A deep visual-magnetic sensor fusion approach for endoscopic capsule robots," in *2018 IEEE international conference on robotics and automation (ICRA)*. IEEE, 2018, pp. 5386–5392.

[105] Y. Yan, W. Jing, and M. Mehrmohammadi, "Submillimeter magnetic microrobot tracking using an integrated ultrasound and photoacoustic imaging system," in *2019 IEEE International Ultrasonics Symposium (IUS)*. IEEE, 2019, pp. 1057–1060.

[106] G. Bao, K. Pahlavan, and L. Mi, "Hybrid localization of microrobotic endoscopic capsule inside small intestine by data fusion of vision and rf sensors," *IEEE Sensors Journal*, vol. 15, no. 5, pp. 2669–2678, 2014.

[107] A. Denasi, F. Khan, K. J. Boskma, M. Kaya, C. Hennersperger, R. Göbl, M. Tirindelli, N. Navab, and S. Misra, "An observer-based fusion method using multicore optical shape sensors and ultrasound images for magnetically-actuated catheters," in *2018 IEEE International Conference on Robotics and Automation (ICRA)*. IEEE, 2018, pp. 50–57.

[108] F. Qin, J. Wu, D. Fu, Y. Feng, C. Gao, D. Xie, S. Fu, S. Liu, D. A. Wilson, and F. Peng, "Magnetically driven helical hydrogel micromotor for tumor dna detection," *Applied Materials Today*, vol. 27, p. 101456, 2022.

[109] H. Lee, D.-i. Kim, S.-h. Kwon, and S. Park, "Magnetically actuated drug delivery helical microrobot with magnetic nanoparticle retrieval ability," *ACS applied materials & interfaces*, vol. 13, no. 17, pp. 19 633–19 647, 2021.

[110] I. S. Khalil, A. F. Tabak, K. Sadek, D. Mahdy, N. Hamdi, and M. Sitti, "Rubbing against blood clots using helical robots: Modeling and in vitro experimental validation," *IEEE Robotics and Automation Letters*, vol. 2, no. 2, pp. 927–934, 2017.

[111] I. S. Khalil, D. Mahdy, A. El Sharkawy, R. R. Moustafa, A. F. Tabak, M. E. Mitwally, S. Hesham, N. Hamdi, A. Klingner, A. Mohamed *et al.*, "Mechanical rubbing of blood clots using helical robots under ultrasound guidance," *IEEE Robotics and Automation Letters*, vol. 3, no. 2, pp. 1112–1119, 2018.

[112] I. S. Khalil, A. Adel, D. Mahdy, M. M. Micheal, M. Mansour, N. Hamdi, and S. Misra, "Magnetic localization and control of helical robots for clearing superficial blood clots," *APL bioengineering*, vol. 3, no. 2, p. 026104, 2019.

[113] L. Yang, M. Zhang, H. Yang, Z. Yang, and L. Zhang, "Hybrid magnetic force and torque actuation of miniature helical robots using mobile coils to accelerate blood clot removal," in *2021 IEEE/RSJ International Conference on Intelligent Robots and Systems (IROS)*. IEEE, 2021, pp. 7476–7482.

[114] F. Qiu, S. Fujita, R. Mhanna, L. Zhang, B. R. Simona, and B. J. Nelson, "Magnetic helical microswimmers functionalized with lipoplexes for targeted gene delivery," *Advanced Functional Materials*, vol. 25, no. 11, pp. 1666–1671, 2015.

[115] K. T. Nguyen, S. Zheng, C.-S. Kim, B. Kang, D. Bang, J.-O. Park, E. Choi *et al.*, "A magnetically-controlled 3d-printed helical microrobot for application in photothermal treatment of cancer cells," in *2022 9th IEEE RAS/EMBS International Conference for Biomedical Robotics and Biomechatronics (BioRob)*. IEEE, 2022, pp. 1–5.

[116] A. Caciagli, R. J. Baars, A. P. Philipse, and B. W. Kuipers, "Exact expression for the magnetic field of a finite cylinder with arbitrary uniform magnetization," *Journal of Magnetism and Magnetic Materials*, vol. 456, pp. 423–432, 2018.

[117] B. J. Nelson, I. K. Kaliakatsos, and J. J. Abbott, "Microrobots for minimally invasive medicine," *Annual review of biomedical engineering*, vol. 12, pp. 55–85, 2010.

[118] D. Jang, J. Jeong, H. Song, and S. K. Chung, "Targeted drug delivery technology using untethered microrobots: A review," *Journal of Micromechanics and Microengineering*, vol. 29, no. 5, p. 053002, 2019.

[119] Z. Cai, Q. Fu, S. Zhang, C. Fan, X. Zhang, J. Guo, and S. Guo, "Performance evaluation of a magnetically driven microrobot for targeted drug delivery," *Micromachines*, vol. 12, no. 10, p. 1210, 2021.

[120] L. Yang, Q. Wang, and L. Zhang, "Model-free trajectory tracking control of two-particle magnetic microrobot," *IEEE Transactions on Nanotechnology*, vol. 17, no. 4, pp. 697–700, 2018.

[121] L. Ricotti and A. Menciassi, "Nanotechnology in biorobotics: opportunities and challenges," *Journal of Nanoparticle Research*, vol. 17, no. 2, pp. 1–10, 2015.

[122] Y. Wang, D.-F. Wang, H.-F. Wang, J.-W. Wang, J.-Z. Pan, X.-G. Guo, and Q. Fang, "A microfluidic robot for rare cell sorting based on machine vision identification and multi-step sorting strategy," *Talanta*, vol. 226, p. 122136, 2021.

[123] J.-W. Wang, J. Gao, H.-F. Wang, Q.-H. Jin, B. Rao, W. Deng, Y. Cao, M. Lei, S. Ye, and Q. Fang, "Miniaturization of the whole process of protein crystallographic analysis by a microfluidic droplet robot: from nanoliter-scale purified proteins to diffraction-quality crystals," *Analytical chemistry*, vol. 91, no. 15, pp. 10 132–10 140, 2019.

[124] D. Mahdy, R. Reda, N. Hamdi, and I. S. Khalil, "Ultrasound-guided minimally invasive grinding for clearing blood clots: promises and challenges," *IEEE Instrumentation & Measurement Magazine*, vol. 21, no. 2, pp. 10–14, 2018.

[125] A. Oulmas, N. Andreff, and S. Régnier, "3d closed-loop motion control of swimmer with flexible flagella at low reynolds numbers," in

2017 IEEE/RSJ International Conference on Intelligent Robots and Systems (IROS). IEEE, 2017, pp. 1877–1882.

[126] T. Xu, G. Hwang, N. Andreff, and S. Régnier, "Planar path following of 3-d steering scaled-up helical microswimmers," *IEEE Transactions on Robotics*, vol. 31, no. 1, pp. 117–127, 2015.

[127] A. Oulmas, N. Andreff, and S. Régnier, "Chained formulation of 3d path following for nonholonomic autonomous robots in a serret-frenet frame," in *2016 American Control Conference (ACC)*. IEEE, 2016, pp. 7275–7280.

[128] C. Park, J. Kim, S.-J. Kim, and J. Yoo, "Development of a permanent magnet type micro-robot actuated by external electromagnetic system," *Microsystem Technologies*, vol. 21, no. 6, pp. 1257–1265, 2015.

[129] I. S. Khalil, L. Abelmann, and S. Misra, "Magnetic-based motion control of paramagnetic microparticles with disturbance compensation," *IEEE Transactions on Magnetics*, vol. 50, no. 10, pp. 1–10, 2014.

[130] F. Ongaro, S. Pane, S. Scheggi, and S. Misra, "Design of an electromagnetic setup for independent three-dimensional control of pairs of identical and nonidentical microrobots," *IEEE transactions on robotics*, vol. 35, no. 1, pp. 174–183, 2018.

[131] L. Zheng, Y. Jia, D. Dong, W. Lam, D. Li, H. Ji, and D. Sun, "3d navigation control of untethered magnetic microrobot in centimeter-scale workspace based on field-of-view tracking scheme," *IEEE Transactions on Robotics*, 2021.

[132] H. Janssen, E. Ter Maten, and D. Van Houwelingen, "Simulation of coupled electromagnetic and heat dissipation problems," *IEEE transactions on magnetics*, vol. 30, no. 5, pp. 3331–3334, 1994.

[133] S. Erni, S. Schürle, A. Fakhraee, B. E. Kratochvil, and B. J. Nelson, "Comparison, optimization, and limitations of magnetic manipulation systems," *Journal of Micro-Bio Robotics*, vol. 8, no. 3, pp. 107–120, 2013.

[134] T. W. Fountain, P. V. Kailat, and J. J. Abbott, "Wireless control of magnetic helical microrobots using a rotating-permanent-magnet manipulator," in *2010 IEEE International Conference on Robotics and Automation*. IEEE, 2010, pp. 576–581.

[135] A. W. Mahoney and J. J. Abbott, "Generating rotating magnetic fields with a single permanent magnet for propulsion of untethered magnetic devices in a lumen," *IEEE Transactions on Robotics*, vol. 30, no. 2, pp. 411–420, 2013.

[136] N. D. Nelson and J. J. Abbott, "Generating two independent rotating magnetic fields with a single magnetic dipole for the propulsion of untethered magnetic devices," in *2015 IEEE International Conference on Robotics and Automation (ICRA)*. IEEE, 2015, pp. 4056–4061.

[137] A. W. Mahoney, S. E. Wright, and J. J. Abbott, "Managing the attractive magnetic force between an untethered magnetically actuated tool and a rotating permanent magnet," in *2013 IEEE International Conference on Robotics and Automation*. IEEE, 2013, pp. 5366–5371.

[138] W. Zhang, Y. Meng, and P. Huang, "A novel method of arraying permanent magnets circumferentially to generate a rotation magnetic field," *IEEE transactions on magnetics*, vol. 44, no. 10, pp. 2367–2372, 2008.

[139] T. Qiu, S. Palagi, J. Sachs, and P. Fischer, "Soft miniaturized linear actuators wirelessly powered by rotating permanent magnets," in *2018 IEEE International Conference on Robotics and Automation (ICRA)*. IEEE, 2018, pp. 3595–3600.

[140] I. S. Khalil, A. Alfar, A. F. Tabak, A. Klingner, S. Stramigioli, and M. Sitti, "Positioning of drug carriers using permanent magnet-based robotic system in three-dimensional space," in *2017 IEEE International Conference on Advanced Intelligent Mechatronics (AIM)*. IEEE, 2017, pp. 1117–1122.

[141] A. W. Mahoney and J. J. Abbott, "Five-degree-of-freedom manipulation of an untethered magnetic device in fluid using a single permanent magnet with application in stomach capsule endoscopy," *The*

International Journal of Robotics Research, vol. 35, no. 1-3, pp. 129–147, 2016.

[142] B. Shapiro, K. Dormer, and I. B. Rutel, "A two-magnet system to push therapeutic nanoparticles," in *AIP conference proceedings*, vol. 1311, no. 1. NIH Public Access, 2010, p. 77.

[143] W. Amokrane, K. Belharet, and A. Ferreira, "Design and modeling of a two-magnet actuator for robotic micromanipulation," *Sensors and Actuators A: Physical*, vol. 316, p. 112391, 2020.

[144] M. Abbes, K. Belharet, H. Mekki, and G. Poisson, "Permanent magnets based actuator for microrobots navigation," in *2019 IEEE/RSJ International Conference on Intelligent Robots and Systems (IROS)*. IEEE, 2019, pp. 7062–7067.

[145] A. W. Mahoney and J. J. Abbott, "Managing magnetic force applied to a magnetic device by a rotating dipole field," *Applied Physics Letters*, vol. 99, no. 13, p. 134103, 2011.

[146] A. Hosney, J. Abdalla, I. S. Amin, N. Hamdi, and I. S. Khalil, "In vitro validation of clearing clogged vessels using microrobots," in *2016 6th IEEE International Conference on Biomedical Robotics and Biomechatronics (BioRob)*. IEEE, 2016, pp. 272–277.

[147] G. Pittiglio, M. Brockdorff, T. da Veiga, J. Davy, J. H. Chandler, and P. Valdastri, "Collaborative magnetic manipulation via two robotically actuated permanent magnets," *IEEE Transactions on Robotics*, 2022.

[148] F. Carpi and C. Pappone, "Stereotaxis niobe® magnetic navigation system for endocardial catheter ablation and gastrointestinal capsule endoscopy," *Expert review of medical devices*, vol. 6, no. 5, pp. 487–498, 2009.

[149] Z. Wang, A. Klingner, V. Magdanz, S. Misra, and I. S. Khalil, "Soft bio-microrobots: Toward biomedical applications," *Advanced Intelligent Systems*, p. 2300093, 2023.

[150] D. J. Bell, S. Leutenegger, K. M. Hammar, L. X. Dong, and B. J. Nelson, "Flagella-like propulsion for microrobots using a magnetic

nanocoil and a rotating electromagnetic field," in *Proceedings of the IEEE International Conference on Robotics and Automation (ICRA)*, April 2007, pp. 1128–1133.

[151] A. Ghosh and P. Fischer, "Controlled propulsion of artificial magnetic nanostructured propellers," *Nano Letters*, vol. 9, no. 6, pp. 2243–2245, May 2009.

[152] K. Ishiyama, K. I. Arai, M. Sendoh, and A. Yamazaki, "Spiral-type micro-machine for medical applications," *Journal of Micromechatronics*, vol. 2, no. 1, pp. 77–86, April 2002.

[153] B. J. Nelson, I. K. Kaliakatsos, and J. J. Abbott, "Microrobots for minimally invasive medicine," *Annual Review of Biomedical Engineering*, vol. 12, pp. 55–85, April 2010.

[154] L. Dong and B. J. Nelson, "Tutorial - robotics in the small part ii: nanorobotics," *IEEE Robotics and Automation Magazine*, vol. 14, no. 3, pp. 111–121, 2007.

[155] N. D. Nelson, J. Delacenserie, and J. J. Abbott, "An empirical study of the role of magnetic, geometric, and tissue properties on the turning radius of magnetically driven screws," in *Proceedings of the IEEE International Conference on Robotics and Automation (ICRA)*, Karlsruhe, Germany, May 2013, pp. 5352–5357.

[156] D. Schamel, A. G. Mark, J. G. Gibbs, C. Miksch, K. I. Morozov, A. M. Leshansky, and P. Fischer, "Nanopropellers and their actuation in complex viscoelastic media," *ACS Nano*, vol. 8, no. 9, pp. 8794–8801, June 2014.

[157] D. Walker, B. T. Käsdorf, H.-H. Jeong, O. Lieleg, and P. Fischer, "Enzymatically active biomimetic micropropellers for the penetration of mucin gels," *Science Advances*, vol. 1, no. 11, p. e1500501, December 2015.

[158] Z. Wu, J. Troll, H. Jeong, Q. Wei, M. Stang, F. Ziemssen, Z. Wang, M. Dong, S. Schnichels, T. Qiu, and P. Fischer, "A swarm of slippery micropropellers penetrates the vitreous body of the eye," *Science Advances*, vol. 4, no. 11, p. eaat4388, November 2018.

[159] C. Huang, T. Xu, J. Liu, L. Manamanchaiyaporn, and X. Wu, "Visual servoing of miniature magnetic film swimming robots for 3-d arbitrary path following," *IEEE Robotics and Automation Letters*, vol. 4, no. 4, pp. 4185–4191, 2019.

[160] T. Xu, Y. Guan, J. Liu, and X. Wu, "Image-based visual servoing of helical microswimmers for planar path following," *IEEE Transactions on Automation Science and Engineering*, vol. 17, no. 1, pp. 325–333, 2019.

[161] T. W. R. Fountain, P. V. Kailat, and J. J. Abbott, "Wireless control of magnetic helical microrobots using a rotating-permanent-magnet manipulator," in *Proceedings of the IEEE International Conference on Robotics and Automation (ICRA)*, Alaska, USA, May 2010, pp. 576–581.

[162] A. W. Mahoney, D. L. Cowan, K. M. Miller, and J. J. Abbott, "Control of untethered magnetically actuated tools using a rotating permanent magnet in any position," in *Proceedings of the IEEE International Conference on Robotics and Automation (ICRA)*, Minnesota, USA, May 2012, pp. 3375–3380.

[163] A. W. Mahoney and J. J. Abbott, "Control of untethered magnetically actuated tools with localization uncertainty using a rotating permanent magnet," in *Proceedings of the IEEE RAS/EMBS International Conference on Biomedical Robotics and Biomechatronics (BioRob)*, Rome, Italy, June 2012, pp. 1632–1637.

[164] P. Ryan and E. Diller, "Magnetic actuation for full dexterity microrobotic control using rotating permanent magnets," *Transactions on Robotics*, vol. 33, no. 6, pp. 1398–1409, December 2017.

[165] A. W. Mahoney and J. J. Abbott, "Managing magnetic force applied to a magnetic device by a rotating dipole field," *Applied Physics Letters*, vol. 99, September 2011.

[166] M. E. Alshafeei, A. Hosney, A. Klingner, S. Misra, and I. S. M. Khalil, "Magnetic-based motion control of a helical robot using two synchronized rotating dipole fields," in *Proceedings of the IEEE RAS/EMBS*

International Conference on Biomedical Robotics and Biomechatronics (BioRob), São Paulo, Brazil, August 2014, pp. 151–156.

[167] E. Lauga, "Propulsion in a viscoelastic fluid," *Physics of Fluids*, vol. 19, pp. 083 104–1–083 104–13, August 2007.

[168] Y. Sun, R. Pan, Y. Chen, Y. Wang, L. Sun, N. Wang, X. Ma, and G. P. Wang, "Efficient preparation of a magnetic helical carbon nanomotor for targeted anticancer drug delivery," *ACS Nanoscience Au*, 2022.

[169] E. B. Steager, M. Selman Sakar, C. Magee, M. Kennedy, A. Cowley, and V. Kumar, "Automated biomanipulation of single cells using magnetic microrobots," *The International Journal of Robotics Research*, vol. 32, no. 3, pp. 346–359, 2013.

[170] K. E. Peyer, S. Tottori, F. Qiu, L. Zhang, and B. J. Nelson, "Magnetic helical micromachines," *Chemistry–A European Journal*, vol. 19, no. 1, pp. 28–38, 2013.

[171] L. Wang, H. Xu, W. Zhai, B. Huang, and W. Rong, "Design and characterization of magnetically actuated helical swimmers at submillimeter-scale," *Journal of Bionic Engineering*, vol. 14, no. 1, pp. 26–33, 2017.

[172] F. Ullrich, F. Qiu, J. Pokki, T. Huang, S. Pané, and B. J. Nelson, "Swimming characteristics of helical microrobots in fibrous environments," in *2016 6th IEEE International Conference on Biomedical Robotics and Biomechatronics (BioRob)*. IEEE, 2016, pp. 470–475.

[173] H. C. Berg and L. Turner, "Movement of microorganisms in viscous environments," *Nature*, vol. 278, no. 5702, pp. 349–351, 1979.

[174] Y. Magariyama and S. Kudo, "A mathematical explanation of an increase in bacterial swimming speed with viscosity in linear-polymer solutions," *Biophysical journal*, vol. 83, no. 2, pp. 733–739, 2002.

[175] C. Ye, J. Liu, X. Wu, B. Wang, L. Zhang, Y. Zheng, and T. Xu, "Hydrophobicity influence on swimming performance of magnetically driven miniature helical swimmers," *Micromachines*, vol. 10, no. 3, p. 175, 2019.

[176] H. Zhou, G. Alici, T. D. Than, and W. Li, "Modeling and experimental characterization of propulsion of a spiral-type microrobot for medical use in gastrointestinal tract," *IEEE Transactions on Biomedical engineering*, vol. 60, no. 6, pp. 1751–1759, 2012.

[177] J. Leclerc, H. Zhao, D. Bao, and A. T. Becker, "In vitro design investigation of a rotating helical magnetic swimmer for combined 3-d navigation and blood clot removal," *IEEE Transactions on Robotics*, vol. 36, no. 3, pp. 975–982, 2020.

[178] N. D. Nelson, J. Delacenserie, and J. J. Abbott, "An empirical study of the role of magnetic, geometric, and tissue properties on the turning radius of magnetically driven screws," in *2013 IEEE International Conference on Robotics and Automation*. IEEE, 2013, pp. 5372–5377.

[179] A. W. Mahoney, D. L. Cowan, K. M. Miller, and J. J. Abbott, "Control of untethered magnetically actuated tools using a rotating permanent magnet in any position," in *2012 IEEE International Conference on Robotics and Automation*. IEEE, 2012, pp. 3375–3380.

[180] Z. Han, S. Liu, Y. Pei, Z. Ding, Y. Li, X. Wang, D. Zhan, S. Xia, T. Driedonks, K. W. Witwer *et al.*, "Highly efficient magnetic labelling allows mri tracking of the homing of stem cell-derived extracellular vesicles following systemic delivery," *Journal of extracellular vesicles*, vol. 10, no. 3, p. e12054, 2021.

[181] J. Kolosnjaj-Tabi, C. Wilhelm, O. Clément, and F. Gazeau, "Cell labeling with magnetic nanoparticles: opportunity for magnetic cell imaging and cell manipulation," *Journal of nanobiotechnology*, vol. 11, no. 1, pp. 1–19, 2013.

[182] P. M. Price, W. E. Mahmoud, A. A. Al-Ghamdi, and L. M. Bronstein, "Magnetic drug delivery: where the field is going," *Frontiers in chemistry*, vol. 6, p. 619, 2018.

[183] E. Kianfar, "Magnetic nanoparticles in targeted drug delivery: a review," *Journal of Superconductivity and Novel Magnetism*, vol. 34, no. 7, pp. 1709–1735, 2021.

[184] S. Tarantino, F. Clemente, D. Barone, M. Controzzi, and C. Cipriani, "The myokinetic control interface: Tracking implanted magnets as a means for prosthetic control," *Scientific reports*, vol. 7, no. 1, p. 17149, 2017.

[185] M. Gherardini, A. Mannini, and C. Cipriani, "Optimal spatial sensor design for magnetic tracking in a myokinetic control interface," *Computer Methods and Programs in Biomedicine*, vol. 211, p. 106407, 2021.

[186] J. Sikorski, A. Denasi, G. Bucchi, S. Scheggi, and S. Misra, "Vision-based 3-d control of magnetically actuated catheter using bigmag—an array of mobile electromagnetic coils," *IEEE/ASME transactions on mechatronics*, vol. 24, no. 2, pp. 505–516, 2019.

[187] Z. Yang, L. Yang, M. Zhang, Q. Wang, S. C. H. Yu, and L. Zhang, "Magnetic control of a steerable guidewire under ultrasound guidance using mobile electromagnets," *IEEE Robotics and Automation Letters*, vol. 6, no. 2, pp. 1280–1287, 2021.

[188] B. Chaluvadi, K. M. Stewart, A. J. Sperry, H. C. Fu, and J. J. Abbott, "Kinematic model of a magnetic-microrobot swarm in a rotating magnetic dipole field," *IEEE Robotics and Automation Letters*, vol. 5, no. 2, pp. 2419–2426, 2020.

[189] Z. Zhang, A. Klingner, S. Misra, and I. S. Khalil, "Control of magnetically-driven screws in a viscoelastic medium," in *Proceedings of the IEEE/RSJ International Conference on Intelligent Robots and Systems (IROS), Las Vegas, NV, USA*, 2020, pp. 25–29.

[190] Q. Cao, Z. Wang, B. Zhang, Y. Feng, S. Zhang, X. Han, and L. Li, "Targeting behavior of magnetic particles under gradient magnetic fields produced by two types of permanent magnets," *IEEE Transactions on Applied Superconductivity*, vol. 26, no. 4, pp. 1–5, 2016.

[191] O. Baun and P. Blümler, "Permanent magnet system to guide superparamagnetic particles," *Journal of Magnetism and Magnetic Materials*, vol. 439, pp. 294–304, 2017.

[192] M. Yousefi, H. N. Pishkenari, and A. Alasty, "A fast and robust magnetic localization technique based on elimination of the orientation variables from the optimization," *IEEE Sensors Journal*, vol. 21, no. 19, pp. 21 885–21 892, 2021.

[193] D. Son, X. Dong, and M. Sitti, "A simultaneous calibration method for magnetic robot localization and actuation systems," *IEEE Transactions on Robotics*, vol. 35, no. 2, pp. 343–352, 2018.

[194] C. Hu, W. Yang, D. Chen, M. Q.-H. Meng, and H. Dai, "An improved magnetic localization and orientation algorithm for wireless capsule endoscope," in *2008 30th Annual International Conference of the IEEE Engineering in Medicine and Biology Society*. IEEE, 2008, pp. 2055–2058.

[195] G. Shao, Y. Tang, L. Tang, Q. Dai, and Y.-X. Guo, "A novel passive magnetic localization wearable system for wireless capsule endoscopy," *IEEE sensors journal*, vol. 19, no. 9, pp. 3462–3472, 2019.

[196] K. M. Popek, A. W. Mahoney, and J. J. Abbott, "Localization method for a magnetic capsule endoscope propelled by a rotating magnetic dipole field," in *2013 IEEE International Conference on Robotics and Automation*. IEEE, 2013, pp. 5348–5353.

[197] K. M. Popek, T. Hermans, and J. J. Abbott, "First demonstration of simultaneous localization and propulsion of a magnetic capsule in a lumen using a single rotating magnet," in *2017 IEEE International Conference on Robotics and Automation (ICRA)*. IEEE, 2017, pp. 1154–1160.

[198] C. Di Natali, M. Beccani, N. Simaan, and P. Valdastri, "Jacobian-based iterative method for magnetic localization in robotic capsule endoscopy," *IEEE Transactions on Robotics*, vol. 32, no. 2, pp. 327–338, 2016.

[199] Y. Xu, K. Li, Z. Zhao, and M. Q.-H. Meng, "A novel system for closed-loop simultaneous magnetic actuation and localization of wce based on external sensors and rotating actuation," *IEEE Transactions on Automation Science and Engineering*, vol. 18, no. 4, pp. 1640–1652, 2020.

Appendices

A

Development of the permanent magnet-based robotic system

A.1 Exact expression for the magnetic field generated by a cylindrical permanent magnet

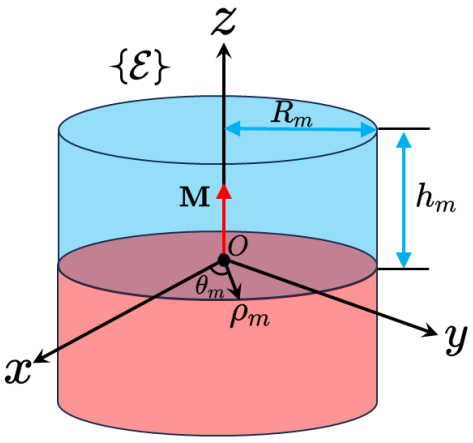

Figure A.1: The schematic diagram of a cylindrical permanent magnet with a semi-height of h_m and a radius of R_m with a longitudinal magnetization vector $\mathbf{M}$ is located in a cylindrical coordinate frame (ρ_m, θ_m, z) and a cartesian coordinate frame $\{\mathcal{E}\}$.

We consider a cylindrical permanent magnet, with its centroid at the origin of both cylindrical coordinate frame (ρ_m, θ_m, z) and cartesian coordinate frame $\{\mathcal{E}\}$, as shown in Fig. A.1. The actuator magnet is longitudinally magnetized with the magnetization vector ($\mathbf{M}$), then the generated magnetic flux density in frame $\{\mathcal{E}\}$ can be modeled by using [116],

$$B_x = \frac{\mu_0 |\mathbf{M}| R_m}{\pi}(a_+ P_1(k_+) - a_- P_1(k_-)) \cos\theta_m \tag{A.1}$$

$$B_y = \frac{\mu_0 |\mathbf{M}| R_m}{\pi}(a_+ P_1(k_+) - a_- P_1(k_-)) \sin\theta_m \tag{A.2}$$

$$B_z = \frac{\mu_0 |\mathbf{M}| R_m}{\pi(\rho_m + R_m)}(b_+ P_2(k_+) - b_- P_2(k_-)) \tag{A.3}$$

where $\mu_0 = 4\pi \times 10^{-7}$ N.A^{-2} is the permeability of free space, R_m is the semi-height of the permanent magnet, B_x, B_y and B_z are the x_-, y_- and z_- axial components of the magnetic flux density, respectively. Two auxiliary functions are calculated as follows,

$$P_1(k) = K - \frac{2}{1-k^2}(K - c) \tag{A.4}$$

$$P_2(k) = -\frac{f}{1-f^2}(G - K) - \frac{1}{1-f^2}(f^2 G - K) \tag{A.5}$$

and the following notations will be employed:

$$g_\pm = z \pm h_m \tag{A.6}$$

$$f = \frac{\rho_m - R_m}{\rho_m + R_m} \tag{A.7}$$

$$a_\pm = \frac{1}{\sqrt{g_\pm^2 + (\rho_m + R_m)^2}} \tag{A.8}$$

$$b_\pm = g_\pm a_\pm \tag{A.9}$$

$$k_\pm^2 = \frac{g_\pm^2 + (\rho_m - R_m)^2}{g_\pm^2 + (\rho_m + R_m)^2} \tag{A.10}$$

The symbols K, c, G are expressed as,

$$K = \int_0^{\frac{\pi}{2}} \frac{d\delta_m}{\sqrt{1-(1-k^2)\sin^2\delta_m}} \tag{A.11}$$

$$c = \int_0^{\frac{\pi}{2}} d\delta_m \sqrt{1-(1-k^2)\sin^2\delta_m} \tag{A.12}$$

$$G = \int_0^{\frac{\pi}{2}} \frac{d\delta_m}{\sqrt{1-(1-f^2)\sin^2\delta_m}\sqrt{1-(1-k^2)\sin^2\delta_m}} \tag{A.13}$$

A.2 Frame parameters of the permanent magnet-based robotic system

The parameters corresponding to each frame shown in Fig. 2.2 are demonstrated as below. In which, for $i = 1$, $d_x^4 = l_5$ and $d_y^4 = -l_6$, and for $i = 2$, $d_x^4 = -l_5$ and $d_y^4 = l_6$.

Table A.1: Frame Parameters of the Permanent Magnet-Based Robotic System

j	q_j	d_x^j	d_y^j	d_z^j	$q_{\min}$	$q_{\max}$
1	q_1 [mm]	-	-	-	-150	150
2	q_2 [°]	-	-	l_2	-720	720
3	q_3 [°]	-	-	l_3	-90	90
4	q_4 [°]	$\pm l_5$	$\mp l_6$	l_4	-180	180

A.3 Characterization of magnetic field

The highest and lowest magnitudes of magnetic field strength, along with the highest magnitude of magnetic field gradient, observed within the central spherical space at various radii under the influence of two synchronized rotating permanent magnets, are presented below.

Table A.2: Characterization of Magnetic Field

r [mm]	20	30	40	50
$\|\mathbf{B}\|_{hig}$ [mT]	3.615	3.973	4.526	5.337
$\|\mathbf{B}\|_{low}$ [mT]	1.605	1.489	1.340	1.167
$\|\nabla\mathbf{B}\|_{hig}$ [T/m]	0.028	0.045	0.067	0.097
$\|\nabla\mathbf{B}\|_{low}$ [T/m]	0	0	0	0

A.4 Algorithm to obtain the distance between two synchronized rotating permanent magnets for a desired size gradient-free space

The algorithm to obtain the distance between two synchronized rotating permanent magnets based on a desired size gradient-free space and a given threshold is demonstrated below.

Table A.3: Solving the Desired Distance Between Two Synchronized Rotating Permanent Magnets

Input: Desired radius of gradient-free spherical space r_g^d
Output: Desired distance between two actuator magnets $\boldsymbol{L}_{mag}^d$

Define $\mathcal{P}_n \in$ spherical space $\mathcal{S}(r^d)$ and threshold ϱ
$|\nabla\mathbf{B}|_{hig} = 0$; $\theta_s = 90°$;
$L_{mag} \in [\ L_{mag}^0, L_{mag}^1\ ]$
for $L_{mag} = L_{mag}^0 : L_{mag}^1$
    $\mathcal{P}_n = [L_{mag}/2, 0, 0]$
    $|\nabla\mathbf{B}|_{hig} = |\nabla\mathbf{B}|\ (\mathcal{P}_n)$
  if $|\nabla\mathbf{B}|_{hig} \leq \varrho$
    $\boldsymbol{L}_{mag}^d = \boldsymbol{L}_{mag}$
    break;
  end
end
Return $\boldsymbol{L}_{mag}^d$

B

Modeling for the Localization of Magnetic Devices Using a Synchronized Rotating Magnetic Actuation System

B.1 Introduction

Magnetic devices hold significant promise in biomedical applications, spanning magnetic labeling [180], [181], magnetic drug delivery [182], [183], and magnetic prosthetics and implants [184], [185]. Accurate localization of these devices is paramount for the success of such endeavors. While image tracking technologies, leveraging image sensing devices [186], [187], are commonly employed for motion control in various scenarios, magnetic tracking technology becomes indispensable in low-light or no-light conditions, when the appearance of objects hinders imaging, or when information cannot be obtained through visual means.

The configuration of actuator magnets, including the actuation mode and the quantity of actuator magnets, can impact the localization strategy of a magnetic device. Three main actuation modes are utilized for driving magnetic devices: torque-driven mode, force-driven mode, and torque-force-driven mode. Torque-driven mode involves the rotation of magnetic devices induced by magnetic torque from a rotating magnetic field [188], [189]. Force-driven mode involves dragging movement of magnetic devices induced by gradient force from a gradient magnetic field [190], [191]. In contrast, the torque-force-driven mode involves both rotation and dragging movement of magnetic devices induced by magnetic torque and gradient,

respectively [145], [146]. This consideration also applies to whether the actuator magnets must maintain rotational motion around their own axes. Moreover, the number of actuator magnets is a critical factor in determining the localization strategy. Regardless of the configuration of actuator magnets, the most commonly employed method for calculating the position and orientation of a magnetic device from the magnetic sensor data is through iterative methods [192], [193]. Nonetheless, magnetic localization using iterative methods is susceptible to drift caused by magnetic noise and uncertain initial guesses during optimization. Researchers have explored numerous approaches to mitigate this issue and enhance localization accuracy, yet have not achieved a complete resolution [194], [195]. Developing a non-iterative method may potentially offer a complete solution to this problem.

Most research focused on localizing magnetic devices under the actuation of a single actuator magnet. Using one single actuator magnet with torque-driven mode, Popek *et al.* have offered a non-iterative approach for determining the six degree-of-freedom (6-DOF) position and orientation of a magnetic capsule endoscope. Thus, the localization of a magnetic device under the actuation of a single rotating actuator magnet has been solved [196], [197]. Using one single actuator magnet with force-driven mode, Natali *et al.* have introduced a novel method for localizing a wireless capsule endoscopy through the utilization of an iterative Jacobian-based approach [198]. Using one single actuator magnet with torque-force-driven mode, Xu *et al.* have presented an innovative system incorporating a rotating magnetic actuator alongside an external sensor array to enable closed-loop simultaneous magnetic actuation and localization of wireless-capsule endoscopy [199]. The localization is achieved by optimizing the error functions. Using multiple actuator magnets with force-driven mode, Veiga*et al.* have proposed a method to estimate the localization of a magnetically actuated medical robot without any prior pose information using an iterative method, with the assistance of a millimeter-scale three-dimensional accelerometer and a three-dimensional magnetic field sensor [73]. To the best of our knowledge, non-iterative methods for localizing magnetic devices under the actuation of two synchronized rotating actuator magnets have not been reported in prior works.

In this appendix, the objective is to localize a magnetic device equipped with an embedded magnetic sensor within its body. A schematic diagram

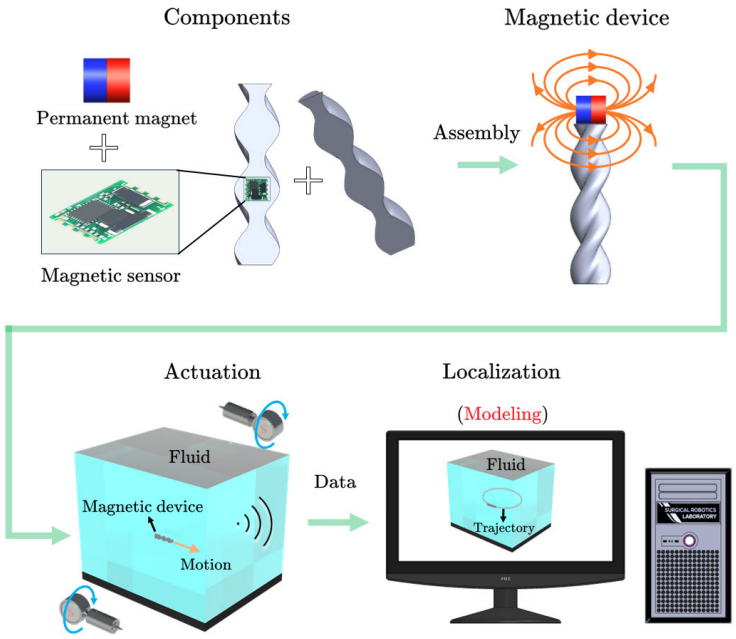

Figure B.1: A schematic diagram demonstrating the assembly, actuation, and localization of a magnetic device, with the magnetic sensor integrated within its body. Localization of the magnetic device is accomplished through a derived model.

demonstrating the assembly, actuation, and localization of a magnetic device is shown in Fig B.1. To achieve this objective, a model designed for the magnetic localization of a magnetic device under the influence of two synchronized rotating permanent magnets is developed. The structure of this paper is as follows: Section B.2 presents the synchronized rotating magnetic actuation system. Section B.3 explores the fundamental properties of the linear map $\mathcal{H}_{\boldsymbol{p}}$, which correlates the instantaneous dipole moment of synchronized rotating permanent magnets to the instantaneous corresponding magnetic field (magnetic flux density). Section B.4 investigates the interrelations among variables within the synchronized rotating magnetic actuation system. Sections B.5 and B.6 derive the linear map $\mathcal{H}_{\boldsymbol{p}}$ under two conditions: when the dipole-rotation axis and the field-rotation axis are perpendicular to each other, and when they are not perpendicular

to each other, respectively. Section B.7 involves inferring the position of the magnetic device using the linear map $\mathcal{H}_{\boldsymbol{p}}$. Finally, Section B.8 concludes the main findings and outlines future directions for research.

B.2 Synchronized Rotating Magnetic Actuation System

Two identical permanent magnets are rotating synchronously, resulting in a time-varying magnetic field $\mathbf{B}$ (magnetic flux density), as shown in Fig B.2. Assume the magnetic device is at the position $\boldsymbol{p}$ between two permanent magnets, and $\theta \in [0, \pi]$ is the angle such that $\langle \bar{\boldsymbol{p}}_+, \bar{\boldsymbol{p}}_- \rangle = \cos\theta$. During a single rotation period of permanent magnets, when $|\mathbf{B}|$ reaches its maximum and minimum magnitudes at point $\boldsymbol{p}$, the corresponding vectors of the magnetic field are denoted as $\mathbf{B}_{max}$ and $\mathbf{B}_{min}$, respectively. Similarly, the vectors of dipole moment are denoted as $\mathbf{M}_{ax}$ and $\mathbf{M}_{in}$ for the maximum and minimum magnitudes of $|\mathbf{B}|$ at point $\boldsymbol{p}$, respectively. The $\mathbf{B}_{max}$ and $\mathbf{B}_{min}$ can be measured in experiments. The vector of field-rotation axis $\boldsymbol{\omega} = \mathbf{B}_{max} \times \mathbf{B}_{min}$ can always be calculated directly, and hence it is also treated as something known from the very beginning. Since the rotation of the magnets is under control, the vector of dipole-rotation axis $\boldsymbol{\Omega}$ (which is the rotation-axis of dipole moment $\mathbf{M}_t$) is also known. Suppose that $|\mathbf{M}_t| = \mathsf{M}$. However, it is hard to measure the corresponding dipole moments $\mathbf{M}_{ax}$ and $\mathbf{M}_{in}$ with accuracy, and hence they are assumed to be unknown. We consider the following question: Deduce the position $\boldsymbol{p} \in \mathbb{R}^3 - \{\boldsymbol{o}_\pm\}$ of the magnetic device from the data $\mathbf{B}_{max}$, $\mathbf{B}_{min}$, M and $\boldsymbol{\Omega}$ (which are measured or directly controlled in the experiment).

We denote by $\langle \mathbf{u}, \mathbf{v} \rangle$ or $\mathbf{u} \cdot \mathbf{v}$ the standard inner product of the vectors $\mathbf{u}, \mathbf{v} \in \mathbb{R}^3$. That is,$\langle \mathbf{u}, \mathbf{v} \rangle = u_1v_1 + u_2v_2 + u_3v_3$. For a non-zero vector $\mathbf{u}$, we adopt the notation $\hat{\mathbf{u}} = \frac{\mathbf{u}}{|\mathbf{u}|}$. Two synchronized rotating permanent magnets are placed at the positions $\boldsymbol{o}_+ = (+a, 0, 0)$ and $\boldsymbol{o}_- = (-a, 0, 0)$ respectively. Given a position $\boldsymbol{p} = (x, y, z)$ in $\mathbb{R}^3$, let $\boldsymbol{p}_+ = \boldsymbol{p} - \boldsymbol{o}_+ = (x - a, y, z)$ and $\boldsymbol{p}_- = \boldsymbol{p} - \boldsymbol{o}_- = (x + a, y, z)$. Then the time-varying magnetic field $\mathbf{B}_t$ at $\boldsymbol{p}$ generated by the synchronized rotating permanent magnets at positions $\boldsymbol{o}_+$ and $\boldsymbol{o}_-$ based on point-dipole model is

$$\mathbf{B}_t = \mathcal{H}_{\boldsymbol{p}} \cdot \mathbf{M}_t. \tag{B.1}$$

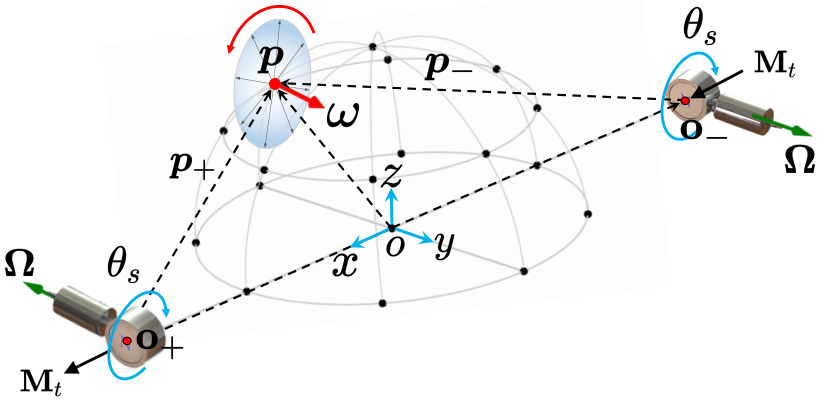

Figure B.2: Two identical magnetic dipoles are synchronously rotating around the dipole-rotation axis $\boldsymbol{\Omega}$ with time-varying $\mathbf{M}_t$ perpendicular to $\boldsymbol{\Omega}$, resulting in time-varying magnetic field $\mathbf{B}$ which rotates around the field-rotation axis $\boldsymbol{\omega}$ at position $\boldsymbol{p}$.

where $\mathcal{H}$ is a 3×3 matrix defined as follows

$$\mathcal{H}_{\boldsymbol{p}} = \frac{1}{|\boldsymbol{p}_+|^3}(3\hat{\boldsymbol{p}}_+\hat{\boldsymbol{p}}_+^{\mathrm{T}} - \mathbf{I}) + \frac{1}{|\boldsymbol{p}_-|^3}(3\hat{\boldsymbol{p}}_-\hat{\boldsymbol{p}}_-^{\mathrm{T}} - \mathbf{I}), \tag{B.2}$$

where $\hat{\boldsymbol{p}}_\pm = \frac{\boldsymbol{p}_\pm}{|\boldsymbol{p}_\pm|}$ and $\mathbf{I}$ is the 3×3 identity matrix. Note that $\mathcal{H}_{\boldsymbol{p}}$ is a symmetric matrix.

B.3 Basic Properties of the Linear Map

The matrix $\mathcal{H}_{\boldsymbol{p}}$ maps the instantaneous dipole moment $\mathbf{M}_t$ to the instantaneous magnetic field $\mathbf{M}_t$. In order to investigate the relationship between the input $\boldsymbol{\Omega}$ and output magnetic field variables such as $\boldsymbol{\omega}$, $\mathbf{B}_{max}$ and $\mathbf{B}_{min}$ at a position $\boldsymbol{p}$, it is essential to explore the basic properties of the linear map $\mathcal{H}_{\boldsymbol{p}}$.

B.3.1 Eigenvalues, invariant subspaces, and trace

Since $\mathcal{H}_{\boldsymbol{p}}$ is real and symmetric, all its eigenvalues are real numbers. It is straightforward to check that $span\{\hat{\boldsymbol{p}}_\pm\}$ is invariant under the action of $\mathcal{H}_{\boldsymbol{p}}$.

$\mathcal{H}_{\boldsymbol{p}}$ is symmetric, the normal space $\mathcal{N}_{\hat{\boldsymbol{p}}_\pm}$ of $span\{\hat{\boldsymbol{p}}_\pm\}$ is also an invariant subspace of $\mathcal{H}_{\boldsymbol{p}}$. Therefore, the eigenvectors of $\mathcal{H}_{\boldsymbol{p}}$ reside in these invariant subspaces: $\mathcal{N}_{\hat{\boldsymbol{p}}_\pm}$ and $span\{\hat{\boldsymbol{p}}_\pm\}$. Also, directly from Equation (B.2) we can verify that the trace of $\mathcal{H}_{\boldsymbol{p}}$ is zero, i.e., $\mathrm{tr}\mathcal{H}_{\boldsymbol{p}} = 0$.

B.3.2 Eigenvalues of the linear map

When $span\{\hat{\boldsymbol{p}}_\pm\}$ is 1-dimensional (note that this happens iff $\boldsymbol{p}$ is on the *x-axis*), $span\{\hat{\boldsymbol{p}}_\pm\} = \{(r,0,0)\big|r \in \mathbb{R}\}$ is an eigenspace of $\mathcal{H}_{\boldsymbol{p}}$ and it holds that

$$\mathcal{H}_{\boldsymbol{p}} \begin{bmatrix} 1 \\ 0 \\ 0 \end{bmatrix} = \big(\frac{2}{|\boldsymbol{p}_+|^3} + \frac{2}{|\boldsymbol{p}_-|^3}\big) \begin{bmatrix} 1 \\ 0 \\ 0 \end{bmatrix}, \tag{B.3}$$

i.e., $\big(\frac{2}{|\boldsymbol{p}_+|^3} + \frac{2}{|\boldsymbol{p}_-|^3}\big)$ is a (positive) eigenvalue. In the meantime, $\mathcal{N}_{\hat{\boldsymbol{p}}_\pm}$ is the yOz plane and it is straightforward to check that it is an eigenspace with eigenvalue $-\big(\frac{1}{|\boldsymbol{p}_+|^3} + \frac{1}{|\boldsymbol{p}_-|^3}\big)$. When $span\{\hat{\boldsymbol{p}}_\pm\}$ is a plane, $\mathcal{N}_{\hat{\boldsymbol{p}}_\pm}$ is 1 dimensional, and then $\mathbf{n} = \hat{\boldsymbol{p}}_+ \times \hat{\boldsymbol{p}}_-$ is an eigenvector of $\mathcal{H}_{\boldsymbol{p}}$. Again, it holds

$$\mathcal{H}_{\boldsymbol{p}}\mathbf{n} = -\big(\frac{1}{|\boldsymbol{p}_+|^3} + \frac{1}{|\boldsymbol{p}_-|^3}\big)\mathbf{n}, \tag{B.4}$$

which means that $-\big(\frac{1}{|\boldsymbol{p}_+|^3} + \frac{1}{|\boldsymbol{p}_-|^3}\big)$ is a (negative) eigenvalue of $\mathcal{H}_{\boldsymbol{p}}$. From the discussion up to this point we can draw the following conclusion: For all $\boldsymbol{p} \in \mathbb{R}^3 - \{\pm\boldsymbol{o}\}$, $\sigma = -\big(\frac{1}{|\boldsymbol{p}_+|^3} + \frac{1}{|\boldsymbol{p}_-|^3}\big)$ is a (negative) eigenvalue of $\mathcal{H}_{\boldsymbol{p}}$. Moreover, if the space $span\{\hat{\boldsymbol{p}}_\pm\}$ is 1-dimensional, then the other two eigenvalues are $\big(\frac{2}{|\boldsymbol{p}_+|^3} + \frac{2}{|\boldsymbol{p}_-|^3}\big)$ and $-\big(\frac{1}{|\boldsymbol{p}_+|^3} + \frac{1}{|\boldsymbol{p}_-|^3}\big)$. Let's first consider the case where $span\{\hat{\boldsymbol{p}}_\pm\}$ is 2 dimensional. It is easy to observe from the definition of $\mathcal{H}_{\boldsymbol{p}}$ (Equation B.2) that if $\mathbf{v} \in \mathbb{R}^3$ is an eigenvector of $\mathcal{H}_{\boldsymbol{p}}$ then it is also an eigenvector of the operator

$$\overline{\mathcal{H}}_{\boldsymbol{p}} = \frac{1}{|\boldsymbol{p}_+|^3}\hat{\boldsymbol{p}}_+\hat{\boldsymbol{p}}_+^{\mathrm{T}} + \frac{1}{|\boldsymbol{p}_-|^3}\hat{\boldsymbol{p}}_-\hat{\boldsymbol{p}}_-^{\mathrm{T}}. \tag{B.5}$$

With $\mathbf{n} = \hat{\boldsymbol{p}}_+ \times \hat{\boldsymbol{p}}_-$, it is easy to see that $\overline{\mathcal{H}}_{\boldsymbol{p}}\mathbf{n} = 0$. To see the other *two* eigenvalues of $\overline{\mathcal{H}}_{\boldsymbol{p}}$, we only need to see its restriction as an endomorphism on the space $span\{\hat{\boldsymbol{p}}_\pm\}$. Let $\mathbf{H}$ be the matrix representation of $\overline{\mathcal{H}}_{\boldsymbol{p}}$ (as a linear map on $span\{\hat{\boldsymbol{p}}_\pm\}$) with respect to the basis $\{\hat{\boldsymbol{p}}_\pm\}$. Then

$$\mathbf{H} = \begin{bmatrix} \frac{1}{|\boldsymbol{p}_+|^3} & \frac{1}{|\boldsymbol{p}_+|^3}\cos\theta \\ \frac{1}{|\boldsymbol{p}_-|^3}\cos\theta & \frac{1}{|\boldsymbol{p}_-|^3} \end{bmatrix}, \tag{B.6}$$

and hence

$$\det\left(t\mathbf{I} - \mathbf{H}\right) = t^2 + \sigma t + \frac{\sin^2\theta}{|\boldsymbol{p}_+|^3|\boldsymbol{p}_-|^3}. \tag{B.7}$$

The eigenvalues of $\overline{\mathcal{H}_{\boldsymbol{p}}}$ are the roots of Equation (B.7)

$$\overline{\sigma}_\pm = \frac{1}{2}\cdot\left(-\sigma \pm \sqrt{\sigma^2 - \frac{4\sin^2\theta}{|\boldsymbol{p}_+|^3|\boldsymbol{p}_-|^3}}\right), \tag{B.8}$$

and then the *two* eigenvalues of $\mathcal{H}_{\boldsymbol{p}}$ other than σ are

$$\sigma_\pm = 3\overline{\sigma}_\pm + \sigma = \frac{3}{2}\cdot\left(-\sigma \pm \sqrt{\sigma^2 - \frac{4\sin^2\theta}{|\boldsymbol{p}_+|^3|\boldsymbol{p}_-|^3}}\right) + \sigma. \tag{B.9}$$

Combining with Section B.3.2, we have the following results. For all $\boldsymbol{p} \in \mathbb{R}^3 - \{o_\pm\}$, it holds that (see Proof 1)

$$\sigma \le \sigma_- \le \frac{|\sigma|}{2} \le \sigma_+ \le 2|\sigma|. \tag{B.10}$$

Equation (B.9) holds for the eigenvalues $\sigma_\pm$ all the time, including the case where $\dim span\{\hat{\boldsymbol{p}}_\pm\} = 1$.

Proof 1: Note that

$$\left(\frac{1}{|\boldsymbol{p}_+|^3} - \frac{1}{|\boldsymbol{p}_-|^3}\right)^2 \le \sigma^2 - \frac{4\sin^2\theta}{|\boldsymbol{p}_+|^3|\boldsymbol{p}_-|^3} = \left(\frac{1}{|\boldsymbol{p}_+|^3} + \frac{1}{|\boldsymbol{p}_-|^3}\right)^2 - \frac{4\sin^2\theta}{|\boldsymbol{p}_+|^3|\boldsymbol{p}_-|^3} \le \sigma^2$$

and hence

$$-|\sigma| \le \sigma_- = \frac{|\sigma|}{2} - \frac{3}{2}\cdot\sqrt{\sigma^2 - \frac{4\sin^2\theta}{|\boldsymbol{p}_+|^3|\boldsymbol{p}_-|^{\mathbf{3}}}}\Bigg) \le \frac{|\sigma|}{2}.$$

Then from $\mathrm{tr}\mathcal{H}_{\boldsymbol{p}} = \sigma_+ + \sigma_- + \sigma = 0$ we deduce

$$\frac{|\sigma|}{2} \le \sigma_+ \le 2|\sigma|.$$

Moreover, the space $span\{\hat{\boldsymbol{p}}_{\pm}\}$ is of dimension 1 if and only if $\sigma_- = \sigma$ (see Proof 2).

Proof 2: From $\sigma_- = \frac{|\sigma|}{2} - \frac{3}{2} \cdot \sqrt{\sigma^2 - \frac{4\sin^2\theta}{|p_+|^3|p_-|^3}}\Big)$ we know that $\sigma_- = \sigma = -|\sigma|$ if and only if

$$\sqrt{\sigma^2 - \frac{4\sin^2\theta}{|\boldsymbol{p}_+|^3|\boldsymbol{p}_-|^3}} = |\sigma|,$$

i.e., $\frac{4\sin^2\theta}{|\boldsymbol{p}_+|^3|\boldsymbol{p}_-|^3} = 0$, which is equivalent to $\langle \hat{\boldsymbol{p}}_+, \hat{\boldsymbol{p}}_- \rangle^2 = \cos^2\theta = 1$, or, say, $span\{\hat{\boldsymbol{p}}_{\pm}\}$ is of dimension 1.

B.3.3 The singular set

Directly from Section B.3.2, we know that $\det \mathcal{H}_{\boldsymbol{p}} = 0$ iff $\sigma_- = 0$ iff

$$2(1+\lambda)^2 = 9\lambda \sin^2\theta. \tag{B.11}$$

with $\lambda = \frac{|p_+|^3}{|p_-|^3}$ (see Proof 3).

Proof 3: $\sigma_- = 0$ gives

$$\frac{|\sigma|}{2} = \frac{3}{2} \cdot \sqrt{\sigma^2 - \frac{4\sin^2\theta}{|\boldsymbol{p}_+|^3|\boldsymbol{p}_-|^3}},$$

and then

$$9\frac{\sin^2\theta}{|\boldsymbol{p}_+|^3|\boldsymbol{p}_-|^3} = 2\sigma^2 = 2\big(\frac{1}{|\boldsymbol{p}_+|^3} + \frac{1}{|\boldsymbol{p}_-|^3}\big)^2,$$

and finally

$$2(1+\lambda)^2 = 9\lambda \sin^2\theta.$$

Equation (B.11) can be re-expressed in terms of $|\boldsymbol{p}_{\pm}|$ as

$$2\big(\frac{1}{|\boldsymbol{p}_+|^3} + \frac{1}{|\boldsymbol{p}_-|^3}\big)\big(|\boldsymbol{p}_+|^3 + |\boldsymbol{p}_-|^3\big) = 9\sin^2\theta, \tag{B.12}$$

demonstrating certain symmetry for being viewed as an equation on S^3. We define the *singular set* $\mathcal{S}$ to be

$$\mathcal{S} = \{\boldsymbol{p} \in \mathbb{R}^3 - \{\pm o\} \big| \det \mathcal{H}_{\boldsymbol{p}} = 0\}.$$

To see "how large´´ this set is, we first observe that the mapping $\boldsymbol{p} \mapsto \det \mathcal{H}_{\boldsymbol{p}}$ is invariant under the rotation of $\boldsymbol{p}$ around the x-axis. Therefore, we can first discuss the subset $\mathcal{S} \bigcap xOy$, and then whole set $\mathcal{S}$ is obtained by rotating $\mathcal{S} \bigcap xOy$ around the x-axis. The points in $\mathcal{S} \bigcap xOy$ can be obtained by first fixing the value $\sin^2\theta = c_0$ and then solving the Equation (B.11) for the positive number λ. Telling from the form of Equation (B.11) (with the value of $\sin^2\theta$ fixed) we know that if $\lambda = s_0 > 0$ is a solution so is $\lambda = \frac{1}{s_0}$. The equation $\sin^2\theta = c_0$ determines two circles $\mathcal{C}_0^{\pm}$ on xOy with the segment $\overline{\mathbf{o}_-\mathbf{o}_+}$ being a chord with the central angle θ on each of these circles. The relation

$$\lambda \in \{s_0, \frac{1}{s_0}\}$$

gives two circles $\mathcal{L}_{s_0}$ and $\mathcal{L}_{\frac{1}{s_0}}$ on xOy with the centers on the x-axis. Together it gives a subset in xOy

$$\left(\mathcal{C}_0^+ \cup \mathcal{C}_0^-\right) \bigcap \left(\mathcal{L}_{s_0} \cup \mathcal{L}_{\frac{1}{s_0}}\right) \subset \mathcal{S}$$

consisting of no more than 8 points. Rewrite the Equation (B.11) as

$$\lambda^2 + (2 - c_\theta)\lambda + 1 = 0 \tag{B.13}$$

with $c_\theta = \frac{9}{2}\sin^2\theta$. Section B.3.3 implies that, if $\boldsymbol{p} \in \mathcal{S}$, then with $c_\theta = \frac{9}{2} - \frac{9}{2}(\hat{\boldsymbol{p}}_+ \cdot \hat{\boldsymbol{p}}_-)^2$, the equation above should have positive solutions (equal to $\frac{|\boldsymbol{p}_+|^3}{|\boldsymbol{p}_-|^3}$ and $\frac{|\boldsymbol{p}_-|^3}{|\boldsymbol{p}_+|^3}$). Solving the Equation (B.13) for λ we get

$$\lambda_\pm = \frac{(c_\theta - 2) \pm \sqrt{(c_\theta - 2)^2 - 4}}{2}. \tag{B.14}$$

It is straightforward to check from Equation (B.14) that $\lambda_\pm > 0$ if and only if $c_\theta - 2 \geq 2$. That is

$$\sin^2\theta \geq \frac{8}{9}. \tag{B.15}$$

This means that if $\sin^2\theta < \frac{8}{9}$, then the Equation (B.13) has no positive solutions, and hence $\boldsymbol{p} \notin \mathcal{S}$.

B.4 Relationships among variables within the magnetic actuation system

With the notation $\hat{\mathbf{\Omega}} = [\Omega_1\ \Omega_2\ \Omega_3]^{\mathrm{T}}$, we have $\hat{\mathbf{\Omega}} \times (\,\cdot\,) = J_{\hat{\mathbf{\Omega}}}(\,\cdot\,)$ for

$$J_{\hat{\mathbf{\Omega}}} = \begin{bmatrix} 0 & -\Omega_3 & \Omega_2 \\ \Omega_3 & 0 & -\Omega_1 \\ -\Omega_2 & \Omega_1 & 0 \end{bmatrix}. \tag{B.16}$$

$J_{\hat{\mathbf{\Omega}}}$ maps $\mathbb{R}^3$ to the space $\mathcal{N}_{\hat{\mathbf{\Omega}}} = \{\mathbf{u} \in \mathbb{R}^3 | \mathbf{u} \cdot \hat{\mathbf{\Omega}} = 0\} = \mathrm{span}\{\mathbf{M}_t\}$ with $\ker J_{\hat{\mathbf{\Omega}}} = \mathrm{span}\{\hat{\mathbf{\Omega}}\}$, and it is restricted to an isomorphism on $\mathcal{N}_{\hat{\mathbf{\Omega}}}$.

B.4.1 Relationships among variables of magnetic dipoles

The operator $\mathcal{A} = J_{\hat{\mathbf{\Omega}}}^T \mathcal{H}_{\boldsymbol{p}}^2 J_{\hat{\mathbf{\Omega}}}$ is symmetric and non-negative with respective to the standard inner product $\langle\ ,\ \rangle$, and it has invariant subspaces $\mathcal{N}_{\hat{\mathbf{\Omega}}}$ and $\ker J_{\hat{\mathbf{\Omega}}}$. Note that when restricted to $\mathcal{N}_{\hat{\mathbf{\Omega}}}$, $\mathcal{A}$ is also symmetric and non-negative with respective to $\langle\ ,\ \rangle$, and hence the quadratic form

$$\mathcal{N}_{\hat{\mathbf{\Omega}}} \cap S^2 \ni \mathbf{u} \mapsto \langle \mathbf{u}, \mathcal{A}\mathbf{u} \rangle \in \mathbb{R}_+$$

takes the maximum and the minimum at the unit eigenvectors of $\mathcal{A}$, with the maximum and the minimum being the corresponding eigenvalues. In the meantime, for any instant t, there is another instant t' such that $\mathbf{M}_{t'} = J_{\hat{\mathbf{\Omega}}}\mathbf{M}_t$ (since $J_{\hat{\mathbf{\Omega}}}\mathbf{M}_t$ is merely a rotation of $\mathbf{M}_t$ around the axis $\hat{\mathbf{\Omega}}$ for 90°), and hence

$$\langle \mathbf{M}_t, \mathcal{A}\mathbf{M}_t \rangle = |\mathbf{B}_{t'}|^2. \tag{B.17}$$

Therefore, $\mathcal{A}$ has eigenvalues $|\mathbf{B}_{max}|^2$ and $|\mathbf{B}_{min}|^2$, with $\pm\mathbf{M}_{in}$ and $\pm\mathbf{M}_{ax}$ being the corresponding unit eigenvectors. Considering the symmetry of $\mathcal{A}$, we know that $\mathbf{M}_{in}$ and $\mathbf{M}_{ax}$ are perpendicular to each other. While the vectors $\mathbf{M}_{in}$ and $\mathbf{M}_{ax}$ are still not explicitly known, by choosing the vectors $\mathbf{B}_{max}$ and $\mathbf{B}_{min}$ properly from the data measured, we can still fix the orientation of $(\mathbf{M}_{ax}, \mathbf{M}_{in}, \hat{\mathbf{\Omega}})$ such that

$$\mathbf{M}_{in} = J_{\hat{\mathbf{\Omega}}}\mathbf{M}_{ax}, \tag{B.18}$$

and then it holds

$$\hat{\mathbf{\Omega}} = \frac{\mathbf{M}_{ax} \times \mathbf{M}_{in}}{\mathsf{M}^2}. \tag{B.19}$$

B.4.2 Relationships among variables of magnetic field

We first explain the relation

$$\mathcal{H}_{\boldsymbol{p}}\boldsymbol{\omega} = (\mathsf{M}^2 \cdot \det \mathcal{H}_{\boldsymbol{p}})\hat{\boldsymbol{\Omega}}. \tag{B.20}$$

Due to the symmetry of $\mathcal{H}_{\boldsymbol{p}}$, it holds for any $\mathbf{u} \in \mathbb{R}^3$ that

$$\begin{aligned} \langle \mathcal{H}_{\boldsymbol{p}}\boldsymbol{\omega}, \mathbf{u}\rangle &= \langle \boldsymbol{\omega}, \mathcal{H}_{\boldsymbol{p}}\mathbf{u}\rangle \\ &= \det \mathcal{H}_{\boldsymbol{p}} \langle \mathsf{M}^2\hat{\boldsymbol{\Omega}}, \mathbf{u}\rangle \\ &= (\mathsf{M}^2 \cdot \det \mathcal{H}_{\boldsymbol{p}})\langle \hat{\boldsymbol{\Omega}}, \mathbf{u}\rangle, \end{aligned} \tag{B.21}$$

where from the first line to the second line, it is due to

$$\det\left[\ \mathcal{H}_{\boldsymbol{p}}\mathbf{u};\quad \mathcal{H}_{\boldsymbol{p}}\mathbf{M}_{ax};\quad \mathcal{H}_{\boldsymbol{p}}\mathbf{M}_{in}\ \right] = \det \mathcal{H}_{\boldsymbol{p}} \cdot \det\left[\ \mathbf{u};\quad \mathbf{M}_{ax};\quad \mathbf{M}_{in}\ \right]. \tag{B.22}$$

The relation $\mathcal{H}_{\boldsymbol{p}}\boldsymbol{\omega} = (\mathsf{M}^2 \cdot \det \mathcal{H}_{\boldsymbol{p}})\hat{\boldsymbol{\Omega}}$ is then implied by the arbitrariness of $\mathbf{u}$. Next we check that $\mathbf{B}_{max}$ is perpendicular to $\mathbf{B}_{min}$.

$$\begin{aligned} \langle \mathbf{B}_{max}, \mathbf{B}_{min}\rangle &= \langle \mathcal{H}_{\boldsymbol{p}}\mathbf{M}_{ax}, \mathcal{H}_{\boldsymbol{p}}\mathbf{M}_{in}\rangle \\ &= \langle -J_{\hat{\boldsymbol{\Omega}}}\mathbf{M}_{in}, \mathcal{H}_{\boldsymbol{p}}^2(J_{\hat{\boldsymbol{\Omega}}}\mathbf{M}_{ax})\rangle \\ &= \langle \mathbf{M}_{in}, \mathcal{A}\mathbf{M}_{ax}\rangle \\ &= 0. \end{aligned} \tag{B.23}$$

B.4.3 Relationships among the eigenvalue of the linear map, dipole moment and magnetic field

Given any vector $\mathbf{u} \in \mathbb{R}^3$, from the definition of $\mathcal{H}_{\boldsymbol{p}}$ in Equation (B.2) we know that

$$\mathcal{H}_{\boldsymbol{p}}\mathbf{u} - \sigma \cdot \mathbf{u} \in \mathrm{span}\{\hat{\boldsymbol{p}}_{\pm}\}. \tag{B.24}$$

Also, $\overline{\mathbf{o}_{-}\mathbf{o}_{+}} \in \mathrm{span}\{\hat{\mathbf{p}}_{\pm}\}$. As a result, for any $\mathbf{u}, \mathbf{v}, \mathbf{w} \in \mathbb{R}^3$, the following equations hold:

$$\det[\mathcal{H}_{\boldsymbol{p}}\mathbf{u} - \sigma \cdot \mathbf{u}, \mathcal{H}_{\boldsymbol{p}}\mathbf{v} - \sigma \cdot \mathbf{v}, \overline{\boldsymbol{o}_{-}\boldsymbol{o}_{+}}] = 0; \tag{B.25}$$

$$\det[\mathcal{H}_{\boldsymbol{p}}\mathbf{u} - \sigma \cdot \mathbf{u}, \mathcal{H}_{\boldsymbol{p}}\mathbf{v} - \sigma \cdot \mathbf{v}, \mathcal{H}_{\boldsymbol{p}}w - \sigma \cdot \mathbf{w}] = 0. \tag{B.26}$$

In particular, by taking $\mathbf{u} = \mathbf{M}_{ax}$, $\mathbf{v} = \mathbf{M}_{in}$ and $\mathbf{w} = \boldsymbol{\omega}$, we have:

$$\det\left[\ \mathbf{B}_{max}-\sigma\mathbf{M}_{\mathrm{ax}},\quad \mathbf{B}_{min}-\sigma\mathbf{M}_{\mathrm{in}},\quad \overline{\boldsymbol{o}_{-}\boldsymbol{o}_{+}}\ \right]=0 \tag{B.27}$$

and

$$\det\left[\ \mathbf{B}_{max}-\sigma\mathbf{M}_{\mathrm{ax}},\quad \mathbf{B}_{min}-\sigma\mathbf{M}_{\mathrm{in}},\quad (\mathsf{M}^2\cdot\det\mathcal{H}_{\boldsymbol{p}})\hat{\mathbf{\Omega}}-\sigma\omega\ \right]=0. \tag{B.28}$$

B.4.4 A fundamental lemma for calculating dipole moments

As mentioned at the beginning, the vectors $\mathbf{M}_{ax},\mathbf{M}_{in}$ are not directly measured in the experiments. We now give a lemma (Lemma 1) showing how $\mathbf{M}_{ax},\mathbf{M}_{in}$ can be calculated from $\mathbf{B}_{max},\mathbf{B}_{min}$ (and $\hat{\mathbf{\Omega}}$, M) under certain conditions. This lemma will play an important role in later discussion. From the symmetry of $\mathcal{H}_{\boldsymbol{p}}$ and the skew-symmetry of $J_{\hat{\mathbf{\Omega}}}$ we have:

$$\langle\mathbf{M}_{in},\mathcal{H}_{\boldsymbol{p}}J_{\hat{\mathbf{\Omega}}}\mathbf{M}_{in}\rangle=\langle J_{\hat{\mathbf{\Omega}}}^{T}\mathcal{H}_{\boldsymbol{p}}\mathbf{M}_{in},\mathbf{M}_{in}\rangle=-\langle\mathbf{M}_{in},J_{\hat{\mathbf{\Omega}}}\mathcal{H}_{\boldsymbol{p}}\mathbf{M}_{in}\rangle \tag{B.29}$$

and

$$\langle\mathbf{M}_{ax},\mathcal{H}_{\boldsymbol{p}}J_{\hat{\mathbf{\Omega}}}\mathbf{M}_{ax}\rangle=\langle J_{\hat{\mathbf{\Omega}}}^{T}\mathcal{H}_{\boldsymbol{p}}\mathbf{M}_{ax},\mathbf{M}_{ax}\rangle=-\langle\mathbf{M}_{ax},J_{\hat{\mathbf{\Omega}}}\mathcal{H}_{\boldsymbol{p}}\mathbf{M}_{ax}\rangle. \tag{B.30}$$

Note that $\mathcal{H}_{\boldsymbol{p}}J_{\Omega}\mathbf{M}_{in}=-\mathbf{B}_{max}$ and $J_{\hat{\mathbf{\Omega}}}\mathcal{H}_{\boldsymbol{p}}\mathbf{M}_{in}=\hat{\mathbf{\Omega}}\times\mathbf{B}_{min}$, and then Equation (B.29) yields

$$\langle\mathbf{M}_{in},\mathbf{B}_{max}-\hat{\mathbf{\Omega}}\times\mathbf{B}_{min}\rangle=0. \tag{B.31}$$

Similarly, $\mathcal{H}_{\boldsymbol{p}}J_{\hat{\mathbf{\Omega}}}\mathbf{M}_{ax}=\mathbf{B}_{min}$ and $J_{\hat{\mathbf{\Omega}}}\mathcal{H}_{\boldsymbol{p}}\mathbf{M}_{ax}=\hat{\mathbf{\Omega}}\times\mathbf{B}_{max}$, and then Equation (B.30) gives

$$\langle\mathbf{M}_{ax},\mathbf{B}_{min}+\hat{\mathbf{\Omega}}\times\mathbf{B}_{max}\rangle=0. \tag{B.32}$$

Define

$$\mathbf{V}=\mathbf{B}_{max}-\hat{\mathbf{\Omega}}\times\mathbf{B}_{min} \tag{B.33}$$

and

$$\mathbf{W}=\mathbf{B}_{min}+\hat{\mathbf{\Omega}}\times\mathbf{B}_{max}. \tag{B.34}$$

The discussion above leads to the following lemma.

Lemma 1: If $\hat{\mathbf{\Omega}}\times\mathbf{V}\neq 0$, then

$$\mathbf{M}_{in}=\pm\mathsf{M}\frac{\hat{\mathbf{\Omega}}\times\mathbf{V}}{|\hat{\mathbf{\Omega}}\times\mathbf{V}|}.$$

Similarly, if $\hat{\mathbf{\Omega}} \times \mathbf{W} \neq 0$, then

$$\mathbf{M}_{ax} = \pm \mathsf{M} \frac{\hat{\mathbf{\Omega}} \times \mathbf{W}}{|\hat{\mathbf{\Omega}} \times \mathbf{W}|}.$$

Lemma 2: If $\hat{\mathbf{\Omega}} \times \mathbf{V} = 0$, then $\hat{\mathbf{\Omega}} \cdot \mathbf{B}_{min} = 0$ and $\mathbf{W} = 0$.

Lemma 1 follows directly from that fact that $\mathbf{M}_{in} \perp \mathbf{V}, \hat{\mathbf{\Omega}}$ and $\mathbf{M}_{ax} \perp \mathbf{W}, \hat{\mathbf{\Omega}}$. While the Lemma 1 guarantees the calculation of $\mathbf{M}_{in}$ and $\mathbf{M}_{ax}$ when specific conditions hold. Lemma 2 tells the implication of the failure(s) of these conditions, which will also be exploited in later discussion (see Proof 4).

Proof 4: Note that $\hat{\mathbf{\Omega}} \times \mathbf{V} = \hat{\mathbf{\Omega}} \times \mathbf{B}_{max} - \hat{\mathbf{\Omega}} \times (\hat{\mathbf{\Omega}} \times \mathbf{B}_{min}) = \hat{\mathbf{\Omega}} \times \mathbf{B}_{max} - (\hat{\mathbf{\Omega}} \cdot \mathbf{B}_{min})\hat{\mathbf{\Omega}} + \mathbf{B}_{min} = \mathbf{W} - (\hat{\mathbf{\Omega}} \cdot \mathbf{B}_{min})\hat{\mathbf{\Omega}}$. If $\hat{\mathbf{\Omega}} \times \mathbf{V} = 0$, then

$$0 = \langle \hat{\mathbf{\Omega}} \times \mathbf{V}, \mathbf{B}_{max} \rangle = (\hat{\mathbf{\Omega}} \cdot \mathbf{B}_{min})(\hat{\mathbf{\Omega}} \cdot \mathbf{B}_{max}),$$

implying either $\hat{\mathbf{\Omega}} \cdot \mathbf{B}_{min} = 0$ or $\hat{\mathbf{\Omega}} \cdot \mathbf{B}_{max} = 0$. We show that when $\hat{\mathbf{\Omega}} \cdot \mathbf{B}_{max} = 0$, $\hat{\mathbf{\Omega}} \cdot \mathbf{B}_{min} = 0$ also holds. In this case, $|\hat{\mathbf{\Omega}} \times \mathbf{B}_{max}|^2 = |\mathbf{B}_{max}|^2 > 0$, and then

$$0 = \langle \hat{\mathbf{\Omega}} \times \mathbf{V}, \hat{\mathbf{\Omega}} \times \mathbf{B}_{max} \rangle = |\mathbf{B}_{max}|^2 + \langle \mathbf{B}_{min}, \hat{\mathbf{\Omega}} \times \mathbf{B}_{max} \rangle.$$

Since $|\langle \mathbf{B}_{min}, \mathbf{B}_{max} \times \hat{\mathbf{\Omega}} \rangle| \leq |\mathbf{B}_{min}| \cdot |\mathbf{B}_{max} \times \hat{\mathbf{\Omega}}| \leq |\mathbf{B}_{max}|^2$, the equation above implies

$$|\langle \mathbf{B}_{min}, \mathbf{B}_{max} \times \hat{\mathbf{\Omega}} \rangle| = |\mathbf{B}_{min}| \cdot |\mathbf{B}_{max} \times \hat{\mathbf{\Omega}}|,$$

which only holds when $\mathbf{B}_{min}$ is parallel to the nonzero vector $\mathbf{B}_{max} \times \hat{\mathbf{\Omega}}$, yielding $\hat{\mathbf{\Omega}} \cdot \mathbf{B}_{min} = 0$. From the equation at the beginning we get: $\mathbf{W} = \hat{\mathbf{\Omega}} \times \mathbf{V} + (\hat{\mathbf{\Omega}} \cdot \mathbf{B}_{min})\hat{\mathbf{\Omega}} = 0$.

B.5 Deducing the linear map at the case that the field-rotation axis is not perpendicular to the dipole-rotation axis

In this section, we discuss how to deduce the matrices of $\mathcal{H}_{\boldsymbol{p}}$ in certain coordinate systems from the data $\mathbf{B}_{max}$, $\mathbf{B}_{min}$, $\hat{\mathbf{\Omega}}$ and M. In this section,

we work on the case $\boldsymbol{\Omega} \cdot \boldsymbol{\omega} \neq 0$. Note that in this case, $\mathbf{B}_{min} \neq 0$. Note that we always have the following relation

$$\mathcal{H}_{\boldsymbol{p}} \left[\begin{array}{cccc} \mathbf{M}_{ax}; & \mathbf{M}_{in}; & \boldsymbol{\omega} \end{array} \right] = \left[\begin{array}{cccc} \mathbf{B}_{max}; & \mathbf{B}_{min}; & (\mathsf{M}^2 \cdot \det \mathcal{H}_{\boldsymbol{p}}) \hat{\boldsymbol{\Omega}} \end{array} \right]. \quad \text{(B.35)}$$

When $\boldsymbol{\Omega} \cdot \boldsymbol{\omega} \neq 0$, the matrix $\left[\begin{array}{cccc} \mathbf{M}_{ax}; & \mathbf{M}_{in}; & \boldsymbol{\omega} \end{array} \right]$ (with respect to the orthonormal basis $(\hat{\mathbf{B}}_{max}, \hat{\mathbf{B}}_{min}, \hat{\boldsymbol{\omega}})$ is invertible. Since $\mathbf{M}_{in} = J_{\hat{\boldsymbol{\Omega}}} \mathbf{M}_{ax}$, the inverse matrix

$$\left[\begin{array}{cccc} C_1; & C_2; & C_3 \end{array} \right]^T = \begin{bmatrix} C_1^T \\ C_2^T \\ C_3^T \end{bmatrix} := \left[\begin{array}{cccc} \mathbf{M}_{ax}; & \mathbf{M}_{in}; & \boldsymbol{\omega} \end{array} \right]^{-1} \quad \text{(B.36)}$$

is determined by $\mathbf{M}_{ax}$, where C_i are column vectors. Then

$$\mathcal{H}_{\boldsymbol{p}} = \left[\begin{array}{cccc} \mathbf{B}_{max}; & \mathbf{B}_{min}; & (\mathsf{M}^2 \cdot \det \mathcal{H}_{\boldsymbol{p}}) \hat{\boldsymbol{\Omega}} \end{array} \right] \cdot \left[\begin{array}{cccc} \mathbf{M}_{ax}; & \mathbf{M}_{in}; & \boldsymbol{\omega} \end{array} \right]^{-1} \quad \text{(B.37)}$$

is determined by $\mathbf{M}_{ax}$ (or $\hat{\mathbf{M}}_{ax} := \frac{\mathbf{M}_{ax}}{\mathsf{M}}$ equivalently) and $\det \mathcal{H}_{\boldsymbol{p}}$.

B.5.1 Dimensionality/Degrees of freedom

Note that we always have the following relation

$$\mathcal{H}_{\boldsymbol{p}} \left[\begin{array}{cccc} \mathbf{M}_{ax}; & \mathbf{M}_{in}; & \boldsymbol{\omega} \end{array} \right] = \left[\begin{array}{cccc} \mathbf{B}_{max}; & \mathbf{B}_{min}; & (\mathsf{M}^2 \cdot \det \mathcal{H}_{\boldsymbol{p}}) \hat{\boldsymbol{\Omega}} \end{array} \right]. \quad \text{(B.38)}$$

When $\boldsymbol{\Omega} \cdot \boldsymbol{\omega} \neq 0$, the matrix $\left[\begin{array}{cccc} \mathbf{M}_{ax}; & \mathbf{M}_{in}; & \boldsymbol{\omega} \end{array} \right]$ (with respect to the orthonormal basis $(\hat{\mathbf{B}}_{max}, \hat{\mathbf{B}}_{min}, \hat{\boldsymbol{\omega}})$ is invertible. Since $\mathbf{M}_{in} = J_{\hat{\boldsymbol{\Omega}}} \mathbf{M}_{ax}$, the inverse matrix

$$\left[\begin{array}{cccc} C_1; & C_2; & C_3 \end{array} \right]^T = \begin{bmatrix} C_1^T \\ C_2^T \\ C_3^T \end{bmatrix} = \left[\begin{array}{cccc} \mathbf{M}_{ax}; & \mathbf{M}_{in}; & \boldsymbol{\omega} \end{array} \right]^{-1} \quad \text{(B.39)}$$

is determined by $\mathbf{M}_{ax}$, where C_i are column vectors. Then

$$\mathcal{H}_{\boldsymbol{p}} = \left[\begin{array}{cccc} \mathbf{B}_{max}; & \mathbf{B}_{min}; & (\mathsf{M}^2 \cdot \det \mathcal{H}_{\boldsymbol{p}}) \hat{\boldsymbol{\Omega}} \end{array} \right] \cdot \left[\begin{array}{cccc} \mathbf{M}_{ax}; & \mathbf{M}_{in}; & \boldsymbol{\omega} \end{array} \right]^{-1} \quad \text{(B.40)}$$

is determined by $\mathbf{M}_{ax}$ (or $\hat{\mathbf{M}}_{ax} = \frac{\mathbf{M}_{ax}}{\mathsf{M}}$ equivalently) and $\det \mathcal{H}_{\boldsymbol{p}}$. Note that $\hat{\mathbf{M}}_{ax} \in S^1_{\hat{\boldsymbol{\Omega}}} := S^2 \bigcap \mathcal{N}_{\hat{\boldsymbol{\Omega}}}$ and $\det \mathcal{H}_{\boldsymbol{p}} \in \mathbb{R}$. Since $S^1_{\hat{\boldsymbol{\Omega}}} \times \mathbb{R}$ is a two dimensional space, we need at least two equations to determine the pair $(\mathbf{M}_{ax}, \det \mathcal{H}_{\boldsymbol{p}})$ (or $(\hat{\mathbf{M}}_{ax}, \det \mathcal{H}_{\boldsymbol{p}})$). As we will see, these equations come from the properties that the trace of $\mathcal{H}_{\boldsymbol{p}}$ is zero and that $\mathcal{H}_{\boldsymbol{p}}$ is symmetric.

B.5.2 Calculation of the inverse matrix

From $C_1 \cdot \mathbf{M}_{ax} = 1$ and $C_1 \cdot \mathbf{M}_{in} = 0$ we know that C_1 takes the form

$$C_1 = \frac{\mathbf{M}_{ax}}{\mathsf{M}^2} + a\hat{\mathbf{\Omega}}, \tag{B.41}$$

where a is a real number satisfying the relation

$$\langle C_1, \boldsymbol{\omega} \rangle = \frac{\boldsymbol{\omega} \cdot \mathbf{M}_{ax}}{\mathsf{M}^2} + a\hat{\mathbf{\Omega}} \cdot \boldsymbol{\omega} = 0. \tag{B.42}$$

Similarly, we have

$$C_2 = \frac{\mathbf{M}_{in}}{\mathsf{M}^2} + b\hat{\mathbf{\Omega}} \tag{B.43}$$

for some real number b with

$$\langle C_2, \boldsymbol{\omega} \rangle = \frac{\boldsymbol{\omega} \cdot \mathbf{M}_{in}}{\mathsf{M}^2} + b\hat{\mathbf{\Omega}} \cdot \boldsymbol{\omega} = 0. \tag{B.44}$$

From $C_3 \cdot \mathbf{M}_{ax} = C_3 \cdot \mathbf{M}_{in} = 0$ we know that $C_3 = \mathrm{k}\hat{\mathbf{\Omega}}$, and then from $C_3 \cdot \boldsymbol{\omega} = 1$ we know

$$C_3 = \frac{1}{\hat{\mathbf{\Omega}} \cdot \boldsymbol{\omega}} \hat{\mathbf{\Omega}}. \tag{B.45}$$

Although the vectors C_1, C_2 and C_3 seems to be defined in the first place in a certain coordinate system w.r.t. some specific orthonormal basis, they are actually the Riez representations (w.r.t. $\langle\ ,\ \rangle$) of the functionals f_{ax}, f_{in}, f_{om} which form the dual basis (f_{ax}, f_{in}, f_{om}) to the basis $(\mathbf{M}_{ax}, \mathbf{M}_{in}, \boldsymbol{\omega})$.

B.5.3 The trace and the determinant of the linear map

In this subsection we exploit the property $\mathrm{tr}\mathcal{H}_{\boldsymbol{p}} = 0$ to represent $\det \mathcal{H}_{\boldsymbol{p}}$ as a function of $\mathbf{M}_{ax}$. We first derive and express such a relation in the coordinate system with respect to the orthonormal basis $(\hat{\mathbf{B}}_{max}, \hat{\mathbf{B}}_{min}, \hat{\boldsymbol{\omega}})$ as Equation (B.49), and then re-derive and re-express the relation as Equations (B.57) (and (B.58), equivalently) in a coordinate-independent way. In $(\hat{\mathbf{B}}_{max}, \hat{\mathbf{B}}_{min}, \hat{\boldsymbol{\omega}})$-coordinate system, the matrix of $\mathcal{H}_{\boldsymbol{p}}$ is

$$\mathcal{H}_{\boldsymbol{p}} = \begin{bmatrix} |\mathbf{B}_{max}| & 0 & \mathrm{h}\Omega_1 \\ 0 & |\mathbf{B}_{min}| & \mathrm{h}\Omega_2 \\ 0 & 0 & \mathrm{h}\Omega_3 \end{bmatrix} \cdot \begin{bmatrix} C_1^T \\ C_2^T \\ C_3^T \end{bmatrix} \tag{B.46}$$

with $\mathrm{h}=\mathsf{M}^2 \cdot \det \mathcal{H}_{\boldsymbol{p}}$. Then,

$$\begin{aligned} &\operatorname{trace}\begin{bmatrix} |\mathbf{B}_{max}| & 0 & \mathrm{h}\Omega_1 \\ 0 & |\mathbf{B}_{min}| & \mathrm{h}\Omega_2 \\ 0 & 0 & \mathrm{h}\Omega_3 \end{bmatrix} \cdot \begin{bmatrix} C_1^T \\ C_2^T \\ C_3^T \end{bmatrix} = \\ &\operatorname{trace}\begin{bmatrix} C_1^T \\ C_2^T \\ C_3^T \end{bmatrix} \cdot \begin{bmatrix} |\mathbf{B}_{max}| & 0 & \mathrm{h}\Omega_1 \\ 0 & |\mathbf{B}_{min}| & \mathrm{h}\Omega_2 \\ 0 & 0 & \mathrm{h}\Omega_3 \end{bmatrix} = 0 \end{aligned} \tag{B.47}$$

yields

$$|\mathbf{B}_{max}|\left(\frac{m_1}{\mathsf{M}^2}+\mathbf{a}\Omega_1\right)+|\mathbf{B}_{min}|\left(\frac{\Omega_3 m_1-\Omega_1 m_3}{\mathsf{M}^2}+\mathbf{b}\Omega_2\right)+\frac{\mathsf{M}^2\cdot\det\mathcal{H}_{\boldsymbol{p}}}{\hat{\boldsymbol{\Omega}}\cdot\boldsymbol{\omega}}=0. \tag{B.48}$$

Since $\mathbf{a}$ and $\mathbf{b}$ are both functions of $\mathbf{M}_{ax}=(m_1,m_2,m_3)^{\mathrm{T}}$ (Equations (B.42) and (B.44)), Equation (B.48) realizes $\det\mathcal{H}_{\boldsymbol{p}}$ as a function of $\mathbf{M}_{ax}$ in the $(\hat{\mathbf{B}}_{max},\hat{\mathbf{B}}_{min},\hat{\boldsymbol{\omega}})$-coordinate system. Multiplying both of its sides by $\hat{\boldsymbol{\Omega}}\cdot\boldsymbol{\omega}=\Omega_3|\boldsymbol{\omega}|$ (which is not 0), Equation (B.48) gives

$$\det\mathcal{H}_{\boldsymbol{p}}=\frac{|\boldsymbol{\omega}|}{\mathsf{M}^4}\langle\hat{\boldsymbol{\Omega}}\times\mathcal{U},\mathbf{M}_{ax}\rangle \tag{B.49}$$

with

$$\mathcal{U}=(0,|\mathbf{B}_{max}|+\Omega_3|\mathbf{B}_{min}|,-|\mathbf{B}_{min}|\Omega_2)^{\mathrm{T}}. \tag{B.50}$$

Recall that $(\bar{\mathbf{M}}_{ax},\det\mathcal{H}_{\boldsymbol{p}})\in S^1_{\hat{\boldsymbol{\Omega}}}\times\mathbb{R}$ determines the matrix of $\mathcal{H}_{\boldsymbol{p}}$, and then Equation (B.48) just reduces our question to 1 degree of freedom. That is, with Equation (B.48), $[\mathcal{H}_{\boldsymbol{p}}]$ is a (matrix-value) function of $\mathbf{M}_{ax}$. Now we re-derive and re-express the relation Equation (B.48) in a coordinate-independent way. Let (f_{ax},f_{in},f_{om}) be the dual basis to the basis $(\mathbf{M}_{ax},\mathbf{M}_{in},\boldsymbol{\omega})$. Then

$$\begin{aligned} \mathrm{tr}\mathcal{H}_{\boldsymbol{p}} &= f_{ax}\big(\mathcal{H}_{\boldsymbol{p}}\mathbf{M}_{ax}\big)+f_{in}\big(\mathcal{H}_{\boldsymbol{p}}\mathbf{M}_{in}\big)+f_{om}\big(\mathcal{H}_{\boldsymbol{p}}\boldsymbol{\omega}\big) \\ &= f_{ax}\big(\mathbf{B}_{max}\big)+f_{in}\big(\mathbf{B}_{min}\big)+f_{om}\big(\mathrm{h}\hat{\boldsymbol{\Omega}}\big)=0. \end{aligned} \tag{B.51}$$

Note that the Riez representations of the linear functions f_{ax},f_{in},f_{om} with respect to the standard Euclidean form $\langle\ ,\ \rangle$ are exactly $\mathbf{M}_{ax}+a\hat{\boldsymbol{\Omega}}$, $\mathbf{M}_{in}+b\hat{\boldsymbol{\Omega}}$ and $\frac{1}{\hat{\boldsymbol{\Omega}}\cdot\boldsymbol{\omega}}\hat{\boldsymbol{\Omega}}$, respectively, where $a=-\frac{\boldsymbol{\omega}\cdot\mathbf{M}_{ax}}{\mathsf{M}^2\hat{\boldsymbol{\Omega}}\cdot\boldsymbol{\omega}}$ and $b=-\frac{\boldsymbol{\omega}\cdot\mathbf{M}_{in}}{\mathsf{M}^2\hat{\boldsymbol{\Omega}}\cdot\boldsymbol{\omega}}$. As a result, we get

$$\frac{\mathbf{B}_{max}\cdot\mathbf{M}_{ax}}{\mathsf{M}^2}+a\hat{\boldsymbol{\Omega}}\cdot\mathbf{B}_{max}+\frac{\mathbf{B}_{min}\cdot\mathbf{M}_{in}}{\mathsf{M}^2}+b\hat{\boldsymbol{\Omega}}\cdot\mathbf{B}_{min}+\frac{\mathsf{M}^2\cdot\det\mathcal{H}_{\boldsymbol{p}}}{\hat{\boldsymbol{\Omega}}\cdot\boldsymbol{\omega}}=0. \tag{B.52}$$

Plugging the expressions for a and b above into Equation (B.52) gives

$$\frac{(\hat{\mathbf{\Omega}}\cdot\boldsymbol{\omega})\langle\mathbf{B}_{max},\mathbf{M}_{ax}\rangle}{\mathsf{M}^2(\hat{\mathbf{\Omega}}\cdot\boldsymbol{\omega})}-\frac{(\hat{\mathbf{\Omega}}\cdot\mathbf{B}_{max})\langle\boldsymbol{\omega},\mathbf{M}_{ax}\rangle}{\mathsf{M}^2(\hat{\mathbf{\Omega}}\cdot\boldsymbol{\omega})}+\frac{(\hat{\mathbf{\Omega}}\cdot\boldsymbol{\omega})\langle\mathbf{B}_{min},\mathbf{M}_{in}\rangle}{\mathsf{M}^2(\hat{\mathbf{\Omega}}\cdot\boldsymbol{\omega})}$$
$$-\frac{(\hat{\mathbf{\Omega}}\cdot\mathbf{B}_{min})\langle\boldsymbol{\omega},\mathbf{M}_{in}\rangle}{\mathsf{M}^2(\hat{\mathbf{\Omega}}\cdot\boldsymbol{\omega})}+\frac{\mathsf{M}^4\cdot\det\mathcal{H}_{\boldsymbol{p}}}{\mathsf{M}^2(\hat{\mathbf{\Omega}}\cdot\boldsymbol{\omega})}=0. \tag{B.53}$$

Using the following formula for cross-products

$$\hat{\mathbf{\Omega}}\times(\boldsymbol{\omega}\times\mathbf{B})=(\hat{\mathbf{\Omega}}\cdot\mathbf{B})\boldsymbol{\omega}-(\hat{\mathbf{\Omega}}\cdot\boldsymbol{\omega})\mathbf{B}, \tag{B.54}$$

we obtain from Equation (B.53) the following equation

$$-\langle\hat{\mathbf{\Omega}}\times(\boldsymbol{\omega}\times\mathbf{B}_{max}),\mathbf{M}_{ax}\rangle-\langle\hat{\mathbf{\Omega}}\times(\boldsymbol{\omega}\times\mathbf{B}_{min}),\mathbf{M}_{in}\rangle+\mathsf{M}^4\cdot\det\mathcal{H}_{\boldsymbol{p}}=0, \tag{B.55}$$

or, equivalently,

$$\langle\boldsymbol{\omega}\times\mathbf{B}_{max},\hat{\mathbf{\Omega}}\times\mathbf{M}_{ax}\rangle+\langle\boldsymbol{\omega}\times\mathbf{B}_{min},\hat{\mathbf{\Omega}}\times\mathbf{M}_{in}\rangle+\mathsf{M}^4\cdot\det\mathcal{H}_{\boldsymbol{p}}=0. \tag{B.56}$$

Therefore,

$$\det\mathcal{H}_{\boldsymbol{p}}=-\frac{\langle\boldsymbol{\omega}\times\mathbf{B}_{max},\hat{\mathbf{\Omega}}\times\mathbf{M}_{ax}\rangle+\langle\boldsymbol{\omega}\times\mathbf{B}_{min},\hat{\mathbf{\Omega}}\times\mathbf{M}_{in}\rangle}{\mathsf{M}^4}. \tag{B.57}$$

Or, with $\boldsymbol{\omega}\times\mathbf{B}_{max}=|\mathbf{B}_{max}|^2\mathbf{B}_{min}$ and $\boldsymbol{\omega}\times\mathbf{B}_{min}=-|\mathbf{B}_{min}|^2\mathbf{B}_{max}$,

$$\det\mathcal{H}_{\boldsymbol{p}}=\frac{\langle\hat{\mathbf{\Omega}}\times|\mathbf{B}_{max}|^2\mathbf{B}_{min}-|\mathbf{B}_{min}|^2\mathbf{B}_{max},\mathbf{M}_{ax}\rangle}{\mathsf{M}^4}. \tag{B.58}$$

It is straightforward to check that in $(\hat{\mathbf{B}}_{max},\hat{\mathbf{B}}_{min},\hat{\boldsymbol{\omega}})$-coordinate system, Equation (B.58) (and Equation (B.57) as well) becomes Equation B.49). Note that for Equation (B.51) to be valid, $(\mathbf{M}_{ax},\mathbf{M}_{in},\boldsymbol{\omega})$ should be a basis, for which the condition that $\hat{\mathbf{\Omega}}\cdot\boldsymbol{\omega}\neq 0$ is sufficient and necessary.

B.5.4 The mag-det system and a brief discussion

Combining Equation (B.58) with the magnetic Equations (B.27) and (B.28), we get the following system of 3 equations for 3 variables, $\mathbf{M}_{ax}$, σ and

$\det \mathcal{H}_{\boldsymbol{p}}$:

$$\begin{cases} \det \left[\begin{array}{lll} \mathbf{B}_{max} - \sigma \mathbf{M}_{ax}, & \mathbf{B}_{min} - \sigma \mathbf{M}_{in}, & \overline{o_- o_+} \end{array} \right] = 0, \\ \det \left[\begin{array}{lll} \mathbf{B}_{max} - \sigma \mathbf{M}_{ax}, & \mathbf{B}_{min} - \sigma \mathbf{M}_{in}, & (\mathsf{M}^2 \cdot \det \mathcal{H}_{\boldsymbol{p}}) \hat{\boldsymbol{\Omega}} - \sigma \boldsymbol{\omega} \end{array} \right] = 0, \\ \det \mathcal{H}_{\boldsymbol{p}} = \frac{\langle \hat{\boldsymbol{\Omega}} \times |\mathbf{B}_{max}|^2 \mathbf{B}_{min} - |\mathbf{B}_{min}|^2 \mathbf{B}_{max}, \mathbf{M}_{ax} \rangle}{\mathsf{M}^4}. \end{cases} \tag{B.59}$$

Hopefully, these equations will be sufficient to determine the values of $\mathbf{M}_{ax}$ (or $\mathbf{M}_{in}$, equivalently), σ and $\det \mathcal{H}_{\boldsymbol{p}}$ in general cases, by which we can write down the matrix of $\mathcal{H}_{\boldsymbol{p}}$. However, the nonlinearity of Equations (B.27) and (B.28) might complicate the computation. Therefore, we would avoid dealing with the geo-det system (B.59) directly unless necessary. Fortunately, by Lemma B.4.4, in the case $\hat{\boldsymbol{\Omega}} \times \mathbf{V} \neq 0$, we immediately solve $\mathbf{M}_{in} = \pm \mathsf{M} \frac{\hat{\boldsymbol{\Omega}} \times \mathbf{V}}{|\hat{\boldsymbol{\Omega}} \times \mathbf{V}|}$, then calculate the value $\det \mathcal{H}_{\boldsymbol{p}}$ by Equation (B.58), and eventually, obtain the matrix $[\mathcal{H}_{\boldsymbol{p}}]$ by Equation(B.46).

B.6 Deducing the linear map at the case that the field-rotation axis is perpendicular to the dipole-rotation axis

In this section, further work in deducing the linear map must take into account whether the field-rotation axis vector is the zero vector in the case that the field-rotation axis is perpendicular to the dipole-rotation axis.

B.6.1 The field-rotation axis vector is not equivalent to the zero vector

Now we deal with the case where $\boldsymbol{\Omega} \cdot \boldsymbol{\omega} = 0$ with $\boldsymbol{\omega} \neq 0$. Let $\mathbf{u} = \hat{\boldsymbol{\Omega}} \times \hat{\boldsymbol{\omega}}$, and then $(\hat{\boldsymbol{\omega}}, \mathbf{u}, \hat{\boldsymbol{\Omega}})$ constitutes an orthonormal frame of $\big(\mathbb{R}^3, \langle\ ,\ \rangle\big)$. Note that in this case, $(\hat{\boldsymbol{\omega}}, \mathbf{u})$ constitutes an orthonormal basis of the plane $\mathcal{N}_{\hat{\boldsymbol{\Omega}}} = \mathrm{span}\{\mathbf{M}_t\}$. Since $(\mathbf{M}_{ax}, \mathbf{M}_{in})$ is also an orthonormal basis of $\mathcal{N}_{\hat{\boldsymbol{\Omega}}}$ and $\mathbf{M}_{ax} \times \mathbf{M}_{in} = \hat{\boldsymbol{\Omega}} = \hat{\boldsymbol{\omega}} \times \mathbf{u}$, there exists a rotation

$$\mathcal{R}_\theta = \begin{bmatrix} \cos\beta_0 & -\sin\beta_0 \\ \sin\beta_0 & \cos\beta_0 \end{bmatrix} \tag{B.60}$$

on $\mathcal{N}_{\hat{\mathbf{\Omega}}}$ such that

$$(\hat{\boldsymbol{\omega}}, \mathbf{u}) \begin{bmatrix} \cos\beta_0 & -\sin\beta_0 \\ \sin\beta_0 & \cos\beta_0 \end{bmatrix} = (\mathbf{M}_{ax}, \mathbf{M}_{in}), \tag{B.61}$$

or, equivalently,

$$(\hat{\boldsymbol{\omega}}, \mathbf{u}) = (\mathbf{M}_{ax}, \mathbf{M}_{in}) \begin{bmatrix} \cos\beta_0 & \sin\beta_0 \\ -\sin\beta_0 & \cos\beta_0 \end{bmatrix}. \tag{B.62}$$

Therefore, we have

$$\hat{\boldsymbol{\omega}} = \cos\beta_0 \cdot \mathbf{M}_{ax} - \sin\beta_0 \cdot \mathbf{M}_{in}. \tag{B.63}$$

Since $\mathcal{H}_{\boldsymbol{p}}\hat{\boldsymbol{\omega}} = \frac{\mathsf{M}^2 \det \mathcal{H}_{\boldsymbol{p}}}{|\boldsymbol{\omega}|}\hat{\mathbf{\Omega}}$ is perpendicular to $\mathbf{u}$, we have

$$0 = \langle \mathcal{H}_{\boldsymbol{p}}\hat{\boldsymbol{\omega}}, \mathbf{u}\rangle = \cos\beta_0 \cdot \langle \mathbf{B}_{max}, \mathbf{u}\rangle - \sin\beta_0 \cdot \langle \mathbf{B}_{min}, \mathbf{u}\rangle, \tag{B.64}$$

which means

$$\begin{bmatrix} \cos\beta_0 \\ \sin\beta_0 \end{bmatrix} = k \cdot \begin{bmatrix} \langle \mathbf{B}_{min}, \mathbf{u}\rangle \\ \langle \mathbf{B}_{max}, \mathbf{u}\rangle \end{bmatrix} \tag{B.65}$$

with $k = \pm\frac{1}{\sqrt{\langle \mathbf{B}_{min},\mathbf{u}\rangle^2 + \langle \mathbf{B}_{max},\mathbf{u}\rangle^2}}$. (note that the sign $\pm$ needs to be determined by experimental data). With Equation (B.65), $\mathbf{M}_{ax}$ and $\mathbf{M}_{in}$ can be calculated by Equation (B.61). To calculate $\det \mathcal{H}_{\boldsymbol{p}}$, we exploit the inner product

$$\langle \mathcal{H}_{\boldsymbol{p}}\hat{\boldsymbol{\omega}}, \hat{\mathbf{\Omega}}\rangle = \frac{\mathsf{M}^2 \det \mathcal{H}_{\boldsymbol{p}}}{|\boldsymbol{\omega}|},$$

which, together with Equation (B.65), gives

$$\frac{\mathsf{M}^2 \det \mathcal{H}_{\boldsymbol{p}}}{|\boldsymbol{\omega}|} = \pm\frac{\langle \mathbf{B_{min}}, \mathbf{u}\rangle \cdot \langle \mathbf{B}_{max}, \hat{\mathbf{\Omega}}\rangle - \langle \mathbf{B_{max}}, \mathbf{u}\rangle \cdot \langle \mathbf{B_{min}}, \hat{\mathbf{\Omega}}\rangle}{\sqrt{\langle \mathbf{B_{min}}, \mathbf{u}\rangle^2 + \langle \mathbf{B_{max}}, \mathbf{u}\rangle^2}}. \tag{B.66}$$

Since $\hat{\mathbf{\Omega}}$, $\boldsymbol{\omega}$, $\mathbf{u}$, $\mathbf{B}_{max}$, $\mathbf{B}_{min}$, M are either measured or calculated from the data obtained in the experiments, Equation (B.66) indeed gives the value of $\det \mathcal{H}_{\boldsymbol{p}}$. Now we proceed to calculate the linear map $\mathcal{H}_{\boldsymbol{p}}$. With respect to the orthonormal basis $(\hat{\boldsymbol{\omega}}, \mathbf{u}, \hat{\mathbf{\Omega}})$, the matrix representation $[\mathcal{H}_{\boldsymbol{p}}]$ of $\mathcal{H}_{\boldsymbol{p}}$ is symmetric and has trace 0. We have

$$\mathcal{H}_{\boldsymbol{p}}\big[\hat{\boldsymbol{\omega}}; \mathbf{u}; \hat{\mathbf{\Omega}}\big] = \left[\frac{\mathsf{M}^2 \det \mathcal{H}_{\boldsymbol{p}}}{|\boldsymbol{\omega}|}\hat{\mathbf{\Omega}}; \mathcal{H}_{\boldsymbol{p}}\mathbf{u}; \mathcal{H}_{\boldsymbol{p}}\hat{\mathbf{\Omega}}\right]. \tag{B.67}$$

The matrix $[\hat{\boldsymbol{\omega}}; \mathbf{u}; \hat{\boldsymbol{\Omega}}]$ with respect to $(\hat{\boldsymbol{\omega}}, \mathbf{u}, \hat{\boldsymbol{\Omega}})$ is just

$$\left[\hat{\boldsymbol{\omega}}; \mathbf{u}; \hat{\boldsymbol{\Omega}}\right] = \begin{bmatrix} 1 & 0 & 0 \\ 0 & 1 & 0 \\ 0 & 0 & 1 \end{bmatrix}, \tag{B.68}$$

and hence the 0-trace symmetric matrix $[\mathcal{H}_{\boldsymbol{p}}]$ has the form

$$[\mathcal{H}_{\boldsymbol{p}}] = \left[(\mathsf{M}^2 \cdot \det \mathcal{H}_{\boldsymbol{p}})\frac{\hat{\boldsymbol{\Omega}}}{|\boldsymbol{\omega}|}; \mathcal{H}_{\boldsymbol{p}}\mathbf{u}; \mathcal{H}_{\boldsymbol{p}}\hat{\boldsymbol{\Omega}}\right] = \begin{bmatrix} 0 & 0 & \frac{\mathsf{M}^2 \cdot \det \mathcal{H}_{\boldsymbol{p}}}{|\boldsymbol{\omega}|} \\ 0 & -b & c \\ \frac{\mathsf{M}^2 \cdot \det \mathcal{H}_{\boldsymbol{p}}}{|\boldsymbol{\omega}|} & c & b \end{bmatrix}. \tag{B.69}$$

The matrix representation for the linear map $\mathcal{A} = J_{\hat{\boldsymbol{\Omega}}}^T \mathcal{H}_{\boldsymbol{p}}^2 J_{\hat{\boldsymbol{\Omega}}}$ with respect to $(\hat{\boldsymbol{\omega}}, \mathbf{u}, \hat{\boldsymbol{\Omega}}$ is then

$$[\mathcal{A}] = \begin{bmatrix} b^2 + c^2 & -cD & 0 \\ -cD & D^2 & 0 \\ 0 & 0 & 0 \end{bmatrix} \tag{B.70}$$

with $D = \frac{\mathsf{M}^2 \cdot \det \mathcal{H}_{\boldsymbol{p}}}{|\boldsymbol{\omega}|}$. From Equation (B.69) we get the following equation

$$\det \mathcal{H}_{\boldsymbol{p}} = b \cdot \left(\frac{\mathsf{M}^2 \cdot \det \mathcal{H}_{\boldsymbol{p}}}{|\boldsymbol{\omega}|}\right)^2 = b \cdot D^2. \tag{B.71}$$

Meanwhile, as is discussed in Section B.4, the restriction of $\mathcal{A}$ to the plane $pl_{\{\mathbf{M}_t\}} = \text{span}\{\hat{\boldsymbol{\omega}}, \mathbf{u}\}$ has eigenvalue $|\mathbf{B}_{max}|^2$ and $|\mathbf{B}_{min}|^2$, and hence from Equation (B.69) we have

$$\det \mathcal{A} = b^2 D^2 = |\mathbf{B}_{max}|^2 |\mathbf{B}_{min}|^2 \tag{B.72}$$

and

$$\text{trace}\mathcal{A} = b^2 + c^2 + D^2 = |\mathbf{B}_{max}|^2 + |\mathbf{B}_{min}|^2. \tag{B.73}$$

Now we are ready to compute b and c, by which we will have complete information about the matrix $[\mathcal{H}_{\boldsymbol{p}}]$. Since $\boldsymbol{\omega} = \mathbf{B}_{max} \times \mathbf{B}_{min}$, $\boldsymbol{\omega} \neq 0$ if and only if $\mathbf{B}_{max}$ and $\mathbf{B}_{min}$ are both non-zero, and then with Equation (B.72) it implies that $b, D \neq 0$. Combining Equations (B.72) with (B.71) gives

$$b = \frac{|\mathbf{B}_{max}|^2 |\mathbf{B}_{min}|^2}{\det \mathcal{H}_{\boldsymbol{p}}}. \tag{B.74}$$

To calculate c, note that $c = \langle \mathcal{H}_{\boldsymbol{p}}\mathbf{u}, \hat{\mathbf{\Omega}}\rangle$, and then from Equation (B.62), we get

$$\begin{aligned} c &= \langle \mathcal{H}_{\boldsymbol{p}}\mathbf{u}, \hat{\mathbf{\Omega}}\rangle \\ &= \sin\theta \cdot \langle \mathbf{B}_{max}, \hat{\mathbf{\Omega}}\rangle + \cos\theta \cdot \langle \mathbf{B}_{min}, \hat{\mathbf{\Omega}}\rangle \\ &= \pm \frac{\langle \mathbf{B}_{max}, \mathbf{u}\rangle \cdot \langle \mathbf{B}_{max}, \hat{\mathbf{\Omega}}\rangle + \langle \mathbf{B}_{min}, \mathbf{u}\rangle \cdot \langle \mathbf{B}_{min}, \hat{\mathbf{\Omega}}\rangle}{\sqrt{\langle \mathbf{B}_{max}, \mathbf{u}\rangle^2 + \langle \mathbf{B}_{min}, \mathbf{u}\rangle^2}}. \end{aligned} \tag{B.75}$$

The calculation of $[\mathcal{H}_{\boldsymbol{p}}]$ is thus completed.

B.6.2 The field-rotation axis vector is equivalent to the zero vector

Now we deal with the case where $\mathbf{\Omega}\cdot\boldsymbol{\omega} = 0$ with the case $\boldsymbol{\omega} = 0$. Recall that $\mathbf{B}_{min}$ is always perpendicular to $\mathbf{B}_{max}$ (Section B.4) and $|\mathbf{B}_{min}| \leq |\mathbf{B}_{max}|$. Therefore, $\boldsymbol{\omega} = \mathbf{B}_{max} \times \mathbf{B}_{min} = 0$ if and only if

$$\mathbf{B}_{min} = \mathcal{H}_{\boldsymbol{p}}\mathbf{M}_{in} = 0. \tag{B.76}$$

In this case, $\mathbf{M}_{in}$ is an eigenvector corresponding to the eigenvalue $\sigma_- = 0$. As a consequence,

$$\mathcal{N}_{\mathbf{M}_{in}} = \{\mathbf{u} \in \mathbb{R}^3 \big| \mathbf{u}\cdot\mathbf{M}_{in} = 0\} = \mathrm{span}\{\mathbf{M}_{ax}, \mathbf{\Omega}\}$$

is an invariant subspace of the linear operator $\mathcal{H}_{\boldsymbol{p}}$, which contains the eigenspaces of σ_+ and σ. Thus $\mathbf{B}_{max} = \mathcal{H}_{\boldsymbol{p}}\mathbf{M}_{ax}$ is then contained in $\mathcal{N}_{\mathbf{M}_{in}}$. Note that since the rank of $\mathcal{H}_{\boldsymbol{p}}$ is at least 2, $\mathbf{B}_{max}$ is always non-zero.

Although the vectors $\hat{\mathbf{M}}_{ax}$ and $\hat{\mathbf{M}}_{in}$ are still to be determined, we can still write down the form of the matrix representation $[\mathcal{H}_{\boldsymbol{p}}]$ with respect to the orthonormal basis $(\hat{\mathbf{M}}_{ax}, \hat{\mathbf{M}}_{in}, \hat{\mathbf{\Omega}})$. Representing the vectors with their coordinates w.r.t. the basis $(\hat{\mathbf{M}}_{ax}, \hat{\mathbf{M}}_{in}, \hat{\mathbf{\Omega}})$ and considering that $\mathbf{B}_{min} = 0$, we have

$$[\mathcal{H}_{\boldsymbol{p}}][\hat{\mathbf{M}}_{ax}; \hat{\mathbf{M}}_{in}; \hat{\mathbf{\Omega}}] = [\frac{\mathbf{B}_{max}}{\mathsf{M}}; \frac{\mathbf{B}_{min}}{\mathsf{M}}; \mathcal{H}_{\boldsymbol{p}}\hat{\mathbf{\Omega}}] = [\frac{\mathbf{B}_{max}}{\mathsf{M}}; \mathbf{0}; \mathcal{H}_{\boldsymbol{p}}\hat{\mathbf{\Omega}}]. \tag{B.77}$$

Note that w.r.t. $(\hat{\mathbf{M}}_{ax}, \hat{\mathbf{M}}_{in}, \hat{\mathbf{\Omega}})$, $\mathbf{B}_{max} = [k_1\ 0\ k_3]^T$. Because $\hat{\mathbf{M}}_{ax}, \hat{\mathbf{M}}_{in}, \hat{\mathbf{\Omega}}$ is an orthonormal frame, the matrix $[\mathcal{H}_{\boldsymbol{p}}]$ is symmetry with 0 trace, and

the relations $|\mathbf{B}_{max}|^2 = k_1^2 + k_3^2$ and $k_3 = \langle \mathbf{B}_{max}, \hat{\mathbf{\Omega}} \rangle$ holds. Therefore,

$$[\mathcal{H}_{\boldsymbol{p}}] = \begin{bmatrix} k_1 & 0 & k_3 \\ 0 & 0 & 0 \\ k_3 & 0 & -k_1 \end{bmatrix}. \tag{B.78}$$

Since $\sigma_+\sigma = -\big(\frac{1}{|\boldsymbol{p}_+|^3} + \frac{1}{|\boldsymbol{p}_-|^3}\big)^2$ is the determinant of the restriction of $\mathcal{H}_{\boldsymbol{p}}$ to $\mathcal{N}_{\mathbf{M}_{in}} = \text{span}\{\mathbf{M}_{ax}, \hat{\mathbf{\Omega}}\}$, and hence

$$-\big(\frac{1}{|\boldsymbol{p}_+|^3} + \frac{1}{|\boldsymbol{p}_-|^3}\big)^2 = \det \begin{bmatrix} k_1 & k_3 \\ k_3 & -k_1 \end{bmatrix} = -k_1^2 - k_3^2 = -|\mathbf{B}_{max}|^2, \tag{B.79}$$

yielding

$$|\mathbf{B}_{max}| = \frac{1}{|\boldsymbol{p}_+|^3} + \frac{1}{|\boldsymbol{p}_-|^3}. \tag{B.80}$$

In the case $\hat{\mathbf{\Omega}} \times \mathbf{B}_{max} \neq 0$, the vector $\mathbf{V}$ in Section(B.4.4) becomes

$$\mathbf{V} = \mathbf{B}_{max} - \hat{\mathbf{\Omega}} \times \mathbf{B}_{min} = \mathbf{B}_{max}. \tag{B.81}$$

Then by Lemma 1 in Section(B.4.4), we deduce that If $\hat{\mathbf{\Omega}} \times \mathbf{B}_{max} \neq 0$, or, equivalently, $|\mathbf{B}_{max}|^2 \neq \langle \mathbf{B}_{max}, \hat{\mathbf{\Omega}} \rangle^2$, then

$$\mathbf{M}_{in} = \pm \mathsf{M} \frac{\hat{\mathbf{\Omega}} \times \mathbf{B}_{max}}{|\hat{\mathbf{\Omega}} \times \mathbf{B}_{max}|}. \tag{B.82}$$

In the case $\hat{\mathbf{\Omega}} \times \mathbf{B}_{max} = 0$, it holds $\mathbf{B}_{max} = \langle \mathbf{B}_{max}, \hat{\mathbf{\Omega}} \rangle \hat{\mathbf{\Omega}}$, and then

$$[\mathcal{H}_{\boldsymbol{p}}] = \begin{bmatrix} 0 & 0 & \langle \mathbf{B}_{max}, \hat{\mathbf{\Omega}} \rangle \\ 0 & 0 & 0 \\ \langle \mathbf{B}_{max}, \hat{\mathbf{\Omega}} \rangle & 0 & 0 \end{bmatrix}. \tag{B.83}$$

The linear map $[\mathcal{H}_{\boldsymbol{p}}]$ has a negative eigenvalue $\sigma = -|\langle \mathbf{B}_{max}, \hat{\mathbf{\Omega}} \rangle|$. If $\langle \mathbf{B}_{max}, \hat{\mathbf{\Omega}} \rangle > 0$, then $\mathbf{w} = [1\ 0\ -1]^{\mathrm{T}}$ is an eigenvector with eigenvector σ. If $\langle \mathbf{B}_{max}, \hat{\mathbf{\Omega}} \rangle < 0$, then $\mathbf{w}$ can be taken as $[1\ 0\ 1]^{\mathrm{T}}$. Note that from the definition of $\mathcal{H}_{\boldsymbol{p}}$ in Equation (B.2), the vector $\overline{\boldsymbol{o}_-\boldsymbol{o}_+}$ should be perpendicular to the eigenvector $\mathbf{w}$. That is,

$$\begin{cases} (\hat{\mathbf{M}}_{ax} - \hat{\mathbf{\Omega}}) \cdot \overline{\boldsymbol{o}_-\boldsymbol{o}_+} = 0 & \textit{when } \langle \mathbf{B}_{max}, \hat{\mathbf{\Omega}} \rangle > 0, \\ (\hat{\mathbf{M}}_{ax} + \hat{\mathbf{\Omega}}) \cdot \overline{\boldsymbol{o}_-\boldsymbol{o}_+} = 0 & \textit{when } \langle \mathbf{B}_{max}, \hat{\mathbf{\Omega}} \rangle < 0. \end{cases} \tag{B.84}$$

From the geometric point of view, Equation (B.84) gives the intersection of the plane

$$\mathcal{N}_{\overline{\boldsymbol{o}_-\boldsymbol{o}_+}=0\}} := \{u \in \mathbb{R}^3 \big| \mathbf{u} \cdot \overline{\boldsymbol{o}_-\boldsymbol{o}_+} = 0\}$$

with the circle $S^1_{\hat{\mathbf{\Omega}}} - \hat{\mathbf{\Omega}}$ in the case $\langle \mathbf{B}_{max}, \hat{\mathbf{\Omega}} \rangle > 0$, and with $S^1_{\hat{\mathbf{\Omega}}} + \hat{\mathbf{\Omega}}$ in the case $\langle \mathbf{B}_{max}, \hat{\mathbf{\Omega}} \rangle < 0$. Such an intersection in both cases consists of at most two points on $S^1_{\hat{\mathbf{\Omega}}}$, one of which is $\hat{\mathbf{M}}_{ax}$. To solve $\hat{\mathbf{M}}_{ax}$ algebraically, note that it also satisfies $\hat{\mathbf{\Omega}} \cdot \hat{\mathbf{M}}_{ax} = 0$. Combined with Equation (B.84) it yields the following linear equations for $\hat{\mathbf{M}}_{ax}$ with $\left|\hat{\mathbf{M}}_{ax}\right| = 1$

$$\begin{cases} \hat{\mathbf{\Omega}} \cdot \hat{\mathbf{M}}_{ax} = 0, \\ \overline{\boldsymbol{o}_-\boldsymbol{o}_+} \cdot \hat{\mathbf{M}}_{ax} = \hat{\mathbf{\Omega}} \cdot \overline{\boldsymbol{o}_-\boldsymbol{o}_+} \quad when\ \langle \mathbf{B}_{max}, \hat{\mathbf{\Omega}} \rangle > 0, \\ \overline{\boldsymbol{o}_-\boldsymbol{o}_+} \cdot \hat{\mathbf{M}}_{ax} = -\hat{\mathbf{\Omega}} \cdot \overline{\boldsymbol{o}_-\boldsymbol{o}_+} \quad when\ \langle \mathbf{B}_{max}, \hat{\mathbf{\Omega}} \rangle < 0. \end{cases} \tag{B.85}$$

To be more clear, let A be the 2×3 matrix with $A = \begin{bmatrix} \hat{\mathbf{\Omega}}^{\mathrm{T}} \\ \overline{\boldsymbol{o}_-\boldsymbol{o}_+}^{\mathrm{T}} \end{bmatrix}$ and $Y_\pm$ be 2×1 matrix with $Y_\pm = \begin{bmatrix} 0 \\ \pm\hat{\mathbf{\Omega}} \cdot \overline{\boldsymbol{o}_-\boldsymbol{o}_+} \end{bmatrix}$. Then, $\hat{\mathbf{M}}_{ax}$ is a unit vector in the solution space of the linear equation

$$AX = Y_\pm. \tag{B.86}$$

When $\hat{\mathbf{\Omega}}$ and $\overline{\boldsymbol{o}_-\boldsymbol{o}_+}$ are linearly independent, the kernel of the operator A is 1 dimensional, and then the solution space of Equation (B.86) is a line (not necessarily passing through the origin O). When $\hat{\mathbf{\Omega}}$ and $\overline{\boldsymbol{o}_-\boldsymbol{o}_+}$ are linearly dependent, then it should hold $\hat{\mathbf{\Omega}} \cdot \hat{\mathbf{M}}_{ax}$ and $\overline{\boldsymbol{o}_-\boldsymbol{o}_+} \cdot \hat{\mathbf{M}}_{ax}$ can only be either both zero or both non-zero, and then in the case Equation (B.86) has no solution. Upon solving Equation (B.86), $\hat{\mathbf{M}}_{ax}$ can be determined. Equivalently, once $\hat{\mathbf{M}}_{ax}$ (or $\hat{\mathbf{M}}_{in}$) is known, $\mathcal{H}_{\boldsymbol{p}}$ is also known.

B.7 Deducing the position of the magnetic device from the linear map

In this section, we assume that the linear operator $\mathcal{H}_{\boldsymbol{p}}$ is already known, and we deduce equations for calculating the field point $\boldsymbol{p}$.

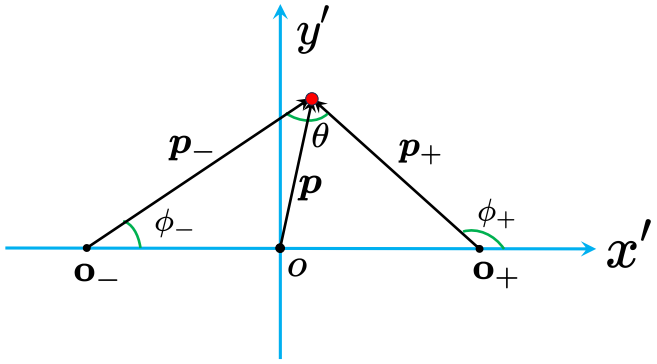

Figure B.3: Definition of an orthonormal frame. In the corresponding coordinate system, $\hat{\mathbf{z}} = [0\ 0\ 1]^{\mathrm{T}}$ is an eigenvector of $\mathcal{H}_{\boldsymbol{p}}$ with eigenvalue σ, and $\mathrm{span}\{\hat{\boldsymbol{p}}_{\pm}\}$ is the $x'oy'$-plane.

For convenience, we choose such an orthonormal frame $x'oy'$, as shown in Fig B.3. In the corresponding coordinate system, $\hat{\mathbf{z}} = [0\ 0\ 1]^{\mathrm{T}}$ is an eigenvector of $\mathcal{H}_{\boldsymbol{p}}$ with eigenvalue σ, and then $\mathrm{span}\{\hat{\boldsymbol{p}}_{\pm}\}$ is the $x'oy'$-plane. As a consequence, there exists $\phi_+, \phi_- \in [0, 2\pi]$ such that $\hat{\boldsymbol{p}}_{\pm} = [\cos\phi_{\pm}\ \ \sin\phi_{\pm}\ \ 0]^{\mathrm{T}}$, and the restriction of $\bar{\mathcal{H}}_{\boldsymbol{p}} = \frac{1}{3}(\mathcal{H}_{\boldsymbol{p}} - \sigma\mathbf{I})$ to the xOy-plane is

$$\begin{aligned}[\bar{\mathcal{H}}_{\boldsymbol{p}}] =& \frac{1}{|\boldsymbol{p}_+|^3}\begin{bmatrix} \cos^2\phi_+ & \sin\phi_+\cos\phi_+ \\ \sin\phi_+\cos\phi_+ & \sin^2\phi_+ \end{bmatrix} \\ &+ \frac{1}{|\boldsymbol{p}_-|^3}\begin{bmatrix} \cos^2\phi_- & \sin\phi_+\cos\phi_- \\ \sin\phi_-\cos\phi_- & \sin^2\phi_- \end{bmatrix}.\end{aligned} \tag{B.87}$$

Then with the notations $a_+ = \frac{1}{|\boldsymbol{p}_+|^3}$ and $a_- = \frac{1}{|\boldsymbol{p}_-|^3}$ we have the following equations

$$\begin{bmatrix} \cos 2\phi_+ & \cos 2\phi_- \\ \sin 2\phi_+ & \sin 2\phi_- \end{bmatrix}\begin{bmatrix} a_+ \\ a_- \end{bmatrix} = \begin{bmatrix} [\bar{\mathcal{H}}_{\boldsymbol{p}}]_{11} - [\bar{\mathcal{H}}_{\boldsymbol{p}}]_{22} \\ [\bar{\mathcal{H}}_{\boldsymbol{p}}]_{12} + [\bar{\mathcal{H}}_{\boldsymbol{p}}]_{21} \end{bmatrix}. \tag{B.88}$$

Moreover, note that the eigenvalues σ_+, σ_- and σ are all known, and from Equation (B.7) we have

$$\sigma_+\sigma_- + 2\sigma^2 = 9a_+a_-\sin^2\theta = 9a_+a_-\frac{1 - \cos 2\phi_+\cos 2\phi_+ + \sin 2\phi_+\sin 2\phi_-}{2}. \tag{B.89}$$

Finally, we have the last constraint:

$$a_+ + a_- = |\sigma| \,. \tag{B.90}$$

Equations (B.88), (B.89) and (B.90) offer 4 equations for 4 variables, a_+, a_-, ϕ_+ and ϕ_-, we can calculate the position of the magnetic device by solving for $\boldsymbol{p}$ relative to frame $x'oy'$, and thus relative to the world coordinate frame. Finally, we can locate the magnetic device under the actuation of two synchronized rotating actuator magnets.

B.8 Conclusion

The model for determining the position of magnetic devices under the actuation of two synchronized rotating permanent magnets has been developed and validated with experimental data. This model for localizing magnetic devices does not rely on an exact match between the immediate poses of the synchronized rotating permanent magnets (characterized by their instantaneous dipole moments) and the magnetic field produced at the magnetic device's location. Consequently, localization of a magnetic device can be achieved under various actuation frequencies. In future work, we will use this model to track a moving magnetic device under the actuation of two synchronized rotating actuator magnets, and we will assess the localization accuracy across different actuation frequencies.

Acknowledgements

The time has come to write the acknowledgments. At this moment, in the quiet of the night, I stand up from my seat and gaze through the window at the distant neon lights flickering on the streets. As I reflect on the journey of my PhD study, my heart is filled with deep reflections and emotions. Through my PhD journey, I have gained valuable insights that will become a significant asset in my life.

First of all, I would like to express my deepest gratitude to my doctoral promoter, Prof. Sarthak Misra, for giving me the opportunity to join the Surgical Robotics Lab. You have not only imparted academic knowledge to me but also shared your methods of work and life wisdom, which have benefited me immensely. I will keep that in my mind, "Do things in the right way". Your mentorship has made a profound impact on my life. I would also like to express my sincere appreciation to my doctoral supervisor, Dr. Islam S. M. Khalil, for patiently guiding me through experiments and paper writing during our weekly progress meetings. You have not only shared your knowledge and skills but also motivated me to develop both personally and professionally. Your wisdom, patience, and encouragement have been immensely valuable to me. Additionally, I want to express my sincere gratitude to my master supervisor, Prof. Fengping Li, for his comprehensive support, including academic guidance, job recommendations, and financial assistance throughout my master's and PhD studies.

I would like to express my appreciation to the members of my reading committee: Prof. Minghui Hong from Xiamen University, Prof. Wei Xue from Wenzhou University, and Dr. Prashant Sharma from University Medical Center Groningen. I am grateful for the time and effort you have dedicated to reviewing my thesis. Your thorough and insightful feedback is invaluable in enhancing the quality of my work. Additionally, I want to thank Dr. Brandon Peterson from University Medical Center Groningen and Dr. Bohuan Lin from Xi'an Jiaotong-Liverpool University for accepting our invitation to serve as members of my thesis committee.

I would like to extend my gratitude to the staff at BBT: Hélder, Henk, Henny, Patrick, Romana, Inge, Theo, Jelmer and Mohammad-Ali Shahbazi. The insightful discussions you contributed during the lunch meetings and

Kolff days have been inspiring. Special thanks to Ed for assisting in fabricating parts for my experimental setup and reviewing the Dutch summary of my thesis. Every time you come to SRL to help us solve problems and talk with us, I am always inspired by your optimistic and cheerful spirit. I'm grateful to Ina for handling orders when I first arrived, unfamiliar with the purchasing process, and to Besty for her assistance in ordering items. Thanks also to Wytse for aiding in processing the necessary documents for my visa application to return to the Netherlands. I also extend my appreciation to other staff of the BBT: Wya, Willy, Willem, Hans, Joop, Jelly, Reinier, Gésinda, Sonja and Marja. Thank you for your assistance during my stay at BBT.

Special thanks to Zihan and Zhuoyue for being my Paranimfens. Zihan, thank you for sharing your image tracking code with me. You are not only outstanding academically but also socially adept. I am confident that you are becoming a rising star in the field of soft robotics research. Zhuoyue, thank you for teaching me photography techniques. Your insightful perspectives on electronics, cars, and photography are impressive. I believe your future life will be colorful and full of achievements. Next, I would like to thank the members at SRL. Jeanine, thank you for coordinating the daily meeting arrangements. Venkat, I appreciate you sharing your academic PowerPoint with me. Fouzia, thank you for teaching me the correct pronunciation of every lab member's name during my initial visit to SRL at the University of Twente. Jakub, your informative tour of the laboratory and patient explanations of the experimental equipment left a lasting impression on me. Chuang, I am grateful for our collaboration in building our experimental platform. Mert, your essential support in printing parts significantly contributed to the development of my experimental setup. Kaixuan, I benefited greatly from your guidance on operating the rheometer. Chen, thank you for instructing me on how to operate your electromagnetic coil device. My thanks also go out to the other members of SRL: Alper Denasi, Christoff M. Heunis, Sumit Mohanty, Federico Ongaro, Theodosia Lourdes Thomas, Morteza Mojarradi, Mina M. M. Farag, Guilherme Phillips Furtado, Luigi Capuano, Michiel Richter, Juan Julian Jesus Huaroto Sevilla, Yu-Hsiang Lin, Simon Frieler, Lukas Masjosthusmann, Yuxin Jin, Fragkiskos Fourlas, Yiyang Li, Adriana Vasi, and Antonio Lobosco. Thank you for your help during my time at SRL.

I would like to show my appreciation to my colleagues. Jeroen, Hong-

ping, Zhiwei and Aldona, my office mates. Thank you for your generous assistance when I initially joined the office. Yuanlong, it's been a pleasure meeting you in Groningen. Thank you for inviting me to your home for meals several times; your cooking skills are excellent. Through our conversations, I've discovered that we have many similar life experiences, which has created a lot of resonance between us. I wish you achieve your desired goals in your career in the future. Yong Chen, you are modest, cautious, and helpful. Thank you for helping me store items temporarily. Ke Ren, thank you for the sincere conversation and advice. Chengxiong and Kaiqi, looking back on our first journey together to the Netherlands brings forth delightful memories. Captain Yuan (Lu), thank you for your assistance with photography during Kolff Day. To all my other colleagues at BBT—Yong Liu, Yuanfeng, Liangliang, Lu Ge, Huaiying, Xiaoxiang, Ruifang, Kecheng, Weihao, Dayuan, Shuang Tian, Sidi, Guimei, Jie Gao, Siran, Fenghua, Tianqi, and Zhuoyi—your help and support made my time in Groningen enjoyable.

I'd also like to extend my gratitude to the friends I met in Groningen. Dr. Bohuan, we met under very coincidental circumstances, and I feel so fortunate to have met you. During many weekends in Groningen, our discussions on various interesting topics were highly enriching for me. What deeply impressed me was your profound mathematical expertise in explaining mathematical conclusions from multiple perspectives. I believe you will achieve great success in your professional field. Ting He, thank you for taking me to your laboratory to collect ultrapure water for my experiments. Dr. Qinghong, I happened to meet you on the 11th floor of Building 3215, and your warm smile made you come across as very friendly. Thank you for providing me with timely and valuable information, which has helped me make the right decisions.

Lastly, my deepest gratitude goes to my family. To my grandparents for their attentive care throughout my childhood, to my parents for their decades of dedication that supported my educational journey, and to my sister, brother-in-law, and niece for their encouragement during challenging times.

Zhengya Zhang
Wenzhou, July 2024